Dynamics of ion Coulomb crystals

Von der Fakultät für Mathematik und Physik
der Gottfried Wilhelm Leibniz Universität Hannover
zur Erlangung des Grades

Doktor der Naturwissenschaften
Dr. rer. nat.

genehmigte Dissertation von
M.Sc. Lars Timm

2023

Referent/-in:
Prof. Dr. Luis Santos
(Gottfried Wilhelm Leibniz Universität Hannover)
Prof. Dr. Tanja E. Mehlstäubler
(Gottfried Wilhelm Leibniz Universität Hannover)
Prof. Dr. Hendrik Weimer
(Technische Universität Berlin)

Korreferentin:
Prof. Dr. Giovanna Morigi
(Saarland University)

Tag der Disputation: 06.09.2023

Abstract

The field of quantum simulations has achieved a remarkable success through the development of highly controllable and accessible quantum platforms, which provide insights into the microscopic properties of complex large-scale systems that are otherwise difficult to analyze. Many of the platforms utilized in this pursuit are derived from the field of atomic, molecular, and optical physics. One particularly popular candidate is provided by trapped ions, whose vibrational and electronic degrees of freedom can be effectively combined through laser pulses to engineer desired model Hamiltonians or quantum circuits. Trapped ions constitute as well the basis for modern atomic clocks, the most precise frequency standards currently available. They find further applications in metrology, geodesy, and fundamental physics experiments.

In this Thesis, we investigate the dynamics of vibrational modes in trapped ion crystals, utilizing them as a versatile platform to explore various many-body phenomena.

We first focus on the expansion dynamics of local excitations and on heat transport within ion crystals hosting structural defects that undergo a sliding-to-pinned transition. We observe a significant reduction in conductivity when the crystal symmetry is spontaneously broken during the transition, and show that resonances between crystal eigenmodes lead to distinct softening signatures associated with energy localization. We then delve into the effects of thermal and quantum fluctuations on the vibrational modes of ion crystals near two distinct structural transitions. We observe the emergence of a prolonged symmetric phase stabilized by thermal and quantum fluctuations, and develop effective theories that reduce the degrees of freedom to the modes that drive the transitions.

Finally, we discuss how to engineer spin-orbit coupling and on-site interaction energies for vibrational quantum excitations using two different external driving schemes. While the simulation of spin models with ions typically involves the use of two electronic states, we propose interpreting the two local oscillation modes in an ion crystal as a pseudospin. We show how using Floquet engineering ideas allows for spin flips in Coulomb-induced vibron hopping, resulting in a non-trivial coupling between spatial motion and spin evolution, that results in a markedly non-

Abelian dynamics. Subsequently, we explore the simulation of Hubbard models in trapped ions by coupling the vibrational Fock states to an internal level system. Our findings include the observation of bound states in the strong interaction limit of the resulting Jaynes-Cummings-Hubbard model.

By investigating these topics, we aim to contribute to the understanding of vibrational dynamics in trapped ion crystals, and shed light on their potential for simulating condensed matter systems, offering insights into phenomena that are otherwise challenging to explore.

Keywords

- Trapped ions
- Nanofriction
- Phase transitions
- Localization
- Topological defects
- Quantum simulation
- Spin-orbit coupling
- Hubbard model

Zusammenfassung

Quantensimulationen haben durch die Entwicklung hochkontrollierbarer und zugänglicher Quantenplattformen zahlreiche Einblicke in die mikroskopischen Eigenschaften komplexer Vielteilchensysteme ermöglicht.

Viele der in diesem Feld verwendeten Plattformen stammen aus dem Bereich der Atom-, Molekül- und Optikphysik.

Ein besonders beliebter Kandidat ist die Verwendung von gefangenen Ionen, deren Schwingungs- und elektronische Freiheitsgrade durch Laserpulse effektiv kombiniert werden können, um gewünschte Modell-Hamiltonians oder Quantenalgorithmen zu implementieren.

Gefangene Ionen bilden auch die Grundlage für moderne Atomuhren, die derzeit genauesten Frequenzstandards. Sie finden weitere Anwendungen in der Metrologie, Geodäsie und in Experimenten der Grundlagenphysik.

In dieser Arbeit untersuchen wir die Dynamik von Schwingungsmoden in gefangenen Ionenkristallen und nutzen sie als vielseitige Plattform zur Erforschung verschiedener Vielteilchenphänomene.

Wir konzentrieren uns zunächst auf die Expansionsdynamik lokaler Anregungen und den Wärmetransport in Ionenkristallen mit strukturellen Defekten, die einen Aubry-Übergang durchlaufen. Wir beobachten eine signifikante Reduzierung der Leitfähigkeit, wenn die Kristallsymmetrie während des Übergangs spontan gebrochen wird, und zeigen, dass Resonanzen zwischen den Eigenmoden des Kristalls zu einer Wiederherstellung des Energietransports führen.

Anschließend widmen wir uns den Auswirkungen thermischer und quantenmechanischer Fluktuationen auf die Schwingungsmoden von Ionenkristallen in der Nähe von zwei verschiedenen strukturellen Phasenübergängen. Wir beobachten die Vergrößerung der symmetrischen Phase, die durch thermische und quantenmechanische Fluktuationen stabilisiert wird, und entwickeln effektive Theorien, die die Freiheitsgrade auf diejenigen Moden reduzieren, die die Übergänge treiben.

Schließlich diskutieren wir, wie Spin-Bahn-Kopplung und Wechselwirkungsenergien für lokale Schwingungsquanten mithilfe von externen Anregungsschemata erzeugt werden können.

Während die Simulation von Spin-Modellen mit Ionen normalerweise zwei elektronische Zustände berücksichtigt, schlagen wir vor, die beiden lokalen Schwingungsmodi in einem Ionenkristall als Pseudospin zu interpretieren.

Wir zeigen, dass durch die Verwendung von ”Floquet-Engineering” Spinflips bei der gekoppelten Bewegung der Ionen auftreten, was zu einer nichttrivialen Wechselwirkung zwischen räumlicher Bewegung und Spin führt, die resultierende Dynamik ist nicht-Abelsch.

Anschließend untersuchen wir die Simulation von Hubbard-Modellen in gefangenen Ionen, indem wir die Fock-Zustände der Schwingungsmoden mit einem internen Niveausystem koppeln. Unsere Ergebnisse umfassen die Beobachtung von gebundenen Zuständen im Bereich starker Wechselwirkung des resultierenden Jaynes-Cummings-Hubbard-Modells.

Durch die Untersuchung dieser Themen tragen wir zum Verständnis der Schwingungsdynamik in gefangenen Ionenkristallen bei und bieten Einblicke in deren Potenzial zur Simulation von Systemen der Festkörperphysik, um Phänomene zu erforschen, die sonst schwer zugänglich sind.

Schlagwörter

- Gefangene Ionen
- Nanoreibung
- Phasenübergänge
- Lokalisierung
- Topologische Defekte
- Quantensimulation
- Spin-Bahn-Kopplung
- Hubbard Modell

Contents

1 Introduction **1**

2 Trapped ion systems **5**

- 2.1 Trapping ions 5
  - 2.1.1 Paul traps 7
  - 2.1.2 Optical trapping and surface traps 9
- 2.2 Laser cooling 11
  - 2.2.1 Doppler cooling 12
  - 2.2.2 Sub-Doppler cooling 13
- 2.3 Ion Coulomb crystals 17
  - 2.3.1 Crystal defects 21
  - 2.3.2 Vibrational system 22
  - 2.3.3 Phonon modes 26
  - 2.3.4 Quantum vibron model 28
  - 2.3.5 Higher-order expansion 29

3 Nanofriction and solitons **31**

- 3.1 Introduction 31
- 3.2 The Frenkel-Kontorova model 33
  - 3.2.1 Continuum approximation 35
  - 3.2.2 Ground states and solitonic excitations 38
  - 3.2.3 Finite-size Frenkel-Kontorova model 44
  - 3.2.4 Quantum Frenkel-Kontorova model 45
- 3.3 Emulation of nanofriction in ion crystals 47
  - 3.3.1 Lattice approach 47
  - 3.3.2 Kink approach 51

4 Energy transport in trapped ion chains with defect **57**

- 4.1 Energy localization in trapped ion crystals with topological defects . 58
  - 4.1.1 Blockade of an energy wave packet 58
  - 4.1.2 Energy imbalance and non-linear resonances 61

4.2 Heat transport in ion Coulomb crystals 66
4.2.1 Langevin heat baths 67
4.2.2 Dynamical equations and heat flux 68
4.2.3 Linearized theory 70
4.2.4 Steady-state temperature profiles 73
4.2.5 Heat flux 80
4.2.6 Resonances 81
4.3 Conclusion 82

5 Fluctuations and phase transitions 85
5.1 Thermal spectrum at linear-to-zigzag transition 85
5.1.1 Molecular dynamics simulations 87
5.1.2 Experimental measurements 92
5.1.3 Effective theory for the mode coupling 93
5.1.4 Conclusion 95
5.2 Quantum fluctuations close to finite Aubry transition 97
5.2.1 Linear ion chain 97
5.2.2 Static quantum effects 99
5.2.3 Tunneling dynamics 104
5.2.4 Conclusion 107

6 Vibron-Hubbard models in ion Coulomb crystals 109
6.1 Non-Abelian dynamics in the vibrational system 110
6.1.1 Floquet driving and hopping matrix shaping 110
6.1.2 Non-Abelian plaquette dynamics 116
6.1.3 Non-Abelian dynamics in a square lattice 120
6.2 Jaynes-Cummings-Hubbard systems in trapped ions 122
6.2.1 Jaynes-Cummings-Hubbard Hamiltonian 122
6.2.2 Superfluid-to-Mott insulator transition in trapped ions . . . 126
6.2.3 Bound polariton states 127
6.3 Conclusion 131

7 Summary and Outlook 133

Glossary 169

Chapter 1

Introduction

In their quest to explore and comprehend the intricacies of nature, quantum physicists face challenges in accessing and controlling the individual constituents of the systems they study. Consequently, their observations often revolve around macroscopic quantities such as electric or thermal conductivities, specific heat, friction coefficients, or total magnetization. Over the years, their measurement and theoretical analysis have led to remarkable discoveries, such as superfluidity, superconductivity, and quantum Hall effects, among others [1–5]. However, the analysis and simulations of the underlying many-body systems are hindered by the exponential growth of the Hilbert space dimension with particle number, imposing limitations on our understanding.

To overcome these limitations, researchers have proposed simulating the systems of interest using artificial quantum systems that provide increased control over individual particles and interactions [6]. This bottom-up approach, employed in various implementations stemming from atomic, molecular, and optical (AMO) physics, utilizes single photons, ultracold atoms and molecules, and, notably, trapped ions [7–31]. Each platform offers different advantages in terms of coherence times, interactions, and accessibility, making them suitable to varying degrees for simulating many-body systems of interest, as for example spin and Hubbard lattice models [32, 33].

Trapped ion systems are nowadays at the forefront of quantum simulation and computation, utilizing the electronic levels of the ions as qubits, and employing common motional modes as buses for two-qubit operations [8, 17, 19, 24]. These systems allow for the exploration of diverse crystal geometries resulting from the interplay between the long-range Coulomb repulsion and trap confinement, leading to one-, two-, and three-dimensional crystals separated by structural phase transitions [34–40]. These transitions break the $\mathbb{Z}_2$ symmetries of a linear ion arrangement, providing opportunities to create crystalline defects within the system. Interestingly, these findings open new possibilities for the emulation of paradigmatic models in the field of nanofriction, encompassing the motion of atomic interfaces [41–48].

This Thesis places a particular emphasis on the observed sliding-to-pinned transition in triangular ion ladders, shedding light on the dynamics of ions within such structures. The low-energy dynamics of these systems is determined by the spectrum of phonon modes, which crucially depend on the equilibrium dictated by the external confinement. Understanding these dynamics is essential for both quantum simulation applications and advanced laser cooling schemes [49–53].

The structure of the Thesis is as follows:

- The Thesis starts with two introductory chapters, in which we set the frame for the rest of the Thesis. In Chapter 2, we review the physics of trapped ion systems, including how to trap and cool ions, and basic elements of the theory of ion Coulomb crystals [38, 39, 54–57]. Chapter 3 briefly introduces nanofriction, and in particular the Frenkel-Kontorova model, and how to emulate nanofriction with ion crystals [41, 43, 45, 46, 58–60].

- Chapter 4 investigates how a topological defect modifies energy transport in an ion Coulomb crystal [61–64]. We explore the delocalization dynamics of local vibrational excitations through the system, observing a controllable valve-like behavior of topological defects. While kinks in the sliding phase are transparent to energy flow, they significantly handicap the dynamics when the trap confinement is tuned into the pinned phase. This behavior arises from the creation of asymmetric phonon modes at the sliding-to-pinned transition. Nonlinear resonances between phonon modes partially weaken the energy blockade, leading to a delicate interplay between harmonic energy localization and nonlinear long-term delocalization. Additionally, we analyze the heat conductivity of ion crystals in the presence of solitonic defects, finding a similar reduction in heat flux in the pinned phase, accompanied by the emergence of abrupt temperature gradients in the steady state. The heat flux exhibits intricate dependencies on confinement arising from the density of trap configurations that result in degenerate phonon modes.

- Chapter 5 focuses on the nonlinear dynamics of the system near structural phase transitions [36, 65, 66]. In the first part, we investigate the motional mode spectrum under the influence of thermal fluctuations at the linear-to-zigzag transition. Numerical simulations support the experimental observation of a smooth crossover in mode frequencies, differing from the soft mode predicted by phonon mode calculations. We attribute this behavior to thermally activated switches between the two equilibrium configurations in the symmetry-broken phase, with fast-rate switches leading to a time-averaged maintenance of system symmetry. Employing a higher-order expansion around this effective crystal shape, we derive an effective mode coupling model for low-energy modes, which agrees well with mode frequencies obtained from Fourier analysis of numerical simulations. Furthermore, we study the manifestation of the quantum nature of the ions in the vicinity of the sliding-to-pinned transition of topological defects. Employing a collective excitation formalism, we distill the essential degree of freedom driving the transition from the many-body problem, and identify a finite window of observable quantum tunneling effects in the pinned phase. Similar to the thermal switches in the first part, these effects connect the two classical equilibria and alter the phonon mode spectrum. We also provide estimates for the required temperature scale at which coherent quantum tunneling dominates the incoherent jumps induced by temperature.

- Finally, in Chapter 6, we present two methods to manipulate the quantum walks of vibrational excitations (vibrons), enabling simulations of spin-orbit coupled particles and interacting Hubbard physics [23, 67–69]. We interpret the two decoupled vibron modes of individual ions as a spin-1/2 degree of freedom, employing Floquet engineering to create anisotropic two-dimensional hopping matrices that allow for spin flips when vibrons move within the lattice structure. The non-commutativity of the hopping matrices along different lattice axes introduces a dependence of the spin state of the vibron on its trajectory and vice versa. We demonstrate this form of spin-orbit coupling in a simple square plaquette, extending it to a larger lattice structure. While lattice vibrations of ion crystals typically do not interact, we discuss the possible coupling to the electronic level structure through sideband dressing, resulting in tunable local interaction strengths controlled by laser intensity and detuning. The resulting JCH model has been analyzed in coupled cavities and trapped ions, featuring a superfluid-to-Mott insulator transition. Building on these findings, we report on the creation of bound states in the many-body spectrum and study their motion within the lattice structure.

In summary, this Thesis advances the field of (quantum) many-body dynamics in trapped ions, showcasing its versatility as a tool for addressing questions arising in crystalline systems.

Chapter 2

Trapped ion systems

2.1 Trapping ions

In order to map out and understand the physics of atoms and eventually harness their properties for a series of applications researchers are motivated to improve the obtainable experimental signals [70]. In the early days of atomic, molecular and optical (AMO) physics, this translated into enlarging the interrogation time for a better signal-to-noise ratio, improving the isolation of the atoms from its environment, and preparing them in a desirable configuration [71, 72]. Although these challenges remain up to date, their boundaries have shifted immensely due to the invention of several key techniques. The two main examples for developments that boosted the field are trapping techniques and laser cooling. Both of them have been awarded with Nobel prizes [73–80]. They enabled the transition from experiments on atomic beams with severe limitations on interrogation times and state preparation, to trapped atoms and ions with much improved readout and preparation precision.

In order to confine charged atoms in a defined spatial region physicists can rely on the coupling between their dynamics and electromagnetic fields [81]. This coupling comes naturally due to the electromagnetic force, and hence simplifies their control in comparison to neutral atoms, for which the connection needs to be engineered, e.g. via laser radiation in a magneto-optical trap [53, 82]. However, all trapping techniques for charged particles face a common obstacle, which is known as Earnshaw's theorem [83]. From the Poisson equation in vacuum for a static electric potential $\Phi = ax^2 + by^2 + cz^2$ it follows that $a + b + c = 0$, or as stated in the words of the theorem: No static electric field can be confining in all three dimensions. Researchers have developed two fundamental ways to circumvent Earnshaw and reach three-dimensional confinement, today known as Penning traps and Paul traps [79, 84].

The former uses a homogeneous magnetic field in order to force the charged particles onto a tight cyclotron orbit perpendicular to the field lines [55]. For strong enough magnetic fields this can be used to counter the deconfining effect of an electric quadrupole field. In Dehmelt's group this technique was first used to trap single electrons and subsequently investigate their properties, in particular its magnetic moment [80, 85–87]. Although this approach bears some advantages, another approach celebrates nowadays a wide success in the field of trapping charged particles.

Simultaneously to the advances made by Dehmelt, Paul's group investigated the focusing of neutral particles with magnetic and electric dipole moments by electromagnetic multipole fields [71, 88–90]. Initially, the particles of a beam passed a series of lenses with alternating sign in the field configurations, which lead to an effective focusing if certain conditions for the spacing of the lenses were met. Paul realized that the time-dependent electric field the particles experience in their own reference frame can be created in the lab frame to confine particles in his so-called "Ionenkäfig" [91]. His ideas are the fundament of modern-day experiments in the field of quantum computing, metrology and condensed matter physics with trapped ions [7, 8, 11, 17, 19, 27, 28, 38, 92–95].

The Paul trap would have not been as successful as it is without the invention of the laser and the associated cooling, manipulation, and readout schemes [53, 56, 57]. With the upcoming of the first lasers, they were first used in the 1970s to slow down neutral and charged atoms via Doppler cooling and lead to the crystallization in the case of ions [78, 96–98]. While the achieved level of isolation and readout is already remarkable, enabling for example the first electronic state detection via electron shelving [99], more involved sub-Doppler schemes were soon after realized, most prominently resolved sideband cooling [100–103]. This marks the departure from the classical motion of the particles, and the entrance into a fully quantized description. Subsequently, physicists succeeded in preparing non-classical motional states of single ions in Paul traps [104, 105]. Today the manipulation of the internal and motional states of single ions is an established technique with fidelities close to perfection and opens not only possibilities to study the particles themselves, but also to build highly sensitive quantum sensors for metrological applications and quantum computing devices [27, 38, 94, 95, 106–123].

In the following sections, we introduce in detail the physics of ions trapped in Paul traps, focusing on the vibrational dynamics of crystalline structures that form for sufficiently low temperatures, reachable by Doppler cooling. In the last part of the chapter, we discuss the discovery of crystal defects, which play a key part in following chapters. All together, the concepts presented here are fundamental for the understanding of the results shown in the second part of this Thesis.

2.1.1 Paul traps

The electrode configuration in a Paul trap, schematically shown in Fig. 2.1, produces an electric potential that can be written in the form [57] :

$$\Phi = \sum_{\mu=x,y,z} \left(\frac{u_{dc}}{2} \phi_\mu + \frac{u_{rf}}{2} \phi'_\mu \cos(\Omega_{rf} t) \right) \mu^2 \tag{2.1}$$

where u_{dc} and u_{rf} denote the relative static and oscillating field strengths which depend on the trap geometry and voltages applied to the electrodes. ϕ_μ and ϕ'_μ describe the anisotropy of the trap and Ω_{rf} is the frequency of the radiofrequency (rf) drive. The Poisson equation $\nabla^2 \Phi = 0$ in the vacuum between the electrodes is fulfilled for $\sum_\mu \phi_\mu = 0$ and $\sum_\mu \phi'_\mu = 0$, which is the central statement of Earnshaw's theorem, as previously mentioned [81, 83]. In a static field this leads to a repulsive potential in at least one dimension.

In a typical linear Paul trap, $\phi'_z = 0$ is chosen such that the confinement along z is purely given by the static term, it follows that $\phi'_x = -\phi'_y$. In addition, we normalize the static potential by fixing $\phi_z = 1$. The Newtonian equations of motion that result from this potential are then commonly written in terms of the so-called stability parameters a_μ and q_μ

$$\left[\frac{d^2}{dt^2} + \frac{\Omega_{rf}^2}{4} (a_\mu + 2 q_\mu \cos(\Omega_{rf} t)) \right] \mu = 0 \tag{2.2}$$

$$a_\mu = \frac{4 Q u_{dc}}{m \Omega_{rf}^2} \phi_\mu, \quad q_\mu = \frac{2 Q u_{rf}}{m \Omega_{rf}^2} \phi'_\mu \tag{2.3}$$

where m is the particles mass and Q its charge.

The three independent equations (2.2) have the form of Mathieu equations and can be solved with the help of Floquet's theorem [54, 124–128]. This theorem states that the solutions of a linear differential equation with a time-periodic coefficient matrix have the form $\mu(t) = e^{s_\mu t} f_\mu(t)$. $f_\mu(t)$ is periodic in time with the same period as the coefficient matrix, and hence we can write it in a Fourier series $f_\mu = \sum_n f_\mu^n \exp(-in\Omega_{rf} t)$, and plug this ansatz into Eq. (2.2). We obtain a recurrence relation for the coefficients f_μ^n that can be formally solved, giving the dependence of s_μ and $f_\mu(t)$ on the stability parameters a_μ and q_μ [129]. Interestingly, there exist regions in the parameter space of a_μ and q_μ for which the trajectory of the ion stays bound for all times, denoted as the stability regions of the trap. The most important one can be found close to the origin, i.e. for $|a_\mu|, q_\mu^2 \ll 1$ (see Fig. 2.1), so that we can expand the solution to lowest order in q_μ and find

$$\mu(t) \propto \cos(\omega_\mu t)(1 + \frac{q_\mu}{2} \cos(\Omega_{rf} t)) \tag{2.4}$$

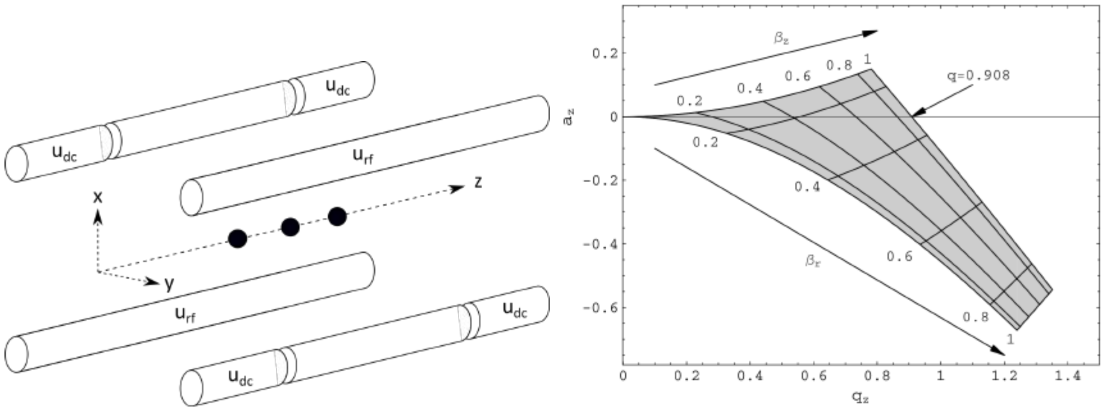

Figure 2.1: Left: Schematic depiction of the electrode alignment in a linear Paul trap. **Right:** Minimal stability region as a function of the Mathieu stability parameters. Picture taken from Ref. [54].

where $4\omega_\mu^2 = \Omega_{rf}^2(a_\mu + q_\mu^2/2)$ is the secular oscillation frequency of the trap [54, 129].

Note that the condition for a stable trap configuration simplifies close to the origin of the parameter space to $a_\mu + q_\mu^2/2 > 0$, which needs to be valid for all $\mu = x, y, z$. Due to our choice of ϕ_z and ϕ_z', the potential along z is always confining, but it is not obviously so for the two other directions. The motion with the secular frequency is superimposed by a term oscillating with the driving frequency Ω_{rf}, as seen in the trajectory depicted in Fig. 2.2. This effect is called micromotion [74, 129, 130]. It comes from the fact that we employ a fast rf drive to create an effective time-averaged confinement along x and y and is absent when the ion is placed exactly on the z axis of the trap. For the stability region close to the origin we have $\omega_\mu \ll \Omega_{rf}$ so that the period of this so-called micromotion is much shorter than $2\pi/\omega_\mu$. However, throughout this Thesis we are interested in effects that occur on a timescale given by the secular frequencies of the trap. We hence separate the micromotion from the discussion due to its off-resonant frequency. When we neglect the micromotion, the dynamics of the charged particle can be described by a harmonic oscillator potential with frequencies ω_μ which we write in the form

$$V = \frac{m\omega_z^2}{2}\left(z^2 + \alpha^2(x^2 + \beta^2 y^2)\right) \tag{2.5}$$

where we have introduced the trap aspect ratios

$$\alpha = \frac{\omega_x}{\omega_z}, \qquad \beta = \frac{\omega_y}{\omega_z} \tag{2.6}$$

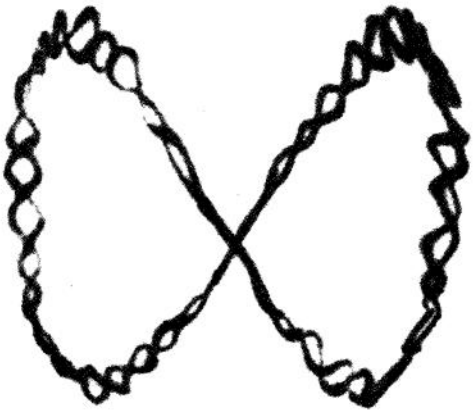

Figure 2.2: Trajectory of a charged microparticle in a Paul trap, taken from Ref. [74]

as the main parameters for the trap configuration. They can be controlled by the applied electrode voltages, but also depend on the charge to mass ratio of the particle, which is of importance in the case of an ion mixture of different species.

2.1.2 Optical trapping and surface traps

Although capturing charged atoms with radiofrequency traps has been very successful, there exist limitations of their applicability. One issue already discussed is that the radiofrequency driving causes micromotion in two-dimensional ion crystals, which in turn can contribute to the heating of the system. Moreover, Paul and Penning traps offer only a limited control over the positions and vibrational frequencies of the ions in the crystal. The ions align in a self assembled way, settling in the minimal energy configuration, which depends on the trap frequencies and the ion number, in addition the quadratic effective potential leads to an inhomogeneous ion density [21, 34, 131–133]. The distances between neighboring particles are smallest in the central region of the trap, while the ions at the edges of the crystal structure are further apart. This effect is particularly relevant when the number of particles is scaled up, as a sufficient ion spacing needs to be maintained for their individual laser addressing [16]. While in general this level of control suffices for the study of structural transitions, when the trap configuration is altered it can create problems for quantum simulation applications, especially in two-dimensional models [28].

These arguments have prompted trapped ion researchers to explore possible extensions or alternatives to conventional trap techniques. A natural choice is the usage of segmented and surface traps, which builds on the Paul trap approach [30, 134–140]. Segmented Paul traps use multiple electrodes to create separated trapping regions via their electrostatic potentials. This design opens the possibility to store several chains of ions, which by default do not interact since they share no motional modes, but can be transferred into the same trap region to e.g. apply quantum gates if necessary. Surface traps add more flexibility, as the integration of the electrodes into a chip enables the creation of a two-dimensional array of trapping regions. Experiments pursuing these approaches have demonstrated already the trapping and shuffling of ions in different trap geometries [141–147]. However, the usage of micro-fabricated surface electrode traps brings on its own some disadvantages. Typically, the depth of the trap potentials is significantly reduced in comparison to three-dimensional Paul traps, which makes the loss of particles more likely [148]. Also, the short distance between the ions and the electrodes themselves makes them prone to electric field noise [149–152]. Researchers have worked towards the compensation and reduction of noise sources, by e.g. reducing the temperature of the trap chip [153–156]. In addition, the integration of the manipulation and readout mechanisms into the chip is another direction of research that enables the upscaling of the system [157–161]. Most of these efforts are targeted at analogue quantum simulations using the internal degrees of freedom of the particles as constituents.

A young approach to circumvent the issues of rf field traps aims to use the dipole force exerted on the ions by strong focused lasers [162–165]. This technique is widely used in the field of neutral atom physics, where the particles do not react to electric fields due to their missing charge monopole [15, 166].

The basic mechanism behind this way of confining atoms can be understood in a classical picture of a particle with an electric dipole moment induced by the lights electric field. Consequently, the interaction of the induced dipole with the electric field creates a potential proportional to the lights intensity $I(\vec{r})$. When the relevant physics of the atom is approximated by an electron that is elastically bound to the nucleus with frequency ω_0 a small derivation for the atoms polarizability yields

$$U_{dip}(\vec{r}) = \frac{3\pi c^2}{2\omega_0^3}\frac{\Delta\omega}{\delta} I(\vec{r}) \tag{2.7}$$

where δ describes the lasers detuning from ω_0, c is the speed of light. $\Delta\omega$ describes the damping of the electrons motion via radiation due to its acceleration. It becomes clear that depending on the detuning high intensity regions become repellent or attractive for the atom in the ground state. This classical picture can be complemented by a derivation of the dressed states in a fully quantum mechanical picture which reveals that the excited state experiences an inversed dipole potential. The functional dependence of the created potential agrees with the classical derivation, ω_0 plays the role of the transition frequency that is adressed by the light and $\Delta\omega$ is its natural linewidth. While a single laser beam creates a single trap region, the creation of a standing wave by counter-propagating beams creates a periodic lattice potential for the atoms [12, 20, 167–170]. This technique impresses with its flexibility concerning the possible crystal structures and bears the opportunity to shuffle single particles around by tunable laser beams, transporting atoms between different traps [171, 172]. Another major advantage of dipole traps is the supression of micromotion, as the oscillation frequency of the confinement field, the electric field of the laser light in this case, lies in the optical regime in comparison to the rf electric field of Paul traps [164]. However, in practice, there are some drawbacks.

The off-resonant absorption of photons that changes the electronic state of the ion will lead to the loss of the particle, as the light field becomes repulsive [165, 173–175]. Moreover, with available laser powers the depth of the created confinement is typically on the order of several mK, much lower than the trap depths achievable in Paul traps. This necessitates the initial trapping in an rf field and the subsequent transfer into an optical trap after the application of a laser cooling routine. While the additional issues of laser-beam amplitude and wavevector noise are inherent to optical trapping techniques, the coupling of the ions to electric fields introduces additional challenges. As already discussed, according to Earnshaw's theorem any electrostatic potential adds a deconfining force, and consequently the depth of the optically-created potential is reduced. In particular, this holds for the electric potential from the electrodes of the Paul trap as well. Unwanted electric stray fields aggravate this issue as they can tilt the potential landscape experienced by the ion, and further lower the effective trap depth. Hence, their careful compensation is essential to enable the confinement of ions by laser fields [176].

Note that the charge of the ions themselves creates an electric field experienced by the other particles in a multi-ion crystal.

When the ions are confined by an array of laser beams, the local trapping potential is affected by the Coulomb repulsion inside the specific geometry, and makes it not only ion-dependent, but also further weakens the confinement strength. Due to these complications mixed experiments employ rf traps due to their robust and deep confinement, while simultaneously shaping the vibrational properties of the ions at will by shining in additional focused laser beams [177].

2.2 Laser cooling

The cooling of ions trapped in rf fields by means of light fields is a pillar of modern-day experiments [53, 57, 178]. It counters the heating of the particles due to imperfections of real setups, leads to the crystallization of the system in the multi-ion case, and reduces the thermal fluctuations of the ions, possibly up to a point for which a quantum mechanical description is required [49, 56, 97, 100, 103, 131]. The

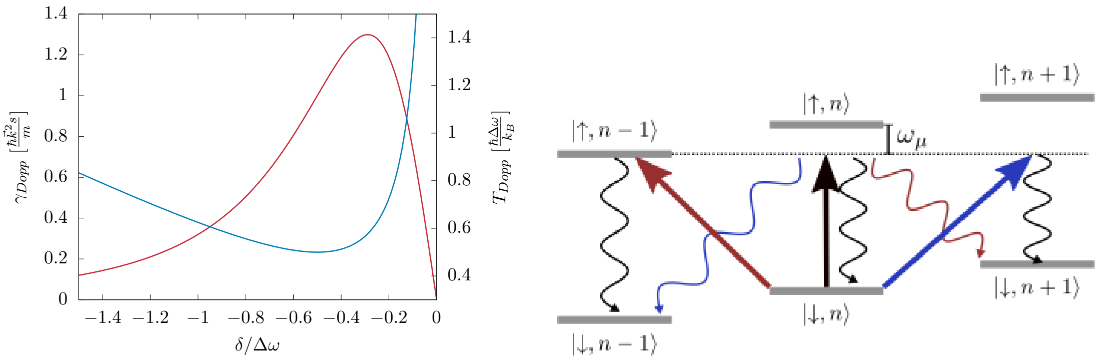

Figure 2.3: Left: Doppler damping rate γ_{Dopp} (red), given by Eq. (2.8), and the Doppler bath temperature T_{Dopp} (blue), given by Eq. (2.9), as a function of the detuning δ. **Right:** Schematic depiction of resolved sideband transitions between the electronic ground state manifold $|g, n\rangle$ and the excited states $|e, n\rangle$. The carrier (black) transition and the sideband transitions are denotes by arrows, the spontaneous decay is sketched by the wavy arrows.

techniques available can be categorized by their attainable temperature regimes into Doppler and sub-Doppler cooling.

2.2.1 Doppler cooling

Usually, the absorption of directed photon momenta is employed in the first experimental stage. When the frequency of a running-wave laser field is tuned close to resonance with a dipole transition, photons are absorbed by the atom, changing the atoms center of mass momentum by the photon momentum $\hbar\vec{k}$ [163, 179]. Subsequently, on the timescale of the transition linewidth ($\approx$ ns), the photon is either spontaneously emitted again or undergoes stimulated emssion into the laser mode. Most importantly, the momentum kick due to absorption happens in the direction of the laser wavevector $\vec{k}$, while the spontaneous emission is isotropic [180]. As a result, on average, a directed momentum transfer occurs [96]. In the case of a stimulated emission event no net momentum transfer occurs as a photon with the same momentum is created.

This mechanism can be employed to effectively cool the motion of the atom when the laser frequency is tuned slightly below the resonance frequency [53, 78, 181]. If the atom moves in any direction with a finite overlap with the wave-vector of the laser, the frequency of the laser field experienced in the rest frame of the atom is Doppler shifted. Depending on the direction of the velocity it is increased or decreased. Consequently, if the projection of the velocity of the atom onto the wave-vector is negative, the atom experiences a laser frequency that is shifted closer to resonance, hence leading to an increased absorption probability and a slowdown of the atom. The opposite is the case if the atom moves along the laser direction so that less photons are absorbed, not further accelerating the atom. As a result, in total, the laser exerts a damping force on the atom if it propagates towards the laser source. This leads to overall cooling along the direction of the wave-vector if a free atom is illuminated by two counter-propagating beams. In the case of ions confined in a Paul trap a single laser beam is sufficient, it dampens the oscillation of the particle during half of the period which results in an average damping rate [53]

$$\gamma_{Dopp} = -\frac{8\hbar\vec{k}^2}{m}\frac{s\delta/\Delta\omega}{\left[1+4\left(\frac{\delta}{\Delta\omega}\right)^2\right]^2} \tag{2.8}$$

where $s = 2\Omega^2/\Delta\omega^2$ is the saturation parameter with the carrier Rabi frequency Ω and $\Delta\omega$ is the natural linewidth of the addressed transition.

For a detuning of $\delta = -\Delta\omega/2$ it has a value $\gamma_{Dopp} = \hbar\vec{k}^{\,2} s/m$ and its maximum is given by $3\sqrt{3}\gamma_{Dopp}/4$ at $\delta = -\Delta\omega/\sqrt{12}$.

However, the undirected spontaneous emission of photons leads to stochastic momentum kicks, which balance the decelerating effect of the directed absorption at a certain temperature given by [53]

$$T_{Dopp} = \frac{\hbar\Delta\omega}{8k_B}\left(\frac{\Delta\omega}{|\delta|} + 4\frac{|\delta|}{\Delta\omega}\right) \tag{2.9}$$

and lead to a diffusive trajectory. The ions temperature is bounded from below by $T_{Dopp} = \frac{\hbar\Delta\omega}{2k_B}$. This value is often referred to as Doppler temperature. It is solely determined by the linewidth of the transition, and lies typically on the range of hundreds of µK. However, it is important to note that, as shown in Fig. 2.3, the temperature can be increased by choosing a different detuning. In order to reach colder temperatures, a more involved cooling scheme needs to be employed, which we briefly discuss in the following.

2.2.2 Sub-Doppler cooling

A variety of sub-Doppler cooling schemes have been introduced in the past in order to overcome the limitations of Doppler cooling, and to reach the quantum mechanical ground-state of the atomic oscillations. This is not only desirable in order to reduce the thermal fluctuations of the ions, but also as a first step in the initialization process of quantum computations, such that the motional degree of freedom of the atom is in a fixed known state [183]

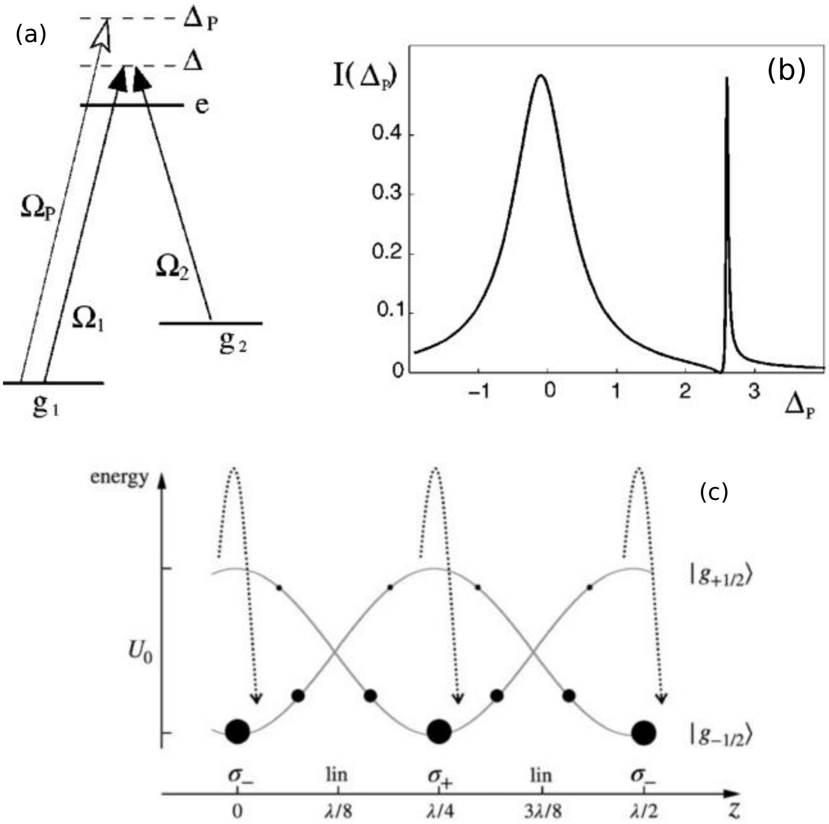
(a)
Δ_P
Δ
e
Ω_P
Ω_2
Ω_1
g_2
g_1
(b)
$I(\Delta_P)$
0.4
0.3
0.2
0.1
0
−1
0
1
2
3
Δ_P
(c)
energy
U_0
$|g_{+1/2}\rangle$
$|g_{-1/2}\rangle$
σ_-
lin
σ_+
lin
σ_-
0
$\lambda/8$
$\lambda/4$
$3\lambda/8$
$\lambda/2$
z

Figure 2.4: (a) Λ level scheme considered for Electromagnetic induced transparency (EIT) cooling with Rabi frequencies Ω_1 and Ω_2 and detuning Δ. (b) Absorption spectrum from the probe laser with detuning Δ_p (in units of decay rate). The detuning of the coupling lasers has been tuned to $\Delta = 2.5$ for which the absorption vanishes. Pictures (a) and (b) have been taken from Ref. [182]. (c) Sketch of the Polarization gradient (PG) cooling scheme. The two ground states experience phase-shifted periodic potentials with circular (σ) and linear polarization. At the potential maxima the ground state occupation flips due to virtual transitions to the excited state manifold, and subsequent decay via a carrier transition, indicated by the dashed arrows. Diagram taken from Ref. [57]

One of the first schemes implemented in a trapped-ion experiment was resolved sideband cooling, which builds on the subsequent destruction of vibration quanta in the so-called strong-confinement limit [57, 100, 129]. When ω_μ is much larger than the cooling transition linewidth $\Delta\omega$, the absorption spectrum is altered. In addition to the so-called carrier transition for $\delta = 0$, sidebands at $\delta = l\omega_\mu$ with integer l appear [179]. They correspond to the transition of the electronic state of the atom accompanied with the creation or destruction of l vibronic quanta as visible from the schematic level scheme depicted in Fig. 2.3 (right). A crucial parameter in this discussion is the so-called Lamb-Dicke parameter, which is given by $\eta_{LD} = |\vec{k}|\sqrt{\hbar/m\omega_\mu}$, assuming that $\vec{k}$ and the direction of the ion oscillation with frequency ω_μ are parallel. It compares the extend of the harmonic oscillator length of the ion with the wavelength of the laser radiation and therefore gives a measure for the coupling strength between light and atomic motion. Another way of interpreting this quantity is the fact that its square gives the ratio between the recoil energy the atom gains upon absorption and the level spacing of the local oscillator states. When $\eta_{LD}^2(2n+1) \ll 1$, often referred to as the Lamb-Dicke regime, only sidebands with $|l| < 2$ contribute significantly to the dynamics as higher sideband contributions decay polynomially with the Lamb-Dicke parameter. The strategy for the manipulation of the motional state of the ion is to detune the laser frequency away from the carrier frequency to make use of the sidebands as they change the electronic and n simultaneously. When the laser is detuned to either of the sidebands $l = -1, 1$ there still exists a finite probability to drive off-resonant transitions like the carrier or the respectively opposite sideband. However, these transitions are negligible in the strong-confinement limit with $\omega_\mu \gg \Delta\omega$ as the respective terms rotate in an appropriate interaction picture with a mulitple of ω_μ. After the application of a π-pulse to the first red or blue sideband the excited electronic state spontaneously decays due to its finite lifetime. Most importantly, in the Lamb-Dicke regime it does so with the highest probability via the carrier mode, not altering the vibron number during this step. This spontaneous decay completes one cycle of the scheme, which leads to an effective cooling/heating by $|l|$ vibron quanta.

When the motional ground state is reached, the atom cannot further absorb light quanta anymore, and hence it turns dark, since no Fock state with lower energy exists. In that case, the sideband laser light can only lead to heating transitions. The scheme is therefore fundamentally limited by an average vibration quantum number $\bar{n} \propto (\Delta\omega/\omega_\mu)^2$ [54, 184].

On a side note, the sidebands can also be used to assess the motional state, i.e. the temperature or displacement amplitude, of the ion [63, 185–190]. This technique relies on the change of the absorption probability of the sidebands, which scales like $\propto n$ for the red sideband, and like $\propto n+1$ for the blue sideband.

In the most extreme case $n = 0$, it is clear that the absorption amplitude at the red sidebands needs to vanish, whereas a blue sideband transition is always possible. In a more general scheme, the measurement of the absorption probabilities can be used to infer the average Fock number of a thermal state or the amplitude of a displaced state by comparing the strength of the sidebands.

Note that in the traditional red sideband cooling scheme only one mode of oscillation with frequency ω_μ is efficiently cooled. Other vibrational modes introduce additional sidebands that can be substantially off-resonant depending on their frequency. Hence the cooling of a wide range of vibrational frequencies requires additional effort, by changing the cooling laser frequency in time or employing more laser fields [191]. Since sideband cooling is only possible in the strong confinement regime, it is typically performed on a quadrupole transition, in contrast to the Doppler cooling scheme, which works as well for a dipole-allowed transition. This fact can drastically reduce its speed because it involves spontaneous decay events, which occur on a timescale given by the linewidth of the selected cooling transition. This effect can be countered by repumping the population of the excited state into the ground state with the help of an intermediate state [52].

In addition to sideband cooling more complicated schemes have been implemented. The two most prominent ones are EIT cooling and PG cooling. They make use of a more involved level scheme of the electronic states to boost the performance of sideband cooling.

In EIT cooling schemes, typically a Λ scheme is considered, containing two ground states $|f\rangle$ and $|g\rangle$ and an excited state $|e\rangle$ [50, 182, 192–195]. When the ground states are coupled to the excited state by strong, blue-detuned laser fields with equal detuning δ, the eigenstates are given by a set of dressed states. One of them is called a dark state because it has no projection onto the excited state, which is prone to decay. Consequently, the whole population is trapped in this state after a characteristic decay time. Most importantly, the absorption spectrum obtained by a weak probe laser, driving the transition between one of the ground-states and the excited state, vanishes if the probe laser is detuned by δ. In addition, it exhibits Fano-like resonances centered around the frequencies of the other dressed states, see Fig. 2.4 (top). If the shift of one of the dressed states from δ is equal to the motional vibration frequency ω_μ, transitions involving the reduction of oscillation quanta are possible. The key point of EIT cooling lies in the elimination of carrier transitions during the cooling, as the absorption spectrum vanishes for δ, leaving blue sideband transitions as the only heating process. Their probability is reduced due to the asymmetry of the absorption spectrum. The cooling cycle after a red sideband transition is again completed by the decay of the excited state, returning to the dark state. This scheme hence enables a speedup of the sideband cooling scheme discussed above, but also can lead to an efficient cooling of a wider motional frequency range, determined by the width of the resonances in the absorption spectrum.

PG cooling employs two counter-propagating laser beams with different polarizations, which off-resonantly excite an electronic transition $|j_g = 1/2, m_g = \pm 1/2\rangle \rightarrow |j_e, m_e\rangle$, where j are total angular momentum numbers, and m the magnetic quantum numbers [51, 196–201]. Due to the position-dependent polarization of the electric field, the two magnetic sub-levels $|m_g = \pm 1/2\rangle$ experience periodic light shifts, which are phase-shifted by π. These potentials alone do not result in cooling of the motion, as the atom in any ground-state can travel in the potential landscape, given it has sufficient kinetic energy. The trick of PG cooling lies in the transition probability via virtual transitions to the excited state manifold, that is increased at the respective potential maxima, see Fig. 2.4 (bottom). Let us consider that the atom is in the state $|j_g, m_g = -1/2\rangle$, and climbs up the respective potential barrier. At the potential maximum it experiences the maximal probability to get transferred to the $|j_g, m_g = 1/2\rangle$ ground state, which has a potential minimum at that position via virtual excitation and subsequent spontaneous emission. As a result, the atom has lost an amount of kinetic energy given by the amplitude of the periodic potentials. Since the atom only moves uphill during this cycle, this scheme is also referred to as Sisyphus cooling. The above discussion only holds for slow velocities, as it relies on spontaneous emission processes which occur on a timescale given by the linewidth of the electronic transition.

2.3 Ion Coulomb crystals

If many ions are captured in a rf trap, they repel each other since they have the same charge, which introduces an additional energy scale given by their Coulomb potential. For large temperatures, the presence of multiple ions does not qualitatively change their dynamics, as their kinetic energy is the dominating energy scale, the system is in a plasma-like state [132]. When the system temperature is brought below that Coulomb energy scale by laser cooling schemes, the ions crystallize since the temperature does not suffice to bring the ions close [38, 39]. The appearance of trapped ion clusters was observed in early experiments demonstrating the power of laser cooling [97, 202]. As the temperature plays a subordinate role in the crystalline phase, the shape of the system is determined by the competition between the two potential energy terms, i.e. the trap energy V_{trap}, and the Coulomb repulsion of the ions V_{Coul}. The former can be controlled by the choice of the Paul trap electrode voltages and the ion species while the latter is solely given by the ion charge. The overall Hamilton function is of the form:

$$\begin{aligned} H &= E_{kin} + V_{trap} + V_{Coul} \\ &= \sum_i \frac{\vec{p}_i^{\,2}}{2m_i} + \frac{m_i \omega_{iz}^2}{2}\left(z_i^2 + \alpha_i^2(x_i^2 + \beta_i^2 y_i^2)\right) + \frac{1}{2}\sum_{i,j\neq i} \frac{Q_i Q_j}{4\pi\epsilon_0 |\vec{r}_i - \vec{r}_j|}, \end{aligned} \tag{2.10}$$

where ϵ_0 is the vacuum permittivity. The trap frequencies depend on the ion charges and their masses, as indicated by the index i [129]. This dependence needs to be considered in a system with mixed ion species. However, in this Thesis we study only crystals containing a single type of ions, which allows for the uniform definition of the Coulomb strength $C_0 = \frac{Q^2}{4\pi\epsilon_0}$. We also drop from now on the ion index for the masses and trap frequencies, as the confinement is uniform for all particles, solely altered by the electrode voltages. When writing Eq. (2.10) as a function of dimensionless quantities, in addition to the particle number N, the only parameters of the system are the trap aspect ratios α and β:

$$H' = \sum_i \frac{\vec{p}_i^{\,2}}{2} + \frac{1}{2}\left(z_i^2 + \alpha^2(x_i^2 + \beta^2 y_i^2)\right) + \frac{1}{2}\sum_{i,j\neq i} \frac{1}{|\vec{r}_i - \vec{r}_j|}. \tag{2.11}$$

In the previous expression, positions are given in units of $\sqrt[3]{C_0/m\omega_z^2}$, time is measured in units of $1/\omega_z$, and the energy unit $\sqrt[3]{m\omega_z^2 C_0{}^2}$ is used [21]. We consider $\alpha, \beta > 1$ such that the ions tend to stay close to the z-axis in most cases. Note that the Hamiltonian is invariant under inversion in all three dimensions separately, i.e. crystals that are mirror images along one of the trap axes are guaranteed to have the same energy. Whereas the Coulomb repulsion favors larger ion distances, the trap pushes the ions closer together, the competition between these two forces finds expression in several phases of the crystal structure, segregated by transitions that spontaneously break one of the inversion symmetries [34–36, 40, 203–206].

The simplest arrangement with the highest level of symmetry occurs for large values of α, namely an ion chain where all ions align on the z-axis of the trap, i.e. $x_i = y_i = 0$, for all i [131]. In this phase, the trap frequencies perpendicular to the string are so stiff that the Coulomb term is unable to push the particles away from the z-axis. All $\mathbb{Z}_2^\mu$ symmetries of the potential terms are independently preserved. Due to this unique configuration, the z-axis is often referred to as axial dimension, and the other two dimensions as radial or transversal directions. The relatively large frequencies in the radial directions make the ions motion in these directions suitable for sideband cooling schemes. Moreover, as discussed in Sec. 2.1.1, micromotion is suppressed when the particles stay close to the z-axis. These properties make linear ion crystals preferable for a variety of applications in the fields of quantum simulation and computation [19].

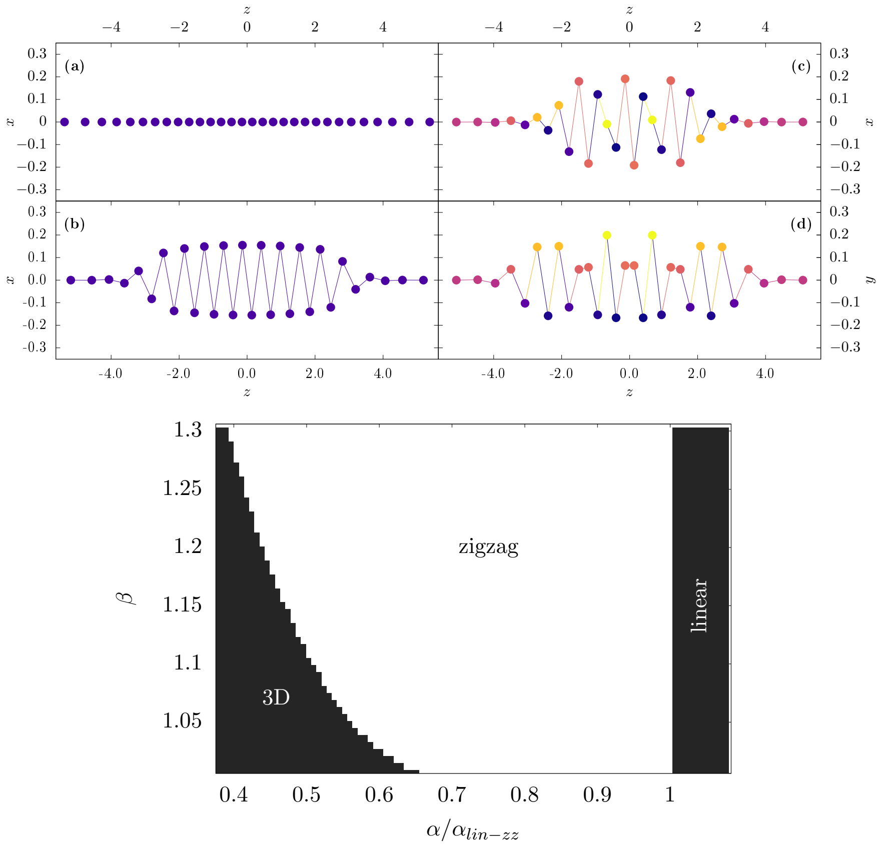

Figure 2.5: Top: Ion crystal for $N = 30$ in the linear phase for $\alpha = 12.5$ (a), zigzag phase for $\alpha = 8.0$ (b) and three-dimensional helix for $\alpha = 7.0$ and $\beta = 1.0$ (c) and (d). All lengths are given in units of $\sqrt[3]{C_0/m\omega_z^2}$. **Bottom:** Phase diagram of the crystal structure with zigzag, linear chain and three-dimensional phase as a function of the trap aspect ratios for $N = 30$.

As seen in Fig. 2.5 (top), the spacing of the particles is not homogeneous. The central ions are closer together than the outer particles, which can be partially corrected by higher-order potentials or by employing ring traps [133, 207–209]. Consequences of this breaking of translational invariance will be observable at various points, most dominantly at the transition to the two-dimensional phase.

Decreasing α weakens the transversal trapping, such that at a critical point α_{lin-zz} the ions buckle into the x-direction. This structural transition into a two-dimensional alignment is known as the linear-to-zigzag transition and has been intensely studied [36, 203, 210–214]. Its critical value is in good approximation given by

$$\alpha_{lin-zz} \approx \sqrt{\frac{7\zeta(3)C_0}{2m\omega_z^2}}\sqrt{\frac{1}{d^3(N)}} \tag{2.12}$$

where $\zeta(x)$ is the Riemann zeta-function and $d(N)$ is the distance between neighboring ions. It occurs when the energy gain from the increased ion distances in the Coulomb potential overcomes the energy penalty due to the transversal trap energy when displacing the ions radially. Since the former depends not only on the ion charges but also on the ion spacing, we can infer that the transition occurs first at the center where the distances $d(N)$ are minimal, as also clear from Eq. (2.12). The larger ion distances at the edges of the chain reduce the α at which the ions buckle locally, such that there exists a window of the trap aspect ratio in which the inhomogeneous spacings translate into a crystal with two structural phases, a zigzag at the center and a linear chain at the boundaries [213, 215]. For simplicity, we nonetheless refer to these structures in the following as two-dimensional crystals. Their name ”zigzag” comes from the triangular ladder alignment, see Fig. 2.5 (top).

It has been shown that in a properly defined thermodynamic limit, restoring the translational invariance of the linear chain, the linear-to-zigzag transition is a second-order phase transition [36]. At α_{lin-zz} the Landau free energy develops a double-well structure as a function of the radial diameter of the crystal, which serves as an order parameter [66, 216]. As such, it also spontaneously breaks one of the $\mathbb{Z}_2$ symmetries of the potential (2.10). For odd N, the inversion symmetry along x is broken, while for even N the two-dimensional crystal exhibits neither $\mathbb{Z}_2^x$ nor $\mathbb{Z}_2^z$ symmetry, but conserves their combination [217].

Consequently, the minimal energy configuration in the two-dimensional phase is two-fold degenerate. The positions of the ions can be flipped along the x-axis (independent of N), which yields a non-equivalent state with the same energy, called zagzig. This feature is a precondition for the existence of stable solitonic excitations, as we will discuss in Sec 2.3.1 [60, 218].

Upon further reduction of α, the system exhibits other structural transitions introducing more strings in the triangular lattice. Ultimately, at $\alpha = 1$ the trap has rotational symmetry around the y-axis and the ground state of the crystal describes a circular disk shape [97, 205, 206, 219, 220]. The discussion above is valid for strong enough ω_y, such that the ions are forced into the $z - x$ plane. Three-dimensional crystals are created when β is quenched below a critical value. The structures typically have a ellipsoidal form, consisting of helical ion chains or stacked shells, with increasing radial size for larger ion numbers, see Fig. 2.5 (top) [40, 221, 222]. A diagram of the different phases as a function of the trap aspect ratios α and β is depicted in Fig. 2.5 (bottom). These structures typically show other forms of degeneracy, e.g. by the chirality of the helical chain, so that the creation of crystal defects is not restricted to two-dimensional systems.

2.3.1 Crystal defects

Due to their degeneracies of the ground-state structure, two- and three-dimensional ion crystals can host a set of solitonic defects (kinks). They have been categorized in Ref. [217] and are subject of research until today [40, 46, 222–224]. All of them can be understood as a domain wall between different, energetically equivalent, ground-states. They share many physical properties with the topological solitons introduced in models discussed in Chap. 3, which is why we focus here on their characteristics specific to ion crystals.

Within this Thesis, we focus on the defects in the zigzag phase, where defects are only stable if the extension of the central zigzag phase is large enough, i.e. for $\alpha < \alpha_K$. In that case, they can take one out of three different shapes [217, 225]. For large α, the defect is given by an excess ion close to the z-axis located in between the regular zigzag alignment. This localized form is sometimes referred to as an odd defect. At smaller α, there exists a crossover that converts the localized defect into one of two possible extended kinks, as the excess ion slips away from $x = 0$ [226, 227]. The two types of extended kinks are denoted according to the orientation of the ion link that breaks the regular zigzag configuration. We speak of an horizontal kink when two neighboring ions have $x_i \cdot x_{i+1} > 0$ (assuming z ordering of the ions), and of a vertical kink for $z_i - z_{i+1} = 0$. All three types of defects are shown in Fig. 2.6. Which of the two extended kink forms is adopted by the system at the crossover from the localized regime depends on the position of the defect, as well as on the particle number.

In experiments, defects are created when α is quenched below α_K, crossing the linear-to-zigzag transition at a sufficient rate [227–233]. Intuitively, the creation process can be understood as an inhomogeneous choice of the ground-state adopted at the transition. The information about the chosen configuration (zigzag or zagzig) is transmitted with the speed of sound inside the crystal, if α is quenched on a faster timescale the information cannot reach the whole region that is driven into the two-dimensional alignment. This leads to the formation of defects with a finite probability.

The mechanism behind the creation of defects when a continuous phase transition is crossed at a finite quench rate is described by a theory developed by Kibble and Zurek [234, 235]. In general, it makes predictions about the scaling of the mean distance between created kinks with the quench rate at which the transition parameter is changed. It is based on the polynomial scaling of the so-called healing length and the equilibration time when the critical point of the transition is approached. As the equilibration time increases at the transition there exists a point at which it is equal to the inverse of the quench rate, i.e. the system cannot relax into the instantaneous ground state since the transition parameter is changed at a similar timescale as the equilibration would take. Kibble-Zurek theory assumes that the defects occur at an average distance equal to the healing length at this point. Ultimately, a scaling of the defect density can be derived which crucially depends on the critical exponents of the transition.

A careful correction to this theory has to be taken into account in inhomogeneous systems since not the whole system undergoes the transition simultaneously [228, 230]. Most importantly, the system undergoes the transition at different times at different positions when the control parameter is quenched due to the spatial dependence of its critical value. The dependence yields a propagating phase front at which the critical value is reached and whose velocity v_F needs to be compared to the speed of a local perturbation, typically given by the sound velocity v_s. For $v_s \gg v_F$ in the whole system the dynamics is adiabatic as the information about the new ground state can be transported at a sufficient speed, leading to the suppression of defect creation. In turn, when $v_s \ll v_F$ the homogeneous Kibble-Zurek theory is applicable as the transition is crossed almost simultaneously in the region of interest. Consequently, the inhomogeneous Kibble-Zurek mechanism shows significant deviations from the regular Kibble-Zurek scaling for comparable phase front velocity and speed of sound, i.e. it predicts a pronounced dependence of the defect density on the quench rate. Experiments have demonstrated the validity of the Kibble-Zurek scaling in a finite window of the quench rate, limited by the capability to detect the defects and their finite lifetime [227, 232]. When the quench rate is increased outside this window, more than a single defect are likely to be created, their possibly attractive interaction can lead to their annihilation such that the counting statistics becomes inaccurate. In addition to the experimental validation of the Kibble-Zurek scaling, the discussed crystal defects are fundamental for the study of nanofriction in two-dimensional ion crystals as discussed below in Sec. 3.3.

2.3.2 Vibrational system

In the crystalline phase, the ions oscillate around their equilibrium positions $\vec{r}_{i,0}$ [131, 221]. For small kinetic energies, this dynamics is captured by a Taylor expansion of the potential energy terms for small fluctuations in the ion positions. The first non-vanishing term is quadratic in the displacements and describes the coupled harmonic oscillations of the ions [21, 236, 237]. Higher-order terms become more relevant with increasing energies and lead to non-linear corrections to the ion oscillations [111, 113, 238].

The benefit from the calculation of the Taylor expansion is two-fold. It provides linear equations of motion that are analytically solvable and provide insight into

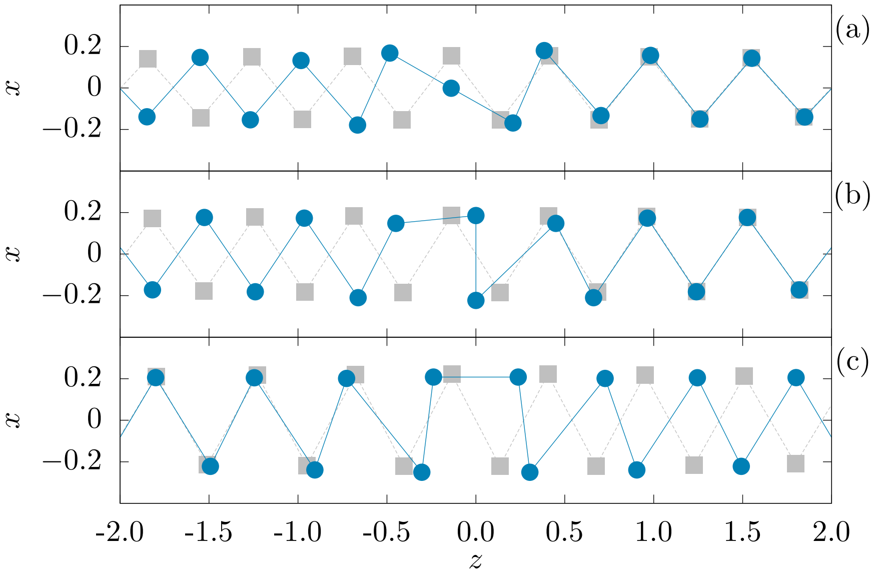

Figure 2.6: Different shapes of crystal defects in the zigzag phase. Localized (odd) kink for $\alpha = 8.0$ (a), vertical defect for $\alpha = 7$ (b) and horizontal defect for $\alpha = 6$ (c). For comparison the respective configuration without defect is shown in grey. All lengths are in units of $\sqrt[3]{C_0/m\omega_z^2}$.

the fundamental motional excitations of the crystal, the phonon modes. In addition, the computational effort for the analysis of the crystal dynamics is drastically reduced since the determination of the equilibrium positions and the second order derivatives of the Hamiltonian are sufficient to describe all dynamical properties of the system. Moreover, by comparing the results obtained from the approximation with a calculation considering the full, non-linear Hamilton equations, we may assess the importance of the non-linearity of the Coulomb interaction for the dynamics. This analysis is of particular interest close to phase transitions and for questions regarding the equilibration and conductivity in a thermal ensemble [61, 239–242]. On a side note, the second-order expansion also provides a benchmark for all numerical calculations of the dynamics in the low-energy limit. All results should converge to the prediction of the approximation if e.g. the system energy scale is reduced. In the following, we present a derivation of the expansion up to second order, and its diagonalization.

We consider the deviations of the ion positions from a static configuration, $d\vec{r}_i = \vec{r}_i - \vec{r}_{i,0}$, to be small in comparison to the ion spacings in equilibrium $\vec{r}_{ij,0}$.

We then expand $V_{trap} + V_{Coul} = V^{(0)} + V^{(1)} + V^{(2)} + \mathcal{O}(d\vec{r}_i^{\,3})$, where

$$V^{(0)} = \frac{1}{2}\sum_i m\vec{r}_{i,0} \cdot \omega^2 \cdot \vec{r}_{i,0} + \frac{1}{2}\sum_{j\neq i} \frac{C_0}{|\vec{r}_{ij,0}|} \tag{2.13}$$

$$V^{(1)} = \sum_i \left[m\omega^2 \cdot \vec{r}_{i,0} - \sum_{j\neq i} \frac{C_0 \vec{r}_{ij,0}}{|\vec{r}_{ij,0}|^3} \right] \cdot d\vec{r}_i \tag{2.14}$$

$$V^{(2)} = \frac{1}{2}\sum_i d\vec{r}_i \cdot \left[m\omega^2 + \sum_{j\neq i} W_{ij} \right] \cdot d\vec{r}_i - \frac{1}{2}\sum_{i,j\neq i} d\vec{r}_i \cdot W_{ij} \cdot d\vec{r}_j \tag{2.15}$$

with $\vec{r}_{ij,0} = \vec{r}_{i,0} - \vec{r}_{j,0} = (x_{ij,0}, y_{ij,0}, z_{ij,0})$, $\omega = \omega_z \mathrm{diag}(1, \alpha, \alpha\beta)$ and

$$W_{ij} = \frac{C_0}{|\vec{r}_{ij,0}|^3} \left(\frac{3}{|\vec{r}_{ij,0}|^2} (\vec{r}_{ij,0}) \otimes (\vec{r}_{ij,0}) - \mathbb{1} \right). \tag{2.16}$$

We used the notation $(\vec{a} \otimes \vec{b})_{ij} = a_i b_j$ for the outer product. For a mixed species ion crystal, the trap frequencies experienced by the ions become species-dependent and the Coulomb interaction strength is different for intra- and inter-species couplings. Both effects lead to modifications of the expansion.

The zeroth-order term $V^{(0)}$ is a constant and can hence be ignored for the dynamics. The first-order term can be written in the form $V^{(1)} = -\sum_i \vec{F}_i \cdot d\vec{r}_i$, where $\vec{F}_i$ is the force vector the ion i experiences due to the trap confinement and the Coulomb repulsion at the static position $\vec{r}_{i,0}$. Per definition $\vec{F}_i = \vec{0}$, so that $V^{(1)} = 0$. Therefore, the first non-vanishing term in the expansion is given by $V^{(2)}$, which is a sum of local oscillator terms and the coupling of the ions vibrations through the matrices W_{ij}. The first term describes the local confinement the ion experiences at its equilibrium position, which can be interpreted as a three-dimensional harmonic oscillator. It consists of the trap confinement regularized by the repulsion from the other crystal ions. The second term describes the harmonic coupling of the local oscillations as a consequence of the Coulomb interaction.

A special case occurs for $\alpha > \alpha_{lin-zz}$, when the equilibrium configuration is a linear chain along the z-axis of the trap. Then, W_{ij} becomes diagonal for all i and j, as $\vec{r}_{ij,0} = |\vec{r}_{ij,0}|\vec{e}_z$ and the dynamics in the three different directions decouple, so that we can treat them separately [21]. We can write the potential as a sum of contributions in the different dimensions $\mu = x, y, z$ via

$$V_\mu^{(2)} = \frac{1}{2}\sum_i m\omega_{i\mu}^2 d\mu_i^2 - \frac{1}{2}\sum_{i,j\neq i} W_{ij}^\mu d\mu_i d\mu_j \tag{2.17}$$

where $W_{ij}^\mu = \frac{C_0}{|\vec{r}_{ij,0}|^3}(3\delta_{\mu z} - 1)$ and $\omega_{i\mu}^2 = \omega_\mu^2 + \frac{1}{m}\sum_{j\neq i} W_{ij}^\mu$. Note that $\omega_{i\mu}$ is the local vibrational frequency of ion i in the direction μ.

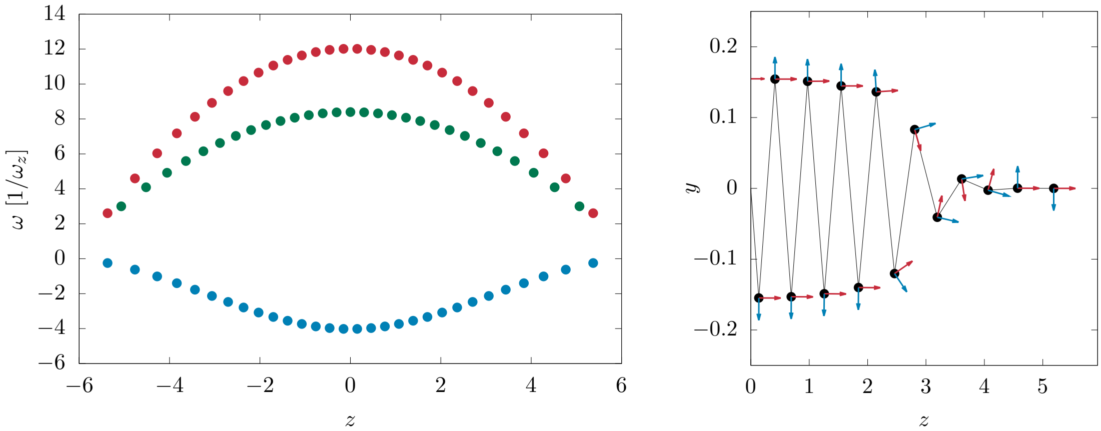

Figure 2.7: Left: Local harmonic oscillator frequencies $\omega_{iz} - \omega_z$ (red) and $\omega_{ix} - \alpha\omega_z$ (blue) and $\sqrt{W^z_{ii+1}/m}$ (green) in units of ω_z. **Right:** Right half of a zigzag crystal with local vibrational principal axes in the crystal plane. All lengths are given in units of $\sqrt[3]{C_0/m\omega_z^2}$.

Note the opposite sign of the coupling strengths of the z vibrations in comparison to the radial W^{μ}_{ij}. This results below in a inverted ordering of the phonon modes. As the Coulomb potential is reduced for larger ion distances, it favors the in-phase vibration of neighboring ions along the chain (the ion distance is not reduced) and the out-of-phase motion in any of the radial directions (the distances between neighboring ions increase). This effect is also seen in the oscillator frequencies, which are inhomogeneous due to the position dependent distances in the linear chain. The axial frequencies ν_{iz} are maximal in the central region with minimal distances, whereas the radial frequencies are minimal there, as seen in Fig. 2.7 (left).

For a higher-dimensional crystal, the principal axes of the local vibrations of the ions are generally rotated away from the trap axes, which is caused by the off-diagonal terms of W_{ij}, see Fig. 2.7 (right). In that case, a diagonalization of the local confinement matrices $m\omega^2 + \sum_{j\neq i} W_{ij} = mU_i \cdot N_i^2 \cdot U_i^T$ provides the local principal axes of vibrations in the columns of the 3×3 matrices U_i, and the respective frequencies $\Omega_i = \mathrm{diag}(\omega_{i1}, \omega_{i2}, \omega_{i3})$. We can locally change the basis via $d\vec{R}_i = U_i^T \cdot d\vec{r}_i$ and obtain

$$V^{(2)} = \frac{1}{2}\sum_i m d\vec{R}_i \cdot \Omega_i^2 \cdot d\vec{R}_i - \frac{1}{2}\sum_{i,j\neq i} d\vec{R}_i \cdot t_{ij} \cdot d\vec{R}_j \tag{2.18}$$

where $t_{ij} = U_i^T \cdot W_{ij} \cdot U_j$ is the coupling matrix in the rotated bases. In many cases it is convenient to condense the displacement vectors into a state vector

$d\vec{R} = (d\vec{R}_1, \ldots, d\vec{R}_N)$, which allows for the short-hand notation

$$V^{(2)} = \frac{1}{2} d\vec{R} \cdot K \cdot d\vec{R}. \tag{2.19}$$

K is often referred to as the Hessian matrix of the potential.

2.3.3 Phonon modes

The diagonalization of the Hessian matrix K provides the phonon modes of the system. They describe the fundamental excitations in second-order approximation, and their shape results from the coupling of the local harmonic oscillators [236, 237, 243, 244]. We denote by $\vec{\theta} = V^T \cdot d\vec{R}$ the amplitude vector of the phonon modes, where V is a $3N \times 3N$ matrix containing the eigenvectors of K as columns. The potential in this basis takes the simple form of $3N$ uncoupled harmonic oscillators:

$$V^{(2)} = \frac{1}{2} \sum_{r=1}^{3N} \lambda_r \theta_r^2 \tag{2.20}$$

where λ_r are the eigenvalues of K. The shape of the phonon mode vectors and their frequency dispersion constitute the crystal properties that determine the dynamics in second-order approximation, and are essential for the analysis of the structural phase transitions [36, 237]. When $\vec{r}_{i,0}$ describe a stable equilibrium, $\lambda_r > 0$, $\forall r$, such that the modes oscillation frequency is given by $\omega_r = \sqrt{\lambda_r / m}$.

There exist three special modes in the spectrum independent of the crystal structure, which are referred to as the common modes. They describe the rigid oscillation of the whole crystal inside the Paul trap and hence have a mode frequency equal to one of the three trap frequencies and an equal projection onto all ions [21]. They are also the only modes that translate the center of mass of the crystal and therefore are isolated from the coupling to other phonon modes via higher order terms in the Taylor expansion, see Sec. 2.3.5 [238].

The form of the rest of the phonon modes depends on the equilibrium positions. For a crystal that possesses any inversion symmetry, the phonon modes are either symmetric or antisymmetric under the transformation that leaves the crystal invariant, see Fig. 2.8 (right). This enables the ordering of the modes by the number of their nodes in the mode vectors.

As already visible from the vibration potential given by Eq. (2.17), the modes for a linear chain arrangement can be separated into three sets of N modes that only have support in one of the dimensions [21]. We can therefore speak of axial and radial modes in the x and y direction. Due to the fact that $W_{ij}^{\mu} / W_{ij}^{\mu'} = const$ the spatial shapes of the phonon modes in each of the decoupled sets is the same. As an example, a mode with a single node in the mode vector, often referred to as

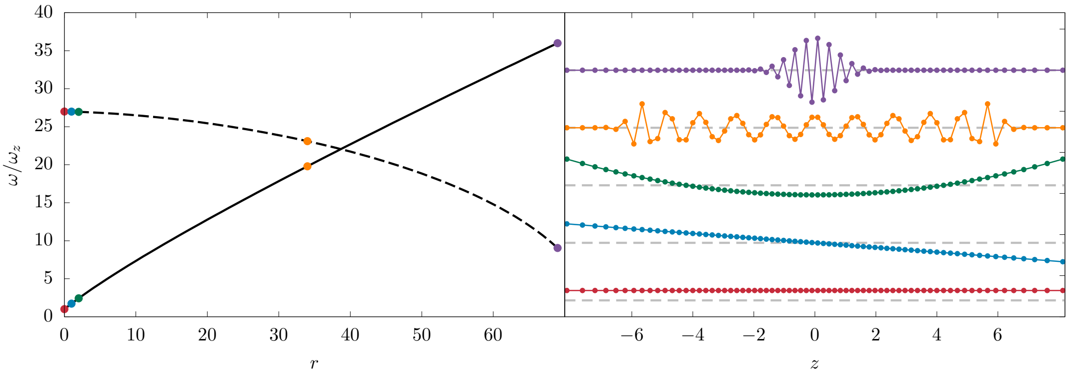

Figure 2.8: Left: Phonon mode dispersion relation in a linear chain when the modes are ordered with ascending number of nodes r for $N = 70$. The solid lines shows the dispersion in the axial direction, the dashed line depicts the dispersion of the x modes. **Right:** A set of phonon mode vectors containing the common mode (red), breathing mode (blue) and zigzag mode (purple). Their frequencies in the dispersion relations is shown by the points with the same color coding.

breathing mode (see Fig. 2.8), can be found in the axial as well as the two radial phonon mode sets, their projections onto the motion of the single ions has the same spatial shape . However, their mode vectors that determine the phonon mode shapes are still perpendicular as they are restricted to one dimension respectively. Due to the different sign in the coupling terms W_{ij}^{μ}, the ordering of the phonon modes in the axial direction is different than in the two radial directions. While axially the mode with the lowest frequency is the common mode, the other two common modes in the radial directions are the modes with the highest eigenvalues in the respective set. The breathing mode has an eigenvalue with a fixed relation to the eigenvalue of the common mode [21]. The frequencies of modes with more nodes can only be calculated numerically.

The dispersion relation of the phonon modes is acoustic in the axial dimension and optical in the transversal modes, see Fig. 2.8 (left) [237]. This has consequences for the delocalization dynamics of vibrational excitations. In a chain, axial wave packets travel with a substantial group velocity, but dephase only weakly and get reflected at the crystal boundaries. The linear dispersion relation leads to revivals for which the excitation returns to it initial state as seen in Fig. 2.9 [63, 64]. The opposite is the case for radial excitations, which dephase on a larger timescale.

At the linear-to-zigzag transition, the lowest radial mode in x-direction, having $N-1$ nodes in the mode vector, becomes soft as seen in Fig. 2.10 [36]. It describes the motion of the central ions in the x-direction with alternating sign, and it therefore is often denoted as the zigzag mode, as it drives the transition into the

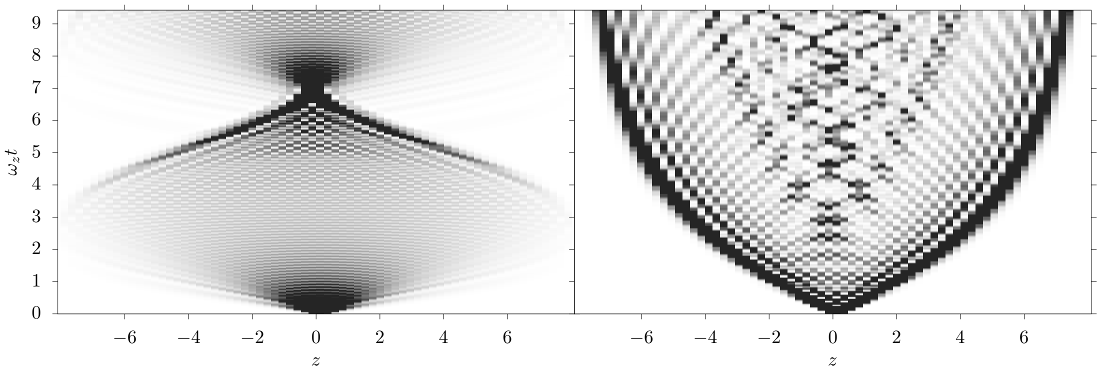

Figure 2.9: Vibrational energy evolution in a linear chain ($N = 70$, $\alpha = 26$) after an initial displacement of a single ion in the axial direction (left) and a radial direction (right). z is given in units of $\sqrt[3]{C_0/m\omega_z^2}$.

two-dimensional phase. Due to the coupling of the vibrations in the plane via W_{ij}, we cannot speak of axial and radial modes in the two-dimensional phase. The motion out of the plane still decouples from the other degrees of freedom in second-order approximation. -

2.3.4 Quantum vibron model

When the ion oscillations are cooled down into a sub-Doppler regime, potentially to the motional quantum ground state, the continuous classical displacements need to be described by quantum Fock states [100, 183, 196]. This leads to the quantum equivalent of second order Hamiltonian described so far. We refer to the quantum excitations of the ion harmonic oscillations as vibrons, they are created (destroyed) by the ladder operators $a_{i\mu}^\dagger$ ($a_{i\mu}$). They enter via the conventional quantization of $\vec{X}_i = L_i \cdot (\vec{\psi}_i^\dagger + \vec{\psi}_i)/\sqrt{2}$ where we have introduced the matrix $L_i = \mathrm{diag}(L_{i1}, L_{i2}, L_{i3})$ which contains the harmonic oscillator lengths given by $L_i^2 = \hbar\Omega_i^{-1}/m$. The ladder vectors $\vec{\psi}_i = (a_{i1}, a_{i2}, a_{i3})^T$ are a short-hand notation for the vibron ladder operators. Together with the quantized momentum $\vec{p}_j = i\hbar L_j^{-1}(\vec{\psi}_j^\dagger - \vec{\psi}_j)/\sqrt{2}$ the quantization results in the Hamilton operator

$$H = \sum_i \hbar\vec{\psi}_i^\dagger \cdot \Omega_i \cdot \vec{\psi}_i - \frac{\hbar}{2}\sum_{i,j\neq i}\left(\vec{\psi}_i^\dagger + \vec{\psi}_i\right) \cdot T_{ij} \cdot \left(\vec{\psi}_j^\dagger + \vec{\psi}_j\right) \tag{2.21}$$

with $\hbar T_{ij} = L_i \cdot t_{ij} \cdot L_j$. The hopping term contains parts that are not vibron number conserving but are typically neglected as they are oscillating with $\omega_{i\mu}+\omega_{j\nu}$ in a frame rotating with the vibron frequencies [64, 110]. If this frequency sum is much larger than the hopping rates t_{ij} it is justified to apply the rotating wave

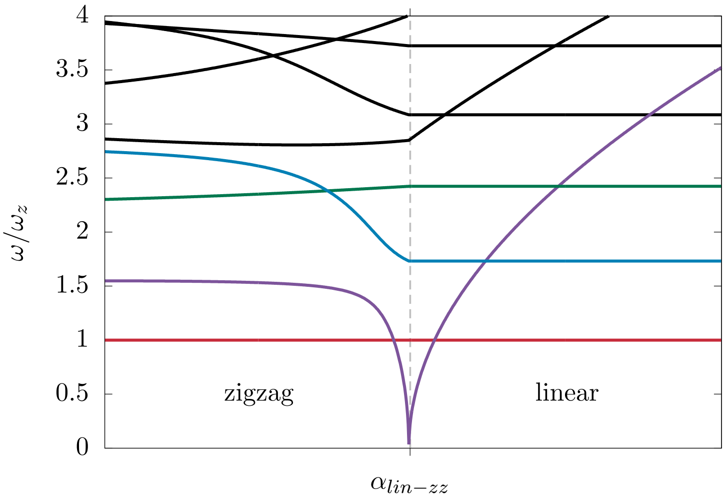

Figure 2.10: Phonon mode spectrum as a function of α close to the linear-to-zigzag transition. The zigzag mode frequency (purple) vanishes at α_{lin-zz}.

approximation. This condition might be met or not depending on the geometry of the ion crystal and the trap frequencies, if it is then we arrive at the Vibron-Hubbard (VH) model

$$H = \sum_i \hbar \vec{\psi}_i^\dagger \cdot \Omega_i \cdot \vec{\psi}_i - \frac{\hbar}{2} \sum_{i,j \neq i} \vec{\psi}_i^\dagger \cdot T_{ij} \cdot \vec{\psi}_j + \vec{\psi}_i \cdot T_{ij} \vec{\psi}_j^\dagger \tag{2.22}$$

2.3.5 Higher-order expansion

For larger fluctuations, the description of the ion vibrations in a harmonic approximation becomes eventually invalid as the kinetic energy reaches a regime in which the particles probe the non-linearity of the Coulomb potential.

A direct calculation of the higher orders up to the fourth order of the expansion of the potential V_{Coul} yields

$$V^{(3)} = \frac{1}{6} \sum_{i,j \neq i} L_{ij}^{\mu\nu\sigma} d\mu_i (d\nu_i d\sigma_i + 3 d\nu_j d\sigma_j) \tag{2.23}$$

$$V^{(4)} = \frac{1}{24} \sum_{i,j \neq i} M_{ij}^{\mu\nu\sigma\xi} d\mu_i d\nu_i (d\sigma_i d\xi_i - 4 d\sigma_i d\xi_j + 6 d\sigma_j d\xi_j) \tag{2.24}$$

$$\tag{2.25}$$

where

$$L_{ij}^{\mu\nu\sigma} = \frac{3C_0}{|\vec{r}_{ij,0}|^5}\left(-5\frac{\mu_{ij,0}\nu_{ij,0}\sigma_{ij,0}}{|\vec{r}_{ij,0}|^2} + \frac{1}{2}\sum_p \delta_{\mu\nu}\sigma_{ij,0}\right) \tag{2.26}$$

$$M_{ij}^{\mu\nu\sigma\xi} = \frac{3C_0}{|\vec{r}_{ij,0}|^5}\left(35\frac{\mu_{ij,0}\nu_{ij,0}\sigma_{ij,0}\xi_{ij,0}}{|\vec{r}_{ij,0}|^4} + \frac{1}{4}\sum_q \delta_{\mu\nu}\left[\frac{\delta_{\sigma\xi}}{2} - 5\frac{\sigma_{ij,0}\xi_{ij,0}}{|\vec{r}_{ij,0}|^2}\right]\right) \tag{2.27}$$

are, respectively, the three- and four-dimensional tensors describing the higher-order dynamics. In the previous expressions, p and q denote all possible permutations of (μ, ν, σ) and (μ, ν, σ, ξ) respectively, such that the two tensors are symmetric under permutation of any of the indices [238].

They translate to interaction terms for the phonon modes when written as

$$V^{(3)} = \frac{1}{6}\sum_{r,s,m} \tilde{L}_{rsm}\theta_r\theta_s\theta_m \tag{2.28}$$

$$V^{(4)} = \frac{1}{24}\sum_{r,s,m,n} \tilde{M}_{rsmn}\theta_r\theta_s\theta_m\theta_n \tag{2.29}$$

where we have applied the same change of basis that resulted in (2.20), i.e.

$$\tilde{L}_{rsm} = \sum_{i,j\neq i} L_{ij}^{\mu\nu\sigma} v_{i\mu}^r (v_{i\nu}^s v_{i\sigma}^m + 3v_{j\nu}^s v_{j\sigma}^m) \tag{2.30}$$

$$\tilde{M}_{rsmn} = \sum_{i,j\neq i} M_{ij}^{\mu\nu\sigma\xi} v_{i\mu}^r v_{i\nu}^s (v_{i\sigma}^m v_{i\xi}^n - 4v_{i\sigma}^m v_{j\xi}^n + 6v_{j\sigma}^m v_{j\xi}^n) \tag{2.31}$$

where $v_{i\mu}^r$ is the projection of the r-th phonon mode onto $d\mu_i$. They describe the nonlinearity of the local oscillation potentials via their diagonal terms, but also the off-diagonal interaction of vibrational excitations. The common modes constitute a special case, as they couple neither via $\tilde{L}$, nor via $\tilde{M}$ to the rest of the phonon mode spectrum, because the rigid center-of-mass motion of the crystal is unaffected by the internal dynamics.

Chapter 3

Nanofriction and solitons

In recent years trapped ion systems have successfully proven to be a suitable scenario for the investigation of nanofriction models [43, 45, 46]. Nanofriction is the field of physics that deals with friction phenomena on the atomic scale when two surfaces come into contact [58, 245]. Since its main ideas and results are fundamental to understand the physics of topological defects in ion crystals, we review them in this chapter, in particular the Frenkel-Kontorova model, and then elaborate how these ideas translate into the trapped-ion context.

3.1 Introduction

Friction is a phenomenon encountered almost constantly [59, 246–248]. It is well understood on the macroscopic scale, given by the phenomenologically deducted laws by Amontons and Coulomb, which state that two solids dragged across each other experience a force [249–251]:

$$|\vec{F}_{fric}| = \mu_{fric}|\vec{F}_N| \tag{3.1}$$

that damps their motion. Its strength, which is independent of the contact surface area, is determined by the normal force $\vec{F}_N$ that is applied perpendicular to the surface plane, and by a material- and roughness-specific friction constant μ_{fric}. There are different types of friction forces, with different friction constants each. Most notably, the forces can be categorized into static friction and kinetic friction, observable when the applied force exceeds the static friction force.

The field of nanofriction focuses on the friction phenomena appearing on the atomic scale, i.e. considering the lattice or atomic structure of the two surfaces, and their connection to macroscopic friction [58, 60]. Ultimately, one goal is to employ the results on the nanoscale to engineer the macroscopic friction behavior into a desired regime for a specific application.

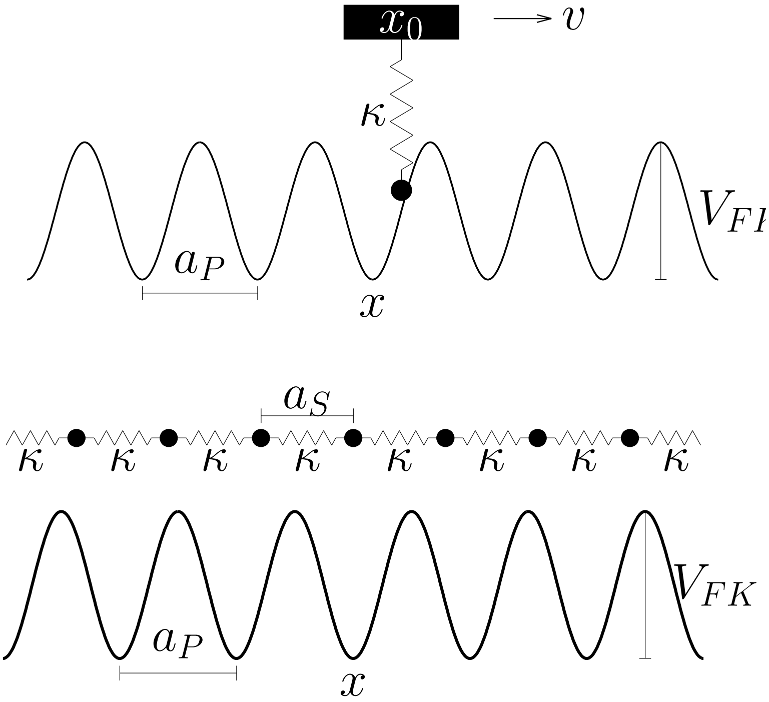

Figure 3.1: Top: Schematic depiction of the Prandtl-Tomlinson (PT) model; single classical particle harmonically coupled to a support, dragged across the periodic corrugation potential. **Bottom:** Harmonically coupled particle chain in the Frenkel-Kontorova (FK) model.

In theoretical models, the physics of nanofriction is typically simplified by emulating the effect of one of the surfaces by a static sinusoidal potential, commonly denoted as corrugation potential, and assuming a harmonic interaction among the particles of the moving solid [58, 252–255]. In most cases, the surprisingly rich physics of nanofriction is ultimately caused by the competition between these two energies and their length scales.

The simplest model of nanofriction is the so-called Prandtl-Tomlinson (PT) model and consists of a single particle that is harmonically coupled to a support that moves with a finite velocity parallel to a surface emulated by a sinusoidal potential, see Fig. 3.1(top) [252, 256, 257]. Its potential term is given by

$$V_{PT} = \frac{\kappa}{2}(x - x_0)^2 + \frac{V_0}{2}\left[1 - \cos\left(\frac{2\pi}{a_P}x\right)\right] \tag{3.2}$$

where $x_0 = vt$ is the position of the support, κ is the spring constant connecting the atom to the support, V_0 is the amplitude of the corrugation potential, and a_P is its period. When using a_P as a length unit and $\kappa {a_P}^2$ as an energy unit, the model is characterized by the relative corrugation strength $\eta = V_0/\kappa {a_P}^2$. We will write all quantities in dimensionless form by using these units in the rest of the chapter.

For weak η, the particle prefers to minimize its interaction with the support and hence follows its movement in a continuous trajectory [258–261]. Although the presence of the corrugation potential leads to a modulation of the particle velocity around v, it is not strong enough to pin the particle in one of its wells. Consequently, no energy is dissipated in this phase, and the motion is frictionless. Above a critical value of η, the particle enters a stick-slip regime. In this regime, the particle favors to minimize its potential energy, and remains in one potential well until the support forces it to slip into the neighboring well abruptly. The sudden slip across a potential maximum is followed by an oscillation of the particle inside a neighboring potential well, this kinetic energy marks the onset of friction forces as it is subsequently dissipated. This friction force depends on the velocity v of the support in a logarithmic fashion [262, 263]. In a typical experiment the lateral force applied by the support is measured as a function of the support position, see Fig. 3.2. In the frictionless regime the lateral force follows the corrugation potential and is of sinosoidal shape as a function of x_0. This changes in the friction regime as the slip events lead to an abrupt drop in the lateral force which adopts a sawtooth structure. Lastly, an obvious distinction between the two cases is the reversibility of the trajectory in the frictionless regime, i.e. inverting the direction of the motion of the support ($v \to -v$) yields the same lateral forces. In the friction regime a finite offset between the two directions exists which can be taken as a measure for the dissipated energy in a hysteresis loop, moving the support to a neighboring potential minimum and back. Despite the simplicity of the model, it demonstrates first signs of the non-trivial dynamics of nano-tribological systems due to the competition of inter-particle interaction with the pinning effect of the corrugation potential.

While the PT model aims to simulate the bulk of the solid by the support that drags the particle across the corrugation, it neglects the effect of the particle lattice in a solid. Therefore, this basic idea has been extended to a chain of harmonically coupled particles subject to the corrugation potential. This model has become famous as the so-called Frenkel-Kontorova (FK) model, named after their Soviet inventors, and is discussed in more detail in the following section [60, 254, 254].

3.2 The Frenkel-Kontorova model

The original Frenkel-Kontorova model deals with a one-dimensional system of an infinite number of particles of mass m, with neighboring atoms coupled by springs with constant κ and equilibrium length a_S [60]. The particles experience a potential

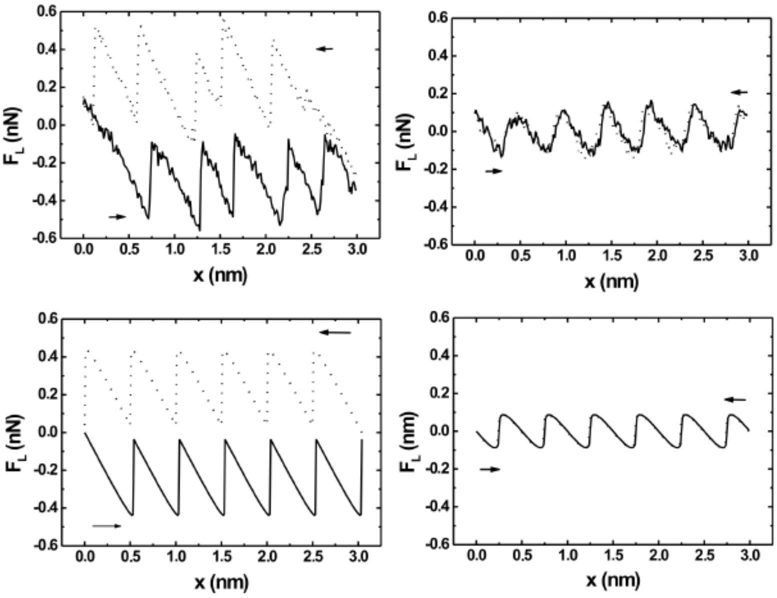

Figure 3.2: Top: Measurement of the lateral force as a function of the support position x_0 in a friction force microscope experiment in the stick-slip regime (left) and the frictionless regime (right). The solid line and the dotted line show the results for opposite directions of the support motion. **Bottom:** The corresponding numerical results from the PT model. Diagrams taken from Ref. [261].

with period a_P, simulating the surface of the solid the particle chain slides across, see Fig. 3.1 (bottom). Using the same units as in the PT model together with $\sqrt{\kappa/m}$ as a time unit we can write the Hamiltonian of the model as:

$$H_{FK} = \sum_i \frac{p_i^2}{2} + \frac{1}{2}(x_{i+1} - x_i - \theta_{FK})^2 + \frac{V_{FK}}{2}(1 - \cos(2\pi x_i)) \tag{3.3}$$

where $p_i = \frac{\partial x_i}{\partial t}$ is the particle momentum. In addition to the parameter V_{FK}, which compares the strength of the coupling amongst the particles κ and the potential amplitude V_0, as in the PT model, the ratio $\theta_{FK} = a_S/a_P$ is also of relevance for the FK model. The FK model is called commensurate if $\theta_{FK} = \frac{p}{q} \in \mathbb{Q}$, since the two lengths scales a_S and a_P possess a least common multiple. The system is therefore invariant under translations by $qa_S = pa_P$, which is not the case if θ_{FK} is irrational, in which case the FK model is referred to as incommensurable [264]. This difference has essential consequences for the minimal energy configuration of the particle chain as well as its excitations. Moreover, the choice of the boundary conditions alters details in the ground state and their excitations.

The Hamiltonian (3.3) gives rise to the equations of motion

$$\frac{d^2x_i}{dt^2} + 2x_i - x_{i-1} - x_{i+1} + V_{FK}\pi\sin(2\pi x_i) = 0. \tag{3.4}$$

In the following, we first discuss the properties of the FK model in the continuum limit, since many concepts and mechanisms found in the discrete FK model are already present there.

3.2.1 Continuum approximation

In the case of small values of θ_{FK}, we can derive a continuum limit approximation of the dynamical equations (3.4), promoting the discrete deviations of the particles from their equilibrium in the absence of the corrugation potential to a scalar field of continuous space $x_i - i\theta_{FK} \to \varphi(i\theta_{FK}) \approx \varphi(x)$ [265]. For simplicity we take $\theta_{FK} \in \mathbb{N}$ in the following derivation but analogue arguments hold for arbitrary rational coverage parameters that lead to a unit cell with more than one atom. We can then approximate the positions of the neighboring particles that enter the equation of motion for the atom i by a Taylor expansion, i.e. $x_{i\pm1} \approx (i\pm1)\theta_{FK} + \varphi(x) \pm \frac{\partial\varphi}{\partial x}\theta_{FK} + \frac{1}{2}\frac{\partial^2\varphi}{\partial x^2}{\theta_{FK}}^2 + \mathcal{O}({\theta_{FK}}^3)$. Inserting the expansion up to second order into Eq. (3.4) yields in lowest order:

$$\frac{\partial^2\varphi}{\partial t^2} - {\theta_{FK}}^2\frac{\partial^2\varphi}{\partial x^2} + V_{FK}\pi\sin(2\pi\varphi) = 0 \tag{3.5}$$

which has the form of a Sine-Gordon equation (SGE) [224]. This model has attracted attention due to its Lorentz invariance (note the invariant d'Alembert operator $\frac{\partial^2}{\partial t^2} - {\theta_{FK}}^2\frac{\partial^2}{\partial x^2}$) and integrability, but it is most famous due to its solitonic excitations, which we elaborate later [266–268].

For the SGE, there exist three different classes of excitations, one of them describes small fluctuations in φ around the trivial vacuum state $\varphi(x,t) = 0$ [269]. For the calculation of the resulting phonon modes it is valid to linearize the SGE $\sin(2\pi\varphi) \approx 2\pi\varphi$ and insert a plane-wave ansatz $\varphi(x,t) \propto \exp(i(kx - \omega_{phon}t))$. This results in the dispersion relation of the phonons [224]

$$\omega^2_{phon}(k) = \omega_0^2 + {\theta_{FK}}^2k^2 \tag{3.6}$$

with $\omega_0^2 = 2\pi^2 V_{FK}$. It is always gaped and non-linear for a finite value of the corrugation potential strength, and it is asymptotically linear for large k values. The group velocity of the phonons is bounded by $\frac{\partial\omega_{phon}}{\partial k} \leq \theta_{FK}$, indicating the Lorentz invariance of the model, with θ_{FK} taking the role of the speed of light in special relativity.

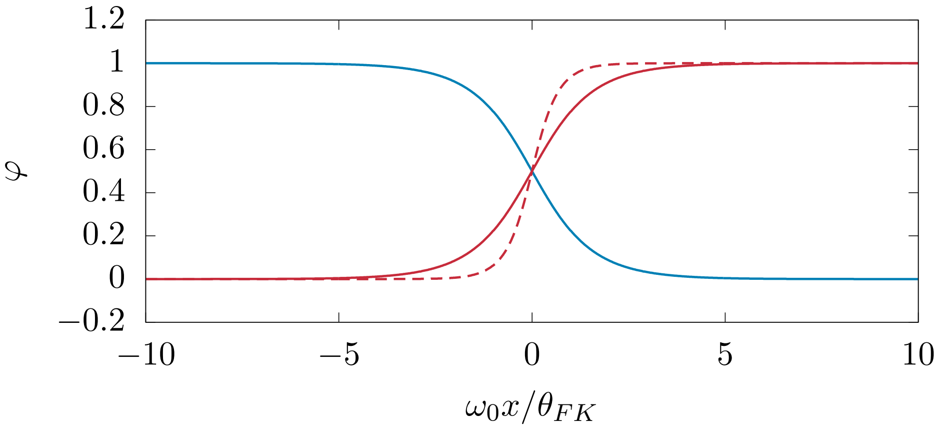

Figure 3.3: The kink solution $s_K = +1$ for $v = 0$ (solid red) and $v = 0.9\theta_{FK}$ (dashed red), as well as the antikink solution $s_K = -1$ for $v = 0$ (blue).

While the phonon spectrum describes small oscillations and hence it is not probing the non-linearity of the SGE, there exists another class of solutions, referred to as solitons, that are only possible due to the non-linearity [223, 266, 269, 270]. They can be found by assuming a solution with a time-independent profile, their dynamics is then determined solely by a Lorentz boost with a velocity v. The fact that these solutions do not change their spatial shape during the time evolution distinguishes them from the phononic excitations, which always disperse due to their non-linear dispersion relation. The ansatz $\varphi(x,t) = \varphi_K(x - vt)$ results in the solution

$$\varphi_K(x,t) = \frac{2}{\pi} \arctan \exp\left[s_K \frac{\omega_0}{\theta_{FK}} \frac{x - vt}{\sqrt{1 - \frac{v^2}{\theta_{FK}{}^2}}} \right], \tag{3.7}$$

which is commonly denoted as kink for the $s_K = +1$ solution and antikink for $s_K = -1$. These solutions are shown in Fig. 3.3. Centered around the kink position $X = vt$ the kink solutions interpolate over a finite length the two degenerate values $\varphi = 0$ and $\varphi = s_K$. They carry a topological charge $\varphi(x \to \infty) - \varphi(x \to -\infty) = s_K$, which is preserved during the dynamics. Simply speaking, these solutions are stable since their destruction requires to change $\varphi(x > X)$ by an integer, a process that requires an infinite amount of energy [268].

We can understand their emergence and many of their properties by noting that the trivial ground state $\varphi = 0$ is infinitely degenerate since adding an integer gives the same vacuum energy $\sin(2\pi\varphi) = 0$. The kink solutions are connections between neighboring degenerate vacuum solutions, schematically shown in Fig. 3.3, in the periodical potential landscape $V_{FK}(1 - \cos(2\pi\varphi))/2$. In this picture it is not surprising that they move with a constant velocity v, since the translation of the point at which the two solutions are connected leaves the potential energy untouched [270–272]. In the quasiparticle picture this results in a flat effective potential for the kink solutions. They move like a free particle, a feature worth noting since it relies on the continuity approximation of the original FK model.

In addition to their obvious Lorentz invariance, these solutions also exhibit Lorentz contraction, a phenomenon known from special relativity, as the width of the area with non-trivial φ given by $\sqrt{1 - v^2/{\theta_{FK}}^2}$ shortens for increasing velocities. It becomes also obvious that the solution only exists for $v < \theta_{FK}$. These analogies make them interesting for the study of special relativity [266].

The presence of a kink in the system modifies the phonon mode spectrum discussed above. Assuming small perturbations of the kink solution by writing $\varphi = \varphi_{K/AK} + \delta\varphi(x)e^{-i\omega_{phon}t}$, we find the emergence of a localized mode with $\omega_{phon} = 0$ [224]. This mode corresponds to the translation of the kink and consequently has vanishing frequency. The rest of the phonon modes keep their gapped dispersion relation $\omega_{phon}^2 = \omega_0^2 + {\theta_{FK}}^2 k^2$ but their shape $\delta\varphi(x)$ is distorted close to the position of the kink. The creation of a localized kink mode that is detached from the rest of the spectrum, and the distortion of the residual phonon modes due to the presence of the soliton, are important observations for this Thesis.

So far we only discussed solutions that include a single soliton, however the analysis of multi-soliton states reveals the third class of solutions of the SGE, namely breathers [273–281]. Analyzing the collision of two solitons reveals that equal sign solutions repel each other, i.e. a kink experiences a repulsive effective potential in the vicinity of another kink. However, the interaction between a kink and an antikink is attractive. In addition to the scattering states for large relative velocities there exist states that can be interpreted as bound kink-antikink solutions and describe their localized relative oscillations around each other. These solutions are known as breathers and have similar solitonic properties, although their spatial shape is not time-invariant as in the case of the (anti-)kink. It is important to note that the total topological charge of the breather vanishes as for the phonon excitations and hence in the presence of dissipation they exhibit a finite lifetime, a property which distinguishes them from the topologically protected (anti-)kinks.

While the SGE gave meaningful insight to understand the properties of the FK, we now come back to the discretized description, emphasizing the effects of the discreteness of the particle chain that lead to a modification of the minimal energy state and its excitations.

3.2.2 Ground states and solitonic excitations

The ground state of the SGE proved to be trivial and infinitely degenerate due to the translational invariance with a multiple of θ_{FK}. While the latter still holds in the FK model, the calculation of the ground state is not as simple. According to Eq. (3.4) the ground state requires to find solutions $\{x_i\}$ that fulfill

$$x_{i+1} + x_{i-1} - 2x_i = \pi V_{FK} \sin(2\pi x_i), \tag{3.8}$$

an equation that by defining $d_{i+1} = x_{i+1} - x_i$ can be transformed into the Chirikov Standard map [282, 283]:

$$\begin{pmatrix} d_{i+1} \\ x_{i+1} \end{pmatrix} = \begin{pmatrix} d_i + \pi V_{FK} \sin(2\pi x_i) \\ x_i + d_{i+1} \end{pmatrix} = M \begin{pmatrix} d_i \\ x_i \end{pmatrix}. \tag{3.9}$$

Hence, we can understand each stationary state as a trajectory in the phase space of the vector $\vec{X}_i = (d_i, x_i)$ with a non-linear propagation operator M. Due to the form of Eq. (3.9), the study of the stationary states of the FK model is also interesting for research on chaotic systems [282, 284–286].

For a rational value of $\theta_{FK} = \frac{p}{q}$ the atoms align in a commensurate configuration that can be defined by $x_{i+p} = x_i + q\theta_{FK}$ [60, 264, 287]. In the picture of the standard map this is expressed by the fact that $M^p \vec{X}_i = \vec{X}_i$ if the positions are taken modulo 1. Due to this translational invariance, the particles sit only at a finite number of phases relative to the corrugation potential, the sequence $x_i \; mod \; 1$ repeats after p particles. With increasing V_{FK} the particles are forced closer to the potential minima such that their ground state positions change, however the general properties of the state given above hold for all values of the corrugation potential amplitude. This is not the case for the irrational values of θ_{FK}.

In the incommensurate FK model, the ground state shows no periodicity of $x_i \; mod \; 1$ due to the mismatch between the equilibrium length of the unperturbed chain a_S and the corrugation period a_P [288]. For small values of V_{FK} the harmonic interaction stabilizes the particles close to their unperturbed equilibrium positions $x_i = i\theta_{FK}$. Hence, we can find particles arbitrarily close to any position relative to the nearest potential minimum or maximum. Another way of interpreting this state is by considering the translation of the chain by external forces. Since all relative positions $x_i mod 1$ are found in the ground state, the translation of particles by any arbitrarily small distance leads to an equivalent realization of the ground state. Hence the system must be friction-less, and this regime is referred to as sliding phase. Note that this is never true in the commensurate phase where the particles are always pinned by the corrugation potential and only a finite set of values of $x_i mod 1$ are allowed.

If V_{FK} is increased above a certain threshold this stationary state becomes unstable, and the particles are pinned by the corrugation potential in its wells [283, 289, 290]. Consequently, particles sitting close to the maximum of the potential are pushed away from their unperturbed positions, and there exist regions in which we do not find particles due to the large potential energy. This transition has been named after its discoverer Serge Aubry, and is sometimes also known as the breaking of analyticity. The naming of this phase transition aims to offset it against continuous phase transitions that are accompanied by the breaking of a symmetry by the ground state. Consequently, its description cannot be cast into a Landau theory as neither the sliding phase nor the pinned phase exhibit any kind of symmetry in the particle positions. Aubry noted that the incommensurate ground state can be characterized by its so-called hull function $x_i = h(i\theta_{FK})$, which describes the position of the particles as a function of their position in absence of the corrugation potential [283, 289]. For $V_{FK} = 0$ it is trivial $h(x) = x$ and remains continuous and analytic for small V_{FK}. At the transition of analyticity, gaps open in the hull function marking the onset of unoccupied regions relative to the potential, see Fig. 3.4. When a dragging force is applied, the particle chain exhibits stick-slip motion, the pinning of the particles leads to a non-zero friction force similar to the PT model. For these reasons this phase is commonly called pinned phase. In the picture of the Chirikov standard map this leads to a breaking of the continuous orbits of vectors $\vec{X}_i$ into Cantor sets [291]. The destruction of the incommensurate trajectories follows an order, i.e. orbits with an θ_{FK} close to a "simple" rational value (1, $1/2$, $1/3$,...) are destroyed for smaller values of V_{FK} with the most robust orbit having a coverage parameter given by the golden mean [285, 286]. Therefore, in most studies the ratio between a_S and a_P is approximated by a rational series of approximants with increasing accuracy to the golden mean to reach a strong signal of the desired incommensurability.

Analogue to the discussion of the SGE we can split the excitations of the ground-state configurations into different categories. The phonon modes describe small amplitude modulations of the particle positions and are always gapped for the commensurate FK model [293–296]. Exemplary, we can calculate for the simple case of $p = 1$ that the phonon spectrum has the form

$$\omega_{phon}^2 = \omega_0^2 + 2(1 - \cos(k)) \tag{3.10}$$

where $\omega_0^2 = 2\pi^2 V_{FK}$ is the same as in the SGE case [60]. In general, the elementary cell of the chain contains p particles and therefore the phonon spectrum contains p gapped bands.

In addition to the phonons, there exist kink excitations that can be once again understood as the localized connection between degenerate ground states. Their existence relies, analogous to the continuum limit, on the infinite degeneracy of the ground state, a global translation of the particles by a multiple of the potential period and/or the relabelling of the atoms leads to another ground state. The kink

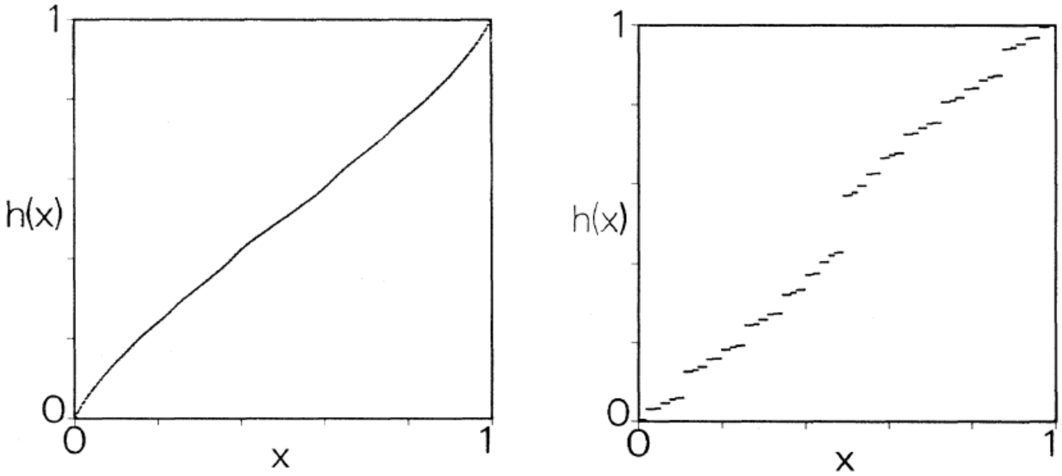

Figure 3.4: Left: Analytic hull function in the sliding phase. **Right:** Hull function with discontinuities in the pinned phase. Both diagrams are from Ref. [292]

solution interpolates between two ground states $\{x_i^-\}$ and $\{x_i^+\}$. Alternatively, they can be interpreted as the result of the removal or addition of particles. In the simple case of $\theta_{FK} = 1$, a kink constitutes a doubly occupied potential well, while an antikink is marked by an empty minimum, see Fig. 3.5.

The properties of kinks in the discrete FK model share many similarities with the solitons of the SGE model. For example, when defining $\varphi_i = x_i - x_i^- \approx \varphi_K(i\theta_{FK})$, they carry a topological charge $\varphi_\infty - \varphi_{-\infty} = s_K$, and we can treat them as a quasiparticle that moves inside the lattice structure by the hopping of single particles over the potential barriers. Moreover, their presence affects the phonon spectrum in a similar way, i.e. a localized kink mode emerges that is energetically decoupled from the residual spectrum, whose dispersion remains untouched. However, the discreteness of the particle chain leads to the emergence of a non-trivial effective potential for the quasiparticle motion, known as the PN potential from dislocation theory [297, 298]. Since the motion of the kink takes place by the transfer of an atom across a potential barrier, which is not energetically compensated by the motion of the neighboring atoms, there exist periodic barriers, called PN barriers. These barriers with amplitude E_{PN} lead to a non-vanishing frequency of the kink mode, something that distinguishes it from the solitons of the SGE. An approximation of of the PN potential in lowest order of a_S yields a periodic form $V_{PN}(X) \propto E_{PN}(V_{FK})(1 - \cos(2\pi X/q)$ with the kink position X. As in the

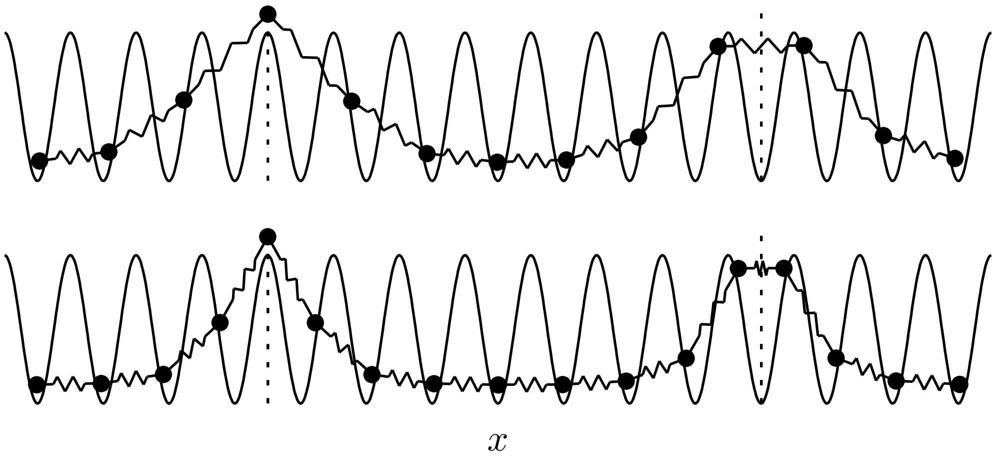

Figure 3.5: The two kink configurations (top: antikink, bottom: kink) for $\theta_{FK} = 1$ in the unstable configuration (left) corresponding to a maximum in the Peierls-Nabarro (PN) potential and the stable configuration (right) in the minimum of the PN potential. The dashed lines indicate the kink positions.

case of the continuum approximation the kink position is calculated via

$$X = s_K \int_{-\infty}^{\infty} dx\; x \frac{d\varphi_i(x)}{dx} \tag{3.11}$$

which can be interpreted as an average position calculated from the kink density $d\varphi_i(x)/dx$.

To describe the dynamics of the kink inside the particle lattice it is instructive to employ a collective variable formalism [299–301]. This framework defines a position and momentum of the quasiparticle and promotes them to canonical variables of the model. Assume that the positions of the particles can be written as a sum of an isolated kink solution with a kink position X and a dressing

$$x_i = \varphi_i(X) + \chi_i\,; \qquad \frac{dx_i}{dt} = \frac{d\varphi_i(X)}{dX}\frac{dX}{dt} + \frac{d\chi_i}{dt}. \tag{3.12}$$

Since writing the particle configuration as a sum of two contributions is ambiguous, we require that for a given set of x_i [302, 303]

$$C_1 = \frac{-1}{2}\frac{d}{dX}\sum_i (x_i - \varphi_i(X))^2 = \sum_i \chi_i \frac{d\varphi_i(X)}{dX} = 0. \tag{3.13}$$

Inserting the velocities into the kinetic energy term yields

$$\sum_i \frac{m}{2}\left(\frac{dx_i}{dt}\right)^2 = \frac{M_\varphi}{2}\left(\frac{dX}{dt}\right)^2 + \sum_i \frac{m}{2}\left(\frac{d\chi_i}{dt}\right)^2 + \frac{m}{2} C_2 \frac{dX}{dt} \tag{3.14}$$

where $M_\varphi = m\sum_i \left(\frac{d\varphi_i}{dX}\right)^2$ is the quasiparticle mass, which is in general dependent on the kink position X [60]. We can set $C_2 = \sum_i \frac{d\varphi_i}{dX}\frac{d\chi_i}{dt} = 0$, and obtain a result that is the sum of the quasiparticle kinetic energy and the dressing kinetic energy. Hence the conjugate momenta for the position variables are given by $P = M_\varphi \frac{dX}{dt}$ and $\rho_i = m\frac{d\chi_i}{dt}$.

Note that we need to constraint the system via $C_1 = C_2 = 0$ in order to make the transformation of variables $(x_i, p_i) \to (\chi_i, \rho_i, X, P)$ canonical. The introduction of two new dynamical variables is countered by the two constraints so that the number of degrees of freedom remains constant. C_1 guarantees that for a given configuration the closest respective kink solution is chosen for the separation (3.12), and hence determines X. In a similar fashion C_2 is necessary for a sensible definition of the kink momentum P leading to a particle-like separation of the kinetic energy [302]. The equations of motion of the new set of variables is given by the Hamilton equations with a modified Poisson bracket

$$\{A, B\}^* = \{A, B\} - \sum_{\alpha,\beta=1,2} \{A, C_\alpha\}(C^{-1})_{\alpha\beta}\{C_\beta, B\} \tag{3.15}$$

where $C_{\alpha\beta} = \{C_\alpha, C_\beta\}$ and $\{A, B\}$ denotes the Poisson bracket with respect to the new variables (χ_i, ρ_i, X, P).

An explicit calculation of $\frac{dP}{dt} = \{P, H\}^*$ and $\frac{d\rho_i}{dt} = \{\rho_i, H\}^*$ reveals a set of coupled equations of motion caused by the potential term $V(\{\varphi_i + \chi_i\})$. This shows that, in addition to the PN potential, the motion of the kink inside the discrete particle lattice causes the excitation of dressing amplitudes χ_i, that are for small energies synonymous with the phonon modes. If the system is initiated with $\chi_i = 0$ but $P \neq 0$, the kinks motion is dampened as it radiates energy into the dressing degrees of freedom, eventually it will become trapped in one of the minima of the PN potential, see Fig. 3.6 [304–310]. This process occurs in different stages with subsequently weaker damping rates. When the kinks kinetic energy surpasses E_{PN} the kink travels across the barriers in the PN potential, its momentum P oscillates with a frequency that depends on its kinetic energy. This oscillation excerts a periodic driving force on the dressing modes leading to the radiation of the kinks kinetic energy into the dressing mode spectrum. This process creates a damping force onto the kinks motion with a damping rate that is determined by the density of states of the phonon spectrum at multiples of the oscillation frequency of P. When initialized at a large momentum the frequency of P lies within the phonon spectrum so that the resonant driving of the dressing leads to a fast decay of the kink momentum, as seen for $v < v_1$ in Fig. 3.6. At a critical P its oscillation frequency falls into the gap of the phonon modes (compare Eq. (3.10)) so that higher order resonances remain the only process enabling the energy transfer which reduces the damping rate, see $v_2 < v < v_1$ in Fig. 3.6.

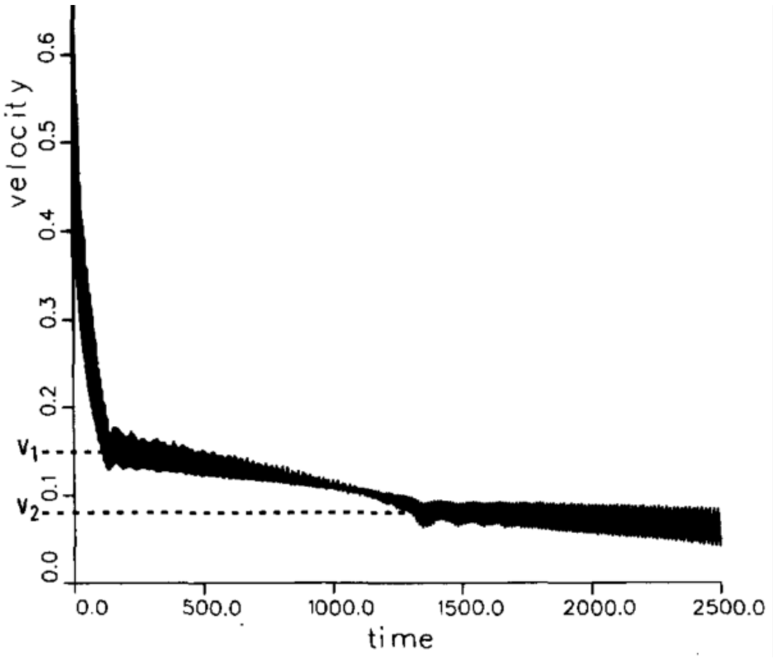

Figure 3.6: Velocity of a kink in the FK model as a function of time. Diagram from Ref. [306]

Remember that the kink solitons in the discrete FK model only exist in the commensurate ground state. However, the discussion of their properties for rational θ_{FK} also helps to understand the dynamics of the incommensurate configuration, as we can think of it as a lattice of kinks in the commensurate state with the closest rational θ_{FK}. The phonon spectrum in the incommensurate ground state breaks into two bands that are associated to the kink translations and the phonon modes. While the phonon modes exhibit an optical dispersion relation similar to the phonons in the commensurate case, the low-wave-number excitations are acoustic in the sliding phase. In particular, the sliding mode with vanishing energy appears due to the friction-less nature of this phase. If the corrugation potential amplitude is tuned across the Aubry transition, the kink modes become gapped as well, a sign of the pinning of the particles by the potential minima.

To conclude, the main features of topological solitons, i.e. the emergence of localized kink modes describing their motion in the PN potential, hold in a discrete FK model. However, the discreteness introduces a damping of their motion and a periodic modulation of the effective potential.

3.2.3 Finite-size Frenkel-Kontorova model

While the original FK model describes an infinite chain of particles it is worthy to understand what remains of its physical phenomena in systems with a finite particle number N, in particular the effect of free-end boundary conditions become important in this case. The results discussed so far in this chapter concentrated on the case of fixed-density boundary conditions, where the length of the chain $x_N - x_1$ and the particle number N are externally fixed and increased to infinity while keeping a fixed ratio between them. For free-end boundary conditions the chain length is not set externally, in the case of a finite particle number it is determined by θ_{FK}. In this context we define L as the integer number of potential periods over which the particles spread [60]. The ground state configurations for a fixed N as a function of the two parameters θ_{FK} and V_{FK} can be categorized via two properties: the chains symmetry and its so-called chain order $n = N - L$. The latter gives the amount of doubly occupied potential wells which coincides with the number of kinks (or anti-kinks for $n < 0$) in the system. Let us first discuss its behavior for the ground state when θ_{FK} is tuned while keeping $V_{FK} > 0$ fixed, starting in the trivial case $\theta_{FK} = 1$ for which all particles sit at a corrugation potential minimum. For small changes of θ_{FK} away from unity $n = 0$ holds as only the boundary particles slightly shift away from $x_i = i$ due to their missing neighbor particles which leads to a reduced pinning via the interaction potential, see the top configuration in Fig. 3.7. In this regime the potential energy of the ground state grows quadratically with θ_{FK} until it becomes energetically favourable to change n by ± 1 and thereby introduce a (anti-)kink. This transition occurs when the energy from the interaction potential (corrected by the particle shifts away from the potential minima at the boundaries) is equal to the kink energy and its repulsion energy from the boundaries. The process of soliton absorption from the systems boundaries here exhibited by the particles through their deviation from the potential minima is known as Frank-van-der-Merwe growth [311–314]. After the introduction of a single (anti-)kink in the systems center, it is stabilized there due to its repulsion from the boundaries, further changing θ_{FK} leads to a repetition of the kink absorption process, however for the subsequent creation of defects their repulsion energy among each other has to be taken into account.

Next to the jumps in n as a function of θ_{FK}, associated with the creation of defects in the ground state, the chains symmetry under reflection on the systems center of mass is a quantity of interest.

For even N and odd N but even n the ground state is symmetric independent of V_{FK} [315], see the top and bottom configuration in Fig. 3.7. Among the stationary states we find in any case asymmetric metastable states next to the ground state, compare the states $\langle 1' \rangle_a$ and $\langle 2 \rangle_a$ in Fig. 3.7 to the respective ground state.

A special case occurs when N and n are odd simultaneously for which we find one particle in the systems center at a potential maximum for small values of V_{FK}, see the state $\langle 1 \rangle_s$ in Fig. 3.7. This kink particle is stabilized there due to the dominating interaction with the other atoms which remain close to the potential minima. This balance becomes unstable when V_{FK} is increased to the critical value of what turns out to be the equivalent of the Aubry transition in finite chains [316, 317]. In the pinned regime of the finite FK model the kink particle rolls away from the potential maximum and the system spontaneously falls into one of two degenerate asymmetric ground states, see the state $\langle 1 \rangle_a$ in Fig. 3.7. Note that the described symmetry breaking cannot be described by a Landau theory as its equivalent in the thermodynamic limit is the breaking of analyticity in the incommensurate FK model. While for the original Aubry transition in the incommensurate FK model the sliding phase was characterized by a zero-frequency sliding mode, the kinks repulsion from the boundaries and potentially existing other defects leads to a gapped phonon spectrum for all values of V_{FK} except the critical value of the transition, where the ground state becomes unstable. The kink mode describes, as in the infinite FK model, the oscillation of the defect in an effective PN potential when the energy of the excitation is insufficient to reach the boundaries.

In addition to the phonon modes there exist two non-linear edge modes when the excitation energy becomes sufficient [318, 319]. They describe the periodic reflection of a kink at the chains edge with the simultaneous conversion to an antikink (and vice versa), which can be understood as a breather excitation bound to the systems boundary. If the excitation energy of this mode and hence the oscillation amplitude of the involved (anti-)kink surpasses a critical value a caterpillar-like motion of the whole chain is triggered [320]. This can be understood as a coupling of the two edge modes as the (anti-)kink reaches the crystals center during the oscillation period. The caterpillar-like motion is desribed by a periodically repeting sequence of defects moving across the chain as follows. A kink travels to one boundary where it gets reflected and transformed into an antikink which subsequently moves to the opposing boundary where its gets reflected and transformed again into a kink (followed by a repetition of the sequence). This process translates the whle chain after one period. Note that the edge mode as well as the caterpillar motion are damped as they feature the motion of (anti-)kinks, see Fig. 3.6 [319].

3.2.4 Quantum Frenkel-Kontorova model

In many cases discussed so far, the particles of the classical FK model are pinned by the corrugation potential, it is therefore intriguing to ask about the role of quantum fluctuations in a quantum mechanical description [322, 323]. Due to tunneling effects, we can expect that the properties of the ground state in the

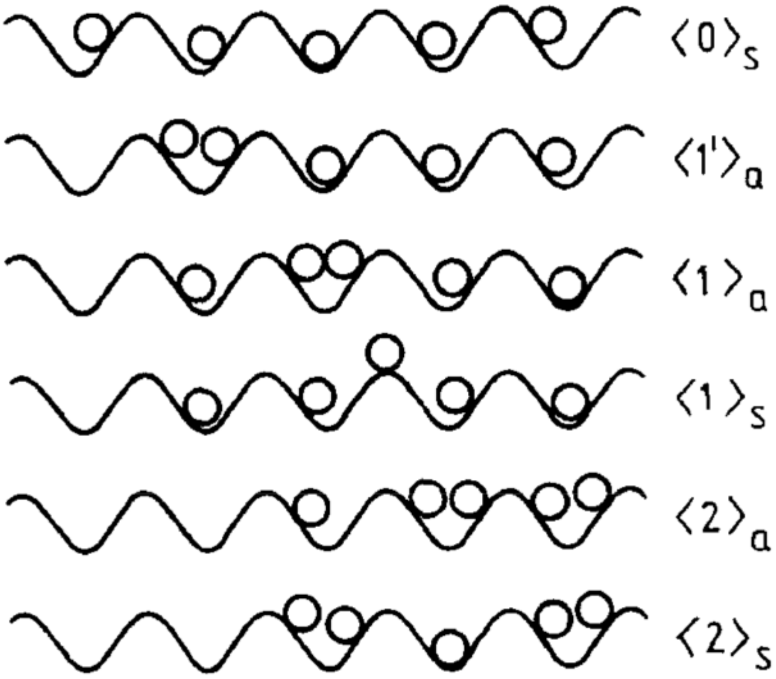

Figure 3.7: Stationary configurations for $N = 5$ with decreasing a_S, from top to bottom. The notation of the states $\langle n\rangle_z$ indicates the chain order and the symmetry, i.e. $z = a$ for asymmetric configurations and $z = s$ form symmetric ones. Diagram from Ref. [321].

pinned regimes are modified as the particle wave function might be delocalized over more than one potential well. Writing the quantum Hamiltonian of the FK in position representation gives rise to an effective Planck's constant [324–327]

$$H = \sum_i \frac{-\tilde{\hbar}^2}{2}\frac{\partial^2}{\partial x^2} + \frac{V_{FK}}{2}(1-\cos(2\pi x_i)) + \frac{1}{2}(x_{i+1}-x_i-\theta_{FK}) \tag{3.16}$$

$$\tilde{\hbar} = \frac{\hbar\omega_\kappa}{m\omega_\kappa^2 {a_P}^2} = \frac{l_\kappa^2}{{a_P}^2} \tag{3.17}$$

where $\omega_\kappa = \sqrt{\kappa/m}$. $\tilde{\hbar}$ is a direct measure for the importance of quantum effects in the model as it is given by the ratio of the quantum mechanical energy or length scales and their classical equivalents, e.g. it can be written as a comparison between the quantum mechanical harmonic oscillator length l_κ due the the harmonic interaction and the corrugation potential period. It is obvious that for small $\tilde{\hbar}$ we approximately recover the physics of the classical FK model.

If $\tilde{\hbar}$ is increased the quantum fluctuations soften the pinning effects of the corrugation potential and result in modifications in the quantities used to characterize the classical ground state, e.g. the hull function. As discussed above, in the pinned regime it shows discontinuities with several gaps that are opened at the critical value of the Aubry transition. When computed with the expectation values of the quantum ground state, these gaps become more and more filled by particles whose wave functions show significantly enhanced fluctuations in comparison to the ones in the plateaus of the hull function. This is a directly observable consequence of quantum tunneling through barriers of the corrugation potential.

Another noteworthy effect of the quantum fluctuations is the departure of the particle positions from the classically allowed ones. To demonstrate this, one may introduce the function

$$g_i = \frac{1}{\pi V_{FK}}(x_{i+1} + x_{i-1} - 2x_i). \tag{3.18}$$

For any stationary state of the classical FK model, it is clear from Eq. (3.8) that the points of g_i as a function of $x_i mod 1$ lie on $g(x) = \sin(2\pi x)$. In the pinned regime, $\{g_i\}$ form a Cantor subset of $\sin(2\pi x)$. In the quantum delocalized regime, however, the particles can explore classically unavailable states. It has been found that $\{g_i\}$ changes into a saw-tooth shaped set, as shown in Fig. 3.8 [322, 323, 328–332].

3.3 Emulation of nanofriction in ion crystals

The experimental investigation of the theoretical predictions of the classical FK model has been successfully performed in well-controllable trapped ion systems. In particular, two different approaches have been followed in order to demonstrate the finite Aubry transition and its accompanied change in the dynamics and phonon spectrum.

There are two main ingredients required for a real implementation of the FK model: a periodic potential and a one-dimensional interacting chain of particles [60, 334–336]. Note that although the original FK model considered harmonic particle interaction with an equilibrium distance θ_{FK}, it can be extended to anharmonic interactions and, most importantly for the case of trapped ions, to repulsive interactions in the presence of an external confinement [60, 292, 337].

3.3.1 Lattice approach

One series of experiments, first proposed in Ref. [45], features a string of ions trapped in a Paul trap subject to the optical lattice created by an off-resonant standing-wave laser field (see Sec. 2.1.2) [169]. A schematic depiction of the setup

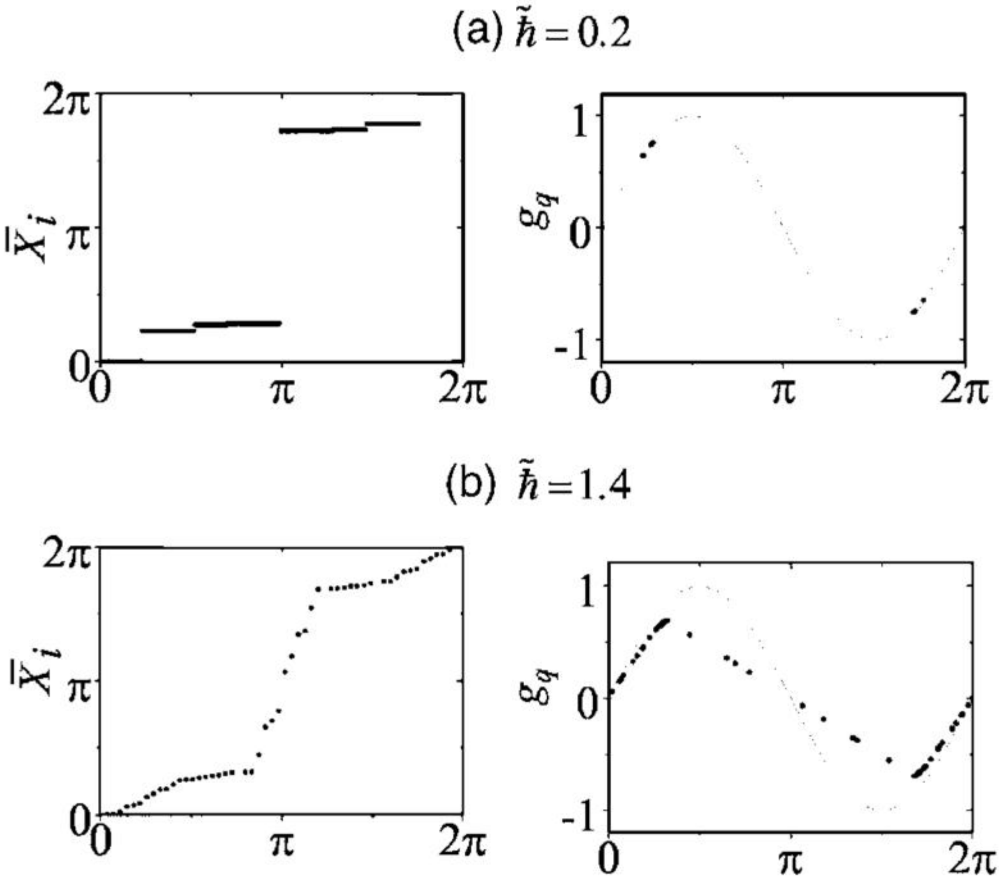

Figure 3.8: Hull function and $\{g_i\}$ for the incommensurate quantum FK model in the pinned regime for different values of the effective Planck's constant $\tilde{\hbar}$. Diagram from Ref. [333]

described by the Hamiltonian

$$H_{ionFK} = \sum_i \frac{p_i^2}{2m} + \frac{m\omega_z^2}{2} z_i^2 + V_{FK} \cos\left(\frac{2\pi}{a_P} z_i + \phi_0\right) + \frac{1}{2} \sum_{j \neq i} \frac{C_0}{|z_i - z_j|} \tag{3.19}$$

is shown in Fig. 3.9. In the case of a single ion system, this approach directly implements the PT model from Eq. (3.2). Its transition from continuous frictionless motion to a stick-slip regime can be probed when the center of the Paul trap is moved with velocity v [42, 47].

In a multi-ion system, the commensurability of the ion chain with respect to the optical lattice is tuned by the value of the trap frequency ω_z, since it determines the average ion distances [45]. When the ion distances are chosen to be incommensurate to the lattice period given by the laser wavelength the ground state exhibits the breaking of analyticity of the hull function when the laser

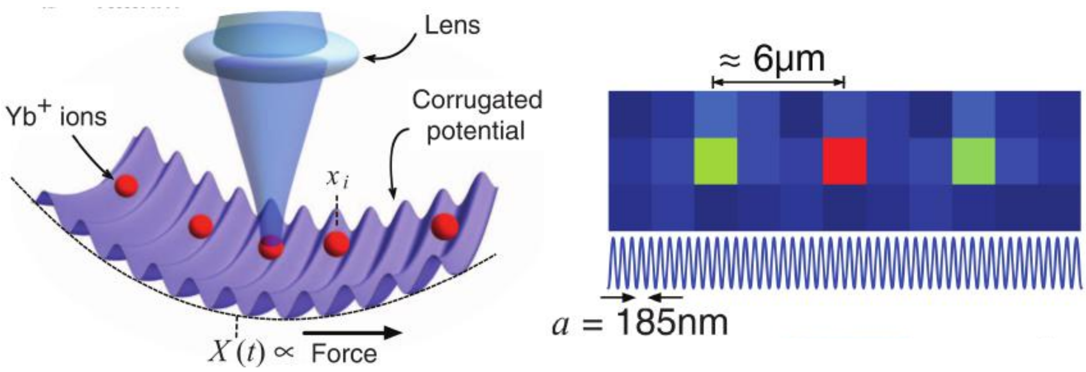

Figure 3.9: Left: Schematic depiction of the one-dimensional implementation of the FK model with trapped ions. The trap potential is corrugated by a standing wave laser. The ion fluorescence due to laser cooling is collected in a lens. **Right:** Fluorescence image of a three-ion chain with an ion distance of 6 µm, for comparison the optical lattice is shown in the same scale. Diagrams from Ref. [42].

amplitude is increased. The gap of the phonon spectrum, depicted in Fig. 3.10 (top), increases significantly at this Aubry transition but stays finite in the sliding phase due to the finite, even number of ions considered. As in the finite FK model, the low-energy phonons exhibit an acoustic dispersion and become optical in the pinned regime [45].

In addition to the analysis of the hull function, which requires the absolute measurement of the ion positions and the phonon dispersion, the hallmark of the Aubry transition for the static friction force has been proposed in Ref. [41] as an experimentally accessible quantity. To measure the static friction force, the trap center is translated adiabatically, which moves the ions against the optical lattice, eventually the ions slip into the neighboring potential well, and the released potential energy is dissipated via continuous laser cooling. Since the electronic states are shifted depending on the lattice laser intensity the fluorescence from the cooling laser depends on the ions position, making it possible to determine at what point the slip event occurs.

Results in the multi-ion case, shown in Fig. 3.10 (bottom), reveal the effect of incommensurability in the system by a substantial reduction of the static friction force [42, 43, 338]. In the case of a commensurate chain, the result follows closely the expectation for the single particle case, i.e. the PT model, independent of the particle number. If the trap frequency is tuned such that the central ion distances do not match the lattice period, the system shows a non-zero static friction force only for much higher V_{FK}. The transition point of this finite-size Aubry transition increases with the total ion number. For larger N, the particle distances in

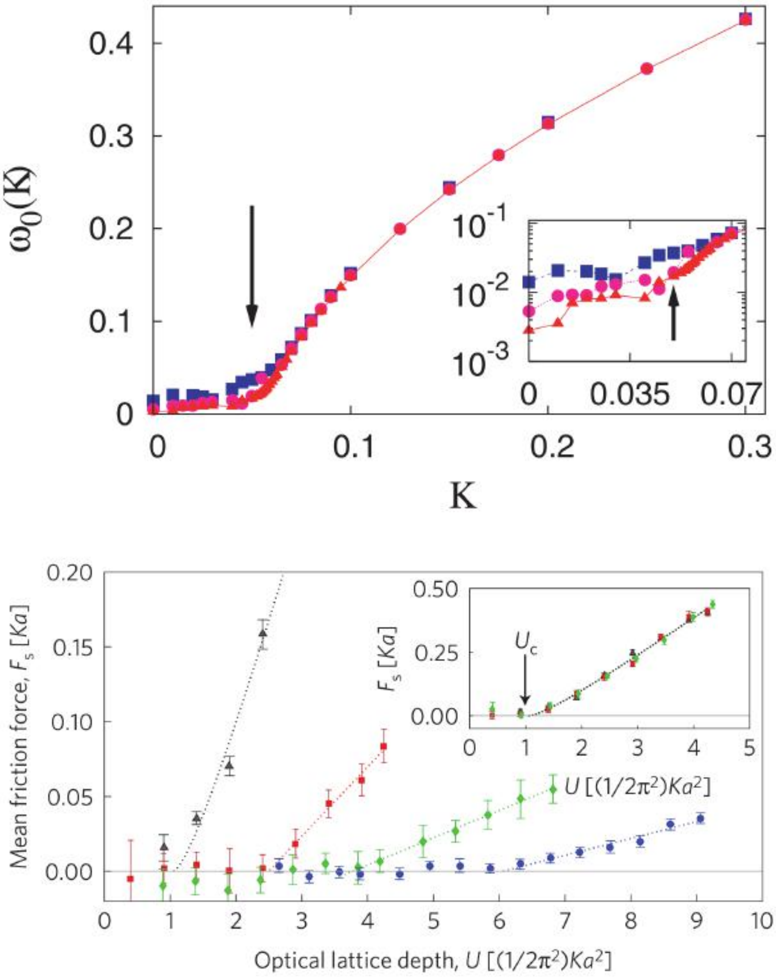

Figure 3.10: **Top:** Minimal phonon mode frequency of a linear ion string subject to a periodic potential as a function of the potential amplitude. The different graphs are for increasing particle numbers: $N = 50$ (blue squares), $N = 150$ (pink circles) and $N = 300$ (red triangles). Diagram taken from Ref. [45]. **Bottom:** Measured static friction force as a function of lattice depth in the incommensurate case. The inset shows the same measurement for the commensurate case, the dashed line indicates the prediction from the PT model. Diagram taken from Ref. [43]

the center of the chain become more uniform, making them all incommensurate, leading to a stronger effect.

This straightforward implementation of the FK model in trapped ion systems can also be used to study the velocity dependence of the friction forces occurring, i.e. when the ramp rate of the trap center is increased [263]. Moreover, the incommensurate regime can be reached for multiple values of the trap frequency. When it is reduced, the ions may exhibit slip events over a distance larger than one lattice period, referred to as multi-slip [339]. This experiment has also some drawbacks, mainly due to the necessity of confining the ions by the rf field. This poses a harsh breaking of the translational invariance that was of importance in many occasions for the FK model. In particular, the location of the trap center is crucial for the ground state of the system. Moreover, the inhomogeneity of the ion distances makes it hard to enter a truly incommensurate regime, since the match between the ion distances and the lattice period changes with position.

Although the measured results clearly indicate the onset of friction at finite values of V_{FK} at the stick-slip transition of the PT model and the Aubry transition already for small ion numbers, inhomogeneous ion distances constitute a modification of the original FK model, which is only negligible for $N < 4$ for which the system can be approximately described by the PT model.

3.3.2 Kink approach

In addition to the implementation discussed above, another experiment has observed the Aubry transition in a two-dimensional ion crystal with a defect [46]. The idea is to understand the zigzag structure (see Sec. 2.3) as the sum of two individual ion chains on top of each other, indicated in Fig. 3.11 (top) by the two different ion colors. Via its charge density, the lower chain creates a corrugation potential for the upper chain. Vice versa, its amplitude V_{FK} is tuned by the distance between the chains determined by the radial trap frequency.

In the absence of a topological defect the two chains are trivially commensurate (corresponding to $\theta_{FK} = 1$), each ion sits in a minimum of the potential created by the opposite chain, and therefore no breaking of analyticity can be observed. If an extended kink is introduced, a local incommensurability is created in the chain center. The situation resembles the finite FK model with odd N and even n (see Sec. 3.2.3), e.g. localized kink modes can be found in the motional mode spectrum of the crystal [60, 224, 294]. Upon change of the trap aspect ratio α, the crystal symmetry is broken due to the increase of the corrugation of the chains [340, 341]. Counter-intuitively, the finite Aubry transition can only be observed for a horizontal kink. The vertical defect with two ions sitting above each other does not exhibit a symmetry breaking. This difference in their behavior is due to the fact that the corrugation potential is not created externally but by the self-organized crystal itself. Hence, a change in the distances of one of the subchains backacts onto the opposite chain, altering the created corrugation potential ultimately leading to the stabilization of the vertical defect. Their difference is also observable in the shape of the PN potential, derived in the following.

Unlike in the original FK model where the kink solution can be approximated

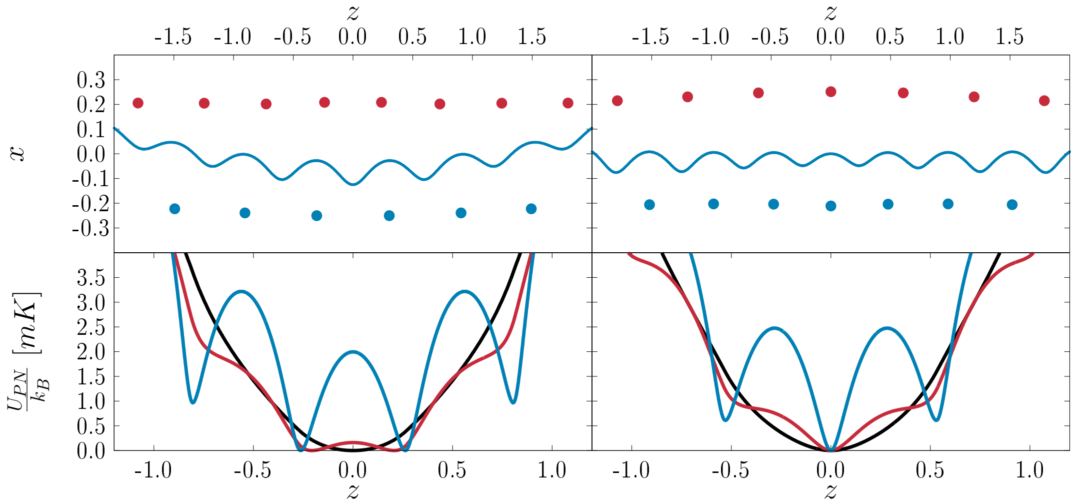

Figure 3.11: Top: Two-dimensional ion crystals with extended horizontal (left) and vertical (right) topological defect, the ions of the two sub-chains ($x > 0$ and $x < 0$) are depicted red and blue, respectively. The line indicates an equipotential surface of the Coulomb potential created by the lower sub-chain, emulating a corrugation potential. **Bottom:** PN potential of the horizontal (left) and vertical (right) kink for different α values: $\alpha - \alpha_A = -0.409$ (black), $\alpha - \alpha_A = 0.191$ (red) and $\alpha - \alpha_A = 0.591$ (blue).

by the continuum soliton solution ($\varphi_i = x_i - x_i^- \approx \varphi_K(i\theta_{FK})$), it is unclear how the ion positions look like as a function of the kink position X in an ion crystal. In this case, we can nonetheless determine them by defining a kink position function K which returns X for given ion positions. In a two-dimensional ion crystal, the kink solution continuously connects the zigzag and the zagzig configuration which are a radial mirror image of each other. Therefore, we only consider the axial ion positions as a measure for the deviation from the regular zigzag alignment because they are the same for both ground states. One useful definition that captures the character of the kink is [225]

$$K(\{\vec{r}_i\}) = \frac{\sum_i \bar{z}_i(\delta z_i - \delta z_i^{zz})^2}{K_0} \tag{3.20}$$

where $\delta z_i = z_{i+1} - z_i$ is the axial ion distance, assuming z ordering of the ions. δz_i^{zz} are the ion distances for a defect-free zigzag crystal and $K_0 = \sum_i(\delta z_i - \delta z_i^{zz})^2$ is a normalization constant. $2\bar{z}_i = z_{i+1} + z_i$ denotes the average axial position of the links between neighboring ions. We can interpret this definition as an expectation value of the link positions $\bar{z}_i$ weighted by the deviations from the ground state distances. The spatial spread of the transition between the two ground states is described by $\delta z_i - \delta z_i^{zz}$ as shown in Fig. 3.12. In the case of the extended

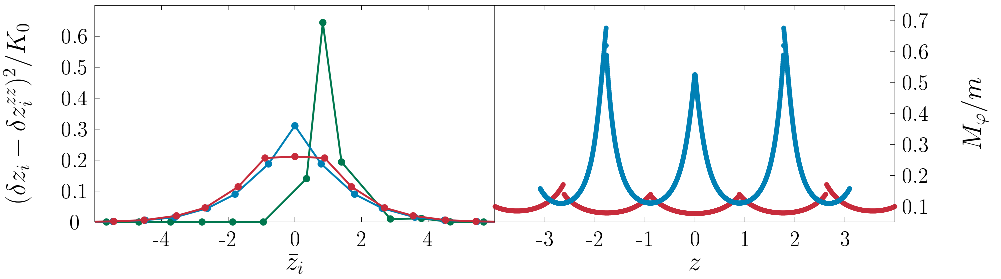

Figure 3.12: Left: Deviations from the ground state distances due to the presence of a horizontal (red, $\alpha = 6$), vertical (blue, $\alpha = 7$) and odd (green, $\alpha = 8.5$) kink as defined in Eq. (3.20). **Right:** Kink mass for a horizontal (red, $\alpha = 6$) and vertical (blue, $\alpha = 7$) kink as a function of the kink coordinate X. Discontinuities at the maxima are caused by numerical instabilities as the z-ordering of the ions changes. All lengths are given in units of $\sqrt[3]{C_0/m\omega_z^2}$.

forms (vertical and horizontal) the configuration changes from zigzag to its radially inverted counterpart over approximately 10 ions with an larger spread in the case of the horizontal kink, while the odd kink is highly localized.

Subsequently, the ion positions for a certain kink positon $\vec{\varphi}_i(X)$ are found by minimizing the systems energy in a Lagrange formalism with the constraint $K(\{\vec{r}_i\}) = X$. This requires solving the $2N + 1$ equations given by

$$(\{\vec{\nabla}_i\}, \partial/\partial\lambda) \left[V_{trap} + V_{Coul} + \lambda(K(\{\vec{r}_i\}) - X)\right] = 0. \tag{3.21}$$

where λ is the introduced Lagrange multiplier corresponding to the constraint. As in the collective excitation formalism discussed in Sec. 3.2.2, we can then canonically transform the classical equations of motion by defining a dressing field $\vec{\chi}_i$, that describes the motion of the ions that do not translate the kink. In that model, the dressing and the kink are coupled by the potential terms of the Hamiltonian, the PN potential is obtained if the dressing field is neglected such that $U_{PN}(X) = (V_{pot} + V_{trap})(\{\vec{\varphi}(X)\})$. In addition, the kink mass is calculated as usual from

$$M_\varphi = m \sum_i \left(\frac{d\vec{\varphi}_i(X)}{dX}\right)^2 . \tag{3.22}$$

Its dependence on the kink position is shown in Fig. 3.12. While the effective kink mass is smaller than the mass of a single ion in all cases it shows a periodic behavior with maxima at those positions for which the kink constitutes two ions at the same value of z. These positions coincide with the maxima of the PN potential for the horizontal kink in the sliding phase and the minima in the case of the generally heavier vertical kink.

At the Aubry transition, the PN potential develops periodical modulations, i.e. the PN barriers, that pin the defects, in addition to the globally confining shape due to the repulsion from the systems boundaries, see Fig. 3.11 (bottom) [225, 341]. For the vertical defect, the modulations have a minimum in the crystal center so that the ground state of the system is not destabilized. The opposite occurs for the horizontal kink, a PN barrier emerges at $z = 0$, destabilizing the ground state of the sliding phase. For $T = 0$, in the classical regime, the defect falls spontaneously into one of the newly build local minima of the PN potential and simultaneously breaks the crystals symmetry, as observed in Fig. 3.13. Analogue to the finite-size Aubry transition, this phenomenon is accompanied by the softening of the localized kink mode that describes the axial motion of the defect. These observables of the Aubry transition, i.e. the breaking of symmetry and the existence of a soft mode, have been experimentally observed at Doppler temperatures [46]. In this system, the translation of the trap center is not able to reveal the change in the systems frictional behavior, as it moves both sub-chains simultaneously. In the experiments conducted, this has been solved by shining in a light field that creates a differential force between the two sub-chains and probes their shear motion, see Fig. 3.13. However, the spectroscopy of the kink mode is limited by the Doppler temperature of the crystal in the experiment, an issue that is addressed in Chapter 5.

This two-dimensional emulation of the FK model has the advantage of removing the effect of the inhomogeneity of the ion spacing in the ion chains [342]. Since the corrugation potential is created by another sub-chain in the same trap potential, the mismatch between the two is spatially homogeneous (in the commensurate configuration), a feature that is missing in the implementation via an optical lattice. For the same reason, the coverage parameter $\theta_{FK} = a_S/a_P$ of the emulated FK model cannot be chosen arbitrarily, but it is always close to unity. This makes it easy to obtain the ion positions in relation to the corrugation potential. A photo of the fluorescence light is sufficient, in comparison to the one-dimensional approach discussed above. There, the ion distances are typically a magnitude larger than the lattice period determined by the lasers wavelength, which necessitates a more involved measurement of the ion fluorescence intensity to determine the ion lattice position.

However, in the two-dimensional case the system exhibits back-action from the sub-chains onto their respective corrugation potential, a feature that can significantly change the system behavior, as seen from the absence of an Aubry transition for the vertical kink.

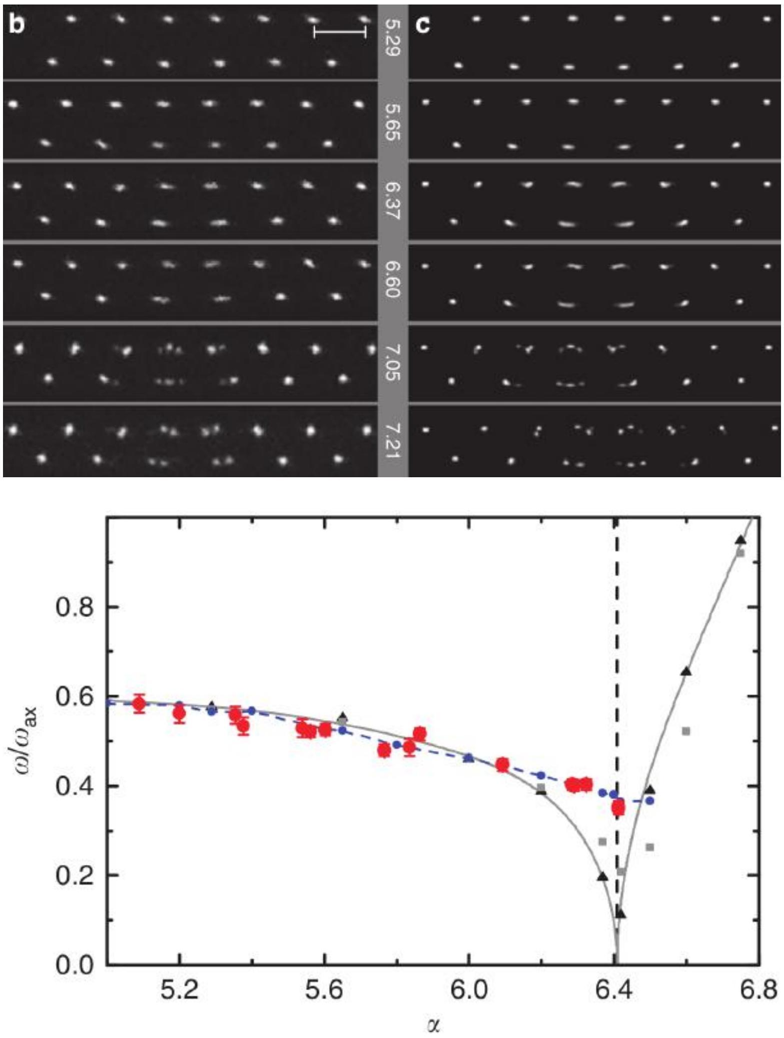

Figure 3.13: Top: Two-dimensional ion crystal with a horizontal defect, with increasing radial trap frequency from top to bottom, the values of α are indicated in the grey bar. (b) Photos from the experiment with an exposure time of 700 ms; (c) Time-averaged ion positions from molecular dynamics simulations with finite temperature $T = 1\,\mathrm{mK}$. The blurring of the central particles close to the Aubry transition ($\alpha_A \approx 6.4$) is caused by their thermal oscillations. **Bottom:** Kink mode frequency (in units of the axial trap frequency) close to the Aubry transition. The solid line indicates the result from the harmonic approximation for $T = 0$. Red points show the experimental data obtained from the parametric excitation of the kink mode by cooling laser with periodically modulated intensity. Frequencies determined from a Fourier analysis of the ion positions calculated by molecular dynamics simulations are shown for $T = 5\,\mu\mathrm{K}$ (black triangles), $T = 50\,\mu\mathrm{K}$ (grey squares) and $T = 1\,\mathrm{mK}$ (blue points). The blue dashed line is shown to guide the eye. Diagrams from Ref. [46].

Chapter 4

Energy transport in trapped ion chains with defect

The transport of energy in crystalline systems through lattice vibrations, and the analysis of the underlying phonon structure constitute quintessential questions of solid-state physics [343]. The study of conductivity properties in condensed matter systems concentrates mostly on macroscopic observables due to the gigantic number of degrees of freedom [344]. Engineered (quantum) many-body systems emerging in AMO physics, such as trapped ions or cold atoms, offer important insights into the microscopic structure and dynamics of toy-model solids [19, 23].

In addition, the zoo of powerful manipulation techniques by means of laser fields, driving internal transitions or creating light forces, and of electric fields allow for the manipulation of the microscopic properties of the constituents [57, 163, 179]. Relevant examples include the engineering of non-linear potentials coming from optical lattices, electric fields from trap electrodes or the dressing of motional states with electronic levels, as well as the control of inter-particle interactions and crystal geometries [12, 20, 27, 36, 69, 209, 345–347]. These systems enable the study of the connection between microscopic and macroscopic observations. This connection is especially intriguing if the microscopic results do not conform with macroscopic expectations, such as in the case of heat transport in one-dimensional oscillator chains discussed in Sec. 4.2 [61, 62].

Of particular interest in this Thesis is the role of solitonic defects in the crystal structure [224]. Trapped-ion systems allow for the detailed study of their influence on the energy conductivity in the system [217, 226, 227, 231]. This topic is the main focus of this chapter. We present in the following our results on the blockade of a vibrational wave packet by a topological defect, and its influence on the temperature profile and heat flux of the crystal coupled to different heat reservoirs. These findings have been published in Refs. [348] and [349].

4.1 Energy localization in trapped ion crystals with topological defects

The dynamics in low-dimensional atomic systems has attracted major interest as a vehicle to understand not only the macroscopic properties of solids, but also fundamental concepts in physics like thermalization and localization. Homogeneous harmonic oscillator chains are probably the oldest example of such systems [350, 351]. In their simplest form their dynamics is fully described by Bloch bands. However, they cannot describe real systems due to the absence of important physical concepts like ergodicity and thermalization. The striking result of Fermi, Pasta, Ulam and Tsingou was that ergodicity is not automatically recovered if a weak non-linear interaction potential is included [352].

Today, the questions of thermalization and transport remain relevant and timely for quantum many-body systems. The effects of disorder and interactions, leading to the celebrated results of Anderson and many-body localization, in conceptually simple one-dimensional systems in the quantum realm, constitute a very active field of research [353–360]. This field has not only a fundamental interest. It also finds applications in quantum chemistry (energy transport in molecules), and biophysical research in DNA strains [334, 361–364].

Trapped-ion experiments have demonstrated their ability to probe (quantum) walks of vibrational excitations in particle chains [365–368]. The controlled creation of displaced states has been achieved by a parametric drive of the ion oscillations by means of an amplitude modulated dipole force [63]. The propagation of this coherent state can be monitored by a sideband measurement relying on the dependency of the transition probability on the quantum vibration number [186, 187]. While the dynamics of classical states in a Doppler cooled crystal has been measured with great accuracy in this way, the quantum walk of a single vibrational energy quantum (vibron) has been realized for small system sizes as well (see Fig. 4.1) [64, 369]. These pioneering works have been conducted in clean systems, that is crystals with a high degree of symmetry.

As discussed in Chapter 3, the presence of defects results in an altered phonon mode spectrum, introducing localized kink modes, and in particular for horizontal kinks, the symmetry-breaking Aubry transition [46, 224, 294, 370]. In this section, we show the consequences of these phenomena caused by the defect onto the motion of coherent vibrational excitations.

4.1.1 Blockade of an energy wave packet

As we are interested in the role played by a topological defect on the transport of vibrational energy, we initialize the crystals by finding the equilibrium positions

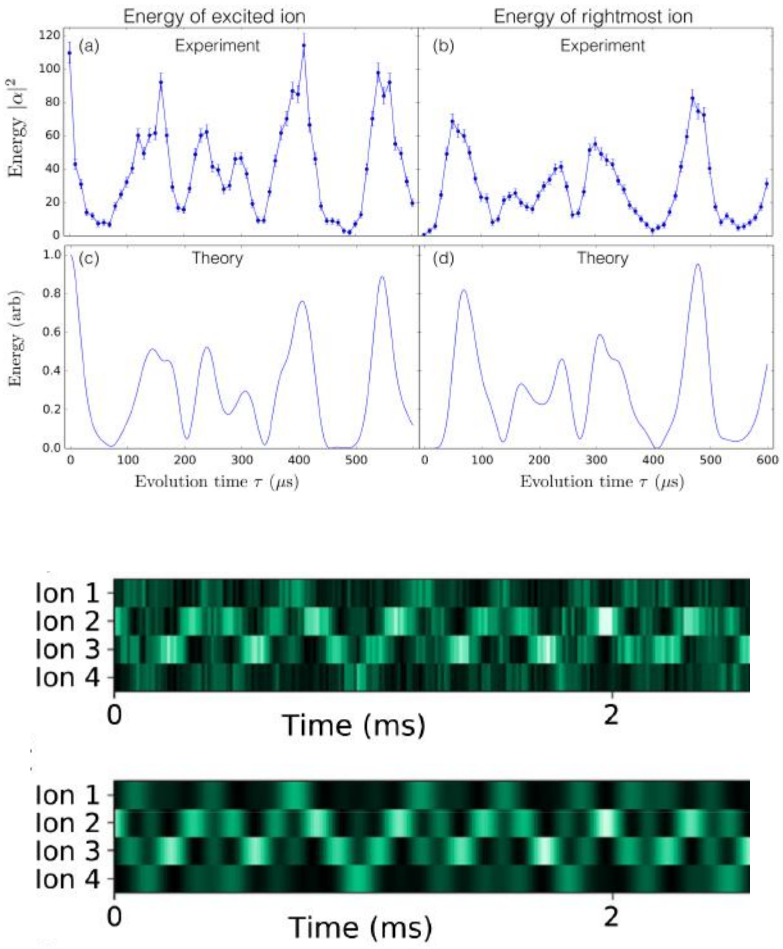

Figure 4.1: Top panel Measured (top) and calculated (bottom) evolution of the displacement amplitude in a linear ion chain of five ions after the leftmost ion has been excited. Figure from Ref. [63] **Bottom panel** Measured (top) and calculated (bottom) propagation of a quantum vibron in a ground state cooled 4 ion chain. A single vibrational quantum is initialized at ion 2. Figure from Ref. [64].

of the particles in the presence of a horizontal topological defect in the systems center. This is done by molecular dynamics simulations of the system with an additional friction term leading to an exponential decay of the kinetic energy of the ions. In the sliding phase the found configurations are stabelized by the repulsion of the defect from the crystals boundaries. While this holds for the horizontal kink in the pinned phase the localized (odd) defect is held inside the system by the PN barriers that emerge at the Aubry transition.

Then, at time $t = 0$, we create a vibrational excitation by displacing a single ion in an arbitrary direction and release it. Since we are interested in the effect of the kink on the conductivity of the underlying crystal structure, i.e. the zigzag, and not the dynamics of the kink itself we choose to excite ions in the outer parts of the crystal. These displacements have in first order little overlap with the translation of the kink. The displacements chosen here have in first order little overlap with the translation of the kink which can be seen from comparing their position with the width of the defect, see Fig. 3.12. The subsequent evolution of the excitation through the crystal is evaluated in two ways, by the numerical solution of the full Hamilton equations, and by a harmonic analysis of the dynamics of the excited phonon modes determined from a second-order approximation.

In Fig. 4.2, we illustrate with an example the time evolution of the kinetic energy after an ion displacement in the axial direction. If the trap aspect ratio is tuned into the sliding regime of the kink the kinetic energy travels through the central region and distributes equally on both sides of the defect. Due to the symmetry of the crystal, and consequently of the phonon modes, the energy of those ions opposite to the site where the displacement was created is increased. The energy distribution maintains its memory of the initial state at large times, indicating the robustness of the harmonic oscillations of the phonon modes from non-linear corrections.

The dynamics becomes restricted when the aspect ratio α is increased and tuned across the Aubry transition. As visible in the right diagram of Fig. 4.2, the defect blocks the propagation of the wave packet, which leads to its localization on one side of the kink.

At the Aubry transition the crystal symmetry is spontaneously broken, such that it exhibits no $\mathbb{Z}_2$ symmetry in the crystal plane. As a consequence, the phonon spectrum hosts asymmetric modes whose amplitude is predominantly localized in one of the system halves. Those of them with a large overlap with the initial state are strongly excited, but do not transfer energy into the opposite crystal half since their mode vector has no support there, see Fig. 4.2.

While the shape of the phonon modes (and their dispersion relation) dictates the excitation dynamics in the low energy limit, we can expect corrections to this picture coming from the non-linear Coulomb potential.

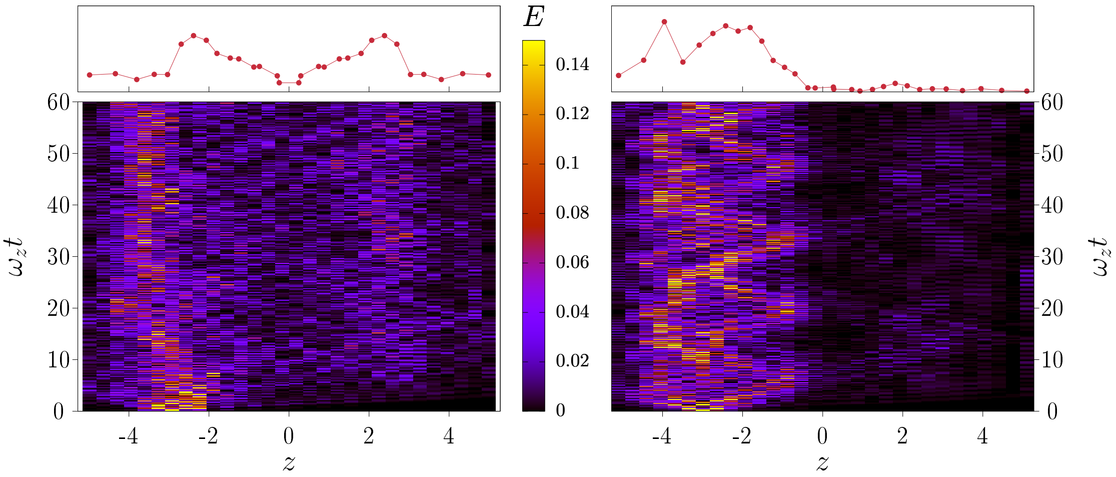

Figure 4.2: Time-evolution of the kinetic energy after an initial axial displacement of the seventh ion in the sliding phase (left, $\alpha = 5.5$) and the pinned phase (right, $\alpha = 6.8$)) of a horizontal defect. The axial ion position is given in units of $\sqrt[3]{C_0/m\omega_z^2}$, and the energy is normalized by the excitation energy. In the top diagrams, we show the spatial structure of the phonon mode with the largest amplitude during the time-evolution by its projection onto the oscillation of the different ions.

4.1.2 Energy imbalance and non-linear resonances

In order to assess the strength of the observed energy localization we define the energy imbalance $\Delta E = \sum_{z<0} \langle E_i \rangle / E$, which gives the ratio between the time averaged kinetic energy $\langle E_i \rangle = \int_0^t \vec{p}_i^{\,2}/2m(t')dt'/t$ of the ions in the left half of the trap and the total kinetic energy introduced by the displacement. With this definition, a symmetric energy distribution, which is expected in the sliding phase, would give $\Delta E = 0.5$, while any form of localization on one side of the crystal would result in a deviation from this value. Note that due to its normalization, this observable is independent from the amplitude of the initial dislocation in the harmonic regime. This definition is only appropriate because the defect is confined by the edges of the inhomogeneous crystal. In a translation invariant zigzag crystal, the kink can be stabilized in various equilibrium positions so that a calculation of the energy imbalance would have to take into account the initial position of the defect.

We depict in Fig. 4.3 the energy imbalance as a function of α for an initial displacement of the leftmost ion along the x-axis. First, we discuss the result from the harmonic approximation for a finite averaging time $t = 100\,\mathrm{ms}$. For $\alpha < \alpha_A$ a calculation of the infinite time limit $t \to \infty$ indicates no energy localization as

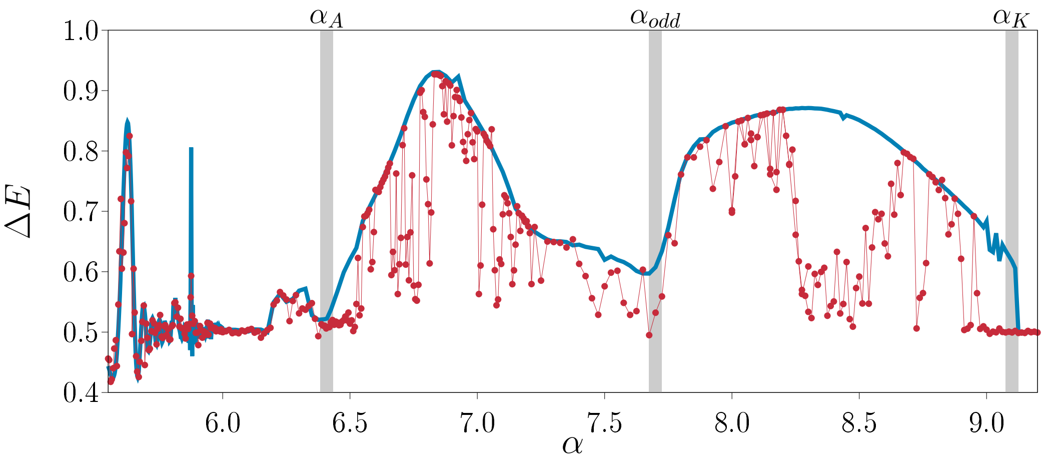

Figure 4.3: Energy imbalance ΔE as a function of α for a crystal with an horizontal kink, for an initial displacement of the leftmost ion of 1 µm in the x-direction The blue solid line indicates the results from harmonic approximation, whereas the red one indicates the numerical results. The averaging time as been set to 100 ms in both cases, which should be compared to $2\pi/\omega_z = 40$ µs. The grey vertical bars mark the Aubry transition, the crossover to the odd form of the defect, and the end of the stability region of the kink α_K.

$\Delta E = 0.5$ holds, independent of the trap aspect ratio.

However, when the averaging time t is set to a finite value, we observe peaks in the energy imbalance in the sliding phase. These can be traced back to degeneracies in the phonon mode spectrum, for distinct values of α the frequencies of two modes participating in the dynamics cross. This leads to an increased relaxation time to the steady state as the modes dephase infinitesimally slow. Ultimately, this effect cannot be attributed to the presence of the defect, similar phenomena can be observed in a zigzag crystal and are of importance in Sec. 4.2.

When the trap confinement is tuned across the Aubry transition, the energy imbalance increases abruptly and peaks at $\alpha \approx 6.8$ with a maximal value of $\Delta E \approx 90\%$. It reduces towards the crossover to the odd kink and another parameter window with strong localization appears in the odd regime at $\alpha \approx 8.4$. For $\alpha > 9.0$ the kink becomes unstable, and the energy imbalance returns to 50%, which indicates the zigzag crystal without defect. Note that additional calculations show that the energy distribution stays symmetric at α_A for a vertical defect and only departs from $\Delta E = 0.5$ at the crossover to the odd kink.

The results from the phonon modes show pronounced energy localization in ion Coulomb crystals, however they are a first-order approximation of the Coulomb interaction between the ions. Hence, we can expect deviations from the discussed results, in particular close to the transition point (see Sec. 5), when the introduced energy is sufficient to probe the higher-order contributions from the Coulomb repulsion. We observe good agreement between the approximation and results of numerical simulations in the sliding phase, which hints at negligible non-linear effects in this regime.

This changes in the symmetry broken phase, as we obtain $\Delta E = 50\%$ when α is tuned close to α_A in the pinned phase. The numerical result departs from $\Delta E = 0.5$ at a larger trap aspect ratio marking the entrance into the energy localized regime. Close to the Aubry transition, the energy injected into the system is sufficient to overcome the PN barriers E_{PN}, which localize the defect off the trap center. Hence, it is possible for the defect to occupy, over time, both potential minima, which are created at the transition, with distinct hopping events in between. During these events the defect is able to transfer energy between the two system halves, reducing the energy imbalance significantly.

The responsible process is clearly not included in the harmonic approximation description, as the non-linear region of the PN potential between the local minima is probed. A detailed discussion of this mechanism and its influence on the motional spectrum of the crystal can be found in Chapter 5. Similar effects can be observed close to the crossover to the odd kink as well as the instability of the kink solution at $\alpha \approx 9$.

In the regime of strong imbalance, the non-linear Coulomb interaction introduces sharp parameter windows with long-term delocalization intertwined with robust localization. While in the former the inclusion of higher-order terms, coupling the phonon modes, leads to the relaxation of the energy imbalance on long timescales, the latter show good agreement with the analytical results again, meaning the absence of relevant non-linear couplings. In Fig. 4.4 (top), we show a zoom of the ΔE graph, resolving the closely alternating linear and non-linear regimes. As visible, the width of the non-linear parameter windows is influenced by the displacement amplitude. A weak excitation narrows the delocalized regimes, as the non-linearities are less relevant. In the limit of an infinitesimal oscillation energy, we recover the harmonic prediction, which always prevails in the low energy limit. The comparison with a smaller time average result indicates a delocalization timescale of tens of ms.

The slow delocalization of the energy is caused by higher order resonances in the phonon spectrum. They occur when the parametric conversion of two (or more) mode amplitudes into a higher frequency mode becomes resonant, i.e. $\omega_r + \omega_{r'} = \omega_s$, see Fig. 4.4 (bottom). As a consequence, the otherwise suppressed higher-order mode-coupling terms derived in Sec. 2.3.5 lead to the occupation of phonon modes with substantial overlap in the opposite crystal half. There are potentially more non-linear resonances than revealed by ΔE since not all of the coupled modes are excited by the initial displacement. This mechanism has been proposed for the

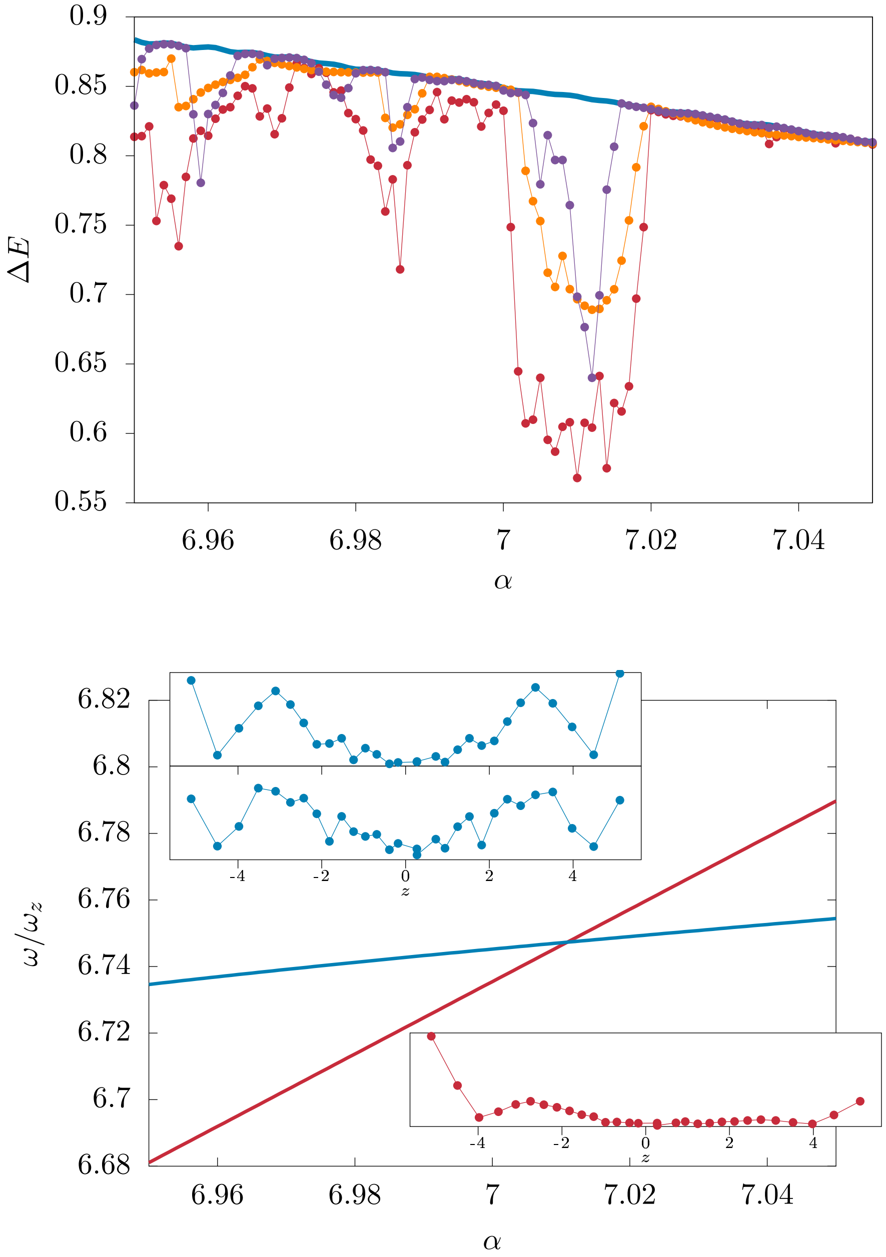

Figure 4.4: Top panel: Energy imbalance ΔE as a function of α for a radial excitation of the leftmost ion. The blue graph depicts the result in harmonic approximation, and the red points correspond to our numerical results for an averaging time of 100 ms, and an initial displacement of 1 µm, as in Fig. 4.3. The orange points show the numerical results for a reduced averaging time of 20 ms, and the purple points correspond to a displacement of 0.5 µm. **Bottom panel:** Frequency of a localized (red) and the sum of two delocalized phonon modes (blue) as a function of α, for the same range as in the top figure. The projection of the respective phonon mode vectors onto the ions oscillations is depicted in the insets, where z is normalized by $\sqrt[3]{C_0/m\omega_z^2}$.

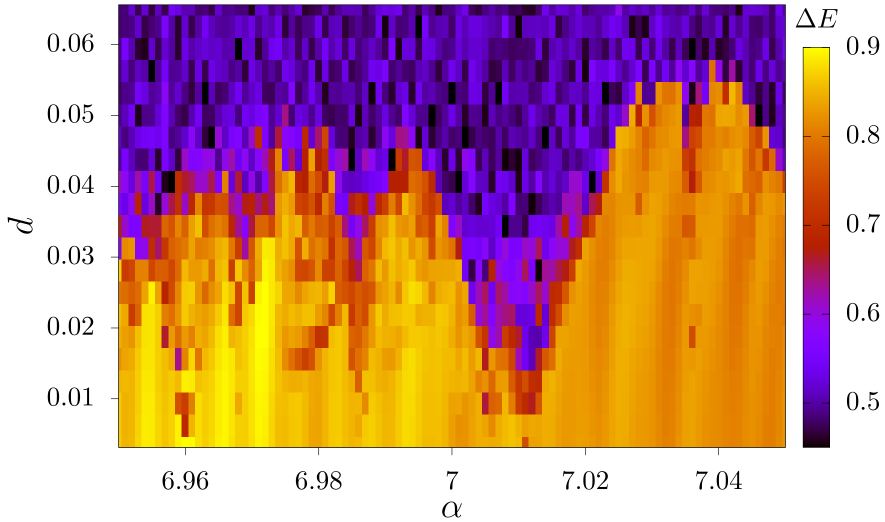

Figure 4.5: Energy imbalance as a function of α and the amplitude of the initial dislocation d of the leftmost ion in the x direction. The averaging time of these numerical results was 100 ms, the same as for Fig. 4.3. The dislocation size has been normalized by the crystal length scale $\sqrt[3]{C_0/m\omega_z^2} = 32\,\mu\text{m}$. In these units the distance of the leftmost ion to its neighbor ion is ≈ 0.625

entanglement of different phonon modes in the quantum regime [238] As observed in the figure, this process makes the non-linearities non-negligible for long-enough averaging times.

A more comprehensive study of the importance of the size of the initial dislocation on the non-linear delocalization is shown in Fig. 4.5, where we show the energy imbalance for a fixed averaging time as a function of α and the displacement amplitude d.

In the ranges of α with robust localization we can observe the substantial effect of the symmetry breaking for excitations up to $d \simeq 1.5\,\mu\text{m}$ in the zoomed in region of α. For stronger dislocations no localization is observable in the long-time limit, independent of α, marking the departure from the validity range of the harmonic approximation.

Close to a resonance, the crossover to a non-linear delocalized regime decreases linearly with α. Figure 4.5 also demonstrates the requirements for the observation of the discussed energy localization imposed on the control of the system. The delicate sensitivity to the trap aspect ratio demands a stable and precise control of the trap potentials on the scale of 1 %. Moreover, the α-independent crossover into the delocalized regime implies a limitation for the temperature of the crystal. If thermal fluctuations surpass the depicted threshold, the localization signal will be lost for long times independent of the displacement amplitude. Note in this sense, that for a fixed temperature the relative importance of thermal fluctuations can be controlled, since the vibrational energy scale can be tuned by the axial trap frequency ω_z (ω_x is dictated by the value of α_A).

In addition, we have neglected the micromotion induced by the traps rf field, which affects the dynamics in the two-dimensional crystal considered here and cannot be countered by any cooling scheme during the time evolution since they would damp the induced coherent dynamics. These issues put aside, the blockade of vibrational excitations by the defect could be probed by experiments similar to Ref. [63]. The arrival of the wave packet at the opposite end of the crystal, possibly quantified by a time average of the displacement of the ions as an experimentally accessible quantity [63], serves as a measure for the conductivity of the system.

4.2 Heat transport in ion Coulomb crystals

One peculiar feature of harmonic oscillator chains is the breaking of Fourier's law, already pointed out by Schrödinger in 1914 [371]. For a solid coupled to thermal reservoirs at opposite boundaries, Fourier's law connects the flux of heat through the system with the slope of the linear temperature profile via a proportionality factor, the thermal conductivity [372–374]. The latter assesses the capability of the solid to transport energy but is unbounded in oscillator chains in the thermodynamic limit [241, 375, 376]. This result is accompanied with a flat temperature profile in the bulk of the system [377, 378]. In the aftermath of Schrödinger's conclusion, researchers were attracted by this stark contrast between this microscopic prediction and the established macroscopic observations described by Fourier. They proposed different mechanisms like non-linearities or quantum fluctuations that would reinstate Fourier's law in one-dimensional systems [242, 379–390].

Trapped ion systems have been proposed as a testbed to study the heat conductivity of low-dimensional systems, and its change under the mentioned effects. A seminal work by L. M. Duan has demonstrated the ability to obtain the absence of temperature gradients in the harmonic regime of the ion fluctuations [391]. Other theoretical works have extended the approach to two-dimensional systems, crossing the linear-to-zigzag transition, or the quantum limit [392–400, 400–407]. Motivated by the observation of a strong energy blockade by a pinned kink, we show in the following its influence on the steady state temperature profiles and heat flux in ion crystals. Our results have been reported in Ref. [349].

4.2.1 Langevin heat baths

The concept of temperature is deeply rooted in the idea of thermal baths or reservoirs that host an infinitely large number of degrees of freedom. When the considered system is brought into contact to such an entity it does not change the state of the bath, but the reservoir ensures the Brownian trajectory of the system while fulfilling an equipartition theorem. While there are multiple ways to emulate such a state, one of the most successful ones is provided by the Langevin formalism. It adds two forces to the dynamical equations of the particles that are attached to the bath: a damping force and stochastic kicks ξ. The Langvin equation of motion for a free particle in one dimension reads

$$\frac{dp}{dt} = -\gamma p + \xi \tag{4.1}$$

with γ the damping rate. This stochastic differential equation describes a form of Wiener process (sometimes also referred to as Brownian motion), so that we can resort to Ito calculus for its analysis and numerical solution [408]. We can formally solve it, which gives for the second order moment in the momentum of the particle:

$$\langle p^2(t)\rangle = e^{-2\gamma t}p^2(0) + 2e^{-2\gamma t}p(0)\int_0^t e^{\gamma t'}\langle\xi(t')\rangle\, dt' \tag{4.2}$$

$$+ e^{-2\gamma t}\int_0^t dt' \int_0^{t'} dt'' e^{\gamma(t'+t'')}\langle\xi(t')\xi(t'')\rangle\,. \tag{4.3}$$

The particle loses its memory of the initial state on a timescale of $1/\gamma$, and subsequently performs a diffusive random walk for $\langle\xi(t)\rangle = 0$. We demand that in the non-equilibrium steady state the particle fulfills the equipartition theorem which leads to the so-called fluctuation-dissipation theorem

$$\langle\xi(t)\xi(t')\rangle = 2m\gamma k_B T\delta(t-t') \tag{4.4}$$

It connects the amplitude of ξ to the bath temperature and damping rate and describes the balance between dissipation and stochastic kicks that is required to equilibrate at the bath temperature.

In this section, we assume that the effect of focused cooling lasers can be modelled by Langevin baths. In the case of Doppler cooling, the damping rate and reservoir temperature depend on the laser parameters as discussed in Sec. 2.2.1. Contrary to the temperatures reachable by Doppler cooling, we do not restrict ourselves to $T > \frac{\hbar\Delta\omega}{2k_B}$, since we expect a temperature-dependent conductivity as already hinted at in Fig. 4.5. Moreover, the laser wavevector generally introduces an anisotropy of the damping rate since it can have different projections onto the trap axes. For the results discussed in this section, we assume that the ion oscillations in all three dimensions experience an equal damping rate.

As mentioned above there are different models to simulate the heat reservoirs that trigger the heat current. A mentionable alternative is the Nose-Hoover bath [61]. In contrast to the Langevin bath, it does not introduce a stochastic force to the equations of motion of the considered particle but introduces an auxiliary particle coupling to the particle motion. This approach has the advantage of producing the usual Hamilton equations for an enlarged phase space and preserves time-reversal symmetry.

4.2.2 Dynamical equations and heat flux

We study the effect of the Aubry transition onto the transport of heat through an ion crystal with the four outermost ions coupled to Langevin reservoirs with different temperatures $T^h > T^c$. The dynamical Langevin equations of the ions are of the form:

$$\frac{d\vec{p}_i}{dt} = m\frac{d^2\vec{r}_i}{dt^2} = -\nabla_i(V_{trap}(\vec{r}_i) + V_{Coul}) - \gamma_i\vec{p}_i + \vec{\xi}_i(t) \tag{4.5}$$

where $\nabla_i = d/d\vec{r}_i$ denotes the gradient with respect to the ion positions, $\gamma_i = \gamma$ for $i = 1, \ldots, 4, N-3, \ldots, N$ and $\gamma_i = 0$ for all other ions. The stochastic force vector $\vec{\xi}_i(t)$ describes the Gaussian noise whose strength is determined by

$$\langle\vec{\xi}_i(t)\rangle = \vec{0} \quad \langle\vec{\xi}_i(t) \otimes \vec{\xi}_j(t')\rangle = 2m\gamma_i k_B T_i \mathbb{1}\delta_{ij}\delta(t-t') \tag{4.6}$$

with $T_i = T^c$ for $i = 1, \ldots, 4$ and $T_i = T^h$ for $i = N-3, \ldots, N$.

When the ions in any initial state are put into contact with the thermal reservoirs at $t = 0$, they start to thermalize and eventually will reach a non-equilibrium steady state. This state is characterized by local dynamical temperatures, which we define as an ensemble average of the kinetic energy

$$\tau_i = \frac{\langle\vec{p}_i^{\,2}\rangle}{3mk_B}. \tag{4.7}$$

The system has reached thermal equilibrium when $d\tau_i/dt = 0$ for all ions.

In addition to the temperature distribution, we are also interested in the amount of heat the crystal can transport per time unit, described by the heat flux J. It is given by the energy that the hotter reservoir pumps into the system per unit time and gets dissipated in the colder bath at the opposite end. In thermal equilibrium, these two quantities possess the same amplitude but opposite signs. In the crystal bulk the ions transport J from one side to the other via their

Coulomb coupled oscillation. To describe this continuous flow of energy, we define an ion energy given by

$$h_i = \frac{\vec{p}_i^2}{2m} + V_{trap}(\vec{r}_i) + \frac{1}{2}\sum_{k\neq i} U(|\vec{r}_i - \vec{r}_k|) \tag{4.8}$$

where $U(x)$ is the interaction energy, $U(x) = C_0/x$ in our case. The change of the ion energy per time is given by the time derivative of h_i. We insert the dynamical equation (4.5), and obtain

$$\frac{dh_i}{dt} = \sum_{k\neq i} \underbrace{-\frac{1}{2m}\vec{p}_i \cdot \nabla_i U(|\vec{r}_i - \vec{r}_k|)}_{j_{ik}} + \underbrace{\frac{\vec{p}_i}{m} \cdot \left(\vec{\xi}_i - \gamma_i \vec{p}_i\right)}_{j_i^B}. \tag{4.9}$$

Here we have introduced the heat flux j_{ik} between ion i and k, accounting for the coherent exchange of energy, and the flux j_i^B describing the dissipation of energy by the reservoirs. Since the first term describes the energy exchange among the ions, fulfilling $j_{ik} = -j_{ki}$ for interactions that only depend on the particle distances, the change in the total energy is given by the heat fluxes from the baths

$$\frac{dH}{dt} = \sum_i \frac{dh_i}{dt} = \sum_i j_i^B. \tag{4.10}$$

The local heat fluxes j_{ik} and j_i^B are stochastic quantities. In order to assess the average properties of the system, independent of the concrete realization of the Wiener process, we take their ensemble averages. For the calculation of $\langle j_i^B \rangle$, we need to compute terms of the form $\langle \vec{p}_i \vec{\xi}_i \rangle$, which can be done via Novikov's theorem [409]

$$\langle f[\xi]\xi(t)\rangle = \int ds\, \langle \xi(s)\xi(t)\rangle \langle \frac{\delta f[\xi]}{\delta\xi(s)ds}\rangle\,, \tag{4.11}$$

where $f[\xi(t)]$ is a functional of the stochastic forces, and $\delta f[\xi]/\delta\xi(s)ds$ denotes the functional derivative. While the first term in the integral of the theorem is given by the fluctuation-dissipation theorem (see Eq. (4.6)), the second factor can be calculated from the formal solution of the Langevin equation (4.5)

Applying this theorem to $p_i[\vec{\xi}_i]$ yields

$$\langle \frac{dH}{dt} \rangle = \sum_i 3k_B\gamma_i(T_i - \tau_i). \tag{4.12}$$

This change in total energy is non-zero during the thermalization process since energy is dissipated (pumped) from (to) the system, depending on the initial state.

After equilibration, these two processes level out as mentioned before and hence $\langle dH/dt \rangle = 0$. We can compute the steady state heat flux by taking

$$J = \frac{3k_B}{2} \sum_i \gamma_i |T_i - \tau_i|. \tag{4.13}$$

The challenge in computing J lies in the determination of the steady state values of τ_i, which requires a sufficiently long equilibration time and the ensemble averaging.

4.2.3 Linearized theory

For small temperatures the dynamics of an ion Coulomb crystal is well approximated by its phonon modes, which result from a second-order approximation of the Coulomb interaction around the equilibrium positions of the ions. As discussed in Sec. 2.3.2, the decisive quantity in this linearized theory is the dynamical matrix K.

Applying the harmonic approximation to the Langevin equations (4.5) yields

$$\frac{d}{dt}\vec{q} = -\begin{pmatrix} 0 & -\mathbb{1}/m \\ K & \Gamma \end{pmatrix} \cdot \vec{q} + \begin{pmatrix} \vec{0} \\ \vec{\xi} \end{pmatrix} \tag{4.14}$$

with $\vec{q} = (d\vec{R}, \vec{P})$, $\vec{P} = (\vec{p}_1, \ldots, \vec{p}_N)^T$ and $d\vec{R}$ defined as in Sec. 2.3.2. In this compact notation, the dissipation rates are included in the matrix $\Gamma = \mathrm{diag}(\gamma_1 \mathbb{1}, \ldots, \gamma_N \mathbb{1})$ and the stochastic forces are aggregated in $\vec{\xi} = (\vec{\xi}_1, \ldots, \vec{\xi}_N)^T$. For later convenience, we also introduce the temperature matrix $T = \mathrm{diag}(T_1 \mathbb{1}, \ldots, T_N \mathbb{1})$.

In addition to the advantages inherent to this approximation, such as its analytical solutions and computational simplicity, addressed in Sec. 2.3.2, it provides as well a hint at the thermalization time. While for non-interacting particles it is trivially given by $1/\gamma$, the motional modes can exhibit extraordinary long equilibration times when they have poor overlap with the spatial distribution of the driving [391]. The calculations in second order can give an upper bound for the necessary computation time in molecular dynamics simulations.

Let us proceed with the solution of Eq. (4.14) by transforming it into the phonon mode picture by diagonalizing the dynamical matrix $K = V \cdot \Lambda \cdot V^T$ with the diagonal eigenvalue matrix Λ and the orthogonal matrix V. The transformation does not simplify the solution of the dynamical equations because it maintains the form of the dynamical equations. The local oscillation and the phonon mode picture are physically equivalent as they are connected by a coordinate change via V. However, it provides a better understanding of the heat transport because the phonon modes are the fundamental vibrational excitations of the system. We introduce the mode vector $\vec{\Theta}$ and obtain

$$\frac{d}{dt}\vec{\Theta} = \begin{pmatrix} V^T & 0 \\ 0 & V^T \end{pmatrix} \cdot \frac{d\vec{q}}{dt} = -\underbrace{\begin{pmatrix} 0 & -\mathbb{1}/m \\ \Lambda & \tilde{\Gamma} \end{pmatrix}}_{A} \cdot \vec{\Theta} + \underbrace{\begin{pmatrix} \vec{0} \\ U^T \cdot \vec{\xi} \end{pmatrix}}_{\vec{\Xi}}, \tag{4.15}$$

with the transformed dissipation matrix $\tilde{\Gamma} = V^T \cdot \Gamma \cdot V$. The stochastic mode forces $\vec{\Xi}$ fulfill a dissipation-fluctuation theorem that reads

$$\langle \vec{\Xi}(t) \otimes \vec{\Xi}(t') \rangle = \underbrace{\begin{pmatrix} 0 & 0 \\ 0 & 2mk_B \tilde{\Gamma} \cdot \tilde{T} \end{pmatrix}}_{B} \delta(t - t') \tag{4.16}$$

with the transformed mode temperatures $\tilde{T} = V^T \cdot T \cdot V$.

Note that the mode dissipation and temperature matrices, $\tilde{\Gamma}$ and $\tilde{T}$, are in general not diagonal. This is a consequence of the inhomogeneous couplings γ_i and bath temperatures T_i, and can be understood as a dissipative mode coupling. During the dynamics, the spatial distribution of the damping and stochastic forces is imprinted in the energy distribution in the ion crystal. For an intuitive example, let us assume an initial state of homogeneous energy distribution that is damped on one end of the system. Consequently, the symmetry of the energy distribution will be broken, as we can expect that the particles coupled to the damping are cooled the fastest. In the phonon mode picture, this process is described by a shift of the relative amplitudes between the symmetric and the antisymmetric modes, given by the respective terms in $\tilde{\Gamma}$. The details of the off-diagonal terms of $\tilde{\Gamma}$ and $\tilde{T}$ therefore depend on the symmetry of the crystal as well as γ_i and T_i.

The Langevin equations (4.15) are formally solved by

$$\vec{\Theta}(t) = e^{-At} \cdot \vec{\Theta}(0) + \int_0^t e^{A(s-t)} \cdot \vec{\Xi}(s) ds. \tag{4.17}$$

In order to calculate the dynamical temperatures and the heat flux we introduce the correlation matrix $C = \langle \vec{\Theta} \otimes \vec{\Theta} \rangle$. Inserting Eq. (4.17) into C gives the result

$$C(t) = e^{-At} \cdot C(0) \cdot e^{-A^T t} + \int_0^t e^{A(t'-t)} \cdot B \cdot e^{A^T(t'-t)} dt'. \tag{4.18}$$

As visible from this solution, the information about the initial steady and simultaneously the timescale to reach the steady state are given by the minimal real part of all eigenvalues of A. Therefore, this value gives an upper bound for the thermalization time in numerical simulations or a possible experiment.

The explicit form of the elements of the $6N \times 6N$ matrix C reads

$$C_{\mu\nu} = \sum_{r,s,u,v}^{6N} N_{\mu r} N_{\nu s} N^*_{ur} N^*_{vs} \left[e^{-(a_r+a_r)t} C_{uv}(0) + B_{uv} \frac{1-e^{-(a_r+a_s)t}}{a_r + a_s} \right], \tag{4.19}$$

where we have diagonalized $A = N \cdot \mathrm{diag}(a_1, \ldots, a_{6N}) \cdot N^H$. In thermal equilibrium, i.e. $t \to \infty$ the only surviving term is given by

$$C_{\mu\nu} = \sum_{r,s,u,v}^{6N} N_{\mu r} N_{\nu s} N^*_{ur} N^*_{vs} \frac{\tilde{B}_{uv}}{a_r + a_s}. \tag{4.20}$$

The dynamical temperature of each mode is described by $\tilde{\tau}_i = C_{i+3N,i+3N}/(3mk_B)$. A derivation of the mode heat flux, analogue to the one resulting int Eq. (4.9), yields

$$\langle \tilde{j}_i \rangle = (\tilde{\Gamma} \cdot \tilde{T})_{ii} - \sum_j^{3N} \tilde{\Gamma}_{ij} C_{j+3N,i+3N} \tag{4.21}$$

Since the phonon mode vectors are spatially delocalized, they couple to both thermal reservoirs simultaneously. Hence, the ensemble-averaged mode heat flux in the steady-state vanishes for each phonon mode individually as the same amount of energy is absorbed from the hotter bath as dissipated into the colder bath. To calculate this amount of energy, we can unambiguously split the dissipation matrix $\tilde{\Gamma} = \tilde{\Gamma}^h + \tilde{\Gamma}^c$ and the temperature matrix $\tilde{T} = \tilde{T}^h + \tilde{T}^c$ into the contributions from the different reservoirs. Inserting one of these summands into Eq. (4.21) gives the individual contributions of the two baths which add up to zero. The absolute value of any of these contributions is the heat that is transported by the respective mode, summing the heat fluxes of all phonon modes results in the total heat flux of the system.

As it is clear from the functional form of the total heat flux (4.21), it vanishes for $\gamma \to 0$ due to its proportionality to $\tilde{\Gamma}$. The analytical solution, obtained for a homogeneous oscillator chain, results in

$$J = \frac{k_B N_\gamma \gamma}{2} \left(T^h - T^c \right), \; \gamma \to 0, \tag{4.22}$$

where N_γ is the number of particles coupled to the reservoirs at each boundary. This result agrees well with the temperature profiles in a linear chain reported in Ref. [391]. Note that the result (4.22) in the vanishing γ limit, coincides with Eq. (4.13) for $\tau_i = \bar{T}$. In the opposite limit $\gamma \to \infty$ the coupled ions adapt the bath temperatures T_i such that the system does not transport energy in the strong

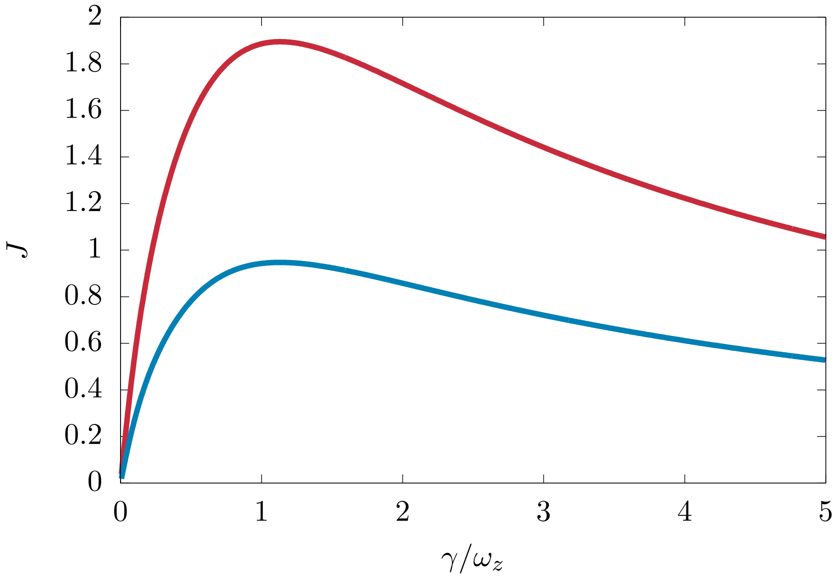

Figure 4.6: Total heat flux computed from linear theory for a linear ion chain with $N = 10$, as a function of the damping rate γ. The two outermost ions are coupled to heat reservoirs with a temperature difference $T^h - T^c$ (red) and $(T^h - T^c)/2$ (blue). J is normalized by $k_B\omega_z(T^h - T^c)/2$.

coupling limit. In that limit the heat flux in a homogeneous system with nearest neighbor coupling κ decays like

$$J = \frac{\kappa k_B N_\gamma}{2m\gamma}\left(T^h - T^c\right), \;\gamma \to \infty \tag{4.23}$$

Between these two limits there exists a value of the damping rate with maximal J, the full dependence of the heat flux on γ for a linear ion chain in the harmonic regime is shown in Fig. 4.6.

4.2.4 Steady-state temperature profiles

In the following section, we apply the theory discussed above to a crystal of $N = 30$ $^{172}\mathrm{Yb}^+$ ions. We fix the damping rate $\gamma = 20\,\mathrm{kHz}$ for the four outermost ions and set the temperature difference of the two reservoirs to $T^h - T^c = 0.2\,\mathrm{mK}$. We keep their average temperature $\bar{T}$ adjustable in order to probe the response of the system to the heat current at different temperatures. We investigate the heat current and the equilibrium temperature profiles as a function of the trap inhomogeneity, which triggers the linear-zigzag transition and the Aubry transition in the presence of a kink.

We employ the results of the linearized theory from Sec. 4.2.3, but also perform direct numerical calculations of the Langevin equations (4.5). In order to calculate the ensemble average of the kinetic energy of the ions we compute 500 independent trajectories of the crystal and build the average of them. Subsequently, we average over 50 ms, a much larger timescale than the typical oscillation period $2\pi/\omega_z = 40\,\mu\mathrm{s}$ of the crystal, after the system has reached its steady state.

In order to choose an adequate simulation time, we show in Fig. 4.7 (top) the thermalization timescale predicted by the linearized dynamical equations. It is given by the inverse of the minimal real part of the eigenvalues of A and lies typically on the order of a second. This extraordinarily long timescale has been already reported in previous studies, and it is due to the inhomogeneous ion density in a harmonic confinement [391]. Since the ion distances are smaller in the trap center, high-frequency modes are more localized in that area and hence couple weakly to the reservoirs at the edges, which slows down their thermalization. Non-linear mode couplings can transfer energy from a strongly coupled mode to the isolated phonons, which reduces the time to reach the steady state. A typical equilibration process is depicted in Fig. 4.7 (bottom).

We show the steady state temperature profiles in Fig. 4.8. The results for the zigzag without defect show a flat profile in the bulk of the crystal and abrupt steps at the ions in contact with the reservoirs. This observation is to some extend independent of the chosen trap asymmetry, however the extend of the region with close to vanishing temperature gradient is reduced when comparing the choice $\alpha = 7.0$ to $\alpha = 6.0$. Note that by increasing the trap aspect ratio also the size of the zigzag phase in the crystal center shrinks, which influences the phonon mode structure.

The graphs resemble those obtained from homogeneous model systems with harmonically coupled particles exhibiting anomalous heat conductivity. It is important to note that this result is supported by the numerical calculations which show a very good agreement to the results from the second order approximation. This indicates the absence of non-linear dynamics at the temperature scales encountered here.

Ref. [404] reported a different result in two-dimensional zigzag crystals for the same particle number, arguing that the transition from a linear to two-dimensional crystal gives rise to a linear temperature slope. We attribute the discrepancy between the two results to the difference in the temperatures and damping rates and claim that the observed gradient is due to non-negligible non-linear mode couplings discussed later. We expect that with increasing $\bar{T}$ above the scale considered here the higher order terms in the Coulomb interaction will activate a non-zero temperature slope in the bulk. In return, our results suggest that the onset of a gradient is not an inherent property of the linear-zigzag transition but rather is caused by

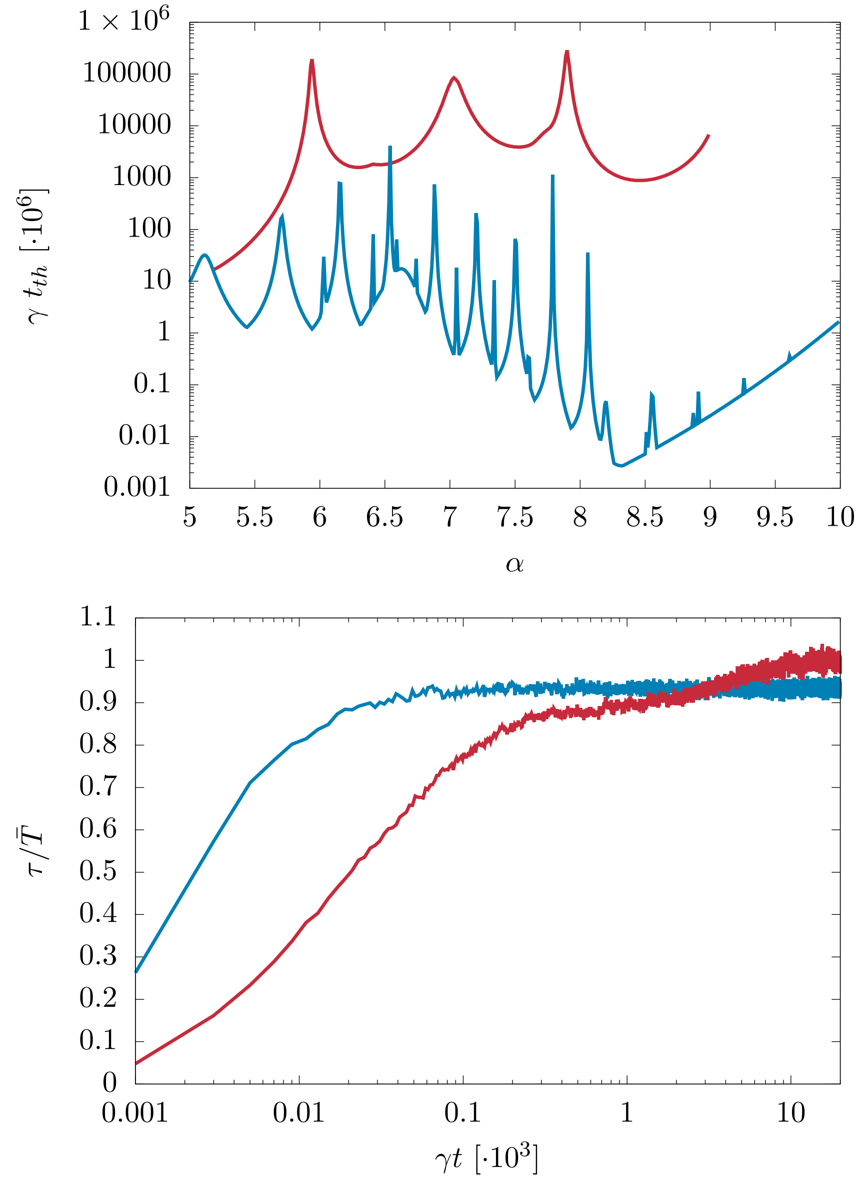

Figure 4.7: Top panel: Thermalization timescale in harmonic approximation given by the minimal real part among the eigenvalues of the matrix A, i.e. $t_{th}^{-1} = 2\min_{a_i}(Re\ a_i)$, for a crystal with (red) and without kink (blue). The four outermost ions are coupled isotropically to the reservoirs with $\gamma = 20\,\mathrm{kHz}$. **Bottom panel:** Thermalization of the 4th (blue) and 15th (red) ion in a zigzag crystal ($\alpha = 7$) calculated from numerical calculations of the Langevin equations (4.5).

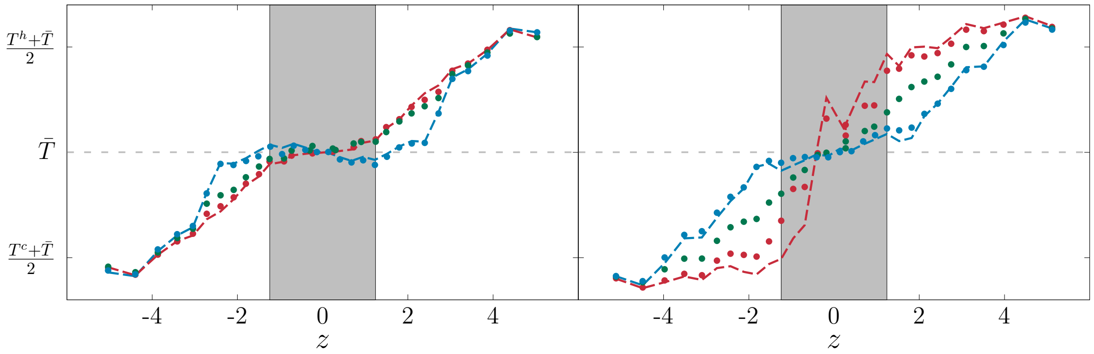

Figure 4.8: Steady state temperature profiles for a defect-less zigzag crystal (blue) and zigzag with horizontal defect (green and red) for $\alpha = 6.0$ (left, sliding phase) and $\alpha = 7.0$ (right, pinned phase). The average bath temperature is $\bar{T} = 0.6\,\mathrm{mK}$ for the blue and green graphs. In addition, the red points shows the result for the kink with $\bar{T} = 0.15\,\mathrm{mK}$. The dashed lines show the corresponding prediction from linear theory. The z coordinates of the ions have been normalized by $\sqrt[3]{C_0/m\omega_z^2}$. The grey boxes indicate the spatial region considered for the calculation of dT.

an increase in the strength of the mode coupling terms.

The presence of a kink in the sliding phase smoothens the profile by shrinking the region of vanishing temperature slope in the center. Since the local translational invariance in the bulk of the crystal is broken by the defect, the shape of the phonon mode vectors is altered, most prominently by creating a localized kink mode, reducing the flat temperature profile. We also observe good agreement with the result from the second-order approximation, which shows that the introduction of the topological defect does not a priori result in non-linear dynamics. This can be understood from the shape of the kinks PN potential. It is in good approximation quadratic in the chosen α regime, see Fig. 2.6. The kink fluctuations around the unique energy minimum are unable to resolve the deviation from the linearized theory prediction for the energy scales depicted.

The temperature profile drastically changes when the trap aspect ratio is tuned into the pinned regime of the defect. Linear theory predicts an abrupt temperature drop at the position of the kink, breaking the point symmetry of the profile. Similar to the energy blockade observed in the coherent energy transport in Sec. 4.1.1, this behavior is due to the emergence of asymmetric phonon modes in the spectrum. Since the mirror symmetry of the crystal is spontaneously broken at the Aubry transition the mode vectors generally possess no fixed symmetry. Moreover, some of them are localized on one side of the defect. These modes are coupled to only one of the reservoirs, and hence adapt the corresponding temperature which leads to a step-like temperature distribution. For low $\bar{T}$, the non-linear result shows an inhomogeneous temperature gradient with the steepest incline at the kink position. This result qualitatively supports the linear theory prediction of a sharp temperature drop due to the symmetry breaking, but demonstrates the relevance of non-linear dynamics for temperatures below the Doppler limit in this phase. Increasing the average bath temperature modifies the temperature profile by smoothening the step in the central region to a close to uniform temperature gradient for $\bar{T} = 0.6\,\mathrm{mK}$. This clearly shows the lack of validity of the linearized theory.

In order to investigate the signal of the Aubry transition in the temperature gradient, we take the temperature difference dT over the ten central ions as a measure for the structure of the steady-state temperature profile. The corresponding region of the crystal is marked by vertical bars in Figs. 4.8. In Fig. 4.9 (top), we show dT as a function of α for $\bar{T} = 0.6\,\mathrm{mK}$ in the case of a defect-free zigzag crystal, serving as a benchmark for the effect of the kink. The gradient in the center remains small for all choices of the trap aspect ratio when compared to the difference of the two reservoirs $T^h - T^c$. This matches the observation of Fig. 4.8. Although the temperature gradient is not identically zero, it is significantly smaller than what can be expected for a uniform temperature gradient. The reason for the nonzero gradient in the harmonic regime is discussed later.

The result for a crystal with a defect is shown as a function of α and $\bar{T}$ in Fig. 4.9 (bottom). In the sliding phase ($\alpha < 6.4$), dT is on the similar order as for the defect-less case, irrespective of the value of α and $\bar{T}$. The temperature slope increases significantly for small $\bar{T}$ as soon as α is tuned across the critical point of the Aubry transition and reaches a maximal value of $dT \approx 0.4(T^h - T^c)$. Note that for the chosen value of γ the outer ions do not thermalize at $\tau_i = T_i$ such that $\tau_N - \tau_1 \approx 0.6(T^h - T^c)$ independent of α. As dT only considers the central 10 ions, a value of $dT \approx 0.4(T^h - T^c)$ indicates a larger temperature slope than can be expected for a linear temperature profile that continuously connects τ_1 and τ_N.

When the $\bar{T}$ is increased for a fixed value of α the steady state of the system changes, as has already been seen in Fig. 4.8. At a crossover temperature the profile adopts a more uniform slope, which consequently decreases dT, since the defect ions do not exhibit a step-like energy distribution. The origin of this behavior can be traced back to the shape of the PN potential discussed in Sec. 2.3.1.

If the thermal energy of the kink is insufficient to overcome the central barrier in the PN potential, it remains in one of the minima for a dwelling time much longer than the typical timescale of its oscillations in that minimum. Therefore, the approximation of the dynamics to second order is adequate to a certain extend, and the temperature profile exhibits the sharp temperature drop at the kink position due to the broken crystal symmetry. Nonetheless, the dynamics of the kink inside

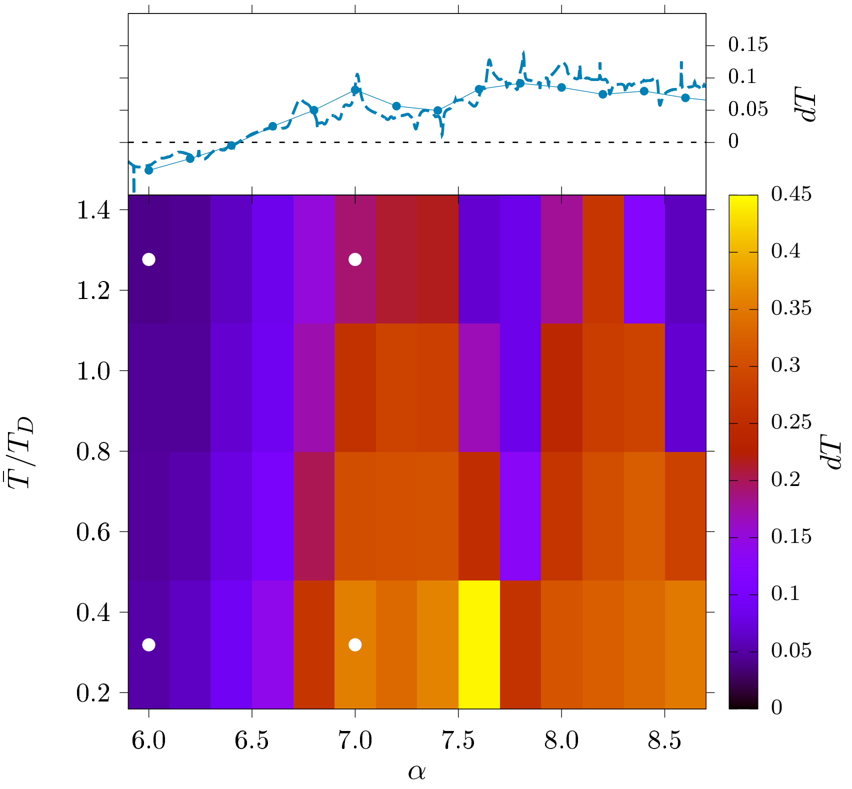

Figure 4.9: **Top:** Temperature gradient dT as a function of α, for a zigzag crystal with $\bar{T} = 1.28T_D$. The dashed line shows the linear theory prediction and the points the numerical results. **Bottom:** The same for a crystal with topological defect, as a function of α and the average bath temperature $\bar{T}$. The latter is normalized by the Doppler limit temperature for Yb ions, i.e. $T_D \approx 0.47\,\mathrm{mK}$.

the double well structure delivers non-linear corrections to the linearized theory for smaller temperatures than in the sliding phase. This increased sensitivity to temperature is observable in Fig. 4.8, for example for $\bar{T} = 0.15\,\mathrm{mK}$.

When the average temperature is increased, the kink has a finite probability to transfer between the two minima in the PN potential and delocalizes via discrete hopping events. They lead to the decrease of the temperature localization, since the defect transports heat at each hopping event between the spatial regions that were separated by the energy step before. The occurrence of the thermally activated hops marks the crossover point $\bar{T}_{deloc}(\alpha)$ into a thermally delocalized phase. Note that the temperature gradient in this phase is still larger than in the defect-less case and therefore a signal of the Aubry transition is observable. We expect that for much larger temperatures the kink dynamics becomes totally insensitive to the PN barriers due to their negligible height in comparison to the thermal energy of the kink ions. In this regime, the global shape of the PN potential determines the steady state of the system, and, since it does not change at the Aubry transition, we expect no sign of energy localization in the $\bar{T} \gg 1\,\mathrm{mK}$ limit.

The crossover temperature $\bar{T}_{deloc}(\alpha)$ is a non-trivial function of the trap aspect ratio. It is determined mostly by the size of the central barrier in the PN potential. For $\alpha > 6.4$, it increases linearly at first, reaching a maximal value at $\alpha \approx 7.0$, and decreases for $\alpha > 7.5$. The initial incline is caused by the growth of the PN barrier in the pinned phase while the existence of a maximal value of $\bar{T}_{deloc}(\alpha)$ is due to the crossover to the odd kink shape around $\alpha \approx 7.8$. As discussed in Sec. 2.3.1, the global form of the PN potential shifts to an inverted harmonic oscillator, so that the PN barriers are the only mechanism to stabilize the defect and protect it from moving to the crystal edges and vanish. At the odd crossover, the kink is less strongly confined in the PN potential minima and therefore $\bar{T}_{deloc}(\alpha)$ decreases. In the odd regime, there exists another parameter window with a temperature step robust against thermal fluctuations, and finally for $\alpha > 8.5$ the size of the stabilizing PN barriers decreases, and with it $\bar{T}_{deloc}(\alpha)$. Note that in the odd phase the hops over the PN barriers introduce a finite chance to lose the kink by successive jumps towards the systems edge. Therefore, the crossover to the thermally delocalized phase has the consequence that some of the system copies in the thermal ensemble do not contain a defect anymore in the calculated steady state. The result shown in Fig. 4.9 does not distinguish between those trajectories in which the kink is lost and those in which, by chance, the kink survives.

While we argued that the behavior of the temperature profile at the kinks position is caused by the changes in the shape of the PN potential, this connection is not rigorous. As suggested in Sec. 2.3.1, the PN potential discussed so far neglects motional excitations, called dressing modes, that are perpendicular to the translation of the kink position X. However, in a comprehensive treatment these

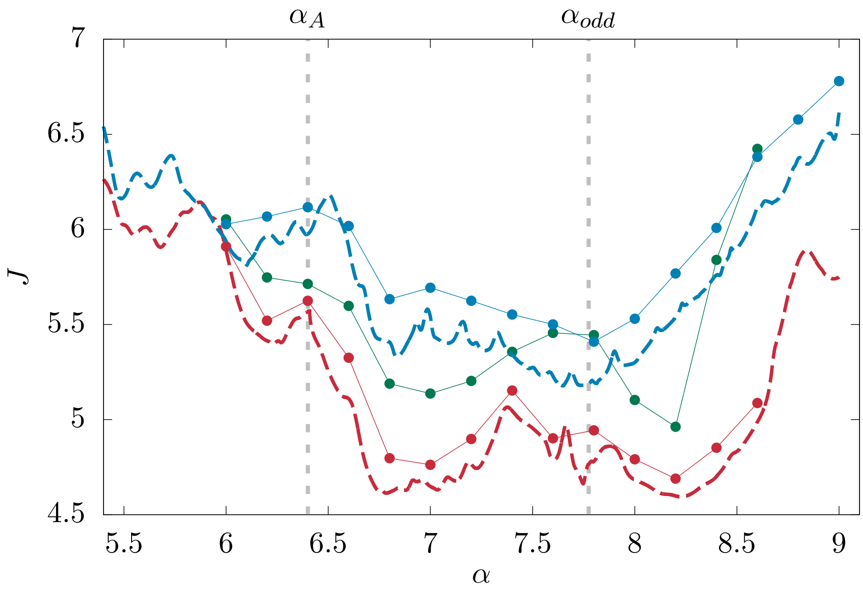

Figure 4.10: Total heat flux J as a function of α, for a zigzag crystal without (blue) and with (green and red) defect. For the blue and green graphs, the average bath temperature is set to $\bar{T} = 0.6\,\mathrm{mK}$. The red graph for the case with kink is calculated for $\bar{T} = 0.15\,\mathrm{mK}$. The dashed lines show the corresponding result from linear theory, whereas the points are obtained from numerical simulations. The heat flux is normalized by $\gamma k_B(T^h - T^c)/2$.

thermally populated modes couple to the dynamics of the defect and consequently inject energy to its motion. A consequence of the simplification made to discuss the crossover to the delocalized regime is that the temperature scale of $\bar{T}_{deloc}(\alpha)$ and the typically barrier size of several mK do not match. Naively, one would expect that the crossover occurs when the defect temperature, i.e. the thermal energy of the ions constituting the kink, becomes comparable to the energy of the barrier E_{PN}. Further work could shine light onto the relation between the dynamics of the crystal dressing and the kink dynamics in a collective excitation formalism, see Sec. 2.3.1.

4.2.5 Heat flux

Fourier's law describes the connection between the temperature slope discussed so far and the total heat flux J. In Fig. 4.10, we show J as a function of α for the different phases in a zigzag crystal. For $\alpha > 8.25$, the heat flux of a defect-less crystal increases linearly with the trap aspect ratio, and has a global minimum in the range of $6.5 < \alpha < 8.0$. For smaller values of α the heat flux increases in an irregular manner.

The inclusion of the non-linear dynamics speeds up the transport of heat but does not change the functional behavior of $J(\alpha)$ as the numerical data points show a constant positive offset in comparison to the analytical result. A similar dependence on α has been reported in Ref. [404], but the authors did not obtain the presence of a minimum of J.

The result for the crystal with defect shows a smaller heat flux for $\alpha > 6$, note that $\alpha_A = 6.4$ for the considered particle number. In the sliding phase, the heat flux of the crystal is reduced due to the distortion of the phonon mode vectors by the presence of the kink. An extreme example is the formation of localized kink modes that are only weakly attached to the heat reservoirs and therefore are not contributing to the transport of heat between them. At the Aubry transition point, J abruptly drops, and subsequently two local minima around $\alpha \approx 7.0$ and $\alpha \approx 8.25$ can be observed. These points match well with the regions of robust temperature gradient (large $\bar{T}_{deloc}$) in Fig. 4.9, and with the largest energy imbalance in Fig. 4.3.

The numerical results for small temperatures show a good agreement with the linear theory. The constant offset due to non-linear coupling mechanisms that speed up the heat transport has already been observed in the zigzag case. Increasing the temperature results in the crossover to the thermally delocalized phase, which shows a larger heat flux due to the thermal hops of the kink. Although in this phase the abrupt change in J at the Aubry transition is washed out, the heat flux stays reduced in comparison to the defect-free curve marking a signal of the presence of the defect.

4.2.6 Resonances

In the following, we address the unexplained presence of a trap configuration exhibiting minimal J in the zigzag structure.

In Ref. [404], the linear increase of the heat flux when approaching the linear-to-zigzag transition was explained by the decreasing ion distances. For larger ion distances the coupling of the ion vibrations becomes weaker and hence the transport of energy slower. However, our results show a violation of this linear trend of J deep in the zigzag phase, which contradicts the connection between the ion distances and the heat flux in the steady state. Since the ion distances are monotonically increasing with decreasing α for $\alpha > 1.0$, the heat flux should be a monotonous function as well if it was dominated by the coupling strength among the ions.

Towards an explanation of this issue, we show in Fig. 4.11 (top) the heat flux in the limit of $\gamma \to 0$. In this diagram, we only show the result of the linearized theory since the choice of a small damping rate requires a larger equilibration time that leads to unrealistically long simulation times for the numerics. However, due to the observed agreement between the numerical results and the harmonic approximation in the considered temperature regime for a zigzag crystal, it is reasonable to assume that the linear theory covers the relevant physics.

We observe a constant normalized heat flux for all values of α in the absence of a kink, and a strong reduction of J at the Aubry transition of a crystal with defect. In addition, the graphs show distinct peaks, which reduce the heat flux for the symmetric crystals (zigzag and sliding phase of a defect) and boost the heat transport on the pinned phase of a crystal with a kink. We study the contribution by a set of phonon modes as a function of α and find that those modes whose frequencies cross exhibit a reduced heat flux, see Fig. 4.11 (bottom). We therefore deduce that the disturbances in J are caused by degeneracies in the phonon mode spectrum

In a zigzag crystal, all phonon mode vectors are either symmetric or antisymmetric upon point reflection on the trap center (for the even particle number case considered here). Therefore, a pair of modes neighboring in frequency consists of one symmetric and one antisymmetric mode. For equal frequencies, the two modes of interest oscillate in a correlated way. Consequently, the shape of their mode vectors leads on one site of the crystal to a constructive amplification, while on the other edge the sum of the two mode vectors leads to an opposed motion. In this way, the heat flux is reduced and the crystal builds up a temperature gradient.

For a crystal with a defect, some phonon modes do not possess point symmetry, such that a resonance can increase or decrease the heat flux. Similar to a damped-driven harmonic oscillator these mode resonances are broadened when the damping coefficient γ is increased. Away from any resonance, we recover the prediction $J = \frac{3k_B\gamma}{2}(T^h - T^c)N_\gamma$ for harmonic oscillator chains in the weak damping limit, that is also valid for a linear chain (see Fig. 4.6). This analysis shows that the heat flux of ion crystals is influenced by the density of resonances in its phonon mode spectrum. It causes the reduction of J when the zigzag phase is entered and explains the observed minimum in the total heat flux. Due to their dense structure and their broadening with stronger damping rates the resonances could not be resolved in Fig. 4.10.

4.3 Conclusion

In this chapter, we have demonstrated the strong influence of the Aubry transition in trapped ion crystals onto its ability to transport energy from one boundary to the other.

We have seen that in the low-energy limit, for which the phonon modes dictate the dynamics, the symmetry breaking leads to a robust and strong energy localization. In the case of a coherent excitation, discussed in the first part of the chapter, this resulted in a prominent blockade observable in the time evolution

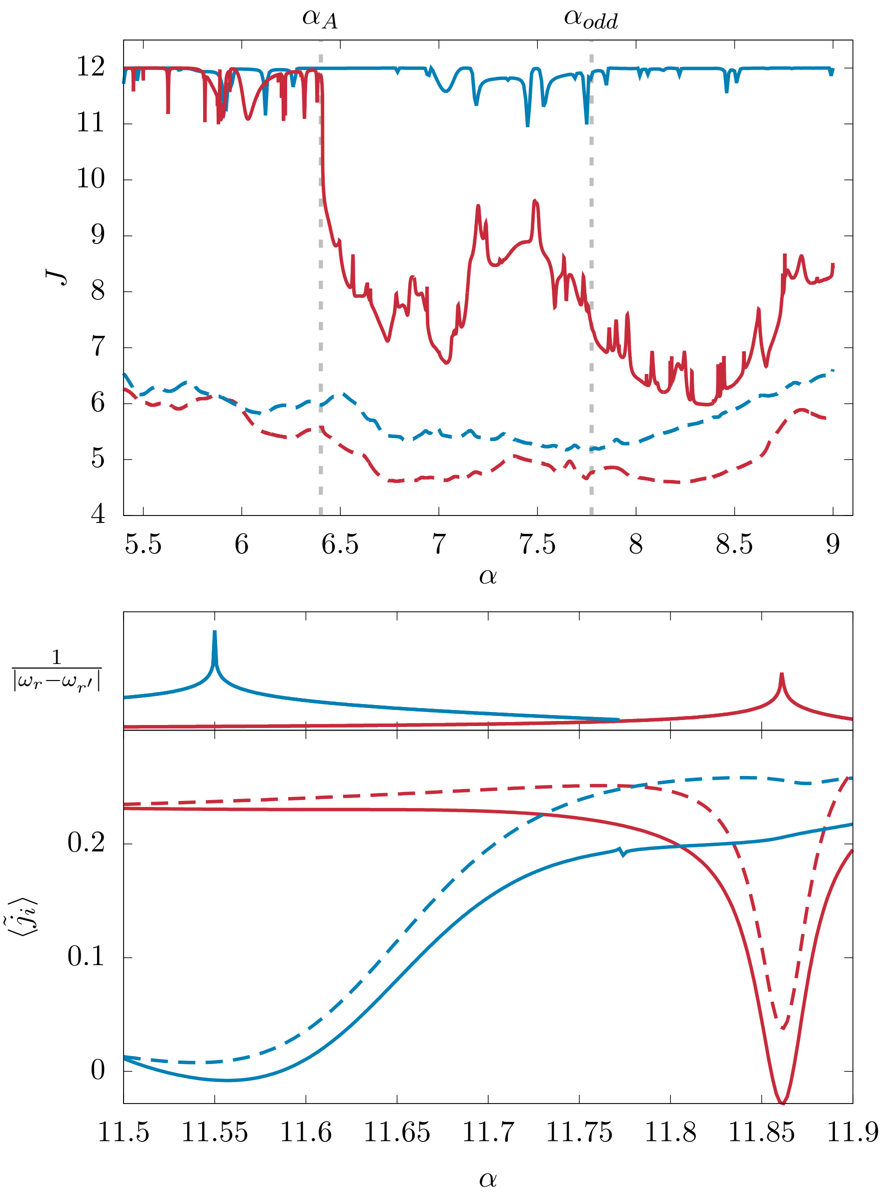

Figure 4.11: Top panel: Total heat flux in linear theory for a zigzag crystal (blue) and crystal with defect (red), normalized by $\gamma k_B(T^h - T^c)/2$. The solid lines are calculated for $\gamma = 2\,\mathrm{Hz}$, the dashed lines are for $\gamma = 20\,\mathrm{kHz}$. **Bottom panel:** Normalized heat flux of selected phonon modes of the zigzag crystal as a function of α. The top diagram shows the inverse frequency difference between the frequencies of the respective phonon modes.

of the system. We analyzed its dependence on the parameters of the trap, and the initial state with the help of the energy imbalance ΔE. For the transport of thermal energy between two heat reservoirs this phenomenon translated into a step-shape temperature profile in the steady state with two thermally isolated regions. Ultimately, these stark observations could always be traced back to the occurrence of asymmetric phonon modes that have a significant support only in one crystal half.

The non-linear form of the Coulomb potential softens these effects. In addition to the trivial departure from the harmonic-approximation regime for large energy scales, we have seen that the strong energy imbalance and the temperature gradient are broken by resonances in the phonon mode spectrum in an intermediate energy regime. In first order, mode crossings lead to a decreased group velocity of the coherent excitations, while their density reduces the heat flux through the crystal. In addition, we observed non-linear resonances that enabled parametric conversion between phonon mode amplitudes and can transfer energy across the defect in this way [238]. We have not been able to pinpoint their effect on the heat conductivity, but we think that they lead to an even finer resonance structure in the $\gamma \to 0$ limit.

Further questions for the heat transport include the scaling of the heat flux J with the ion number N [241]. This issue lies at the root of the breaking of Fourier's law. This analysis would also be interesting from another perspective. For the crystal size considered here, the extend of the defect covers close to all of the zigzag phase in the center. For larger systems, boundary effects by the finite length of the zigzag phase and the relatively large number of ions coupled to the thermal reservoirs are reduced, and the temperature profile could qualitatively change. Moreover, the trapped-ion system is not translationally invariant, and the defect is confined close to the Paul trap center for the majority of cases. The translation of the defect adds a new channel for energy transport in a homogeneous system, as hinted at in our study by the thermal hops between two different equilibrium configurations [306, 370, 395]. The heat transport study discussed in this Thesis may be extended to different geometries that are also able to host solitonic defects, like triangular disk-shaped crystals or helices of ion chains [40, 205–208, 220, 222, 410, 411].

Finally, the observed non-trivial heat transport is very much of practical importance for the sympathetic cooling of ion crystals [412]. As seen, we cannot assume that coupling the ions vibrations to a form of dissipation reaches all degrees of freedom and could leave different regions poorly cooled when no global cooling scheme is accessible or desired.

Chapter 5

Fluctuations and phase transitions

The discovery, study and theoretical description of classical and quantum phase transitions constitute a key issue in physics [66, 413]. Their theoretical description often falls back on simplified models such as Hubbard or Ising models [33, 343, 414, 415]. Interestingly, these models may be controllably studied using cold atoms and ions [27, 32, 69, 219, 345, 416–419]. In particular, ions in rf traps exhibit several structural phase transitions that have been studied theoretically, and probed experimentally [35, 36, 46, 204, 209, 211, 420, 421]. Prominent examples are the linear-to-zigzag transition occurring at the onset of a two-dimensional crystal, and the sliding-to-pinned transition introduced by a topological defect. As most transitions, they are prone to forms of fluctuations close to the critical point, be they of thermal or quantum origin. This has direct consequences for their experimental observation, as both sources of fluctuations cannot be eliminated in experiments and do alter the measurement. In this chapter, we analyze the effect of fluctuations on the linear-to-zigzag transition and the Aubry transition, and investigate the change in the particle dynamics and the motional spectrum.

5.1 Thermal spectrum at linear-to-zigzag transition

In this section, we discuss the thermal modification to the phonon mode spectrum from the second-order expansion introduced in Sec. 2.3.2 in the vicinity of the linear-to-zigzag transition at α_{lin-zz}. As discussed in Sec. 2.3, this structural transition connects the linear phase with $\alpha \gg 1$ in which the equilibrium crystal has $x_i = y_i = 0$, and the zigzag phase with a triangular ladder as the minimal energy configuration, see Fig. 5.1 (top).

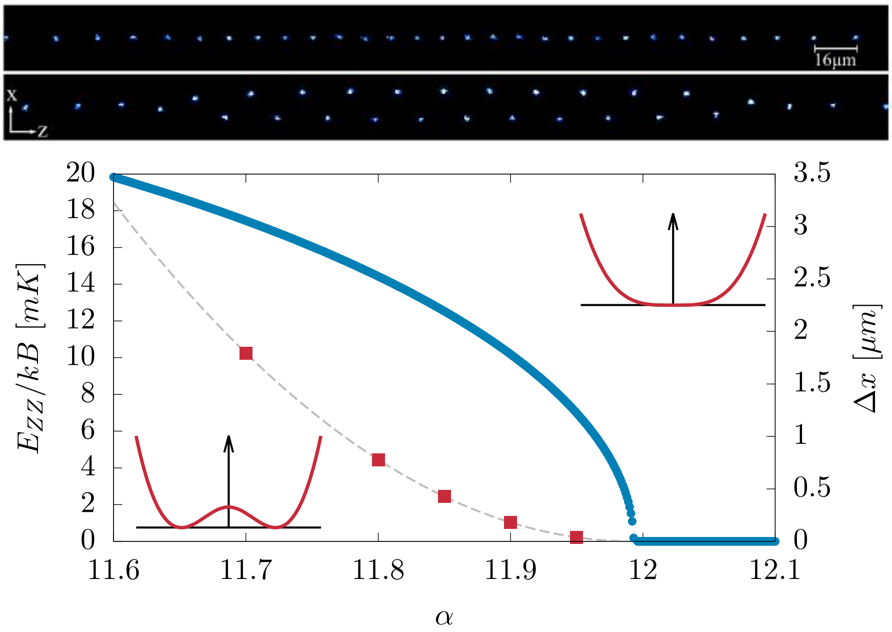

Figure 5.1: Top: Experimental photo of an ion crystal in the linear phase and the zigzag phase. **Bottom:** Size of the zigzag barrier E_{zz} (red squares) and radial size Δx of the equilibrium configuration (blue circles) as a function of α. The dashed line depicts a quadratic fit of the barrier. The insets show the potential along the adiabatic path connecting the two ground states from which E_{zz} is taken, the aspect ratio is chosen as $\alpha = 12$ and $\alpha = 11.8$.

It breaks the reflection symmetry along x of the linear chain as the ions buckle out of the z-axis of the trap, therefore the radial size of the crystal approximated by $\Delta x = x_{N/2} - x_{N/2+1}$ qualifies as an order parameter for the two phases, see Fig. 5.1 (bottom) [36]. In the zigzag phase, it can take two equilibrium values $\Delta x = \pm d_0$ which differ only in sign due to the degeneracy between the zigzag and the zagzig configuration. These two equilibrium states are separated by an energy barrier which emerges at α_{lin-zz}. We map out the adiabatic path connecting the zigzag and the zagzig by employing a Lagrange formalism to minimize the potential energy of the system while dictating a given value for Δx. Towards this, we need to solve

$$\left(\nabla, \frac{\partial}{\partial \lambda}\right)(V_{trap} + V_{Coul} + \lambda(\Delta x - d)) = 0 \tag{5.1}$$

where V_{trap} and V_{Coul} are given by Eq. (2.10). The zigzag energy barrier $E_{zz}(\alpha)$ is given by the difference between the potential energy of the equilibrium configuration and the minimal energy state with $\Delta x = 0$. Close to the transition point, the size of the barrier increases quadratically $\propto (\alpha - \alpha_{lin-zz})^2$ in the zigzag phase [36, 213].

In warm ion crystals the finite temperature causes fluctuations of the systems state in the effective potential landscape approximated by the adiabatic path between the zigzag and the zagzig. For small thermal energies in comparison to E_{zz} the system is unable to overcome the effective potentials barrier and hence remains close to the configuration spontaneously chosen at the linear-to-zigzag transition. However, if transitions of the system between the two degenerate equilibrium positions become thermally activated the dynamics qualitatively change and with it the motional spectrum. We encountered a similar situation in the crossover to the thermally delocalized regime in the pinned phase of a crystal with topological defect discussed in Sec. 4.2. Note that the occurrence of switches between the zigzag and the zagzig does not only depend on the temperature but also on the trap aspect ratio through $E_{zz}(\alpha)$. For any non-zero temperature value we can find a regime for α for which $k_B T > E_{zz}(\alpha)$ so that the value of T should only rescale the α window for which the spectrum is altered, but not change our general results.

In the following, we first show how the motional frequency spectrum changes close to α_{lin-zz} determined by a Fourier analysis of the position of the ions, and experimental spectroscopic measurements. Secondly, we derive an approximate model that include higher-order mode coupling terms in order to describe the frequency shifts of the low-lying phonon modes.

5.1.1 Molecular dynamics simulations

To describe the stochastic motion of the ions when an ion crystal is uniformly Doppler-cooled, we resort to the Langevin equations introduced in Eq. (4.5). Assuming that the Doppler cooling laser has equal projection onto all three trap axes, and a width much larger than the extend of the considered crystal, such that each ion experiences the same field amplitude, we can set the damping rates $\gamma_i = \gamma$ and temperatures $T_i = T$. For all relevant numerical simulations in the following, we set the bath coupling to the experimentally motivated value of $\gamma = 8.75\,\text{kHz}$, but keep the temperature variable to fit the results to experimental observations. Note that the value of the damping rate γ has influence on the width and the location of the resonance peaks when the motional spectrum is spectroscopically mapped out, it is therefore desirable to reduce γ, which increases the thermalization time in turn.

For a certain set of parameters (α and T) we initialize the ions in their equilibrium positions, determined by $\vec{\nabla}_{\vec{r}_i}(V_{trap} + V_{Coul}) = 0$, and subsequently thermalize the system at the chosen temperature over a simulation time of 100 µs, confirming the arrival at a thermal velocity distribution via the equipartition theorem. We then monitor the ions positions with a time resolution of 1.9 µs over a simulation

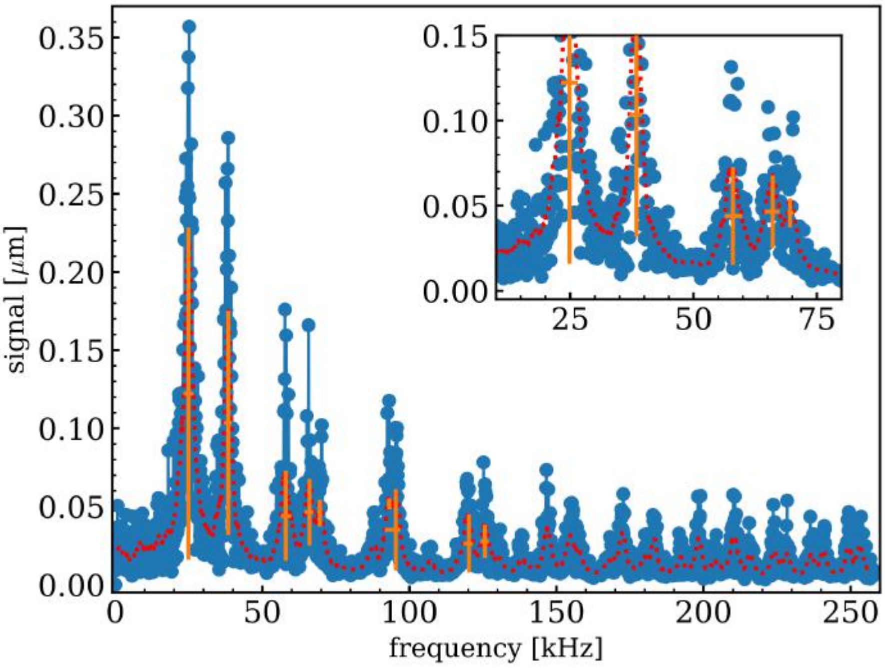

Figure 5.2: Example of a Fourier signal $S_z(\omega)$ depicted by the blue data points for $\alpha = 11.7$ and $T = 0.1\,\mathrm{mK}$. The red dotted line indicates the running mean averaged over 30 data points and the orange vertical bars indicate the automatically detected peak locations. Horizontal orange lines show the peak widths taken from the running mean graph. The inset shows a zoom into the low frequency regime, most relevant for the analysis.

time of 10 ms as input data for the following Fourier analysis. For these choices the Fourier spectrum $\mathcal{F}(\vec{r}_i)$ has a frequency resolution of 100 Hz and a maximal frequency of 263 kHz, much larger than the frequency range of interest that is fixed by the axial trap frequency $\omega_z \approx 2\pi \cdot 25\,\mathrm{kHz}$. For noise reduction, we average the Fourier spectra of five independent simulations and then build the absolute value of the Fourier transform to obtain the spectrum of the motion in the crystal plane of ion i. We expect to observe peaks in the Fourier spectra at the frequencies of the collective motion of the particles. However, they are only observable if the spatial shape of these non-linear modes has a projection onto the motion of ion i. Since the spatial shape of the non-linear modes is unclear, when the dynamics depart from the harmonic approximation we take the sum of the Fourier spectrum in one direction of all ions as a signal to detect the collective mode frequencies

$$S_{\mu=z,x}(\omega) = \sum_i |\bar{\mathcal{F}}(\mu_i)| \tag{5.2}$$

As seen in the example of Fig. 5.2, $S_\mu(\omega)$ typically shows distinct peaks in the low frequency range and a less pronounced peak sequence for large frequencies due to the increased mode density. This enables us to extract the frequencies of the low-frequency modes, which we expect to be affected most by the thermal fluctuations. We build a running mean over $20-30$ data points to smooth out further the fluctuations in the signal and use a peak search algorithm to automatically determine the location of the peaks. This can be repeated for the Fourier signals for both directions $\mu = z, x$ individually.

In Fig. 5.3 we show the motional spectrum determined by the numerical simulation of the Langevin equations as a function of α for different values of the crystal temperature T. In all plots we simultaneously show the peaks in the spectra in both directions. For the smallest temperature shown, $T = 0.1\,\mathrm{mK}$, we recover the harmonic approximation prediction for most values of α. Only directly at the transition point $\alpha_{lin-zz} \approx 12$ we observe an increase of the zigzag mode frequency due to the thermal fluctuations. For larger temperatures, an α window with deviations from the $T = 0$ result appears, with two main effects. Starting already in the linear phase, the finite temperature causes a positive frequency shift of the zigzag mode. The simulation results suggest that the zigzag mode frequency becomes soft at $\alpha_{lin-zz}(T) < \alpha_{lin-zz}$. In addition, the frequency of the axial breathing mode in the linear phase converts smoothly into the frequency of the first non-trivial mode in the zigzag phase (note that the axial common mode is always present at $\omega = \omega_z = const.$). At $\alpha_{lin-zz}(T)$, for which the zigzag mode frequency touches zero, the numerical results begin to fit well with the harmonic approximation. A similar behavior has been observed in other works. It has been argued that the delayed vanishing of the soft mode in the presence of temperature can be interpreted as a thermal shift of the transition point [212–214, 422].

In addition to the Fourier analysis, the molecular dynamics simulations enable us to reveal the time-resolved dynamics of the ions, in particular we are interested in the occurrence of thermal hops between the two minimal energy configurations for $\alpha < \alpha_{lin-zz}$. Towards this end, we show the radial coordinate of the central ion as a function of time for two different values of α in Fig. 5.4 (left). We observe a qualitatively different behavior between the two cases, when α is tuned further away from the transition point the ion oscillates around one of the equilibrium positions for a substantial dwelling time τ_e and occasionally switches its sign. For α tuned closer to α_{lin-zz} we cannot mark discrete switching events anymore since the ions constantly oscillate between the two equilibria with different sign. This behavior is due to the double-well shape of the effective potential described by the adiabatic path between the two degenerate zigzag and zagzig states [423]. At $\alpha = 11.7$ the energy barrier separating the two states has an energy of about $k_B 10\,\mathrm{mK}$, so that the thermal energy of $k_B 2\,\mathrm{mK}$ chosen in the diagram is smaller and only rarely activates the switch. In the other case $E_{zz} \approx k_B T$, so that during

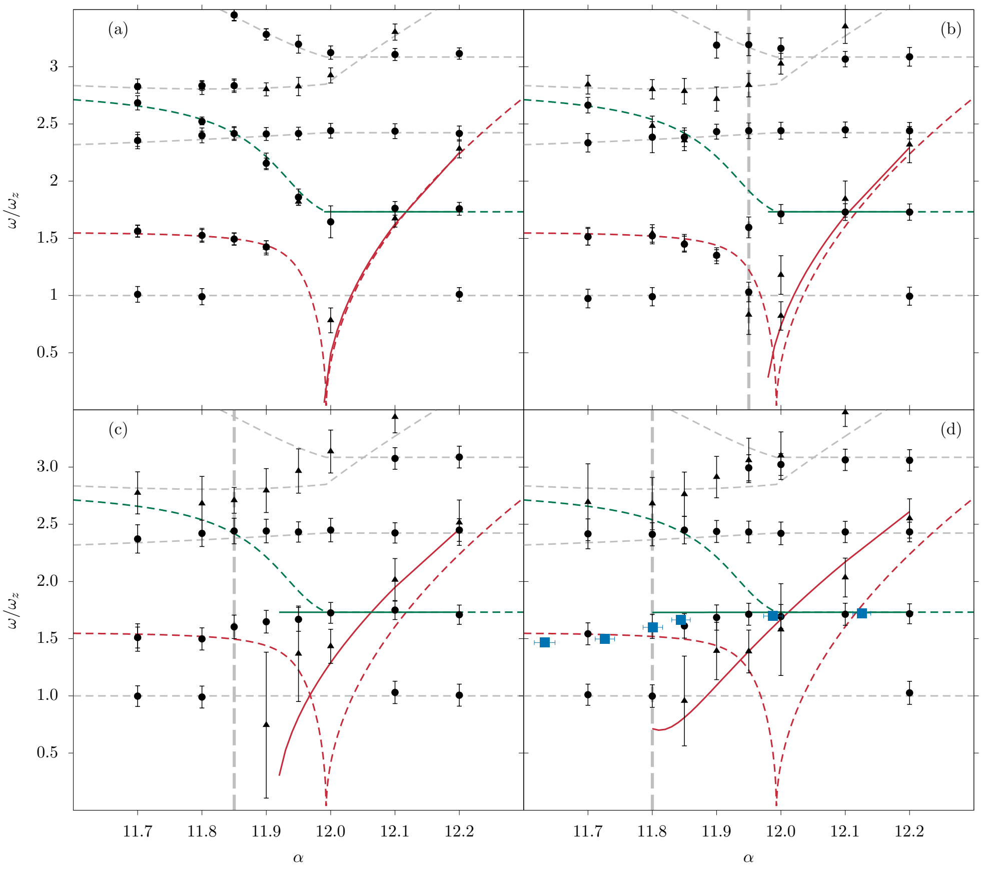

Figure 5.3: Motional spectrum for different temperatures: $T = 0.1\,\mathrm{mK}$ (a), $2\,\mathrm{mK}$ (b) and $3.5\,\mathrm{mK}$ (c). The dashed lines show the phonon mode frequencies calculated from the harmonic approximation around the equilibrium state. Highlighted in red and green are the zigzag and axial breathing mode, respectively. The black data shows the motional frequencies obtained from the axial (circles) and radial (triangles) Fourier spectrum calculated from molecular dynamics simulations, the error bars indicate the FWHM of the running mean average of the peaks. In (d) we show additionally the experimental results in the blue squares. The solid lines show the motional frequencies calculated from the effective theory presented in Sec. 5.1.3, with the zigzag mode (red) and axial breathing mode (green) taken as system modes.

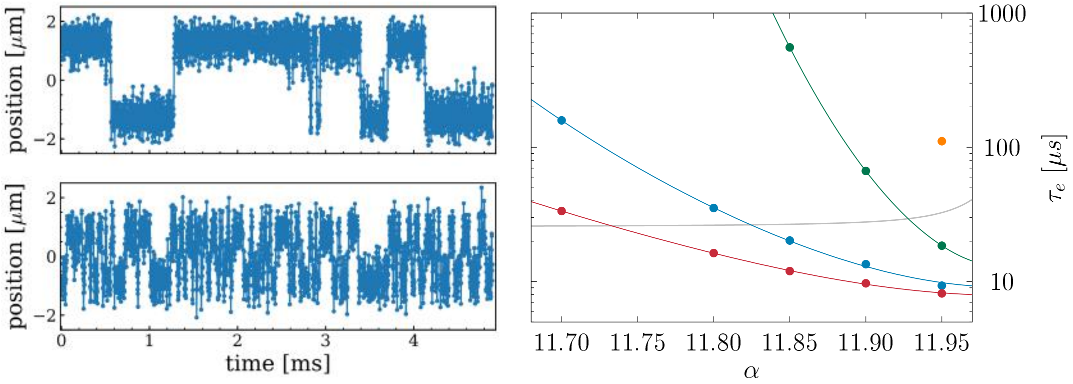

Figure 5.4: Left: Radial dynamics of the central ion in a crystal of $N = 30$ particles from molecular dynamics simulations. In the top graph $\alpha = 11.7$, whereas in the bottom one $\alpha = 11.85$. The temperature is $T = 2\,\mathrm{mK}$ in both cases. **Right:** Average dwelling time τ_e as a function of α for different temperatures: $T = 3.5\,\mathrm{mK}$ (red points), $2\,\mathrm{mK}$ (blue points), $0.5\,\mathrm{mK}$ (green points) and $0.1\,\mathrm{mK}$ (orange point). The solid lines show an exponential fit $\propto \exp[(\alpha - \alpha_{lin-zz})^2]$. The zigzag mode period T_{ZZ} is indicated by the grey line.

almost every oscillation period around one of the equilibrium configurations a switch is thermally triggered. To pinpoint the deviations in the motional spectrum from the harmonic approximation to the thermal switches, we compare the average dwelling time τ_e in one of the minima of the effective potential to the period T_{zz} of the first non-trivial harmonic phonon mode in the zigzag. To calculate the average dwelling time, we divide the simulation time by the number of sign changing events of the radial coordinate of the center ion. In Fig. 5.4 (right), we observe the expected decrease of the ratio τ_e/T_{zz} when the linear-to-zigzag transition is approached from underneath, and when the systems temperature is increased.

For $\tau_e/T_{zz} > 1$ the crystal fulfills at least one full oscillation of the motional mode, so that we expect the motional spectroscopy to deliver a motional frequency close to the harmonically approximated result. The opposite is the case for $\tau_e < T_{zz}$, we expect strong modifications to the motional spectrum in this regime. We take $\alpha = \alpha_{lin-zz}(T)$ such that $\tau_e/T_{zz} = 1$ as a crossover point between the (close to) harmonic approximation phase and the regime for which the non-linearity of the effective Landau potential is probed, and hence strong spectral modifications occur. We show these values in the numerically calculated spectrum and see good agreement with the transition points taken from the extrapolation of the thermal zigzag mode frequency.

5.1.2 Experimental measurements

The experimental measurement of the motional frequency spectrum close to the linear-to-zigzag transition is shown in Fig. 5.3 by blue points. It shows a good agreement with the numerical results for a crystal temperature of $T = 3.5\,\mathrm{mK}$. In the conducted experiment, the ion crystal, trapped in a linear rf trap, is illuminated uniformly by a Doppler-cooling laser addressing the ${}^2S_{1/2} \rightarrow {}^2P_{1/2}$ transition of Yb. In addition, another Doppler-cooling laser incident from a different angle is focused to a beam waist of $80\,\mu\mathrm{m}$ and aligned such that it only addresses a fraction of the crystal. Its intensity is modulated in time with a tunable frequency ω_d, which results in a periodic light force that triggers coherent ion oscillations. When ω_d is tuned in resonance to a collective mode frequency the amplitude of the oscillations of the ions increases linearly in time in the absence of damping. The global Doppler-cooling laser leads to a simultaneous damping of the ion velocities, such that after a thermalization time a steady state amplitude of the addressed collective mode is reached. The amplitude of the created displacements is observable from the ion fluorescence light collected via an EMCCD camera. As the exposure time of the camera is on the order of hundreds of milliseconds, a much larger timescale than the typical periods of the ion oscillation, the spatial extension of the washed-out region from which fluorescence light is collected increases on resonance. Moreover, the amplified ion velocity Doppler-shifts the frequency of the cooling laser experienced by the ion, resulting in a decreased scattering rate. In total, we can take the light intensity collected from a small region covering the equilibrium position of a selected ion as a signal to detect the motional resonances. It shows dips when the oscillations of the ions are driven by the resonantly modulated laser light, such that the ion partly leaves the selected square, see Fig. 5.5.

Note that the presented motional spectroscopy by means of parametric driving necessarily increases the crystals temperature leading to stronger non-linear effects. As seen in Fig. 5.3 the experimental data fits best with the simulated Fourier spectra for $T = 3.5\,\mathrm{mK}$, a value which is considerably larger than the temperature of the crystal without driving close to the Doppler cooling limit $T_D \approx 0.5\,\mathrm{mK}$. This effect also depends on the driving lasers intensity, as it dictates the steady state amplitude of the excited mode. A consequence of this increase in non-linear dynamics can be seen in the resonance dips shown in Fig. 5.5, the peak for the axial breathing mode shows a shift for stronger laser powers. In addition, the line shape becomes more asymmetric for larger amplitudes. The measurement results shown in Fig. 5.3 have been taken from an experiment with a laser power of $6\,\mu\mathrm{W}$. In addition, the selected method is unable to effectively excite collective modes with a short wavelength, such as the zigzag mode in the linear phase, due to their small spatial overlap with the driving force. The excitation laser drives several ions close to uniformly such that a motion with a finer spatial resolution than the

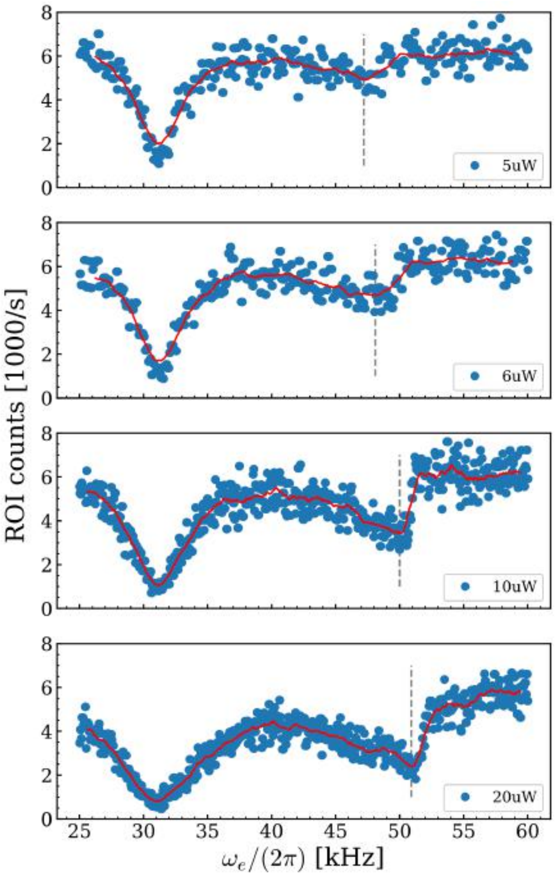

Figure 5.5: Experimental measurement of the motional frequencies via the fluorescence collected from a square region, covering the equilibrium position of the ion. The power of the driving laser has been subsequently increased, see legend. The red line indicates a running mean over 50 data points, the vertical dashed line marks the maximal excitation of the axial breathing mode.

size of the beam waist cannot be addressed. This problem can be solved in modern experiments with single-ion addressing techniques.

5.1.3 Effective theory for the mode coupling

It has become clear that the thermally activated switching between the two degenerate ground states in the zigzag phase causes the altered motional spectrum close to the transition point. In the following, we derive an effective theory for the thermal spectrum based on the expansion of the Coulomb potential discussed in Sec. 2.3.2. In order to include non-linear effects, we extend the expansion to fourth order in the mode amplitudes, which leads to the higher-order tensors $\tilde{L}$ and

$\tilde{M}$ given by Eqs. (2.28) and (2.29). The resulting approximated potential cannot describe the existence of multiple local minima when the expansion is done around one of the ground states as usual and is therefore not suitable for the description of the switching dynamics observed. At this point it is important to note that in the α window with substantial deviations from the harmonic spectrum, bounded by $\tau_e < T_{zz}$ as shown above, the time-averaged state is given by the linear chain even though it is a stationary but unstable state for $\alpha < \alpha_{lin-zz}$. It is therefore justified in this regime to expand the Coulomb potential around the linear chain corresponding to the maximum of the central barrier in the effective Landau potential. This choice is also capable to reproduce the double-well structure of the potential in the zigzag phase, we can write the fourth-order expansion

$$V \approx \frac{1}{2}\sum_r m\omega_r^2\theta_r^2 + \frac{1}{6}\sum_{r,s,m}\tilde{L}_{rsm}\theta_r\theta_s\theta_m + \frac{1}{24}\sum_{r,s,m,n}\tilde{M}_{rsmn}\theta_r\theta_s\theta_m\theta_n. \tag{5.3}$$

Since we expand around an unstable configuration, we have that the zigzag mode frequency $\omega_r^2 < 0$ for $\alpha < \alpha_{lin-zz}$.

As a next step, we employ timescale separation arguments to reduce the system to the modes of interest, i.e. the low-lying modes like the zigzag mode. In this regard, the axial common mode takes a special role, as it has typically the lowest frequency but does not couple to any other mode through the non-linear tensors, since it is one of the three phonon modes that translate the crystals center of mass [238]. In the following, we focus on the l modes with the lowest frequencies ω_r^2 close to the transition point, excluding the common mode. We refer to them as system modes, while the rest of the phonon modes are denoted as bath modes in the following. In the finite-size crystal, the gaps between the mode frequencies in harmonic approximation remain finite such that we can identify a timescale $2\pi/\omega_l < \delta t < 2\pi/\omega_{l+1}$, when the mode frequencies are ordered in ascending order. We are interested in slow oscillations and neglect dynamics occurring on timescales larger than δt. For that reason, we time average the potential given by Eq. (5.3), and make the simplifying assumption that the l low-lying-mode amplitudes vary slowly on the timescale δt, such that

$$\langle\theta_i(t)\rangle_{\delta t} = \frac{1}{\delta t}\int_{t-\delta t/2}^{t+\delta t_2}\theta_i(t')dt' \approx \theta_i(t), \quad i \le l \tag{5.4}$$

while $\langle\theta_i(t)\rangle_{\delta t} \approx 0$ for $i > l$. Moreover, due to their stochastic motion, we neglect all higher-order correlations between different modes so that the only terms surviving after taking the time average of the fourth-order potential are

$$\langle V\rangle_{\delta t} \approx \frac{1}{2}\sum_r^l\left(\sum_{s=l+1}^{3N}\tilde{L}_{rss}\langle\theta_s^2\rangle_{\delta t}\right)\theta_r + \frac{1}{2}\sum_{r,r'}^l\left(m\omega_r^2\delta_{rr'} + \frac{1}{2}\sum_{s=l+1}^{3N}\tilde{M}_{rr'ss}\langle\theta_s^2\rangle_{\delta t}\right)\theta_r\theta_{r'}. \tag{5.5}$$

Here, we did not include terms that do not contribute to the dynamics of the system modes. Finally, we assume that the bath modes are in thermal equilibrium and fulfill the equipartition theorem resulting in $\langle\theta_s^2\rangle_{\delta t} \approx k_B T/m\omega_s^2$ for $s > l$.

From Eq. (5.5), we can determine effective mode frequencies since we have reduced the time-averaged non-linear expansion back to an effective quadratic potential. The first term is linear in the system mode amplitudes and yields a constant force but does not affect their oscillatory frequency. The second term is quadratic and gives the modified mode frequencies after diagonalization. From the form of the derived potential, it is visible that the resulting mode frequencies are proportional to the square root of the temperature through $\sum_s \tilde{M}_{rr'ss}\frac{k_B T}{m\omega_s^2}$.

In addition, the effective mode frequencies depend on α through the non-linear tensor elements $\tilde{M}_{rr'ss}$ and the unperturbed bath mode frequencies ω_s. The model breaks down if the minimal eigenvalue of the quadratic term becomes zero as a function of α and T.

In Fig. 5.3, we plot the effective frequencies when only the zigzag mode and the axial breathing mode are considered as system modes, i.e. $l = 2$. In that case, the two system modes are not coupled by M_{12ll}, since M can only couple two axial with two radial modes for a linear chain. For the smallest temperature considered the effective model converges towards the harmonic approximation, which is valid in the regime $T \to 0$. With increasing temperature, we observe positive shifts of the zigzag frequency together with an approximately unaffected breathing-mode frequency up to the breakdown of the effective model.

The observed results agree within the full-width at half maximum of the Fourier peaks from the molecular dynamics simulations. For lower α, the expansion of the Coulomb interaction up to fourth order around the linear chain becomes invalid as it cannot capture the shape effective Landau potential when the equilibria depart further away from $\Delta x = 0$. The breakdown of the effective coupling model occurs at larger values of α than the transition to the harmonic approximated spectrum, determined from the dwelling time τ_e. However, the crossover point $\tau_e = T_{zz}$ has been chosen arbitrarily. The α and T resolution of our calculations is insufficient to precisely determine at which ratio between the two timescales the harmonic approximation fails. In order to increase the precision of the effective model, the number of considered system modes l could be increased and terms in even higher order of the expansion of the Coulomb potential could be included.

5.1.4 Conclusion

To conclude, we have observed positive frequency shifts of the transition driving zigzag mode that are caused by thermally activated switches between the degenerate ground states. They effectively stabilize the linear-chain configuration for α values below the critical point. In addition, the axial breathing mode smoothly converts into the frequency of the zigzag mode in the symmetry broken phase, a phenomenon that has been experimentally observed as well. Based on timescale separation arguments and the equipartition theorem, we have derived an effective model that is able to reproduce the spectrum determined from the Fourier analysis of molecular dynamics simulations. Both the effective model and the simulations show a crossover to a regime at which the harmonic expansion around one of the ground states of the zigzag phase becomes valid away from the critical point.

5.2 Quantum fluctuations close to finite Aubry transition

In addition to the fluctuations caused by finite temperatures in classical systems, quantum mechanics is the dominant origin of fluctuations in the positions of the ions on a much lower energy scale [100, 129]. In this section, we focus on the alteration of the dynamics and motional spectrum caused by the quantum-mechanical ion fluctuations close to the Aubry transition occurring in two-dimensional ion crystals with a topological defect [46]. It is important to note that the concepts of this chapter are directly applicable to the structural linear-to-zigzag transition, a detailed study of the quantum linear-to-zigzag transition can be found in Refs. [36, 203, 204, 210, 424, 425] In reality, both fluctuation sources are nonzero such that special care needs to be taken when trying to backtrack physical observations close to the transition to either one of the fluctuation sources.

5.2.1 Linear ion chain

The quantum equivalent of the emulation of the FK model with a one-dimensional ion chain has been investigated theoretically in Refs. [45, 331, 426]. They commonly demonstrate the departure from the classical results if the effective Planck's constant introduced in Sec. 3.2.4 has a considerable value. In the single-particle case, the stick-slip motion of the PT model is modified by a sequence of Landau-Zener tunneling events, which can be seen as quantum slips, visible in Fig. 5.6. They are caused by resonances between the Wannier states of neighboring potential minima when the center of the harmonic confinement is dragged across the optical lattice. When initialized in a chosen Wannier state most resonances lead to the occupation of a different Wannier state after the transfer of the confinements center to the neighboring potential well, their individual importance for the dynamics is determined by the velocity of the process. In this way the support velocity influences the overall friction force, only in the small velocity regime the adiabatic dynamics yields the same (translated by one corrugation potential period) Wannier state, i.e. vanishing quantum friction force. At sufficient transfer rates the drag triggers Wannier excitations whose energies are subsequently dissipated, giving rise to a non-zero friction force. Its amplitude is significantly reduced in comparison to the classical PT model due to the quantum slips that precede the classical slip event.

For a chain of ions subject to an optical corrugation potential, quantum tunneling results in a delocalization of the ion wavefunctions. In particular, the pinning effect of the potential is countered by the ability of the ions to transfer through the potential maxima. For strong quantum effects, quantified by $\tilde{\hbar}$, this results

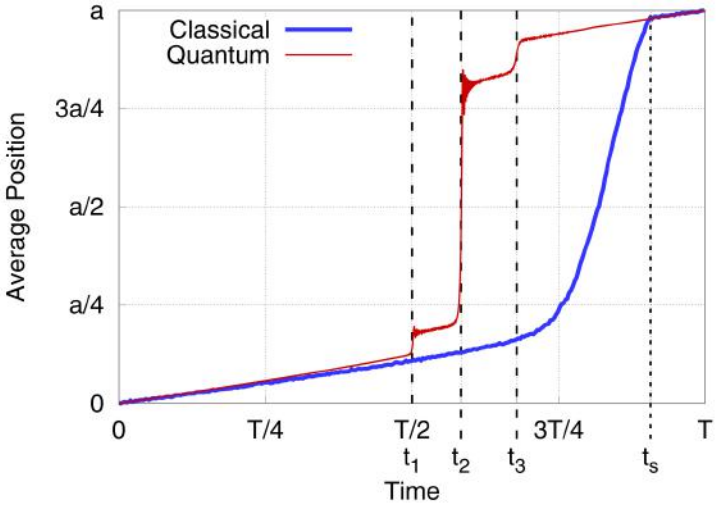

Figure 5.6: Average position of the particle in a quantum equivalent of the PT model introduced in Sec. 3.2.4. The confinement is translated with a finite velocity. The red line for the quantum particle shows tunneling slips, the classical equivalent slips over the corrugation potential maxima at a later point. The vertical lines at $t_{1,2,3}$ indicate resonances of Wannier states of neighboring potential wells, t_s is the time at which the classical particle is forced to slip. Plot from Ref. [426].

in the loss of the discrete structure of the classical result [45]. This has been described in the literature in the framework of instanton excitations, which couple the stationary classical states with quasi-degenerate energies for intermediate values of $\tilde{\hbar}$ [328]. In this regime, ion wavefunctions with a double-peak structure are observable due to the splitting by the emerging potential maxima [323, 331]. This departure of the classical regime with an occupation of two (or more) potential wells by a single ion leads to a softening of the Hull function, see Sec. 3.2.4. To quantify the emergence of quantum effects, the Binder cumulant has been investigated. This cumulant is defined as

$$B = 1 - \frac{\langle (x - \langle x \rangle)^4 \rangle}{3 \left\langle (x - \langle x \rangle)^2 \right\rangle^2}. \tag{5.6}$$

A non-zero value of B indicates a double-peak form, whereas B vanishes for a Gaussian state. In the case of odd N and a potential maximum located at the center of the trap, the wavefunction of the middle ions is split exactly, as shown in Fig. 5.7. When taken as a measure of the Aubry transition, the onset of incommensurability is seen in the increase of the critical value of V_{FK} at which B becomes non-zero.

These results are limited to the emulation of the FK model with a linear string

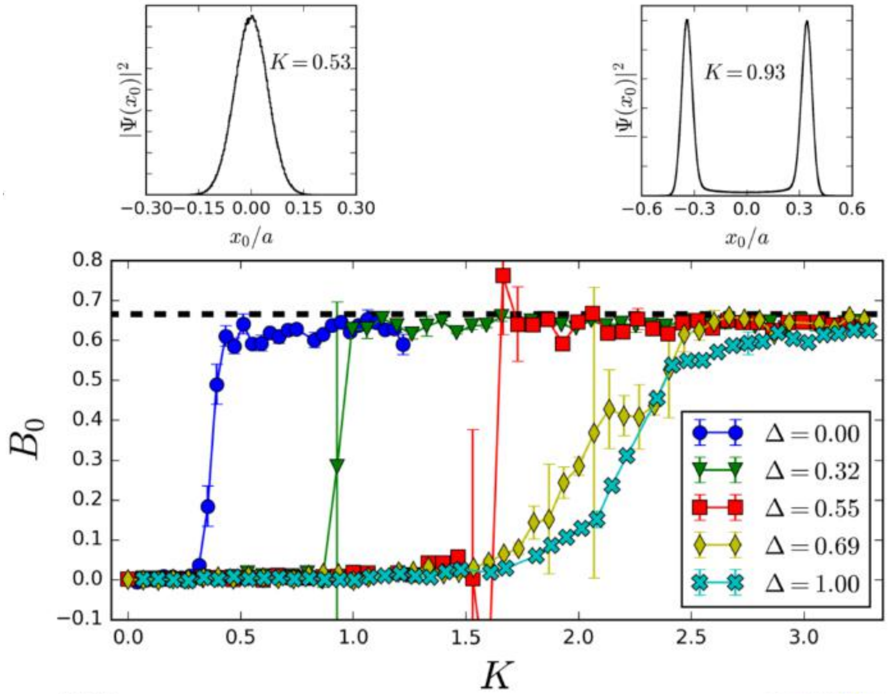

Figure 5.7: Binder cumulant of the central ion in an $N = 5$ particle chain exposed to a sinusoidal corrugation potential with amplitude K (V_{FK} in our notation). The different graphs correspond to different values of the incommensurability parameter Δ, the chain is maximally incommensurate to the potential for $\Delta = 1$. The results have been obtained from a path integral Monte Carlo calculation. The wave functions of the central particle for two values of K in the case $\Delta \approx 0.22$ are shown above. Plots from Ref. [331].

of ions and relied on Monte Carlo methods with a small but finite temperature. This method overestimates the parameter regime for which coherent quantum tunneling is observable as we discuss below. In order to investigate the quantum effects close to the Aubry transition in a two-dimensional ion crystal with a topological defect, we aim to simplify the problem with the knowledge of the PN potential. This approach enables the exact diagonalization of the effective kink Hamiltonian.

5.2.2 Static quantum effects

We consider the effective potential landscape of the kink given by the PN potential introduced in Sec. 3.3. In the collective excitation formalism employed to determine the potential, the dressing field and the kink degrees of freedom are then coupled by the potential terms of the Hamiltonian [301]. For the purpose of a subsequent quantification of the problem, we assume that we can neglect this coupling due to sufficient cooling of the ion crystal. In addition, close to the Aubry transition the kink degrees of freedom and the dressing excitations are typically energetically separable. The axial kink mode describing the oscillation of X inside the PN potential has the smallest frequency in comparison to the delocalized phonon modes. Therefore, in what follows, we consider that the important quantum features are covered by the single-particle dynamics of the kink with coordinate X in the classical PN potential given by $U(X)$.

To introduce quantum fluctuations we promote the kink to a quantum particle with a wavefunction $\psi(X)$. The Hamiltonian of the problem can be written as

$$\hat{H} = \hat{P}\frac{1}{2\hat{M}}\hat{P} + U(\hat{X}) \tag{5.7}$$

where we denote quantum operators with hats. Note that due to the position dependence of the effective kink mass, the momentum operator $\hat{P}$ and $\hat{M}$ do not commute, so that extra care needs to be taken when writing the kinetic energy of the kink in a Hermitian form.

Since we reduced the complexity of the quantum Aubry transition in two-dimensional ion crystals to a single particle problem, we can exactly diagonalize the Hamiltonian to obtain its eigenstates and eigenvalues as a function of α. In Fig. 5.8, we show the two eigenstates with the lowest energy together with the PN potential in the vicinity of the Aubry transition. We can divide the results into three regimes, depending on α.

In the classical sliding phase with $\alpha - \alpha_A < 0$, the PN potential is in very good approximation harmonic due to the repulsion of the kink from the boundaries of the inhomogeneous crystal. Therefore, it is no surprise that the eigenstates are given by Hermite polynomials, and that the ground state is of a Gaussian shape.

At the Aubry transition the smooth PN potential develops periodic modulations caused by the enhanced influence of the two sub-chains with $x_i > 0$ and $x_i < 0$ onto each other. In particular, a PN barrier emerges at $X = 0$ that leads to the spontaneous symmetry breaking in the classical model as it yields two new equilibrium positions away from the crystal center, see Fig. 5.8. For α slightly above α_A, we observe a quantum delocalized regime with substantial consequences of the quantum nature of the kink. In this phase, the small size of the PN barrier yields a non-negligible tunnel effect such that the two potential wells are coupled, the low-lying states exhibit a double peak structure. It is important to note that the shown tunnel coupling on a length-scale of 1 µm is fulfilled by the quasiparticle. In reality, the ground state describes the coherent superposition of ion states that are separated in space by $d\vec{r}_i/dX \cdot 1\,\mu\mathrm{m}$, which typically lies on the order of 100 nm.

The central PN barrier grows quadratically $\propto (\alpha - \alpha_A)^2$ in size in the pinned phase, making the quantum coupling of the two classical equilibrium states less

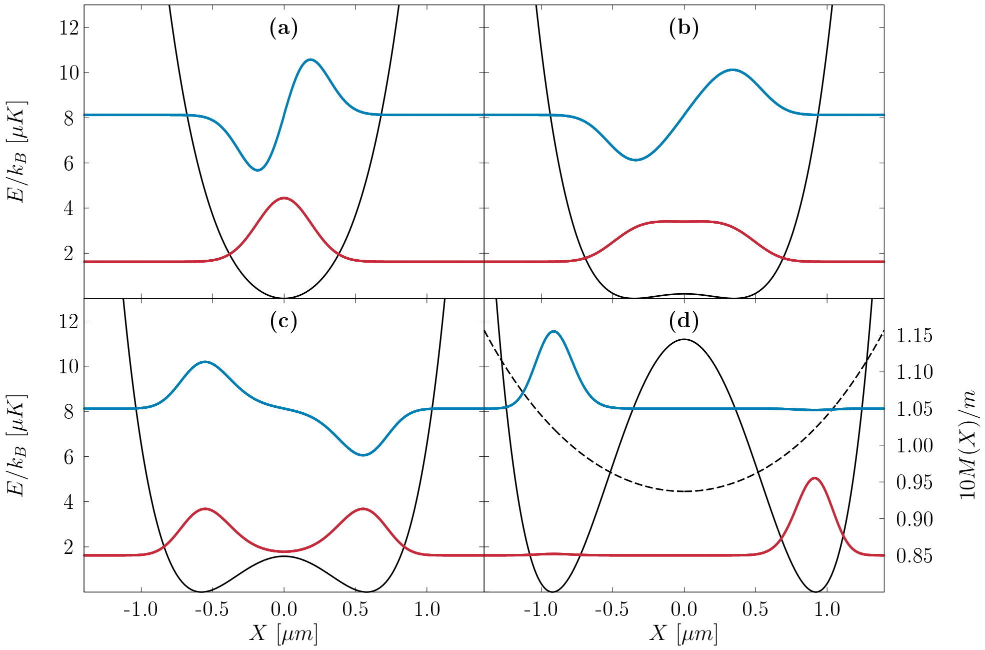

Figure 5.8: PN potentials (black) and ground-state (red) and first-excited state (blue) wavefunctions for different values of $\alpha - \alpha_A$: -0.14 (a), 0.04 (b), 0.11 (c) and 0.29 (d). In (d) we additionally show by the dashed line the kink mass $M(X)$ in units of $0.1m$. We do not see significant changes of the mass position dependence when α is tuned.

important. As a consequence, for values further away from the critical point the ground state symmetry is broken and the two lowest eigenstates describe the Gaussian harmonic oscillator ground states of the two unconnected potential wells. This suppression of their tunnel coupling marks the entry of the quasi-classical regime that was not observable in the path integral Monte Carlo calculations in Ref. [331]. In analogy to the thermal fluctuations close to the linear-to-zigzag transition discussed in the section above, the transition into the quasi-classical regime can be seen as a shifted transition into a quantum pinned phase. Its critical point does not coincide with the classical value due to the quantum fluctuations that stabilize a symmetric configuration in the classical supercritical regime. For comparison we calculated the eigenstates of the Hamiltonian with a constant kink mass, set to the value at the minimum of the PN potential, and do not observe any significant effect of the position dependence of $\hat{M}$ in all regimes.

We can assess the extend of the quantum delocalized region by calculating the Binder cumulant of the kinks ground state wavefunction, see Fig. 5.9 (top). It is zero in the sliding phase as expected from the Gaussian shape centered around

$X = 0$, and increases at the Aubry transition point. In the quantum delocalized regime, we observe the maximal value of $B = 2/3$ due to the double peak structure caused by the tunnel coupling. We terminate the graph of B when the quasi-classical regime is entered as the value of the Binder cumulant becomes ambiguous; the negligible tunnel coupling leads to two independent harmonic oscillator copies around the local minima of the PN potential. Hence, any superposition of the Gaussian ground-state wave functions shown in Fig. 5.8 is a ground state of the kink. However, the resulting Binder cumulant depends on the chosen amplitudes in the superposition. It is therefore possible to find a minimal energy eigenstate for any arbitrary value of B so that its value is insufficient for the assessment of the presence of quantum tunneling. In particular, an incoherent superposition for $T \neq 0$ will yield $B = 2/3$ [331].

The decoupling of the two potential minima can also be observed in the energy spectrum depicted in Fig. 5.9 (bottom). Deep in the pinned phase the eigenstates consist of degenerate pairs of harmonic oscillator states that are centered around the two potential minima. When reducing α quantum tunneling couples the states of one set and consequently a gap between them opens. In a Wentzel, Kramers and Brillouin (WKB) approximation the tunneling probability scales exponentially with the square root of the energy of the considered Wannier states, thus higher energy states are coupled for larger α and enter the quantum delocalized phase.

In the subsequent quantum delocalized regime, the eigenenergies of the pair states are smaller than the PN barrier size but are non-degenerate due to the non-negligible tunnel coupling, leading to a maximal Binder cumulant. When the eigenstates energies become larger than the PN barrier, they are approximately given by perturbed harmonic oscillator states, e.g. the ground state exhibits a flat top profile due to the increased potential energy at $X = 0$. Finally, for $\alpha - \alpha_A < 0$ the energy spectrum is equispaced, as expected for a harmonic potential.

It is important for the discussion of the quasi-classical regime that the tunnel coupling between the two potential minima is never exactly zero, but only becomes exponentially small as suggested by WKB theory. The discussion above holds for all practical purposes but is not rigorously exact, e.g. the α value at which the pairs of states become degenerate ultimately depends on the precision of our calculations. The two pair states remain non-degenerate in the quasi-classical regime, but their energy gap will not have any observable consequences, e.g. for the dynamics of the kink.

The importance of quantum effects, i.e. the extend of the quantum delocalized regime, can be quantified by an effective Planck's constant like for the quantum FK model

$$\tilde{\hbar} = \hbar \left(\frac{\omega_z}{m C_0} \right)^{1/3} \tag{5.8}$$

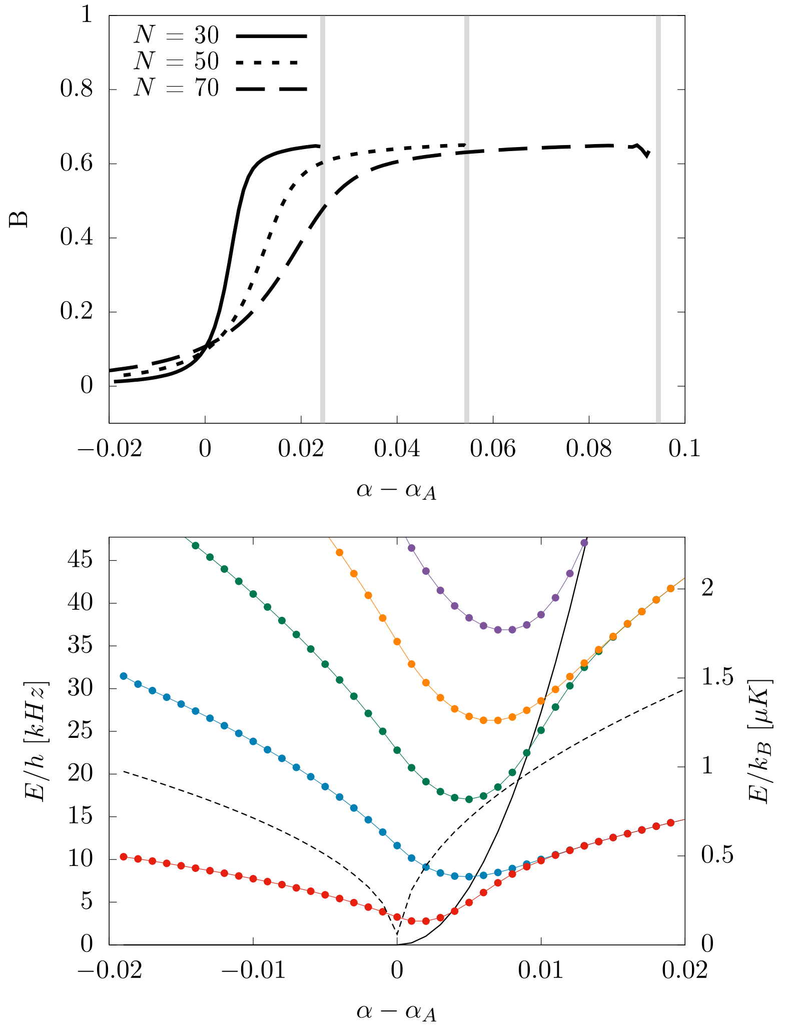

Figure 5.9: Top: Binder cumulant of the kinks ground state wavefunction as a function of α for different particle numbers N. The vertical bars show the beginning of the quasi-classical regime for which there is not a unique value of the Binder cumulant. **Bottom:** Energy spectrum of the kink as function of α. The black solid line shows the size of the central PN barrier E_{PN}, the dashed line indicates the classical kink mode energy calculated from a harmonic approximation of the ion dynamics.

Clearly, the choice of the ion species entering via the mass m influences the amplitude of the quantum fluctuations through the kinetic energy term. Moreover, the axial trap frequency ω_z determines the overall length scale of the crystal, i.e. the interaction energies. In agreement with Eq. (5.8), we observe an increased size of the quantum tunneling regime for stronger confinement, see Fig. 5.10.

As visible from Fig. 5.9 (top), the ion number N shows an additional influence on the transition point to the quasi-classical regime. As discussed above, E_{PN} is the deciding quantity that causes the emergence of degenerate eigenstate pairs due to negligible tunneling. It is raised by the mutual Coulomb repulsion of the ions with $x_i > 0$ and $x_i < 0$, determined by the radial extend of the crystal Δx. The necessary increase of α in order to decrease Δx by a certain amount depends on the particle number, more ions mean stronger stiffness against the radial squeeze by the trap. Therefore, the increased extend of the regime with $B \neq 0$ of Fig. 5.9(top) for larger particle numbers can be explained by the different derivatives $d\,\Delta x/d\alpha(N)$, and is not a sign of stronger quantum effects.

For the Aubry transition occurring in two-dimensional ion crystals, the two length scales a_S and a_P of the emulated FK model cannot be tuned independently. The creation of the corrugation potential of one of the sub-chains by the system itself effectively cancels the influence of the inhomogeneous ion density but restricts the ratio of the two competing length scales to values close to unity. It is therefore impossible to tune $\tilde{\hbar}$ arbitrarily, as it is in principle the case for the system consisting of a linear ion string subject to an optical lattice potential.

A possible strategy to measure the presence of quantum effects at the Aubry transition aims to probe the modified spectrum of the kink motion presented in Fig. 5.9 (bottom). Due to the close to vanishing energy of the ground state, the cooling of the crystal is done more conveniently away from the transition point deep in the pinned phase, making sure that the kink motion stays energetically isolated from the residual spectrum. There, a typical ground state cooling scheme consisting of Doppler and subsequent sub-Doppler cooling could in principle be implemented, see Sec. 2.2.2. Experiments have demonstrated the common cooling of the phonon modes into a regime of $\bar{n} \approx 8$, which is sufficient to suppress the coupling between the dressing modes $\vec{\chi}_i$ of the crystal and the kink motion. The latter can be further cooled to even lower temperatures $\bar{n} \approx 1$, which means reaching a temperature scale of µK in the effective kink model. Experiments have shown that the kink mode is less prone to dc electric field noise than other low-frequency modes, which leads to a suppressed kink heating and enables effective cooling [427]. Subsequently, the trap aspect ratio can be ramped down to approach the Aubry transition point in an adiabatic way. The ramping rate is limited by the average lifetime of the defect. As the ground-state population is kept fixed during the ramp, the motional spectrum of the kink can be spectroscopically mapped out, e.g. by blue sideband transitions.

5.2.3 Tunneling dynamics

The presence of quantum tunneling has significant implications for the dynamics of the kink and can therefore provide another powerful approach to demonstrate

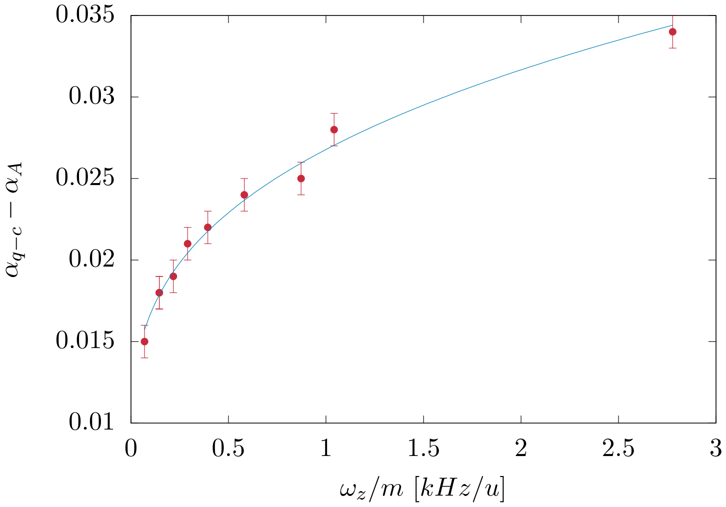

Figure 5.10: The extend of the quantum delocalized regime as a function of the ratio of the axial trap frequency and the ion mass. The red points are taken from a calculation of the Binder cumulant of the kinks ground state wavefunction, α_{q-c} is the trap aspect ratio at which the Binder cumulant becomes inconclusive. The error bars indicate the α resolution of the calculations. The blue line shows a fit $\propto \left(\frac{\omega_z}{m}\right)^{1/3}$.

the different regimes close to the Aubry transition. Moreover, we can expect to observe thermal effects that wash out the tunneling dynamics if the temperature approaches a value comparable to E_{PN}.

In order to observe the coherent oscillation between the left and the right potential minimum we need to initialize the kink on one side of the PN barrier. We do so by breaking the potentials symmetry with a linear potential that uniformly pushes the kink into the region $X > 0$. We assume that

$$V(\hat{X}) = U(\hat{X}) - h\hat{X} \tag{5.9}$$

with the force h. In order to localize the kink close to the classical equilibrium $X_0 > 0$ irrespective of the temperature we choose h such that the two potential minima are gapped by the thermal energy $k_B T$. In an experiment, this external breaking of the systems symmetry along z could be done by controllable higher-order potentials of the Paul trap.

We then assume that the kink is in a thermal state of the tilted Hamiltonian described by a diagonal density matrix

$$\rho = \frac{1}{Z} \sum_i \exp\left(-E_i^h / k_B T\right) \left|\psi_i^h\right\rangle \left\langle\psi_i^h\right| \tag{5.10}$$

with Z the partition function. The elements are written in the basis of the eigenstates of the tilted Hamiltonian $|\psi_i^h\rangle$, such that E_i^h are the eigenenergies if h is non-zero. At $t = 0$, we set $h = 0$ in order to trigger the inter-well tunneling dynamics. The evolution of the density matrix is dictated by the von Neumann equation $i\hbar\frac{d\rho}{dt} = [H, \rho]$ where H is given by Eq. (5.7), which has the solution

$$\rho(t) = \frac{1}{Z}\sum_{lmn} \exp\left[-\left(\frac{E_l^h}{k_B T} + \frac{it}{\hbar}(E_m - E_n)\right)\right] c_{lm}c_{ln}^* \left|\psi_m\right\rangle \left\langle\psi_n\right|, \tag{5.11}$$

where $H\left|\psi_i\right\rangle = E_i\left|\psi_i\right\rangle$. $c_{ik} = \langle\psi_k|\psi_i^h\rangle$ describes the basis change of the set of eigenstates at $t = 0$. In order to monitor the tunneling dynamics of the kink, we investigate the probability to find the kink at $X < 0$. We therefore introduce the projection operator $\hat{P}^< = \theta(-\hat{X})$, where $\theta(x)$ is the Heaviside step function. We then find the probability

$$P^<(t) = \mathrm{tr}(\hat{P}^<\rho(t)) = \sum_{lmn} \exp\left[-\left(\frac{E_l^h}{k_B T} + \frac{it}{\hbar}(E_m - E_n)\right)\right] c_{lm}c_{ln}^* P_{mn}^< \tag{5.12}$$

where $P_{mn}^< = \left\langle\psi_m\right| \hat{P}^< \left|\psi_n\right\rangle = \int_{-\infty}^{0} dx \psi_m^*(x)\psi_n(x)$.

In Fig. 5.11, we plot $P^<$ as function of time after the switch to $h = 0$ for different values of the temperature T. When the trap aspect ratio has been tuned into the quantum delocalized regime, we observe coherent oscillations between the two potential minima for low T. The maximal amplitude of the oscillations is determined by the employed gradient, i.e. increasing h leads to a stronger initial localization and consequently to larger values of $P^<$.

For increasing temperatures, states that are higher in energy than E_{PN} become thermally populated, so that the long timescale oscillation of the quantum tunneling is washed out by faster oscillations. Consequently, the signal strength of the tunneling dynamics gets reduced. Values of $P^< \neq 0.5$ are caused by dephasing of fast oscillating modes. We plot a running mean of 20 data points of $P^<(t)$ to suppress the fast oscillating terms. We observe oscillations on the timescale expected for the coherent quantum tunneling.

In the inset, we compare the amplitude of the oscillations of the running mean with the fluctuations within the blocks used for the determination of the running mean, in order to assess the signal-to-noise ratio. The results show that for $T < 5\,\mu\mathrm{K}$ the running mean variance is larger than the fast fluctuations such that a tunneling signal could in principle be observed, given the chosen value of α.

On the contrary, in the quasi-classical regime we observe the absence of dynamics in $P^<$. As the kink is unable to reach the opposite end of the PN barrier, it stays localized at $X > 0$. With increasing temperature, $P^<$ departs from the minimal value obtained in Fig. 5.11 only due to the thermally populated states above E_{PN}.

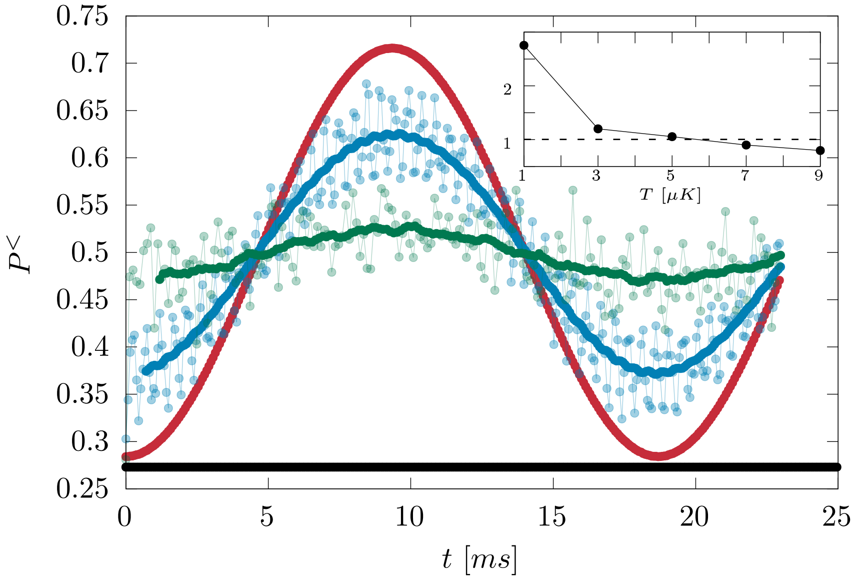

Figure 5.11: Tunneling dynamics indicated by $P^<$ for different temperatures $T = 0.1\,\mu\text{K}$ (red),$T = 1\,\mu\text{K}$ (blue) and $T = 10\,\mu\text{K}$ (green). The trap aspect ratio has been tuned to $\alpha - \alpha_A = 0.11$ for the colored data. The black line shows the result for $T = 1\,\mu\text{K}$ and $\alpha - \alpha_A = 0.31$. The transparent points show the time evolution, the opaque graph indicate a running mean over 20 subsequent data points. In the inset, we show the ratio between the variance of the running mean and the variance of $P^<$ within the running mean data blocks as a function of the temperature.

5.2.4 Conclusion

To conclude, we have observed direct consequences of quantum tunnelling in the vicinity of the classical Aubry transition point. Similar to the thermal stabilization of the linear chain in the zigzag phase, the quantum fluctuations shift the breaking of the symmetry of the ground state to larger α. Deep in the supercritical regime, the system exhibits negligible quantum tunneling with degenerate eigenstates describing the classical equilibria. The importance of the quantum effects is determined by the trap confinement through ω_z and the ion mass m, unlike the one-dimensional case in which the corrugation potential period can be tuned independently. The experimental observation of the altered energy spectrum or the dynamics triggered by the presence of quantum tunneling poses a challenge due to the required control of the temperature on the order of µK and trap frequencies $\delta\alpha \approx 0.01$ [49, 428].

Chapter 6

Vibron-Hubbard models in ion Coulomb crystals

The simulation of quantum many-body systems is a major driving force for research on trapped ions [16, 17, 19, 24]. The hopping of local oscillations of the ions in a crystal lattice, described in Sec. 2.3.2, already provides one natural step towards the simulation of Hubbard-type models [33, 347, 417, 429–432]. Moreover, spin degrees of freedom may be encoded in a selected level scheme of the electronic states of the atoms, allowing for the simulation of spin lattice models [11, 32, 114, 416, 433–438]. These subsystems can be manipulated separately or brought together by external driving, either in the form of laser radiation or a temporal modulation of the trap parameters [439–444]. The combination of these ingredients can then be used to study a variety of phenomena of relevance for condensed-matter physics to high-energy physics, while their sensitivity to fundamental constants can be used for tests of paradigmatic models and their possible extensions [92, 94, 445].

Here we build on this extensive field and present an approach to mimic a spin system by means of vibrational excitations in different directions, instead of electronic states. Their hopping in a two-dimensional ion crystal exhibits a non-trivial coupling between their external motion and spin in the simple form of spin-orbit coupling [67, 68]. Moreover, vibrational excitations can be brought into an interacting regime by means of sideband laser addressing, leading to the simulation of Jaynes-Cummings-Hubbard (JCH) models [69, 419, 446–459]. This type of Hubbard model offer some advantages compared to the competing platform of cold neutral atoms in optical lattices [23].

6.1 Non-Abelian dynamics in the vibrational system

Due to their high degree of tunability of the model parameters, cold atoms and ions are particularly suitable scenarios for the simulation of many-body systems with broken time-reversal symmetry and topological properties. Prominent examples are provided by the creation of artificial gauge fields and spin-orbit coupling [67, 460–467]. Particularly relevant in this sense is the possibility to drive periodically the system, allowing for the Floquet engineering of the specific Hamiltonians, and in particular for the external breaking of time-reversal symmetry [124, 439, 441, 468–471].

In the context of trapped ions there have been proposals to harness the power of external driving to simulate gauge fields [417, 430, 435, 472]. First experiments have demonstrated the controlled hopping of vibrational excitations in a simple triangular crystal [469, 473, 474]. There, the flexibility of a surface electrode trap is used to prohibit the dynamics by off-resonant oscillator frequencies. Hopping is re-established in a controlled way by modulating the trap voltages. In this section, we report on the creation of non-Abelian dynamics of vibrational excitations, building on similar ideas.

6.1.1 Floquet driving and hopping matrix shaping

In the following, we consider a two-dimensional ion array in microtraps with local vibrations described by harmonic oscillators with two different frequencies $\omega_1 > \omega_2$ in two perpendicular directions within the array plane. We assume external control of these frequencies, as well as the orientation of the oscillator modes. We discuss possible experimental strategies below in the chapter.

Since the dynamics perpendicular to the plane decouple in second-order approximation (see Sec. 2.3.2), we can separate it, and only consider in-plane motion. When the ions are cooled close to the motional ground state, the excitations of the systems are quanta of vibrations, called vibrons in the following, in the two directions. We may then define the Fock states $|\psi\rangle = |n_1, n_2\rangle$, which for each ion characterize the number of vibrons in each of the two local directions. The local vibron Hamiltonian can be written in the form

$$H_{vib} = \hbar \sum_i \vec{\psi}_i^\dagger \cdot \Omega \cdot \vec{\psi}_i \tag{6.1}$$

where we employ a similar notation as that employed in Sec. 2.3.4 restricted to the in-plane vibrons. Here $\Omega = \mathrm{diag}(\omega_1, \omega_2)$ is the homogeneous vibron frequency matrix, $\vec{\psi}_i = (\psi_{i,1}, \psi_{i,2})$, and $\psi_{i,\alpha}$ destroys a vibron in the direction α for ion i.

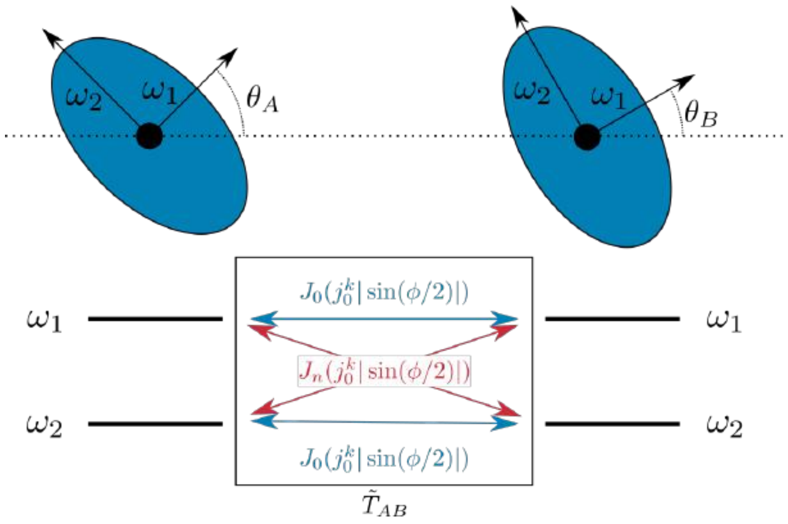

Figure 6.1: (top) Schematic depiction of two ions subject to vibron frequencies ω_1 and ω_2 that are rotated away from the vector $\vec{r}_{AB,0}$ joining the two equilibrium positions. (bottom) Sketch of the vibron levels and their coupling via the hopping elements of the matrix $\tilde{T}_{AB}$, together with the respective amplitude factors.

The vibrations of the ions are coupled by their Coulomb repulsion via the hopping matrix T_{ij}, the quantum equivalent of the classical t_{ij} discussed in Sec. 2.3.2. The hopping Hamiltonian can be written as

$$H_{hop} = -\hbar \sum_{i,j\neq i} \vec{\psi}_i^\dagger \cdot T_{ij} \cdot \vec{\psi}_j. \tag{6.2}$$

The overall strength of the hopping matrix is determined by the distance between the ions, whereas the relative importance of the different components depends on the vibron orientation relative to $\vec{r}_{ij,0} = \vec{r}_{i,0} - \vec{r}_{j,0}$. We consider that the ω_1 vibron mode of ion i forms an angle θ_i with the vector connecting the two equilibrium positions $\vec{r}_{i,0}$, as depicted in Fig. 6.1. This yields the hopping matrix

$$\hbar T_{ij} = L \cdot U_i^T \cdot W_{ij} \cdot U_j \cdot L \tag{6.3}$$

$$= \frac{\hbar C_0}{m|\vec{r}_{ij,0}|^3} \begin{pmatrix} \frac{2c_ic_j - s_is_j}{\omega_1} & -\frac{2s_jc_i + c_js_i}{\sqrt{\omega_1\omega_2}} \\ -\frac{2c_js_i + s_jc_i}{\sqrt{\omega_1\omega_2}} & \frac{2s_js_i - c_jc_i}{\omega_2} \end{pmatrix} \tag{6.4}$$

where $U_j = \exp(-i\theta_j\sigma^y)$ is a two-dimensional rotation matrix, s_i/c_i is a shorthand notation for $\sin(\theta_i)/\cos(\theta_i)$, $L^2 = \hbar\Omega^{-1}/m$, and $W_{ij} = C_0\,\mathrm{diag}(2,-1)/|\vec{r}_{ij,0}|^3$ is the classical coupling matrix for $\theta_i = 0$, introduced in Sec. 2.3.2.

Note that the resulting hopping matrix is generally not diagonal and hence the two directions of local oscillations are coupled even for a linear chain crystal. The assumed shaping of the local vibrons enables the external control of the relative strength of diagonal and off-diagonal hopping rates, which is not possible in a self-assembled crystal. Note that T_{ij} is diagonal, as in a linear chain crystal, only if both angles θ_i and θ_j are a multiple of $\pi/2$, i.e. one of the vibron modes is parallel to $\vec{r}_{ij,0}$.

The overall Hamiltonian is then given by the sum of H_{vib} and H_{hop}. The vibrons are the fundamental particles of the model as the total number operator $\mathcal{N} = \sum_i \vec{\psi}_i^\dagger \cdot \vec{\psi}_i$ commutes with the Hamiltonian and therefore is constant during the dynamics.

As already discussed in Sec. 2.3.2, the vibron frequencies and the orientation of the respective modes are generally non-homogeneous in self-organized two-dimensional ion crystals. They are determined by the diagonalization of the matrices $m\omega^2 + \sum_{j\neq i} W_{ij}$ which depend on the crystal geometry through the Coulomb couplings W_{ij}. $\omega = \omega_z \mathrm{diag}(1, \alpha)$ describes the global confinement frequencies coming from the Paul trap.

In order to externally dictate the properties of the local vibron modes and reach the homogeneous frequencies Ω and tunable θ_i the ions can be addressed by strongly focused dipole lasers creating optical trapping potentials as discussed in Sec. 2.1.2. Alternatively, the confinement of the individual ions in separated segments of surface electrode traps offers a robust way to reach the desired model. The departure from the self-organization of the ions in a global rf trap leads to the desired vibron directions and frequencies if we can neglect the effect of the Coulomb repulsion from the other ions. The latter has two effects, it modulates the vibron frequencies dictated by the microtraps via the diagonal terms of W_{ij}, which we can neglect for

$$m\omega_{1,2} \gg \frac{C_0}{d^3} \tag{6.5}$$

where d is the typical ion separation. In addition, the oscillations in the two perpendicular principal axes are coupled by the off-diagonal Coulomb terms. However, we can apply rotating wave arguments to neglect this shift of the vibron orientations away from the microtrap axes if

$$\omega_1 - \omega_2 \gg \frac{3C_0}{4m\sqrt{\omega_1\omega_2}d^3}, \tag{6.6}$$

is fulfilled. In that case the vibron frequencies are strongly off-resonant so that the Coulomb induced coupling between the local vibron modes is suppressed. Note that this second condition for the microtraps is qualitatively different, as it demands a strong asymmetry between the two vibron frequencies, whereas the first one made constraints for their absolute value. It is only necessary if the vibrons need to be rotated away from their crystal geometry dictated orientation for the desired value of θ_i.

An important consequence of the engineering of homogeneous vibron frequencies with flexible orientation is that the off-diagonal hopping is strongly suppressed due to Eq. (6.6). In order to break the separation between the two modes and re-establish the importance of the off-diagonal terms of the hopping T_{ij} we consider a Floquet driving scheme discussed in the following. The implementation of the proposed techniques is in reach of current optical trapping setups and has already been demonstrated in an experiment employing three surface electrode traps [165, 469, 473, 474].

We assume that the local vibron frequencies are externally modulated by a periodic drive of the form:

$$\omega_{i,\mu}(t) = \omega_\mu + \eta_{i\mu}\omega_d \cos(\omega_d t + \phi_{i\mu}) \tag{6.7}$$

where ω_d is the frequency of the drive, $\eta_{i\mu}$ characterizes the driving strength, and $\phi_{i\mu}$ is the driving phase. In order to keep the discussion as general as possible we consider the possibility to have different driving strengths and phases in the two directions $\mu = 1, 2$, although this might be experimentally challenging. The oscillating vibron frequencies affect H_{vib} but also the hopping part through L. We can neglect the fast oscillation of the harmonic oscillator lengths due to the timescale separation between the relatively slow vibron hopping and the much faster driving period. Transforming into the the interaction picture with respect to H_{vib} yields:

$$H^{int}(t) = \hbar \sum_{i,j\neq i} \vec{\psi}_i^{\,\dagger} \cdot T_{ij}^{int}(t) \cdot \vec{\psi}_j \tag{6.8}$$

with

$$\frac{\left(T_{ij}^{int}(t)\right)_{\mu\nu}}{\left(T_{ij}\right)_{\mu\nu}} = e^{i(\omega_\mu - \omega_\nu)t} e^{i(\eta_{i\mu}\sin(\omega_d t + \phi_\mu) - \eta_{j\nu}\sin(\omega_d t + \phi_{j\nu})}. \tag{6.9}$$

In addition to the usual time-dependence due to the phase evolution of the Fock states, the driving results in an exponential term in the hopping matrix. In the absence of the external drive the off-diagonal elements of T_{ij}^{int} would rotate with a frequency $\omega_1 - \omega_2$ while the diagonal terms are constant in time. Through a rotating wave approximation we could neglect the former terms in the limit of $\omega_1 - \omega_2 \gg T_{ij}$. Hence, as discussed above, off-diagonal terms would be negligible. However, for non-zero driving this is not the case as a Jacobi-Anger expansion of the driving terms shows:

$$\frac{\left(T_{ij}^{int}(t)\right)_{\mu\nu}}{\left(T_{ij}\right)_{\mu\nu}} = \sum_{s,s'\in\mathbb{Z}} J_s(\eta_{i\mu}) J_{s'}(\eta_{j\nu}) e^{i(\omega_\mu - \omega_\nu + (s-s')\omega_d)t} e^{i(s\phi_{i\mu} - s'\phi_{j\nu})} \tag{6.10}$$

where $J_s(x)$ is the s-th Bessel function of the first kind. For the diagonal elements $\mu = \nu$, we find the resonant time-independent terms in the expansion by setting $s = s'$, while the residual parts are oscillating with a frequency of multiple ω_d. We neglect the latter in a rotating wave approximation for $\omega_d \gg (T_{ij})_{\mu,\mu}$ as the driving is oscillating much faster than the dynamics we are interested in. For the off-diagonal elements the terms $s = s'$ are rotating with $\omega_1 - \omega_2$, but if the driving frequency is chosen such that $\omega_1 - \omega_2 = n\omega_d$, the terms with $s' = s + n$ become resonant, and hence the corresponding term becomes significant. All other terms in the double sum can be neglected for the same reason as for the $\mu = \nu$ terms.

We may then write the hopping matrix $\tilde{T}_{ij}$ in the rotating wave approximation in the form:

$$\frac{\left(\tilde{T}_{ij}\right)_{\mu\nu}}{\left(T_{ij}\right)_{\mu\nu}} = \mathcal{F}(\eta_{i\mu}, \eta_{j\nu}, f(\mu,\nu), \phi_{i\mu} - \phi_{j\nu}) e^{-if(\mu,\nu)(\phi_{i\mu}+\phi_{j\nu})/2} \tag{6.11}$$

with

$$\mathcal{F}(a, b, f, \phi) = \sum_{s\in\mathbb{Z}} J_s(a) J_{s+f}(b) e^{i(s+f/2)\phi} \tag{6.12}$$

where $f(\mu,\nu) = n(\nu - \mu)$. Using the Neumann-Graf formula and introducing the parameters

$$Z(a, b, \phi)^2 = a^2 + b^2 - 2ab\cos(\phi), \tag{6.13}$$

$$\gamma(a, b, \phi) = \arctan\left(\frac{a\sin(\phi)}{b - a\cos(\phi)}\right), \tag{6.14}$$

which fulfill $Z(a, a, \phi) = 2|a\sin(\frac{\phi}{2})|$ and $\gamma(a, a, \phi) = (\pi - \phi)/2$, we may re-write:

$$\mathcal{F}(a, b, f, \phi) = J_f(Z(a, b, \phi)) e^{i(\gamma(a,b,\phi)+\phi/2)f}. \tag{6.15}$$

Inserting this compact form of $\mathcal{F}$ into Eq (6.11) yields

$$\frac{\left(\tilde{T}_{ij}\right)_{\mu\nu}}{\left(T_{ij}\right)_{\mu\nu}} = J_{f(\mu,\nu)}(Z(\eta_{i\mu}, \eta_{j\nu}, \phi_{i\mu} - \phi_{j\nu})) e^{i(\gamma(\eta_{i\mu},\eta_{j\nu},\phi_{i\mu}-\phi_{j\nu})-\phi_{j\nu})f}. \tag{6.16}$$

The elements of the effective hopping matrix gain an amplitude factor given by a Bessel function, as well as a phase. Note that in the resulting effective Floquet Hamiltonian, the energy gap between the two vibron modes has been overcome by the absorption of n energy quanta from the driving field, and hence the off-diagonal hopping is triggered as seen in Fig. 6.2. In typical schemes aiming at

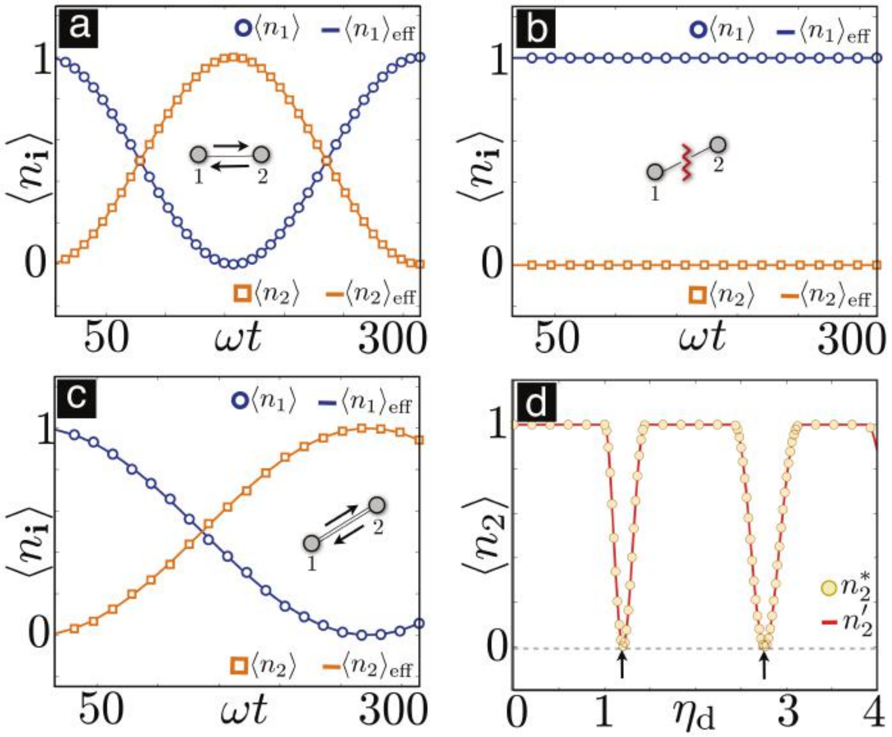

Figure 6.2: Vibron dynamics between two ions for resonant vibron frequencies (a) and detuned vibron frequencies (b). In (c) the hopping is re-established via a parametric drive, the dynamics is slowed down due to the reduction of the hopping amplitude via the Bessel functions. (d) Maximal vibron number observed at ion B after initializing a single vibron at A as a function of the driving amplitude. The dips at which no hopping is observed indicate the dynamical decoupling. Diagrams from Ref. [417].

the creation of artificial gauge fields, the engineered phase, also denoted as Peierls phase, is used to emulate an Aharanov-Bohm phase a charged particle gains in the presence of a magnetic flux through its trajectory [430, 462, 475].

In addition, the amplitude factor possesses roots that can be used to cancel the hopping between sites when the driving parameters are tuned adequately. Note that this cancellation of the hopping amplitude is not to be confused with the suppression of hopping due to off-resonant vibron frequencies. It can also set the resonant hopping via the diagonal elements of the hopping matrix to zero. The set of parameters that lead to $J_f(Z(\eta_{i\mu}, \eta_{j\nu}, \phi_{i\mu} - \phi_{j\nu})) = 0$ are shown in Fig. 6.2.

We can understand the derived model as a spin-1/2 Hubbard model, where an ω_1 (ω_2) vibron corresponds to a spin-up (spin-down) particle. Vibrons hop in the lattice, but due to the generally non-diagonal form of $\tilde{T}_{ij}$, hopping may be accompanied by the flipping of the spin state. As a result, spin and hopping dynamics are not separable leading to a form of spin-orbit coupling.

6.1.2 Non-Abelian plaquette dynamics

With the goal of demonstrating the consequences of the modified hopping in a two-dimensional ion crystal, we consider for simplicity a square alignment of four ions as shown in Fig. 6.4 (left). We label the ions as $i = A, B, C, D$ in a counter-clockwise way. We assume that the tilting angle between the ω_1 mode and the x-axis is uniform with $\theta_i = \pi/4$. In this way, the hopping matrix coupling ions at opposite sites of a diagonal of the plaquette has vanishing off-diagonal terms, since one of the vibron modes becomes parallel to the vector connecting the ions. The hopping amplitude is also reduced by a factor of $2\sqrt{2}$ in comparison to the hopping matrices at the edges of the plaquette due to the increased particle distance along the diagonal.

To exclude diagonal hopping completely we aim to find $\eta_{i\mu}$ and $\phi_{i\mu}$ such that $\tilde{T}_{AC} = 0$ and $\tilde{T}_{BD} = 0$. To reach this regime, the parameters need to fulfill $Z(\eta_{A\mu}, \eta_{C\nu}, \phi_{A\mu} - \phi_{C\nu}) = j_0^k$ and $Z(\eta_{A\mu}, \eta_{C\nu}, \phi_{A\mu} - \phi_{C\nu}) = j_0^{k'}$ where j_i^k is the k-th root of the i-th Bessel function. These constraints do not impose a strong restriction onto the driving amplitudes and phases, as shown by the solutions depicted in Fig. 6.3. The solution with the weakest driving amplitude is obtained for $\eta_{A\mu} = \eta_{C\nu}$ and $\phi_{A\mu} - \phi_{C\nu} = \pi$ (with the same conditions for ions B and D, respectively). Note at this point that the approximations made in the derivation of the effective hopping matrix $\tilde{T}_{ij}$ only impose requirements on ω_d, without constraining the possible driving amplitudes.

In addition to the restrictions imposed by diagonal decoupling, the number of free parameters is further reduced if the hopping matrices along the two dimensions are homogeneous, i.e. $\tilde{T}_{AB} = \tilde{T}_{DC}$ and $\tilde{T}_{AD} = \tilde{T}_{BC}$. This imposes that the amplitude factors and phases given by Eq. (6.16) need to be equal along the respective links. There exists a set of parameter choices that simultaneously lead to homogeneous hopping matrices along the edge links and cancellation along the diagonal links, namely $\eta_{i\mu} = \eta = j_0^k/2$ for all i and μ, and $\phi_{A\mu} - \phi_{C\mu} = \phi_{B\mu} - \phi_{D\mu} = \pi$ for all μ. In that case, the driving phases are equal for both spin states so that $\phi_D - \phi_A = \phi$ and $n = (\omega_1 - \omega_2)/\omega_d$ are the only free parameters left. The hopping matrices along the x and y directions become of the form:

$$\tilde{T}_x = \frac{C_0}{2md^3}\begin{pmatrix} \frac{1}{\omega_1} J_0(j_0^k|\cos(\phi/2)|) & -\frac{3}{\sqrt{\omega_1\omega_2}} J_n(j_0^k|\cos(\phi/2)|)e^{-in\phi/2} \\ -\frac{3}{\sqrt{\omega_1\omega_2}} J_n(j_0^k|\cos(\phi/2)|)e^{in\phi/2} & \frac{1}{\omega_2} J_0(j_0^k|\cos(\phi/2)|) \end{pmatrix}$$

$$\tilde{T}_y = \frac{C_0}{2md^3}\begin{pmatrix} \frac{1}{\omega_1} J_0(j_0^k|\sin(\phi/2)|) & \frac{3i^n}{\sqrt{\omega_1\omega_2}} J_n(j_0^k|\sin(\phi/2)|)e^{-in\phi/2} \\ \frac{3i^n}{\sqrt{\omega_1\omega_2}} J_n(j_0^k|\sin(\phi/2)|)e^{in\phi/2} & \frac{1}{\omega_2} J_0(j_0^k|\sin(\phi/2)|) \end{pmatrix}.$$

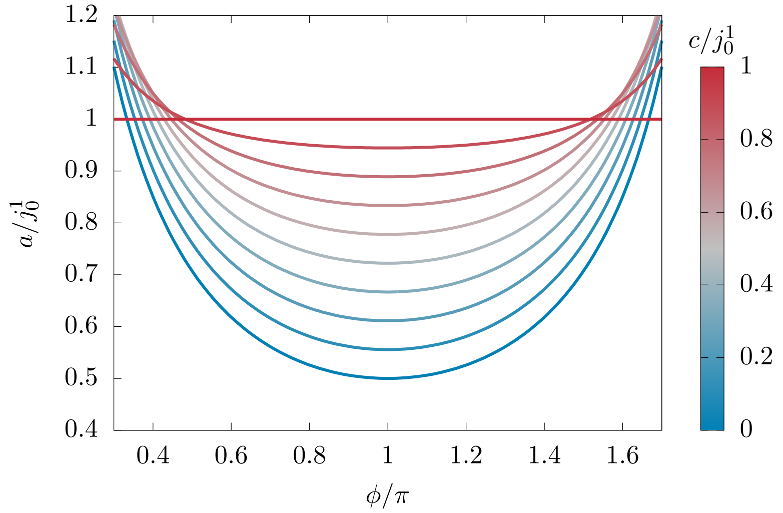

Figure 6.3: Driving amplitude a that leads to $Z(a, a-c, \phi) = j_0^1$, as a function of ϕ. The color of the curves denotes the value of the driving amplitude c between the two linked traps. Using Eq. (6.14), it is given by $2a = c + \sqrt{c^2 + [(j_0^1)^2 - c^2]/\sin^2(\phi/2)}$. These parameter choices lead to a dynamical decoupling of the respective vibron modes.

where d is the length of the square edges. Although the overall form of the two matrices is the same they are generally non-commuting:

$$[\tilde{T}_x, \tilde{T}_y] \propto (\omega_1 - \omega_2)\left(i^n J_0(j_0^k|\cos\frac{\phi}{2}|)J_n(j_0^k|\sin\frac{\phi}{2}|) + J_0(j_0^k|\sin\frac{\phi}{2}|)J_n(j_0^k|\cos\frac{\phi}{2}|)\right).$$

Note that the commutator of the two hopping matrices trivially vanishes for $\phi = \pi/2$ and $n = 2 + 4l,\ l \in \mathbb{Z}$ as $\tilde{T}_x = \tilde{T}_y$ in that case. The non-commutativity of the hopping matrices for any other choice has direct consequences for the dynamics of vibrons and results in an interesting interplay between spatial motion and spin dynamics. In the following, we investigate this form of spin-orbit coupling by monitoring the expansion dynamics of a single vibron.

We initialize a vibron on ion A in a fixed spin state $|\psi(t=0)\rangle = (a^\dagger_{A,1} + a^\dagger_{A,2})\,|0\rangle\,/\sqrt{2}$ and let it evolve along two different paths. In one path the vibron reaches the ion C diagonally opposite in a clockwise path ($\circlearrowright$), whereas in the other it does in counter-clockwise way ($\circlearrowleft$). This can be achieved by tuning the trap frequencies of the sites B or D out of resonance for all hopping processes. Then, the corresponding ion does not participate in the vibron dynamics, and hence the created vibron can only populate 3 of the 4 ions in the plaquette.

In Fig. 6.4 (right), we display for $\phi = \pi/3$ the occupation of the two spin states of the vibron in ion C for the two different trajectories as a function of

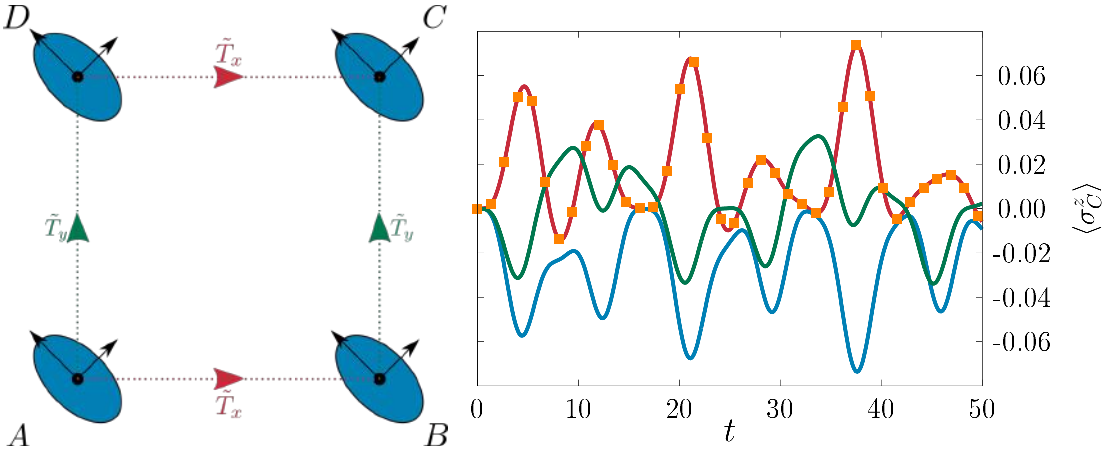

Figure 6.4: Left: Sketch of an ion square plaquette with uniform $\theta_i = \pi/4$ and the respective hopping matrices $\tilde{T}_x$ and $\tilde{T}_y$ along the two crystal axes. **Right:** Spin state of the C ion as a function of time (normalized by $m\omega_2 d^3/C_0$). We use $n = 2$ for all graphs. The system has been initialized with a single vibron at ion A with the spin state $\left(a^\dagger_{A,1} + a^\dagger_{A,2}\right)|0\rangle/\sqrt{2}$. The excitation has been forced onto the clockwise (red) and counter-clockwise (blue) path around the square with $\phi = \pi/3$. The orange squares depict the result from the full time evolution from Hamiltonian (6.8) including the time-dependent hopping matrices with $2\pi/\omega_d = 2\,\mu\mathrm{s}$ and $m\omega_2 d^3/(2\pi C_0) = 238\,\mu\mathrm{s}$. In addition, we show the result for $\phi = \pi/2$, depicted in green. The two paths are equivalent for this parameter choice since $\tilde{T}_x = \tilde{T}_y$.

time. We see clearly that the spin state strongly depends on the chosen path. In contrast, for $\phi = \pi/2$, both paths result in exactly the same spin dependence of the vibron state in ion C. While initially the spin state populations are flipped, they deviate for later times. The timescale of the dynamics is the same for both cases since the overall amplitude of the hopping elements is the same. Therefore, the discrepancy between the graphs can only come from the fact that the two different hopping matrices are probed in a different order for the different trajectories. This constitutes a coupling between the spin of the vibron and its trajectory.

In Fig. 6.4 (right), we compare the results of the theory in rotating wave approximation to calculations in the interaction picture with all rotating terms building the time-dependent hopping matrices $T^{int}_{ij}(t)$. We find good agreement between the two approaches indicating the validity of the approximation employed for typical trap configurations reported in early two-dimensional quantum simulation experiments [469] (the parameters of relevance are included in the caption of the figure).

The non-Abelian character of the time evolution may be characterized by integrating the difference between the vibron occupations for the two paths in time.

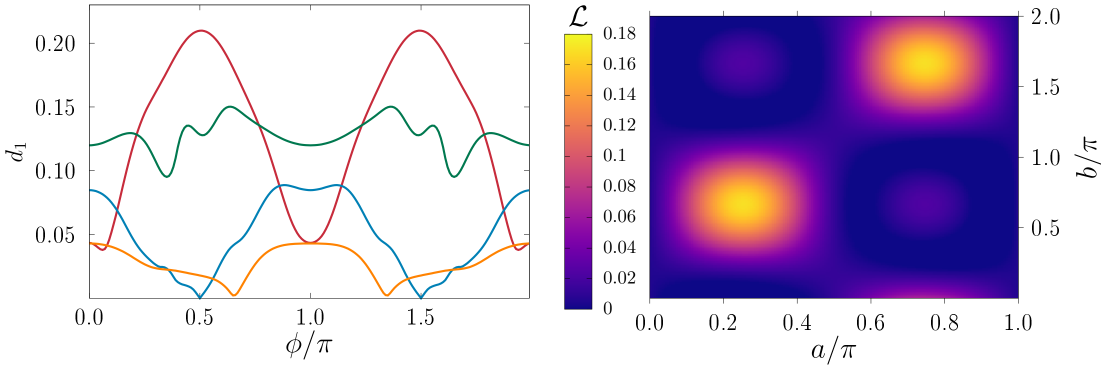

Figure 6.5: Left: Time-averaged vibron occupation difference at ion C, as defined in Eq. 6.17, as a function of ϕ for $n = 1$ (red), $n = 2$ (blue), $n = 3$ (green) and $n = 4$ (orange). **Right:** Time-averaged angular momentum $\mathcal{L}$, as a function of the spin state angles a and b defined in Eq. 6.18. The values are normalized by $m\omega_2 d/C_0$. In both diagrams, the averaging time has been set to $10m\omega_2 d^3/C_0$.

Towards that end we define

$$d_\mu = \frac{1}{T}\int_0^T |n_\mu^{\circlearrowright}(t) - n_\mu^{\circlearrowleft}(t)|dt \tag{6.17}$$

where $n_\mu^{\circlearrowright}$ ($n_\mu^{\circlearrowleft}$) is the occupation of the spin state $\mu = 1, 2$ at site C when the vibron travels in clockwise (counter-clockwise) direction. We compute this quantity for a fixed integration time T for different choices of ϕ and n and show the results in Fig. 6.5 (left).

The observation of non-Abelian dynamics is insensitive to the exact choice of the driving parameters as long as the symmetric parameter set is avoided. Note that the plot in Fig. 6.5 (left) is symmetric around $\phi = \pi$ since this is the symmetry point of the argument $|\sin(\phi/2)|$ ($|\cos(\phi/2)|$) of the amplitude factors. The robustness of the non-Abelian character of the dynamics is beneficial for its experimental observation, as a fine tuning of the drive is not required.

So far we investigated the effect the trajectory of the vibron has on the spin state. Conversely, the spin state of the vibron leads to a different dynamics when we allow it to travel along both paths. To demonstrate this, we consider an excitation initialized in site A with a spin state parametrized as

$$|\psi(t=0)\rangle = (e^{ib}\sin(a)a^\dagger_{A,1} + \cos(a)a^\dagger_{A,2})\,|0\rangle \tag{6.18}$$

with the two angles a and b as spin state parameters. As the vibron expands around the square we characterize its trajectory be the time-averaged angular momentum

$$\mathcal{L} = \frac{1}{T} \int_0^T dt \vec{r}_{vib}(t) \times \vec{v}_{vib}(t) \tag{6.19}$$

where $\vec{r}_{vib}(t) = \sum_i (\vec{\psi}_i^\dagger \cdot \vec{\psi}_i) \vec{r}_{i,0}$ is the vibrons position and $\vec{v}_{vib}(t) = d\vec{r}_{vib}(t)/dt$ its velocity. In Fig. 6.5 (right) we show the angular momentum as a function of the spin state parameters (note the invariance of the initial state under the simultaneous addition of multiples of π to a and b). We observe that the orientation of the trajectory of the vibron depends on its initial spin state, demonstrating the bidirectional coupling between spin and orbit in the vibron dynamics. The orientation for a certain set of (a, b) obviously depends on the driving parameters but is always inverted when changing $\phi \to -\phi$.

Note that the result for $\mathcal{L}$ decreases for larger integration times since the angular momentum oscillates in any case around zero. We can therefore only conclude that for short time scales the vibron exhibits a preferred rotation orientation but does not fulfill a cyclotron like orbit as it is the case for a particle exposed to an artificial gauge field.

6.1.3 Non-Abelian dynamics in a square lattice

We may extend the previous discussion to the case of a two-dimensional square-lattice crystal, by adding copies of the plaquette discussed so far, and monitoring the free expansion dynamics of a vibron excitation initialized in the center of the lattice. Note that in contrast to the small plaquette case, for which we could decouple the vibrons at ions diagonally opposite to each other, the vibron in the lattice can accomplish long-distance hops to the next-nearest and next-next-nearest neighbor sites that cannot be cancelled. They in turn are described by additional hopping matrices whose amplitudes are reduced because of the $1/|\vec{r}_{ij,0}|^3$ decay of the Coulomb interaction. This decay is partly countered by the fact that next-nearest neighbors along the x and y axes have a drive that oscillates in phase such that the amplitude factor for the diagonal hopping rates is maximal ($J_0(0) = 1$).

In Fig. 6.6 we show the expansion of a vibron initially delocalized over the central plaquette with an equal superposition of the two spin states. As the excitation delocalizes its spin state separates as the two vibron spin components perform different trajectories. Note that this is not due to a faster expansion of one of the spin components, but rather to the anisotropy of the relative hopping rates (and not their amplitudes).

We observe, however, a similar phenomenon for the Abelian driving parameters which resulted in $\tilde{T}_x = \tilde{T}_y$. This is explained by the presence of long-distance hops along the diagonals that cause the breaking of the $\mathbb{Z}_4$ symmetry of the system in

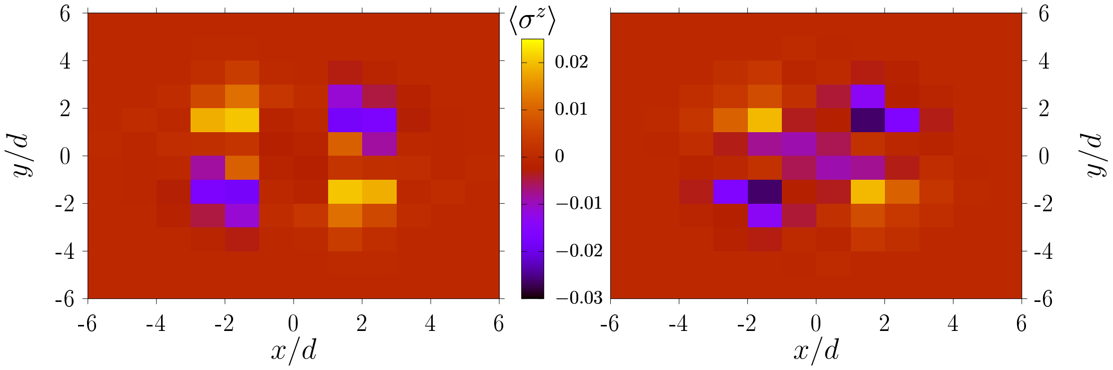

Figure 6.6: Spin magnetization of a vibron expanding in a square lattice after $t = 2m\omega_2 d^3/C_0$, with an initial spin state given by Eq. (6.18), with $a = \pi/4,\ b = 3\pi/5$. The driving parameters are given by $n = 2$ and $\phi = \pi/3$ (left) and $\phi = \pi/2$ (right).

this case. Additional computations confirm this argument by showing the recovery of the $\mathbb{Z}_4$ symmetry of the vibron spin distribution at all times for the isotropic case when the hopping is restricted to nearest neighbors. On the opposite, the spin distribution remains $\mathbb{Z}_4$ broken for all other driving parameter choices in this restricted case.

6.2 Jaynes-Cummings-Hubbard systems in trapped ions

Hubbard models attract a major attention because of their ability to model in a minimal way the interplay between kinetic hopping terms and inter-particle interaction [343, 429]. As discussed in the previous section, the emulation of these models in trapped ion crystals via vibron excitations occurs naturally due to the Coulomb coupling between the ions [63, 64]. However, vibrons are excitations of the quantum harmonic oscillations of the ions, and as such non-interacting. Therefore, the creation of an interaction term by means of non-linear corrections requires additional effort.

There have been several proposals to achieve this goal [113, 238, 347, 418]. One approach deals with the coupling of the motional Fock states to an electronic two-level system via sideband transitions [69, 476]. This leads to the dressing of the vibrons by the highly non-linear electronic subsystem [179]. This model, known as the JCH model, rose to fame first in coupled cavity systems, but has been successfully implemented in trapped ion crystals as well [369, 419]. In the following, we derive its Hamiltonian and discuss its physical properties.

6.2.1 Jaynes-Cummings-Hubbard Hamiltonian

We consider an electronic transition between states $|\downarrow\rangle$ and $|\uparrow\rangle$, with transition frequency ω_0 and linewidth $\Delta\omega$, of ions with vibron frequencies $\omega_{i\mu}$, $\mu = 1, 2, 3$. The ions are illuminated by a laser with frequency ω_l and wavevector $\vec{k}$.

The local Hamiltonian is then given by

$$H_{JC} = \sum_i \hbar \vec{\psi}_i^\dagger \cdot \Omega_i \cdot \vec{\psi}_i + \frac{\hbar\omega_0}{2}\sigma_i^z + H_{i,las} \tag{6.20}$$

where the same notation as in Sec. 2.3.4 is employed, and σ_i^z is the z Pauli matrix acting on the pseudo-spin of ion i. $H_{i,las}$ describes the ion-laser interaction that takes the form

$$H_{i,las} = DE_i^- \sigma_i^- + h.c. \tag{6.21}$$

with

$$E_i^- = E_{i,0} e^{i(\omega_l t + \phi)} e^{i\vec{k}\vec{r}} \tag{6.22}$$

where D is the strength of the dipole moment of the transition, and $E_{i,0}$ is the amplitude of the electric field of the laser at the location of ion i. The ion position operators $\vec{r}_i$ can be expressed by the ladder operators of the vibrons via $\vec{r}_i =$

$\vec{r}_{i,0} + U_i \cdot L_i \cdot (\vec{\psi}_i^\dagger + \vec{\psi}_i)/\sqrt{2}$, as discussed in Sec. 2.3.4. The matrices U_i contain the local principal axes of the ion vibrations as columns, and L_i is a diagonal matrix consisting of the respective harmonic oscillator lengths. The electric field has a different phase $\vec{k} \cdot \vec{r}_{i,0}$ at the equilibrium positions $\vec{r}_{i,0}$ of the ions, however they have no physical consequences for the vibron dynamics, we can absorb them in the definition of the electronic spin states. Inserting the form of the position operator into the ion-light interaction yields

$$H_{i,las} = \hbar\Omega_i e^{i(\omega_l t+\phi)} \exp\left[-i\vec{\eta}_i \cdot (\vec{\psi}_i + \vec{\psi}_i^\dagger)\right] \sigma_i^- + h.c. \tag{6.23}$$

where we have introduced the Rabi frequency $\Omega_i = DE_{i0}/\hbar$ and the Lamb-Dicke parameter vector $\vec{\eta}_i = \vec{k} \cdot U_i \cdot L_i$. The latter depends on the projection of the laser wavevector onto the vibron directions given by the columns of U_i. The laser introduces a distinct direction in the system, as the light field only couples the motion along $\vec{k}$ to the electronic states. It is therefore possible to address multiple vibron modes and generally translational invariance is broken due to the geometry and ion dependent principal axes U_i.

In the following derivation we concentrate on the case where the laser frequency is tuned close to the red sideband of the electronic transition. For the assumed coherent evolution the resulting physics is equivalent if the blue sideband is addressed, this case can be reached by switching the roles of the electronic states, i.e. taking $|\uparrow\rangle \leftrightarrow |\downarrow\rangle$. We transform the Hamiltonian into the interaction picture with respect to

$$H_0 = \sum_i \hbar\omega_x \vec{\psi}_i^\dagger \cdot \vec{\psi}_i + \frac{\omega_x + \omega_l}{2}\sigma_i^z \tag{6.24}$$

where we have selected the trap frequency ω_x as a typical frequency of the vibron dynamics. This choice is arbitrary due to the inhomogeneous vibron frequencies in a multi-ion crystal (see Fig. 2.7) and might be inconvenient for specific laser/crystal configurations. Nonetheless, we take ω_x as a frequency scale for $\omega_{i\mu}$ to keep the derivation as general as possible. The transformation yields

$$H_{JC} = \sum_i \hbar\vec{\psi}_i^\dagger \cdot \tilde{\Omega}_i \cdot \vec{\psi}_i + \frac{\hbar\delta_i}{2}\sigma_i^z + \tilde{H}_{i,las} \tag{6.25}$$

$$\tilde{H}_{i,las} = \hbar\Omega_i e^{-i(\omega_x t+\phi)} \exp\left[-i\vec{\eta}_i \cdot ((\vec{\psi}_i^\dagger e^{i\omega_x t} + \vec{\psi}_i e^{-i\omega_x t})\right] \sigma_i^- + h.c. \tag{6.26}$$

where $\delta = \omega_0 - \omega_x - \omega_l$ describes the detuning of the laser frequency from the red sideband and $\tilde{\Omega}_i = \Omega_i - \omega_x \mathbb{1}$. In the Lamb-Dicke limit with $L_{i\mu} \ll 1/|\vec{k}|$ we can expand the exponential in $H_{i,las}$ up to first order in $\vec{\eta}_i$ and neglect terms $\mathcal{O}(\vec{\eta}_i^2)$ [179].

This approximation needs to hold for all vibron directions simultaneously to guarantee the validity of

$$\tilde{H}_{i,las} \approx \hbar\Omega_i e^{-i(\omega_x t+\phi)} \left[1 - i\vec{\eta}_i \cdot ((\vec{\psi}_i^\dagger e^{i\omega_x t} + \vec{\psi}_i e^{-i\omega_x t})\right] \sigma_i^- + h.c. \tag{6.27}$$

Finally, we apply a rotating wave approximation to neglect all terms oscillating with a multiple of ω_x which is justified for $\Omega_i|\vec{\eta}_i| \ll \omega_x$.

This results in the Jaynes-Cummings Hamiltonian [179, 477]

$$H_{JC} = \sum_i \hbar\vec{\psi}_i^\dagger \cdot \tilde{\Omega}_i \cdot \vec{\psi}_i + \frac{\hbar\delta}{2}\sigma_i^z + \hbar\vec{g}_i \cdot \left(\vec{\psi}_i^\dagger\sigma_i^- + \vec{\psi}_i\sigma_i^+\right) \tag{6.28}$$

where the coupling constants vectors are given by $\vec{g}_i = \Omega_i\vec{\eta}_i$. The total Hamiltonian of the JCH model consists of the local terms derived above and a vibron hopping term which has been derived in Sec. 2.3.4

$$H_{JCH} = H_{JC} - \frac{\hbar}{2}\sum_{i,j\neq i}\left(\vec{\psi}_i^\dagger \cdot T_{ij} \cdot \psi_j + \psi_i \cdot T_{ij} \cdot \psi_j^\dagger\right). \tag{6.29}$$

The JCH Hamiltonian conserves the number of excitations $\mathcal{N} = \sum_i \mathcal{N}_i$ with $\mathcal{N}_i = \vec{\psi}_i^\dagger \cdot \vec{\psi} + \sigma_i^+\sigma_i^-$ which enables the block diagonalization in the subspaces $\mathcal{N} = const.$. Moreover, H_{JC} commutes with $\mathcal{N}_i$, $\forall i$ that has the vibron Fock states $|n_1, n_2, n_3, s\rangle$ as eigenstates. The diagonalization of H_{JC} in the Hilbert subspaces with constant $\mathcal{N}_i$ leads to dressed states denoted by $|N_i, r\rangle$, they are also referred to as polariton states due to the dressing analogy to solid state physics. $r = 1, 2, \ldots, (\mathcal{N}_i + 1)^2$ is an index that indicates the different dressed states in the $\mathcal{N}_i$ subspace with cardinality of $(\mathcal{N}_i + 1)^2$.

In general, the computation of the polariton states is non-trivial in itself due to the inhomogeneous $\vec{g}_i$ and $\tilde{\Omega}_i$ that depend on the crystal structure. Albeit one of the elements of the coupling vector, describing the vibration perpendicular to $\vec{k}$, can vanish, we typically cannot separate the respective vibrons dynamics as it can couple to distant polaritons via the hopping term. One special case occurs in two-dimensional ion crystals, when $\vec{k}$ lies within the crystal plane. In that setup the vibron modes perpendicular to the plane couple neither to the dressing laser nor the in-plane vibrons. As a consequence, the number of different polariton states for a given $\mathcal{N}_i$ shrinks to $2\mathcal{N}_i + 1$.

In order to study the dynamics of the polaritons in a simple setup, we consider in the following a linear chain with the dressing laser parallel to one of the trap axes, say $\vec{e}_x$. The choice of $\vec{k}$ in this scenario does not matter for the discussion. Then, $\vec{g}_i = g_i\vec{e}_x$ since $U_i = \mathbb{1}$ for all ions. Moreover, the vibron dynamics in the three dimensions decouple as W_{ij} becomes diagonal (see Sec. 2.3.2) so that we only consider the x vibrons in the following. The ground state $|0, \downarrow\rangle$ is dark to

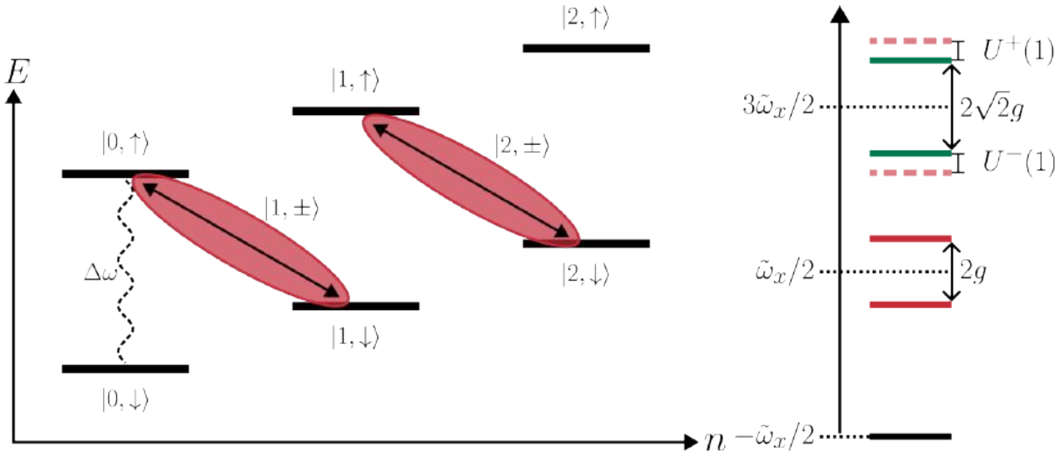
E
$|0,\uparrow\rangle$
$|0,\downarrow\rangle$
$\Delta\omega$
$|1,\pm\rangle$
$|1,\uparrow\rangle$
$|1,\downarrow\rangle$
$|2,\pm\rangle$
$|2,\uparrow\rangle$
$|2,\downarrow\rangle$
n
$U^+(1)$
$3\tilde{\omega}_x/2$
$2\sqrt{2}g$
$U^-(1)$
$\tilde{\omega}_x/2$
$2g$
$-\tilde{\omega}_x/2$

Figure 6.7: Left: Schematic depiction of the creation of dressed states mixing the vibron levels with an electronic two-level system via continuous sideband driving (here depicted by the red sideband). The dashed line depicts the potential carrier decay on the timescale of the linewidth $\Delta\omega$. **Right:** Energy levels of the polariton states in the zero (black), one (red) and two (green) polariton subspace. The red dashed lines indicate the double of the one polariton levels, demonstrating the polariton interaction energies $U^{\pm}(1)$.

the dressing and is therefore always an eigenstate of H_{JC}. The dressed states with $n_i > 0$ are superpositions of the bare states $|n_i, \downarrow\rangle$ and $|n_i - 1, \uparrow\rangle$ which are coupled via g_i, see Fig. 6.7 (left). Since the cardinality of the dressed state subspaces is fixed for all values of n_i we can write the Jaynes-Cummings Hamiltonian as a 2×2 matrix

$$H_{i,JC}(n_i) = \frac{\hbar}{2}\begin{pmatrix} \tilde{\omega}_{ix} - \delta & 2g_i\sqrt{n_i} \\ 2g_i\sqrt{n_i} & \delta - \tilde{\omega}_{ix} \end{pmatrix} + \hbar(n_i - \frac{1}{2})\tilde{\omega}_{ix}\mathbb{1} \tag{6.30}$$

The diagonalization leads to the polariton energies

$$E(0) = -\frac{\hbar\delta}{2} \tag{6.31}$$

$$E_i^{\pm}(n_i) = \hbar\tilde{\omega}_{ix}\left(n_i - \frac{1}{2}\right) \pm \frac{\hbar}{2}\underbrace{\sqrt{(\delta - \tilde{\omega}_{ix})^2 + 4g_i^2 n_i}}_{dE_i^{\pm}(n_i)} \tag{6.32}$$

where ± indicates the polariton type. The energy levels are shifted apart from the equispaced spectrum of the Fock states, see Fig. 6.7 (right). The corresponding polariton state vectors $|n_i, \pm\rangle$ are characterized by an angle $\vartheta_i(n_i)$ via

$$\begin{pmatrix} |n_i, +\rangle \\ |n_i, -\rangle \end{pmatrix} = R^T(\vartheta_i(n_i))\begin{pmatrix} |n_i, \downarrow\rangle \\ |n_i - 1, \uparrow\rangle \end{pmatrix} \tag{6.33}$$

where $R(\vartheta)$ is a two-dimensional rotation matrix and the polariton angles are given by $\tan(2\vartheta_i(n_i)) = \frac{2g_i\sqrt{n_i}}{\tilde{\omega}_{ix}-\delta}$. Obviously, $\vartheta_i(n_i) = 0$ without the dressing laser.

6.2.2 Superfluid-to-Mott insulator transition in trapped ions

The major consequence of the coupling of the vibrons to the ions two level scheme is the rise of an effective on-site vibron interaction due to the departure from the equispaced vibron spectrum [369]. If more than a single polariton is created at the same ion, the energy of the system differs from the states with delocalized excitations. This energy discrepancy depends on the total polariton number, for a homogeneous crystal (neglecting off-diagonal hopping) it would be given by

$$U^{\pm}(n) = E^{\pm}(n+1) + E^{\pm}(n) - 2E^{\pm}(n) \tag{6.34}$$

which is non-zero because $dE^{\pm}(n) \propto \sqrt{n}$.

In a system of more than two ions, the on-site interaction has a more complicated dependency on the position and dressing. As for the Bose-Hubbard model, the competition between the on-site interaction and the hopping term leads to a superfluid-to-Mott insulator transition in the many body ground state [429, 478–480]. It is driven by the ratio between $U^{\pm}(n)$ and the nearest neighbor hopping, for large $U^{\pm}(n)/T_{ij}$ the energy penalty by doubly occupied sites dominates the hopping. Hence, the ground state is given by a Mott insulator with restricted dynamics. On the opposite, for small $U^{\pm}(n)/T_{ij}$ the polaritons delocalize and experience no scattering by other excitations. In the JCH model in ion strings this transition can be driven for a fixed laser intensity by the detuning of the laser frequency from the side-band. In the limit $|\delta - \tilde{\omega}_{ix}| \gg g_{ix}$, the energy shifts $dE_i^{\pm}(n_i) \to |\delta - \tilde{\omega}_{ix}|$ so that $U^{\pm}(n > 2) \to 0$ and $U^{\pm}(1) \to (\tilde{\omega}_x - \delta)\Theta(\pm(\delta - \tilde{\omega}_x))$. In the latter case, the behavior of the two polariton types differs and depends on the sign of $\delta - \tilde{\omega}_x$. For $\delta = \tilde{\omega}_x$ the homogeneous interaction energy simplifies to $U^{\pm}(n) = \pm\hbar g(\sqrt{n+1} + \sqrt{n-1} - 2\sqrt{n})/2$, its amplitude declines with growing n so that the repulsion is the strongest when an ion hosts two polaritons.

Note that with the detuning also the mixing angles $\vartheta_i(n_i)$ changes and hence the composition of the polariton states is not equal in the two phases [448]. A maximal mixing of the spin and vibron states is achieved for the resonant case, interpolating between the bare states for $\delta - \tilde{\omega}_x \to \pm\infty$.

The fluctuation of the local polariton number $\langle \mathcal{N}_i^2 \rangle$ serves as an order parameter for the transition [446, 447, 456]. It is zero in the Mott insulator phase for integer filling factor $\langle \mathcal{N}_i \rangle$, as no particle is able to hop because of the strong interactions with the neighboring polaritons. In the superfluid phase the particles delocalize such that the hopping leads to non-zero fluctuations. Experiments have demonstrated the change of the order parameter at the transition $\delta = \tilde{\omega}_x$ as well as the difference in the polariton states between the two phases [419].

Moreover, an analysis of the hopping dynamics reveals the polariton blockade, i.e. the absence of double occupied sites for $\langle \mathcal{N}_i \rangle = 0$ as measured in Fig. 6.8. This constraints the dynamics in a one-dimensional system like the ion chain and leads ultimately to the emergence of a Tonks-Girardeau gas [481, 482]. In the emulation of the JCH model in trapped ions not only nearest neighbor hops are permitted, such that the effect of the blockade is weakened because the polaritons can change their order by jumping "over" each other. To monitor the polariton dynamics in an experiment it is necessary for the measurement scheme to be sensitive to the vibron number as well as the spin state. This has been solved in Ref. [369] by projecting the different state occupations onto auxiliary electronic states that are long-lived and can be readout independently after freezing out the hopping dynamics [187].

One major drawback of the discussed implementation of the JCH model in trapped ions is the inhomogeneity of the vibron frequencies $\tilde{\omega}_{ix}$. This issue is only absent in the case of a two-ion chain as used in the experiment. In a larger chain this effect leads to an potential landscape for the polaritons similar to the vibron energies, see Fig. 2.7. As a consequence, the superfluid-to-Mott insulator transition does not occur simultaneously across the system, resembling the case of the linear-to-zigzag transition, which also suffered from the inhomogeneous ion distances. In addition, the slopes in the energy landscape can lead to the suppression of hopping dynamics for the polaritons. When the energy levels of polaritons states of neighboring ions are much stronger detuned by $\tilde{\omega}_{ix}$ than the respective hopping rate the dynamics is frozen, as can be easily seen in an interaction picture of H_{JCH}. In special cases, hopping can be enabled by a resonance between adjacent + and − energy levels. Typically, this is only possible for a small subset of the ions. This effect is emphasised in the second-order hopping dynamics of bound polariton states discussed in the next section.

6.2.3 Bound polariton states

In this section, we elaborate on another effect of the effective on-site interaction of the dressed states, namely the presence of bound states [459, 483, 484]. Contrary to the observation of the blockade when two excitations are initialized in separated sites, the on-site interaction also can bind the particles when they are placed on the same site. The dissipation of this bi-polariton state via single vibron hopping needs to overcome the energy difference of $U^{\pm}(1)$ that is released or absorbed when one of the excitations moves away. Hence, in the Mott insulating phase with strong on-site interaction, we can expect that states with two excitations localized at the same site are energetically separated from the scattering states with distant

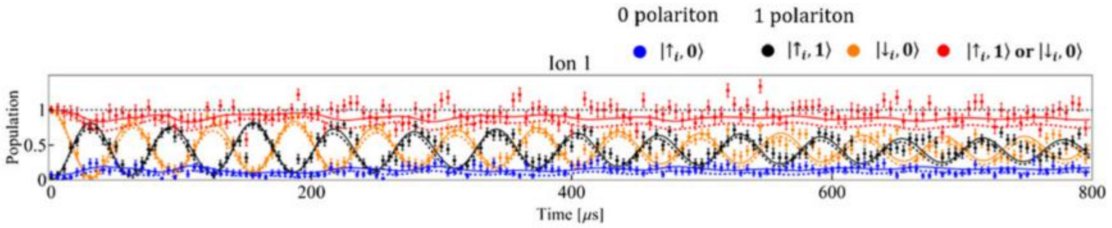

Figure 6.8: Experimental observation of the polariton blockade in the Mott insulator phase when the blue sideband is dressed. During the time evolution of the system, initialized in the bare ground state $|0,\downarrow\rangle\,|0,\downarrow\rangle$, the state maintains a vanishing projection on the zero polariton state $|0,\uparrow\rangle$ at each ion. Diagram taken from Ref. [369].

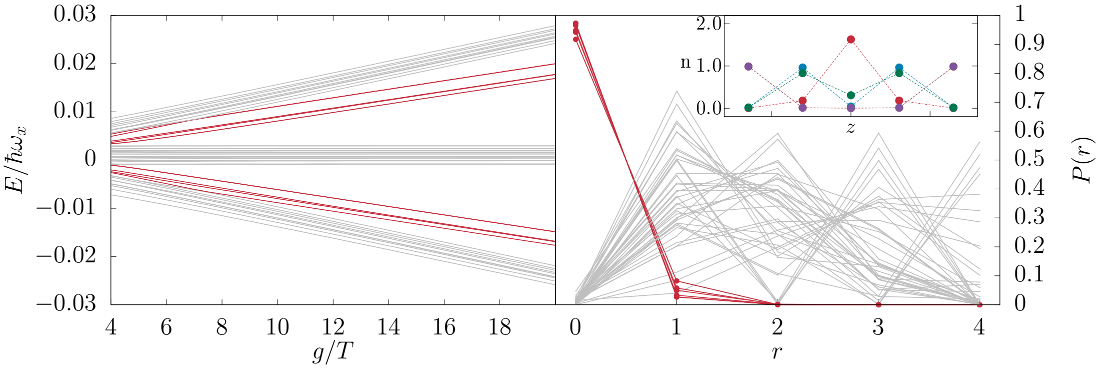

Figure 6.9: Left: Polariton many-body spectrum of a five-ion chain in the $\mathcal{N} = 2$ subspace as a function of the coupling strength. δ has been set to the average of $\tilde{\omega}_{ix}$. T is the average nearest-neighbor hopping rate of the x vibrons and $g = \Omega|\vec{k}|\sqrt{\hbar/m\omega_x}$. **Right:** Probability $P(r)$ to find polaritons at a distance of r ions evaluated for all eigenstates in the $\mathcal{N} = 2$ subspace. The red graphs correspond to the energy levels shown in red on the left. In the inset the respective polariton number distribution of the states is shown.

polaritons. In the context of the Bose-Hubbard model these states are known as repulsively bound pairs and have been predicted as well in coupled cavity systems simulating the JCH model [459, 483].

In Fig. 6.9 (left) we plot the eigenspectrum of a $N = 5$ ion JCH model in the subspace of $\mathcal{N} = 2$ polariton excitations in the system, as a function of the laser parameters. We observe three bands of states that can be explained by the three different possibilities for the polariton types of the two particles, i.e. $(+,+)$, $(+,-)$ and $(-,-)$. In the band gaps for large g, we find N distinct states, marked in red. These describe bound pairs, as an analysis of the correlation function $P(r)$ in Fig. 6.9 (right) shows. $P(r)$ describes the probability to observe the excitations at

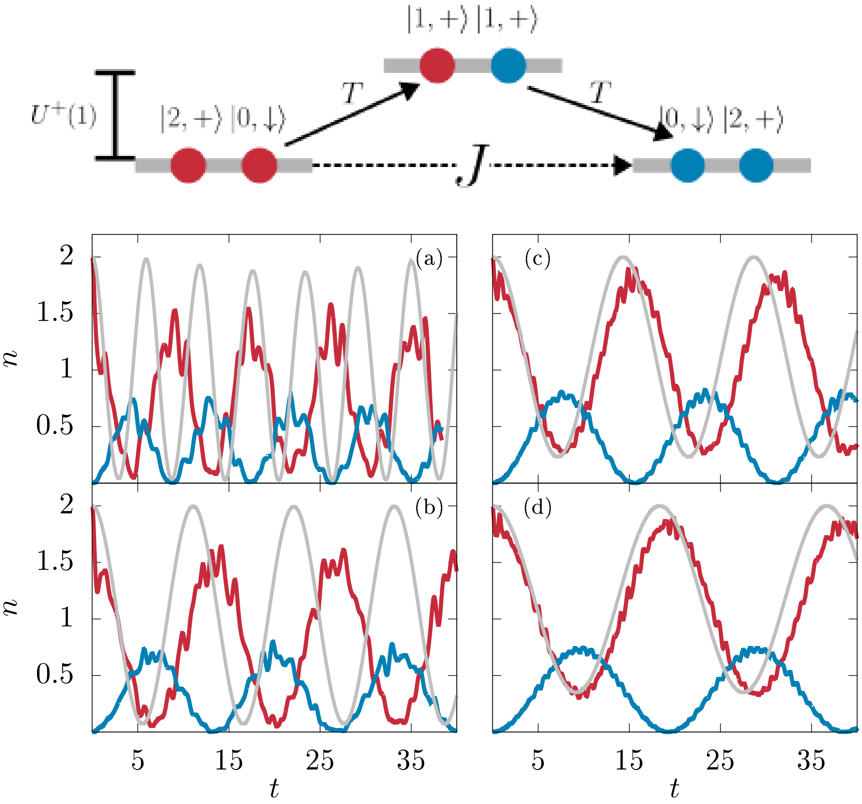

Figure 6.10: Top: Schematic depiction of the second-order hopping that leads to bi-polariton dynamics. The two excitations initially located at one ion (red) separate with the single vibron hopping amplitude T and subsequently reunite at another ion (blue). The intermediate state is detuned by $U(1)$. **Bottom:** Bi-polariton dynamics in the central (red) and neighboring (blue) ions of a equidistant chain of 5 ions. A bi-polariton in the state $|2,-\rangle$ ((a) and (c)) or $|2,+\rangle$ ((b) and (d)) has been initialized at ion 3. In (a) and (b) $g/T = 10$ and in (c) and (d) $g/T = 20$, the quantities are defined as in Fig. 6.9. The laser detuning δ has been set to the average value of $\tilde{\omega}_{ix}$. In grey we show the result from the effective bi-polariton model defined in Eq. (6.36).

a distance of r ions. The states in the gaps exhibit almost maximal probability for $r = 0$ while the scattering states of the bands have a vanishing overlap with the bi-polariton states. The bound pair states do not delocalize as seen from the inset in Fig. 6.9 (right), but are approximately given by the symmetric and antisymmetric superposition of the states $|2_i, \pm\rangle$ and $|2_{N-i}, \pm\rangle$. Since the vibron frequencies are symmetric these two states are degenerate (assuming equal laser intensities) and coupled via a second-order hopping amplitude.

This process describes the subsequent hopping of the two polaritons of the bound pair via an intermediate, off-resonant scattering state, schematically depicted in Fig. 6.10 (top). In order to derive an effective hopping rate for this process we employ a van-Vleck transformation [485, 486]. We divide the $\mathcal{N} = 2$ Hilbert subspace into bi-polariton states $|2_i, \pm\rangle$, and the set $\mathcal{B}$ containing all states with separated polaritons. We diagonalize the JCH Hamiltonian projected to the $\mathcal{B}$ set which results in good approximation in the bands depicted in Fig. 6.9. The effective bi-polariton hopping rate is then given in first order by

$$J_{ij}^{\pm} = \frac{1}{2} \sum_{k \in \mathcal{B}} c_{ik}^{\pm} c_{jk}^{\pm} \left(\frac{1}{E_i^{\pm}(2) - \epsilon_k^{\mathcal{B}}} + \frac{1}{E_j^{\pm}(2) - \epsilon_k^{\mathcal{B}}} \right) . \tag{6.35}$$

where $\epsilon_k^{\mathcal{B}}$ is the k-th eigenenergy in the subset of the scattering states and $c_{ik}^{\pm}$ is the hopping coupling between the respective eigenstate and the bi-polariton state $|2_i, \pm\rangle$ due to vibron hopping. This quantity scales like $T_{ij}^2/U^{\pm}(1)$, i.e. it vanishes for a infinitely strong on-site interaction. This is a remnant of the intermediate scattering state that is energetically separated from the bi-polariton states by $U^{\pm}(1)$. In an intermediate regime of $U^{\pm}(1)/T_{ij}$ the bound states coexist with a finite $J_{ij}^{\pm}$ that is however much reduced in its amplitude in comparison to the single polariton hopping. Then, the dynamics of the bound pairs can be approximated by an effective Bose-Hubbard model given by

$$H_{JCH}^{BP} = \sum_{i, r=\pm} E_i^r(2) B_{ir}^{\dagger} B_{ir} + \frac{1}{2} \sum_{i, j \neq i, r} J_{ij}^r \left(B_{ir}^{\dagger} B_{jr} + B_{ir} B_{jr}^{\dagger} \right) \tag{6.36}$$

where $B_{i\pm}^{\dagger}$ creates a bi-polariton at ion i.

As in the single-polariton hopping case, the bound-pair hopping is countered by the energy differences of the local bi-polariton states which lead to the localization of the bound pair eigenstates depicted in Fig. 6.9 (right). Only the resonant hopping between the ions with the same vibron frequency is non-negligible, however due to the larger distance between the coupled ions the effective hopping rate is further reduced. Hence, we can expect bi-polariton hopping only between the two ions connected by the $\mathbb{Z}_2^z$ symmetry of the linear chain on a slow timescale given by $J_{i,N-i}^{\pm}$. In the energy spectrum depicted in Fig. 6.9 (left) the resulting splitting of the respective symmetric and antisymmetric superposition states is not resolvable, indicating the slow hopping dynamics.

The polariton localization can be mitigated in principle by various strategies. The simplest one is to increase the radial trap frequency so that the ion dependent corrections of the vibron frequency coming from the Coulomb repulsion of the other ions becomes less relevant, in this limit $\tilde{\omega}_{ix} \to 0, \ \forall i$. While this approach also facilitates the cooling stage, it ultimately faces technical limitations. Alternatively, the number of ions in the chain can be increased resulting in a (locally) homogeneous chain in the trap center, since the boundary effects are less relevant, but also in a more complex ground-state cooling stage due to the larger number of motional modes. More involved ways to cancel the spatial variation of $\tilde{\omega}_{ix}$ include the creation of higher-order trap potentials to reach a more equispaced crystal, or the employment of optical dipole traps to engineer the local confinement of the individual ions [133, 174, 207, 487]. All approaches mentioned so far target the bare vibron frequencies, however for the polariton dynamics their energies $E_i^{\pm}(n)$ are crucial. Since they also depend on the dressing laser intensity they can be in principle tuned at will if the ions are addressed independently by fields with spatially inhomogeneous intensity or frequency.

Finally, in Fig. 6.10 (bottom) we show the dynamics of a bound pair assuming equidistant ions, for which we can observe hopping in the systems center. The vibron frequencies of the outer ions are detuned because of the finite size of the chain and therefore do not participate in the dynamics. We compare the result from the calculation of the full JCH Hamiltonian with the effective theory (6.36) and observe good agreement for large values of g_i. However, increasing $U^{\pm}(1)/T_{ij}$ leads to more robust bound pairs but also to a slowdown of the hopping dynamics, as discussed before.

6.3 Conclusion

We have illustrated in this chapter two ways to manipulate the dynamics of vibrational quantum excitations in trapped ion crystals by ways of external drives to engineer spin-orbit coupling and vibron interactions.

The former may be achieved by employing the capabilities for engineering the vibron shapes available in two-dimensional surface traps, or by means of optical trapping methods. We have shown that the two perpendicular local vibron modes can be understood as a spin degree of freedom, which couples with the vibron motion. During hopping processes the spin state is not left invariant as it can flip due to the generally non-diagonal hopping matrices. We showed that these off-resonant processes may be controlled by means of a parametric drive of the vibron frequencies. We derived an effective Hubbard model and demonstrated the dependence of the spin state of the vibron on the chirality of the trajectory in a simple ion plaquette. We showed as well that, conversely, the vibron motion is affected by the initial spin state. This system could be extended to larger ion lattices where the expansion dynamics of a single excitation exhibits spin state separation, but is also more complex due to inevitable long distance hops.

The parametric drive offers great flexibility which could be of use for the study of other crystal geometries or the creation of disordered systems, for which the simultaneous presence of spin-orbit coupling could be an interesting extension of the physics discussed here [358, 488, 489]. Moreover, the model derived here features non-interacting particles which is why we focused on the single-particle regime. A non-linear extension leads to an interaction energy that enriches the physics of spin-orbit-coupled particles.

One possible way to engineer interacting vibrons has been highlighted by the introduction of a dressing of the motional states with an electronic level scheme, resulting in polariton states [69, 179, 446, 447]. Their superfluid-to-Mott insulator transition has been discussed, and the presence of bound polariton states in the strong interaction regime has been worked out. Their dynamics is considerably slowed down and requires additional effort to create homogeneous polariton energies to speed up the hopping. As in the case for the parametric drive of the vibron frequencies, the dressing laser offers in principle the possibility to create arbitrary potential landscapes for the polaritons. While the energies of the polariton states are determined by the laser intensity and detuning, which can be in principle adjusted individually by single-ion techniques, the direction together with the crystal geometry plays an important role as well. Two-dimensional ion crystals exhibit position-dependent vibron orientations, and therefore couple in different ways by the laser dressing resulting in different dressed states.

Moreover, in the derivation of H_{JCH} it is assumed that the hopping dynamics is faster than the decay of the excited electronic state, so that its natural lifetime can be neglected. If this assumption is invalid, an spontaneous decay via a carrier transition creates or destroys polaritonic excitations, depending on whether the dressing laser drives the blue or red side-band. This incoherent process consequently breaks the conservation of $\mathcal{N}$. While the inclusion of a spontaneous decay rate alone leads to a trivial steady state ($\langle\mathcal{N}\rangle \rightarrow 0/\infty$), i.e. cooling or heating, the introduction of a coherent process that counters the decay results in a driven-dissipative version of the JCH model. The study of open Hubbard models has demonstrated a non-trivial steady state phase diagram [490–497]. The simulation of the interplay between particle creation and loss in the JCH model has the advantage that the polaritons are not physical particles unlike the bosonic atoms in optical lattices that are a standard platform for Hubbard models in AMO physics. In those systems, the potential loss of particles can only be countered by the trapping of additional atoms during the systems time evolution.

Chapter 7

Summary and Outlook

We have reported in this Thesis on our theoretical findings on the vibrational dynamics of trapped-ion crystals. We have particularly focused on two-dimensional zigzag crystals with and without topological defects, showing that the dynamics crucially depends on the crystal geometry. Apart from the external control of the shape of the self-assembled crystals in global rf traps, exhibiting multiple structural phase transition, the dynamics can be engineered with great flexibility by external drivings, coming from additional lasers or electric fields [36, 37, 40, 205, 208, 209, 217, 219, 222, 226, 227, 410, 411, 419, 469, 498, 499].

We have divided the results of this Thesis into three major parts treating coherent and incoherent transport of energy, the change of the motional excitations close to phase transitions caused by thermal and quantum fluctuations, and lastly the emulation of peculiar vibron-Hubbard models.

In the first part, discussed in Chapter 4, we have observed a strong reduction in transmission and conductivity in an ion crystal with a topological defect when the Aubry transition is crossed. This has found expression in a robust energy imbalance between the two crystal halves on a long timescale when a local displacement is introduced on one side of the defect. For the driving of a heat current through the crystal, we have seen the decline in steady state heat flux together with the rise of a strong and localized temperature gradient. In the low energy limit, these findings could be traced back to the breaking of mirror symmetry of the crystal at the Aubry transition, which leads to localized phonon modes. The spectrum of the latter plays a crucial role for the non-linear effects for larger energies. Third-order resonances lead to the reestablishment of energy transport through parametric mode couplings. In what concerns the heat flux, the density of degeneracies in the spectrum leads to sharp peaks for small values of the reservoir coupling, which are washed out in a typical intermediate range of the damping rate γ.

In the second part, presented in Chapter 5, we have explored the regime close to structural phase transitions, which is particularly sensitive to the non-linear dynamics introduced by the Coulomb potential and triggered by fluctuations. Independent of the source of the fluctuations, we observed a regime in the symmetry-broken phase in which the system effectively behaves like in the symmetric phase. This can be interpreted as a fluctuation-induced shift of the transition point [212–214, 422]. When we considered the thermal zigzag transition, we observed smooth motional mode frequencies, and the absence of a soft mode when the critical trap aspect ratio is crossed. The experimental measurements where supported by numerical simulations. We have found that this effect is due to thermal jumps between the two symmetry-broken configurations over the energy barrier in a free energy potential. In the parameter window in which these jumps occur, we assumed in a time-scale separation Ansatz that the system Z_2^x stays effectively unbroken, and derived an effective theory that includes the non-linear corrections to the motional mode frequencies, obtaining good agreement with simulations. As for the quantum fluctuations of a crystal with defect, we found that in an ultra cold regime quantum tunneling events through the PN barrier occur. An effective theory based on a collective excitation formalism reduces the problem drastically to a single particle formulation [299, 301].

Finally, in the third part of the Thesis, discussed in Chapter 6, we discussed a scheme to engineer non-Abelian dynamics in an homogeneous two-dimensional ion crystal. Our approach relied on external control of the local vibrational degrees of freedom, which may be realized by means of individual laser addressing of the ions. We propose to make use of their flexibility to implement a Floquet driving scheme that results in effective, non-commuting hopping matrices that act on the pseudo spin of vibrons during their motion. We demonstrated a form of spin-orbit coupling in these systems by revealing the relation between the spin-state and the center of mass dynamics of the vibrons. While this system is non-interacting we discussed as well one possible scheme to create an interaction energy potential by coupling the motional Fock state to an electronic two level system. This emulates the JCH model and exhibits a superfluid-to-Mott insulator transition [419, 446, 447, 456]. We have studied bound pair states in the strong coupling limit and demonstrated the restricted hopping of these modes in the inhomogeneous potential landscape of a small ion chain.

The work presented here could be expanded in several directions. Concerning the energy transport in ion crystals with topological defects open questions remain concerning the scaling of the heat flux and the temperature profiles with increasing particle number. The recovery of a finite heat conductivity in the thermodynamic limit, and possible qualitative changes in the steady state when an extended zigzag region with translational invariance is considered, are potentially interesting. Also, the observation of energy localization rest upon the small radial diameter of the structure. In a truly two-dimensional triangular ion lattice energy could flow around the defect [222]. Lastly, it may be certainly interesting to address the consequences of our results on the sympathetic cooling of ion crystals with defects [412, 500, 501].

Concerning the second part, a comprehensive analysis of the quantum many-body dynamics close to the Aubry transition is still missing. Including the effect of the dressing modes and their non-linear coupling to the kink dynamics in a collective excitation formalism is the correct approach to characterize the tunneling dynamics. A comparison to the simplified effective model discussed here could benchmark its validity. In addition, possible strategies to boost the signal strength of quantum effects at the Aubry transition in ion crystals remain a major challenge.

For the last part, the flexibility of the applied external control of the local vibron modes could be exploited to engineer disorder in the hopping matrices [358]. In addition, we concentrated our effort on a simple square lattice, other geometries like triangular or honeycomb lattices could be of interest due to the different coordination number [219, 502, 503]. Moreover, the creation of vibron interactions by the introduction of non-linear potentials constitutes an interesting extension of the discussed spin-orbit coupled vibron system. Lastly, the study of driven-dissipative JCH models in trapped ion systems is a direction of research widely unexplored but interesting for their steady-state phase diagram [492].

Acknowledgements

All the work reported in this Thesis and my personal growth on the way to it would not have been possible without the help of many people.

I thank my supervisor and long-time office neighbor Prof. Dr. Luis Santos for his guidance and supervision. He was always open for discussions, his remarkable expertise of the field was source for countless good advice and his sharp questions helped improving our work. I also thank my supervisor Prof. Dr. Hendrik Weimer for our discussions and his advice. It was always inspiring and fruitful to hear the opinion from across the hallway and broadened my perspective. Last but not least in the triumvirate, I thank Prof. Dr. Tanja E. Mehlstäubler for her guidance, enduring our theory verbiage and converting it into the real world. She caused my interest in ion Coulomb crystals in a seminar during my Bachelor studies and taught me a lot about scientific research as well as the fascinating field of ion crystals. The exchange with all of you was very professional and prolific in times of work but also refreshing and interesting when away from the desk. I don't take it for granted, especially in times of a global pandemic.

In addition, I want to thank Dr. Jan Kiethe, Luca A. Rüffert from PTB for the nice collaboration we shared in some of the work, and thank Prof. Dr. Giovanna Morigi in particular for agreeing to be a referee for my PhD. I also thank apl. Prof. Dr. Carsten Klempt for chairing my PhD defense.

”All work and no play makes Lars a dull boy” and therefore I thank all the people making the ITP to the madhouse that it is. I thank Russell, Lorenzo, Henning, Wei-Han, Tim, the legendary Amit, Javad, Mouine, Meghana and Florian for making the days in the Appelstraße (and elsewhere) so enjoyable, a big ”Forza Bieroslav Dose” goes to Vincent for coaching me. In particular, I thank Arya and Luis for the time together in the office 248, the bond between office mates is something special for me. I thank the Daniel dynasty of computer admins for their help with my mostly self-inflicted issues. Last but not least, I thank the newer members of ITP Sabhyata, Albert, Gustavo and Eugenia.

I would not have been as motivated and fascinated by physics if it was not for some old friends from my Bachelor studies in Braunschweig. I thank the twin towers Christopher and Gerwin, ”Pineapple” Martin, ”Tapeziermeister” Michel and "Kobold" Alexander for countless invaluable memories. I thank Marco for an incredible 10 years of friendship.

Finally, I am forever indebted to my (soon to be) family. I thank my parents Bettina and Hermann for their unconditional support and love even if they only understand a fraction of what their son is doing in his studies. Most importantly, I am incredibly grateful for my fiancee Rebecca, you are the sunshine in my life and my tower of strength.

Bibliography

[1] J. Bardeen, L. N. Cooper, and J. R. Schrieffer, Phys. Rev. **108**, 1175 (1957).

[2] R. Combescot, *Superconductivity: An Introduction*, 1st ed. (Cambridge University Press, 2022).

[3] D. Vollhardt and P. Wölfle, *The Superfluid Phases of Helium 3*, dover edition ed. (Dover Publications, Inc, Mineola, New York, 2013).

[4] B. Douçot, B. Duplantier, V. Pasquier, and V. Rivasseau, eds., *The Quantum Hall Effect: Poincaré Seminar 2004*, Progress in Mathematical Physics No. 45 (Birkäuser, Basel Berlin, 2005).

[5] R. E. Prange, S. M. Girvin, J. L. Birman, H. Faissner, and J. W. Lynn, eds., *The Quantum Hall Effect*, Graduate Texts in Contemporary Physics (Springer New York, New York, NY, 1990).

[6] R. P. Feynman, Int J Theor Phys **21**, 467 (1982).

[7] J. Benhelm, G. Kirchmair, C. F. Roos, and R. Blatt, Nature Phys **4**, 463 (2008).

[8] J. A. Bergou, M. Hillery, and M. Saffman, *Quantum Information Processing: Theory and Implementation*, Graduate Texts in Physics (Springer International Publishing, Cham, 2021).

[9] U. Bissbort, D. Cocks, A. Negretti, Z. Idziaszek, T. Calarco, F. Schmidt-Kaler, W. Hofstetter, and R. Gerritsma, Phys. Rev. Lett. **111**, 080501 (2013).

[10] R. Blatt and C. F. Roos, Nature Phys **8**, 277 (2012).

[11] B. B. Blinov, D. Leibfried, C. Monroe, and D. J. Wineland, Quantum Information Processing **3**, 45 (2004).

[12] I. Bloch, Nature Phys **1**, 23 (2005).

[13] I. Bloch, J. Dalibard, and W. Zwerger, Rev. Mod. Phys. **80**, 885 (2008).

[14] I. Bloch, J. Dalibard, and S. Nascimbène, Nature Phys **8**, 267 (2012).

[15] A. Browaeys and T. Lahaye, Nat. Phys. **16**, 132 (2020).

[16] C. D. Bruzewicz, J. Chiaverini, R. McConnell, and J. M. Sage, Applied Physics Reviews **6**, 021314 (2019).

[17] J. I. Cirac and P. Zoller, Phys. Rev. Lett. **74**, 4091 (1995).

[18] F. Dalfovo, S. Giorgini, L. P. Pitaevskii, and S. Stringari, Rev. Mod. Phys. **71**, 463 (1999).

[19] H. Haffner, C. Roos, and R. Blatt, Physics Reports **469**, 155 (2008).

[20] D. Jaksch, C. Bruder, J. I. Cirac, C. W. Gardiner, and P. Zoller, Phys. Rev. Lett. **81**, 3108 (1998).

[21] D. James, Applied Physics B: Lasers and Optics **66**, 181 (1998).

[22] D. Leibfried, B. DeMarco, V. Meyer, D. Lucas, M. Barrett, J. Britton, W. M. Itano, B. Jelenković, C. Langer, T. Rosenband, and D. J. Wineland, Nature **422**, 412 (2003).

[23] M. Lewenstein, A. Sanpera, V. Ahufinger, B. Damski, A. Sen(De), and U. Sen, Advances in Physics **56**, 243 (2007).

[24] K. Mølmer and A. Sørensen, Phys. Rev. Lett. **82**, 1835 (1999).

[25] M. A. Nielsen and I. L. Chuang, *Quantum Computation and Quantum Information* (Cambridge University Press, 2010).

[26] C. Noh and D. G. Angelakis, Rep. Prog. Phys. **80**, 016401 (2017).

[27] D. Porras and J. I. Cirac, Phys. Rev. Lett. **92**, 207901 (2004).

[28] T. Schaetz, A. Friedenauer, H. Schmitz, L. Petersen, and S. Kahra, Journal of Modern Optics **54**, 2317 (2007).

[29] T. Schaetz, C. R. Monroe, and T. Esslinger, New J. Phys. **15**, 085009 (2013).

[30] C. Schneider, D. Porras, and T. Schaetz, Rep. Prog. Phys. **75**, 024401 (2012).

[31] J. Q. You and F. Nori, Physics Today **58**, 42 (2005).

[32] S. Korenblit, D. Kafri, W. C. Campbell, R. Islam, E. E. Edwards, Z.-X. Gong, G.-D. Lin, L.-M. Duan, J. Kim, K. Kim, and C. Monroe, New J. Phys. **14**, 095024 (2012).

[33] F. H. L. Essler, H. Frahm, F. Göhmann, A. Klümper, and V. E. Korepin, *The One-Dimensional Hubbard Model*, 1st ed. (Cambridge University Press, 2005).

[34] D. H. E. Dubin, Phys. Rev. Lett. **71**, 2753 (1993).

[35] J. P. Schiffer, Phys. Rev. Lett. **70**, 818 (1993).

[36] S. Fishman, G. De Chiara, T. Calarco, and G. Morigi, Phys. Rev. B **77**, 064111 (2008).

[37] A. Mortensen, E. Nielsen, T. Matthey, and M. Drewsen, Phys. Rev. Lett. **96**, 103001 (2006).

[38] M. Drewsen, Physica B: Condensed Matter **460**, 105 (2015).

[39] R. C. Thompson, Contemporary Physics **56**, 63 (2015).

[40] R. Nigmatullin, A. del Campo, G. De Chiara, G. Morigi, M. B. Plenio, and A. Retzker, Phys. Rev. B **93**, 014106 (2016).

[41] A. Benassi, A. Vanossi, and E. Tosatti, Nat Commun **2**, 236 (2011).

[42] A. Bylinskii, D. Gangloff, and V. Vuleti, Science **348**, 1115 (2015).

[43] A. Bylinskii, D. Gangloff, I. Counts, and V. Vuletić, Nature Mater **15**, 717 (2016).

[44] T. Fogarty, C. Cormick, H. Landa, V. M. Stojanović, E. Demler, and G. Morigi, Phys. Rev. Lett. **115**, 233602 (2015).

[45] I. García-Mata, O. V. Zhirov, and D. L. Shepelyansky, Eur. Phys. J. D **41**, 325 (2007).

[46] J. Kiethe, R. Nigmatullin, D. Kalincev, T. Schmirander, and T. E. Mehlstäubler, Nat Commun **8**, 15364 (2017).

[47] D. Mandelli, A. Vanossi, and E. Tosatti, Phys. Rev. B **87**, 195418 (2013).

[48] T. Pruttivarasin, M. Ramm, I. Talukdar, A. Kreuter, and H. Häffner, New J. Phys. **13**, 075012 (2011).

[49] J. Eschner, G. Morigi, F. Schmidt-Kaler, and R. Blatt, J. Opt. Soc. Am. B **20**, 1003 (2003).

[50] L. Feng, W. L. Tan, A. De, A. Menon, A. Chu, G. Pagano, and C. Monroe, Phys. Rev. Lett. **125**, 053001 (2020).

[51] M. K. Joshi, A. Fabre, C. Maier, T. Brydges, D. Kiesenhofer, H. Hainzer, R. Blatt, and C. F. Roos, New J. Phys. **22**, 103013 (2020).

[52] A. P. Kulosa, O. N. Prudnikov, D. Vadlejch, H. A. Fürst, A. A. Kirpichnikova, A. V. Taichenachev, V. I. Yudin, and T. E. Mehlstäubler, New J. Phys. **25**, 053008 (2023).

[53] H. J. Metcalf and P. van der Straten, *Laser Cooling and Trapping*, edited by R. S. Berry, J. L. Birman, J. W. Lynn, M. P. Silverman, H. E. Stanley, and M. Voloshin, Graduate Texts in Contemporary Physics (Springer New York, New York, NY, 1999).

[54] F. G. Major, V. N. Gheorghe, and G. Werth, *Charged Particle Traps: Physics and Techniques of Charged Particle Field Confinement* (Springer, Berlin, 2005).

[55] M. Vogel, *Particle Confinement in Penning Traps*, Springer Series on Atomic, Optical, and Plasma Physics, Vol. 100 (Springer International Publishing, Cham, 2018).

[56] F. Schmidt-Kaler, J. Eschner, R. Blatt, D. Leibfried, C. Roos, and G. Morigi, in *Laser Physics at the Limits*, edited by H. Figger, C. Zimmermann, and D. Meschede (Springer Berlin Heidelberg, Berlin, Heidelberg, 2002) pp. 243–260.

[57] P. Meystre, *Quantum Optics: Taming the Quantum*, Graduate Texts in Physics (Springer International Publishing, Cham, 2021).

[58] A. Vanossi, N. Manini, M. Urbakh, S. Zapperi, and E. Tosatti, Rev. Mod. Phys. **85**, 529 (2013).

[59] C. M. Mate and R. W. Carpick, *Tribology on the Small Scale: A Modern Textbook on Friction, Lubrication, and Wear*, 2nd ed. (Oxford University PressOxford, 2019).

[60] O. M. Braun and Y. S. Kivshar, *The Frenkel-Kontorova Model* (Springer-Verlag, Berlin, Heidelberg, 2004).

[61] A. Dhar, Advances in Physics **57**, 457 (2008).

[62] S. Lepri, Physics Reports **377**, 1 (2003).

[63] M. Ramm, T. Pruttivarasin, and H. Häffner, New J. Phys. **16**, 063062 (2014).

[64] M. Tamura, T. Mukaiyama, and K. Toyoda, Phys. Rev. Lett. **124**, 200501 (2020).

[65] J. D. Baltrusch, C. Cormick, and G. Morigi, Phys. Rev. A **87**, 032116 (2013).

[66] S. Sachdev, *Quantum Phase Transitions*, 2nd ed. (Cambridge University Press, 2011).

[67] V. Galitski and I. B. Spielman, Nature **494**, 49 (2013).

[68] H. Zhai, Rep. Prog. Phys. **78**, 026001 (2015).

[69] P. A. Ivanov, S. S. Ivanov, N. V. Vitanov, A. Mering, M. Fleischhauer, and K. Singer, Phys. Rev. A **80**, 060301 (2009).

[70] W. Demtröder, *Atoms, Molecules and Photons: An Introduction to Atomic-, Molecular- and Quantum Physics*, Graduate Texts in Physics (Springer Berlin Heidelberg, Berlin, Heidelberg, 2018).

[71] H. G. Bennewitz and W. Paul, Z. Physik **139**, 489 (1954).

[72] H. G. Dehmelt, Phys. Rev. **105**, 1487 (1957).

[73] J. Pierce, Stud. Q. J. UK **21**, 92 (1950).

[74] R. F. Wuerker, H. M. Goldenberg, and R. V. Langmuir, Journal of Applied Physics **30**, 441 (1959).

[75] T. Hänsch and A. Schawlow, Optics Communications **13**, 68 (1975).

[76] D. J. Wineland and H. G. Dehmelt, Journal of Applied Physics **46**, 919 (1975).

[77] A. Ashkin, Phys. Rev. Lett. **40**, 729 (1978).

[78] D. J. Wineland, R. E. Drullinger, and F. L. Walls, Phys. Rev. Lett. **40**, 1639 (1978).

[79] W. Paul, Rev. Mod. Phys. **62**, 531 (1990).

[80] H. Dehmelt, Rev. Mod. Phys. **62**, 525 (1990).

[81] J. D. Jackson, *Classical Electrodynamics*, 3rd ed. (Wiley, New York, 1999).

[82] E. L. Raab, M. Prentiss, A. Cable, S. Chu, and D. E. Pritchard, Phys. Rev. Lett. **59**, 2631 (1987).

[83] S. Earnshaw, Trans. Camb. Phil. Soc. **7**, 97 (1842).

[84] F. M. Penning, Physica **3**, 873 (1936).

[85] H. G. Dehmelt, Phys. Rev. **109**, 381 (1958).

[86] D. Wineland, P. Ekstrom, and H. Dehmelt, Phys. Rev. Lett. **31**, 1279 (1973).

[87] H. Dehmelt, Phys. Scr. **T22**, 102 (1988).

[88] E. D. Courant, M. S. Livingston, and H. S. Snyder, Phys. Rev. **88**, 1190 (1952).

[89] W. Paul and H. Steinwedel, Zeitschrift für Naturforschung A **8**, 448 (1953).

[90] W. Paul and M. Raether, Z. Physik **140**, 262 (1955).

[91] W. Paul, O. Osberghaus, and E. Fischer, *Ein Ionenkäfig* (VS Verlag für Sozialwissenschaften, Wiesbaden, 1958).

[92] S. N. Lea, Rep. Prog. Phys. **70**, 1473 (2007).

[93] V. A. Dzuba, A. Derevianko, and V. V. Flambaum, Phys. Rev. A **86**, 054502 (2012).

[94] A. D. Ludlow, M. M. Boyd, J. Ye, E. Peik, and P. O. Schmidt, Rev. Mod. Phys. **87**, 637 (2015).

[95] T. E. Mehlstäubler, G. Grosche, C. Lisdat, P. O. Schmidt, and H. Denker, Rep. on Progress in Phys. **81**, 064401 (2018).

[96] V. Letokhov and V. Minogin, Physics Reports **73**, 1 (1981).

[97] D. J. Wineland, J. C. Bergquist, W. M. Itano, J. J. Bollinger, and C. H. Manney, Phys. Rev. Lett. **59**, 2935 (1987).

[98] R. Blümel, C. Kappler, W. Quint, and H. Walther, Phys. Rev. A **40**, 808 (1989).

[99] W. Nagourney, J. Sandberg, and H. Dehmelt, Phys. Rev. Lett. **56**, 2797 (1986).

[100] F. Diedrich, J. C. Bergquist, W. M. Itano, and D. J. Wineland, Phys. Rev. Lett. **62**, 403 (1989).

[101] L. S. Brown, Phys. Rev. Lett. **66**, 527 (1991).

[102] J. I. Cirac, R. Blatt, P. Zoller, and W. D. Phillips, Phys. Rev. A **46**, 2668 (1992).

[103] J. I. Cirac, R. Blatt, A. S. Parkins, and P. Zoller, Phys. Rev. Lett. **70**, 762 (1993).

[104] D. M. Meekhof, C. Monroe, B. E. King, W. M. Itano, and D. J. Wineland, Phys. Rev. Lett. **76**, 4 (1996).

[105] C. Monroe, D. M. Meekhof, B. E. King, and D. J. Wineland, Science **272**, 1131 (1996).

[106] A. Steane, Appl. Phys. B **64**, 623 (1997).

[107] Ch. Roos, Th. Zeiger, H. Rohde, H. C. Nägerl, J. Eschner, D. Leibfried, F. Schmidt-Kaler, and R. Blatt, Phys. Rev. Lett. **83**, 4713 (1999).

[108] T. Calarco, J. I. Cirac, and P. Zoller, Phys. Rev. A **63**, 062304 (2001).

[109] L.-M. Duan, J. I. Cirac, and P. Zoller, Science **292**, 1695 (2001).

[110] D. Porras and J. I. Cirac, Phys. Rev. Lett. **93**, 263602 (2004).

[111] C. F. Roos, T. Monz, K. Kim, M. Riebe, H. Häffner, D. F. V. James, and R. Blatt, Phys. Rev. A **77**, 040302 (2008).

[112] K. Kim, M.-S. Chang, R. Islam, S. Korenblit, L.-M. Duan, and C. Monroe, Phys. Rev. Lett. **103**, 120502 (2009).

[113] X. R. Nie, C. F. Roos, and D. F. James, Physics Letters A **373**, 422 (2009).

[114] K. Kim, M.-S. Chang, S. Korenblit, R. Islam, E. E. Edwards, J. K. Freericks, G.-D. Lin, L.-M. Duan, and C. Monroe, Nature **465**, 590 (2010).

[115] K.-A. B. Soderberg and C. Monroe, Rep. Prog. Phys. **73**, 036401 (2010).

[116] M. Harlander, R. Lechner, M. Brownnutt, R. Blatt, and W. Hänsel, Nature **471**, 200 (2011).

[117] K. A. Gilmore, J. G. Bohnet, B. C. Sawyer, J. W. Britton, and J. J. Bollinger, Phys. Rev. Lett. **118**, 263602 (2017).

[118] K. Arnold, E. Hajiyev, E. Paez, C. H. Lee, M. D. Barrett, and J. Bollinger, Phys. Rev. A **92**, 032108 (2015).

[119] H. Denker, L. Timmen, C. Voigt, S. Weyers, E. Peik, H. S. Margolis, P. Delva, P. Wolf, and G. Petit, J Geod **92**, 487 (2018).

[120] F. Riehle, *Frequency Standards: Basics and Applications*, 1st ed. (Wiley, 2003).

[121] C. Audoin and B. Guinot, *The Measurement of Time: Time, Frequency and the Atomic Clock* (Cambridge University Press, Cambridge ; New York, 2001).

[122] P. Delva and J. Lodewyck, Acta Futura , 67 (2013).

[123] H. S. Margolis, Contemporary Physics **51**, 37 (2010).

[124] G. Floquet, Ann. Sci. École Norm. Sup. **12**, 47 (1883).

[125] N. W. McLachlan, *Theory and Applications of Mathieu Fucntions* (Oxford: Clarendon, 1947).

[126] J. H. Shirley, Phys. Rev. **138**, B979 (1965).

[127] J. A. Richards, "The Mathieu Equation," in *Analysis of Periodically Time-Varying Systems* (Springer Berlin Heidelberg, Berlin, Heidelberg, 1983) pp. 93–107.

[128] H. Landa, M. Drewsen, B. Reznik, and A. Retzker, J. Phys. A: Math. Theor. **45**, 455305 (2012).

[129] D. Leibfried, R. Blatt, C. Monroe, and D. Wineland, Rev. Mod. Phys. **75**, 281 (2003).

[130] L. H. Nguyên, A. Kalev, M. D. Barrett, and B.-G. Englert, Phys. Rev. A **85**, 052718 (2012).

[131] M. G. Raizen, J. M. Gilligan, J. C. Bergquist, W. M. Itano, and D. J. Wineland, Phys. Rev. A **45**, 6493 (1992).

[132] D. H. E. Dubin and T. M. O'Neil, Rev. Mod. Phys. **71**, 87 (1999).

[133] G.-D. Lin, S.-L. Zhu, R. Islam, K. Kim, M.-S. Chang, S. Korenblit, C. Monroe, and L.-M. Duan, Europhys. Lett. **86**, 60004 (2009).

[134] J. Chiaverini, R. B. Blakestad, J. Britton, J. D. Jost, C. Langer, D. Leibfried, R. Ozeri, and D. J. Wineland, Quantum Info. Comput. **5**, 419 (2005).

[135] W. K. Hensinger, S. Olmschenk, D. Stick, D. Hucul, M. Yeo, M. Acton, L. Deslauriers, C. Monroe, and J. Rabchuk, Appl. Phys. Lett. **88**, 034101 (2006).

[136] C. E. Pearson, D. R. Leibrandt, W. S. Bakr, W. J. Mallard, K. R. Brown, and I. L. Chuang, Phys. Rev. A **73**, 032307 (2006).

[137] R. Schmied, J. H. Wesenberg, and D. Leibfried, Phys. Rev. Lett. **102**, 233002 (2009).

[138] J. M. Amini, H. Uys, J. H. Wesenberg, S. Seidelin, J. Britton, J. J. Bollinger, D. Leibfried, C. Ospelkaus, A. P. VanDevender, and D. J. Wineland, New J. Phys. **12**, 033031 (2010).

[139] R. D. Graham, S.-P. Chen, T. Sakrejda, J. Wright, Z. Zhou, and B. B. Blinov, AIP Advances **4**, 057124 (2014).

[140] P. C. Holz, S. Auchter, G. Stocker, M. Valentini, K. Lakhmanskiy, C. Rössler, P. Stampfer, S. Sgouridis, E. Aschauer, Y. Colombe, and R. Blatt, Adv Quantum Tech **3**, 2000031 (2020).

[141] V. Kaushal, B. Lekitsch, A. Stahl, J. Hilder, D. Pijn, C. Schmiegelow, A. Bermudez, M. Müller, F. Schmidt-Kaler, and U. Poschinger, AVS Quantum Sci. **2**, 014101 (2020).

[142] R. B. Blakestad, C. Ospelkaus, A. P. VanDevender, J. M. Amini, J. Britton, D. Leibfried, and D. J. Wineland, Phys. Rev. Lett. **102**, 153002 (2009).

[143] R. C. Sterling, H. Rattanasonti, S. Weidt, K. Lake, P. Srinivasan, S. C. Webster, M. Kraft, and W. K. Hensinger, Nat Commun **5**, 3637 (2014).

[144] D.-I. D. Cho, S. Hong, M. Lee, and T. Kim, Micro and Nano Syst Lett **3**, 2 (2015).

[145] Y. Wan, R. Jördens, S. D. Erickson, J. J. Wu, R. Bowler, T. R. Tan, P.-Y. Hou, D. J. Wineland, A. C. Wilson, and D. Leibfried, Adv Quantum Tech **3**, 2000028 (2020).

[146] R. Zimmermann, M. Seidling, and P. Hommelhoff, Nat Commun **12**, 390 (2021).

[147] M. Lee, J. Jeong, Y. Park, C. Jung, T. Kim, and D.-i. Cho, Jpn. J. Appl. Phys. **60**, 027004 (2021).

[148] S. Auchter, C. Axline, C. Decaroli, M. Valentini, L. Purwin, R. Oswald, R. Matt, E. Aschauer, Y. Colombe, P. Holz, T. Monz, R. Blatt, P. Schindler, C. Rössler, and J. Home, Quantum Sci. Technol. **7**, 035015 (2022).

[149] R. Schmied, New J. Phys. **12**, 023038 (2010).

[150] N. Daniilidis, S. Gerber, G. Bolloten, M. Ramm, A. Ransford, E. Ulin-Avila, I. Talukdar, and H. Häffner, Phys. Rev. B **89**, 245435 (2014).

[151] M. Brownnutt, M. Kumph, P. Rabl, and R. Blatt, Rev. Mod. Phys. **87**, 1419 (2015).

[152] B. Ou, J. Zhang, X. Zhang, Y. Xie, T. Chen, C. Wu, W. Wu, and P. Chen, Sci. China Phys. Mech. Astron. **59**, 123011 (2016).

[153] J. Labaziewicz, Y. Ge, P. Antohi, D. Leibrandt, K. R. Brown, and I. L. Chuang, Phys. Rev. Lett. **100**, 013001 (2008).

[154] P. C. Holz, K. Lakhmanskiy, D. Rathje, P. Schindler, Y. Colombe, and R. Blatt, Phys. Rev. B **104**, 064513 (2021).

[155] M. Ghadimi, A. Zappacosta, J. Scarabel, K. Shimizu, E. W. Streed, and M. Lobino, Sci Rep **12**, 7067 (2022).

[156] D. Kiesenhofer, H. Hainzer, A. Zhdanov, P. C. Holz, M. Bock, T. Ollikainen, and C. F. Roos, PRX Quantum **4**, 020317 (2023).

[157] H. Hahn, G. Zarantonello, A. Bautista-Salvador, M. Wahnschaffe, M. Kohnen, J. Schoebel, P. O. Schmidt, and C. Ospelkaus, Appl. Phys. B **125**, 154 (2019).

[158] K. K. Mehta, C. Zhang, M. Malinowski, T.-L. Nguyen, M. Stadler, and J. P. Home, Nature **586**, 533 (2020).

[159] Z. D. Romaszko, S. Hong, M. Siegele, R. K. Puddy, F. R. Lebrun-Gallagher, S. Weidt, and W. K. Hensinger, Nat Rev Phys **2**, 285 (2020).

[160] S. L. Todaro, V. B. Verma, K. C. McCormick, D. T. C. Allcock, R. P. Mirin, D. J. Wineland, S. W. Nam, A. C. Wilson, D. Leibfried, and D. H. Slichter, Phys. Rev. Lett. **126**, 010501 (2021).

[161] M. Siegele-Brown, S. Hong, F. R. Lebrun-Gallagher, S. J. Hile, S. Weidt, and W. K. Hensinger, Quantum Sci. Technol. **7**, 034003 (2022).

[162] V. S. Letkhov and V. G. Minogin, Appl. Phys. **17**, 99 (1978).

[163] C. Cohen-Tannoudji, J. Dupont-Roc, and G. Grynberg, *Atom-Photon Interactions: Basic Processes and Applications* (Wiley, New York, 1992).

[164] C. Cormick, T. Schaetz, and G. Morigi, New J. Phys. **13**, 043019 (2011).

[165] L. Karpa, *Trapping Single Ions and Coulomb Crystals with Light Fields*, SpringerBriefs in Physics (Springer International Publishing, Cham, 2019).

[166] R. Grimm, M. Weidemüller, and Y. B. Ovchinnikov, in *Advances In Atomic, Molecular, and Optical Physics*, Vol. 42 (Elsevier, 2000) pp. 95–170.

[167] T. Sowiński, O. Dutta, P. Hauke, L. Tagliacozzo, and M. Lewenstein, Phys. Rev. Lett. **108**, 115301 (2012).

[168] M. Enderlein, T. Huber, C. Schneider, and T. Schaetz, Phys. Rev. Lett. **109**, 233004 (2012).

[169] L. Karpa, A. Bylinskii, D. Gangloff, M. Cetina, and V. Vuletić, Phys. Rev. Lett. **111**, 163002 (2013).

[170] A. Kawasaki, B. Braverman, E. Pedrozo-Peñafiel, C. Shu, S. Colombo, Z. Li, and V. Vuletić, Phys. Rev. A **102**, 013114 (2020).

[171] D. Barredo, S. de Léséleuc, V. Lienhard, T. Lahaye, and A. Browaeys, Science **354**, 1021 (2016).

[172] K.-N. Schymik, V. Lienhard, D. Barredo, P. Scholl, H. Williams, A. Browaeys, and T. Lahaye, Phys. Rev. A **102**, 063107 (2020).

[173] T. Huber, A. Lambrecht, J. Schmidt, L. Karpa, and T. Schaetz, Nat Commun **5**, 5587 (2014).

[174] T. Schaetz, J. Phys. B: At. Mol. Opt. Phys. **50**, 102001 (2017).

[175] J. Schmidt, A. Lambrecht, P. Weckesser, M. Debatin, L. Karpa, and T. Schaetz, Phys. Rev. X **8**, 021028 (2018).

[176] C. Schneider, M. Enderlein, T. Huber, S. Dürr, and T. Schaetz, Phys. Rev. A **85**, 013422 (2012).

[177] J. D. Arias Espinoza, M. Mazzanti, K. Fouka, R. X. Schüssler, Z. Wu, P. Corboz, R. Gerritsma, and A. Safavi-Naini, Phys. Rev. A **104**, 013302 (2021).

[178] P. K. Ghosh, *Ion Traps*, Oxford Science Publications No. 90 (Clarendon Press ; Oxford University Press, Oxford : New York, 1995).

[179] C. Gerry and P. Knight, *Introductory Quantum Optics*, 1st ed. (Cambridge University Press, 2004).

[180] M. B. Plenio and P. L. Knight, Rev. Mod. Phys. **70**, 101 (1998).

[181] W. Neuhauser, M. Hohenstatt, P. Toschek, and H. Dehmelt, Phys. Rev. Lett. **41**, 233 (1978).

[182] G. Morigi, Phys. Rev. A **67**, 033402 (2003).

[183] B. E. King, C. S. Wood, C. J. Myatt, Q. A. Turchette, D. Leibfried, W. M. Itano, C. Monroe, and D. J. Wineland, Phys. Rev. Lett. **81**, 1525 (1998).

[184] D. J. Wineland, W. M. Itano, J. C. Bergquist, and R. G. Hulet, Phys. Rev. A **36**, 2220 (1987).

[185] B. C. Sawyer, J. W. Britton, A. C. Keith, C.-C. J. Wang, J. K. Freericks, H. Uys, M. J. Biercuk, and J. J. Bollinger, Phys. Rev. Lett. **108**, 213003 (2012).

[186] A. Abdelrahman, O. Khosravani, M. Gessner, A. Buchleitner, H. P. Breuer, D. Gorman, R. Masuda, T. Pruttivarasin, M. Ramm, P. Schindler, and H. Häffner, Nat Commun **8**, 15712 (2017).

[187] R. Ohira, T. Mukaiyama, and K. Toyoda, Phys. Rev. A **100**, 060301 (2019).

[188] P. A. Ivanov, Optics Communications **436**, 101 (2019).

[189] I. Vybornyi, L. S. Dreissen, D. Kiesenhofer, H. Hainzer, M. Bock, T. Ollikainen, D. Vadlejch, C. F. Roos, T. E. Mehlstäubler, and K. Hammerer, (2023), arxiv:2306.07880 .

[190] A. J. Rasmusson, M. D'Onofrio, Y. Xie, J. Cui, and P. Richerme, Phys. Rev. A **104**, 043108 (2021).

[191] G. Stutter, P. Hrmo, V. Jarlaud, M. K. Joshi, J. F. Goodwin, and R. C. Thompson, Journal of Modern Optics **65**, 549 (2018).

[192] G. Morigi, J. Eschner, and C. H. Keitel, Phys. Rev. Lett. **85**, 4458 (2000).

[193] C. F. Roos, D. Leibfried, A. Mundt, F. Schmidt-Kaler, J. Eschner, and R. Blatt, Phys. Rev. Lett. **85**, 5547 (2000).

[194] M. Fleischhauer, A. Imamoglu, and J. P. Marangos, Rev. Mod. Phys. **77**, 633 (2005).

[195] R. Lechner, C. Maier, C. Hempel, P. Jurcevic, B. P. Lanyon, T. Monz, M. Brownnutt, R. Blatt, and C. F. Roos, Phys. Rev. A **93**, 053401 (2016).

[196] P. D. Lett, R. N. Watts, C. I. Westbrook, W. D. Phillips, P. L. Gould, and H. J. Metcalf, Phys. Rev. Lett. **61**, 169 (1988).

[197] J. Dalibard and C. Cohen-Tannoudji, J. Opt. Soc. Am. B **6**, 2023 (1989).

[198] J. I. Cirac, R. Blatt, A. S. Parkins, and P. Zoller, Phys. Rev. A **48**, 1434 (1993).

[199] S. M. Yoo and J. Javanainen, Phys. Rev. A **48**, R30 (1993).

[200] G. Birkl, J. A. Yeazell, R. Rückerl, and H. Walther, Europhys. Lett. **27**, 197 (1994).

[201] S. Ejtemaee and P. C. Haljan, Phys. Rev. Lett. **119**, 043001 (2017).

[202] F. Diedrich, E. Peik, J. M. Chen, W. Quint, and H. Walther, Phys. Rev. Lett. **59**, 2931 (1987).

[203] E. Shimshoni, G. Morigi, and S. Fishman, Phys. Rev. A **83**, 032308 (2011).

[204] E. Shimshoni, G. Morigi, and S. Fishman, Phys. Rev. Lett. **106**, 010401 (2011).

[205] V. Ursekar, J. M. Silvester, Y. S. Nam, and R. Blümel, Eur. Phys. J. D **72**, 165 (2018).

[206] M. D'Onofrio, Y. Xie, A. J. Rasmusson, E. Wolanski, J. Cui, and P. Richerme, Phys. Rev. Lett. **127**, 020503 (2021).

[207] M. Johanning, Appl. Phys. B **122**, 71 (2016).

[208] H.-K. Li, E. Urban, C. Noel, A. Chuang, Y. Xia, A. Ransford, B. Hemmerling, Y. Wang, T. Li, H. Häffner, and X. Zhang, Phys. Rev. Lett. **118**, 053001 (2017).

[209] F. Cartarius, C. Cormick, and G. Morigi, Phys. Rev. A **87**, 013425 (2013).

[210] C. Cormick and G. Morigi, Phys. Rev. Lett. **109**, 053003 (2012).

[211] P. Silvi, G. D. Chiara, T. Calarco, G. Morigi, and S. Montangero, Annalen der Physik **525**, 827 (2013).

[212] Z.-X. Gong, G.-D. Lin, and L.-M. Duan, Phys. Rev. Lett. **105**, 265703 (2010).

[213] J.-B. Delfau, C. Coste, and M. Saint Jean, Phys. Rev. E **87**, 062135 (2013).

[214] J. Li, L. L. Yan, L. Chen, Z. C. Liu, F. Zhou, J. Q. Zhang, W. L. Yang, and M. Feng, Phys. Rev. A **99**, 063402 (2019).

[215] J. Kiethe, L. Timm, H. Landa, D. Kalincev, G. Morigi, and T. E. Mehlstäubler, Phys. Rev. B **103**, 104106 (2021).

[216] L. D. Landau, in *Collected Papers of L.D. Landau* (Elsevier, 1965) pp. 193–216.

[217] H. Landa, B. Reznik, J. Brox, M. Mielenz, and T. Schaetz, New J. Phys. **15**, 093003 (2013).

[218] S. Flach, Phys. Rev. E **50**, 3134 (1994).

[219] C.-C. J. Wang, A. C. Keith, and J. K. Freericks, Phys. Rev. A **87**, 013422 (2013).

[220] D. Podolsky, E. Shimshoni, G. Morigi, and S. Fishman, Phys. Rev. X **6**, 031025 (2016).

[221] G. Birkl, S. Kassner, and H. Walther, Nature **357**, 310 (1992).

[222] M. Arnold and R. Nigmatullin, Phys. Rev. B **106**, 104106 (2022).

[223] P. G. Drazin and R. S. Johnson, *Solitons: An Introduction* (1989).

[224] T. Dauxois and M. Peyrard, *Physics of Solitons* (Cambridge University Press, Cambridge, UK ; New York, 2006).

[225] H. L. Partner, R. Nigmatullin, T. Burgermeister, K. Pyka, J. Keller, A. Retzker, M. B. Plenio, and T. E. Mehlstäubler, New J. of Phys. **15**, 103013 (2013).

[226] M. Mielenz, J. Brox, S. Kahra, G. Leschhorn, M. Albert, T. Schaetz, H. Landa, and B. Reznik, Phys. Rev. Lett. **110**, 133004 (2013).

[227] K. Pyka, J. Keller, H. L. Partner, R. Nigmatullin, T. Burgermeister, D. M. Meier, K. Kuhlmann, A. Retzker, M. B. Plenio, W. H. Zurek, A. del Campo, and T. E. Mehlstäubler, Nat Commun **4**, 2291 (2013).

[228] A. del Campo, G. De Chiara, G. Morigi, M. B. Plenio, and A. Retzker, Phys. Rev. Lett. **105**, 075701 (2010).

[229] J. Dziarmaga, Advances in Physics **59**, 1063 (2010).

[230] A. del Campo, T. W. B. Kibble, and W. H. Zurek, J. of Phys.: Cond. Matter **25**, 404210 (2013).

[231] S. Ejtemaee and P. C. Haljan, Phys. Rev. A **87**, 051401 (2013).

[232] S. Ulm, J. Roßnagel, G. Jacob, C. Degünther, S. T. Dawkins, U. G. Poschinger, R. Nigmatullin, A. Retzker, M. B. Plenio, F. Schmidt-Kaler, and K. Singer, Nat Commun **4**, 2290 (2013).

[233] J. Pedregosa-Gutierrez and M. Mukherjee, New J. Phys. **22**, 073044 (2020).

[234] T. Kibble, Physics Reports **67**, 183 (1980).

[235] W. H. Zurek, Nature **317**, 505 (1985).

[236] G. Morigi and S. Fishman, Phys. Rev. E **70**, 066141 (2004).

[237] G. Morigi and S. Fishman, Phys. Rev. Lett. **93**, 170602 (2004).

[238] C. Marquet, F. Schmidt-Kaler, and D. James, Applied Physics B: Lasers and Optics **76**, 199 (2003).

[239] A. Dhar and J. L. Lebowitz, Phys. Rev. Lett. **100**, 134301 (2008).

[240] E. A. Jackson, Rocky Mountain J. Math. **8** (1978).

[241] S. Lepri, R. Livi, and A. Politi, Phys. Rev. Lett. **78**, 1896 (1997).

[242] B. Hu and L. Yang, Chaos **15**, 015119 (2005).

[243] J. P. Home, D. Hanneke, J. D. Jost, D. Leibfried, and D. J. Wineland, New J. Phys. **13**, 073026 (2011).

[244] H. Landa, M. Drewsen, B. Reznik, and A. Retzker, New J. Phys. **14**, 093023 (2012).

[245] S. Y. Krylov and J. W. M. Frenken, Phys. Status Solidi B **251**, 711 (2014).

[246] F. P. Bowden and D. Tabor, *The Friction and Lubrication of Solids*, Oxford Classic Texts in the Physical Sciences (Clarendon Press ; Oxford University Press, Oxford : New York, 2001).

[247] G. Straffelini, *Friction and Wear: Methodologies for Design and Control*, Springer Tracts in Mechanical Engineering (Springer International Publishing, Cham, 2015).

[248] K. C. Ludema and L. Ajayi, *Friction, Wear, Lubrication: A Textbook in Tribology*, second edition ed. (Taylor & Francis, CRC Press, Boca Raton, 2019).

[249] G. Amontons, Memoires de l'academie royale des sciences , 206 (1699).

[250] C. A. Coulomb, Memoires de Mathematique et de Physique **10**, 161 (1821).

[251] B. N. T. Persson, in *Encyclopedia of Lubricants and Lubrication*, edited by T. Mang (Springer Berlin Heidelberg, Berlin, Heidelberg, 2014) pp. 791–797.

[252] L. Prandtl, Z. angew. Math. Mech. **8**, 85 (1928).

[253] U. Dehlinger, Ann. Phys. **394**, 749 (1929).

[254] T. Kontorova and Y. I. Frenkel, Zh. Eksp. and Teor. Fiz. **8**, 89 (1938).

[255] V. Popov and J. Gray, Z. angew. Math. Mech. **92**, 683 (2012).

[256] G. Tomlinson, The London, Edinburgh, and Dublin Philosophical Magazine and Journal of Science **7**, 905 (1929).

[257] V. L. Popov, "The Prandtl-Tomlinson Model for Dry Friction," in *Contact Mechanics and Friction* (Springer Berlin Heidelberg, Berlin, Heidelberg, 2017) pp. 173–192.

[258] C. M. Mate, G. M. McClelland, R. Erlandsson, and S. Chiang, Phys. Rev. Lett. **59**, 1942 (1987).

[259] D. Tománek, W. Zhong, and H. Thomas, Europhys. Lett. **15**, 887 (1991).

[260] S. Fujisawa, E. Kishi, Y. Sugawara, and S. Morita, Phys. Rev. B **52**, 5302 (1995).

[261] A. Socoliuc, R. Bennewitz, E. Gnecco, and E. Meyer, Phys. Rev. Lett. **92**, 134301 (2004).

[262] E. Gnecco, R. Bennewitz, T. Gyalog, Ch. Loppacher, M. Bammerlin, E. Meyer, and H.-J. Güntherodt, Phys. Rev. Lett. **84**, 1172 (2000).

[263] D. Gangloff, A. Bylinskii, I. Counts, W. Jhe, and V. Vuletić, Nature Phys **11**, 915 (2015).

[264] P. Bak, Reports on Progress in Physics **45**, 587 (1982).

[265] P. Rosenau, Physics Letters A **118**, 222 (1986).

[266] D. J. Bergman, E. Ben-Jacob, Y. Imry, and K. Maki, Phys. Rev. A **27**, 3345 (1983).

[267] R. MacKenzie, M. B. Paranjape, and W. J. Zakrzewski, eds., *Solitons: Properties, Dynamics, Interactions, Applications* (Springer New York, New York, NY, 2000).

[268] N. Manton and P. Sutcliffe, *Topological Solitons*, Cambridge Monographs on Mathematical Physics (Cambridge, Cambridge, U.K. ; New York, 2004).

[269] J. A. Krumhansl and J. R. Schrieffer, Phys. Rev. B **11**, 3535 (1975).

[270] R. Hirota, J. Phys. Soc. Jpn. **33**, 1459 (1972).

[271] R. Ravelo, M. El-Batanouny, C. R. Willis, and P. Sodano, Phys. Rev. B **38**, 4817 (1988).

[272] P. Dash, Physics Letters A **104**, 309 (1984).

[273] S. Aubry, Physica D: Nonlinear Phenomena **103**, 201 (1997).

[274] S. Aubry, Physica D: Nonlinear Phenomena **216**, 1 (2006).

[275] S. V. Dmitriev, J. Micromech. Mol. Phys. **01**, 1630001 (2016).

[276] S. Flach, Phys. Rev. E **58**, R4116 (1998).

[277] S. Flach and C. Willis, Physics Reports **295**, 181 (1998).

[278] S. Flach and A. V. Gorbach, Physics Reports **467**, 1 (2008).

[279] S. Flach, NOLTA **3**, 12 (2012).

[280] E. A. Korznikova, A. Y. Morkina, M. Singh, A. M. Krivtsov, V. A. Kuzkin, V. A. Gani, Y. V. Bebikhov, and S. V. Dmitriev, Eur. Phys. J. B **93**, 123 (2020).

[281] Y. Y. Yamaguchi and Y. Doi, Phys. Rev. E **97**, 062218 (2018).

[282] B. V. Chirikov, Physics Reports **52**, 263 (1979).

[283] S. Aubry and P. Y. L. Daeron, Physica D: Nonlin. Phenom. **8**, 381 (1983).

[284] J. D. Meiss, Rev. Mod. Phys. **64**, 795 (1992).

[285] H. G. Schuster and W. Just, *Deterministic Chaos An Introduction*, 4th ed. (Wiley-VCH, Weinheim, 2006).

[286] A. B. Givental, B. A. Khesin, J. E. Marsden, A. N. Varchenko, V. A. Vassiliev, O. Y. Viro, and V. M. Zakalyukin, eds., "Proof of a theorem of A. N. Kolmogorov on the invariance of quasi-periodic motions under small perturbations of the Hamiltonian," in *Collected Works* (Springer Berlin Heidelberg, Berlin, Heidelberg, 2009) pp. 267–294.

[287] S. C. Ying, Phys. Rev. B **3**, 4160 (1971).

[288] G. Theodorou and T. M. Rice, Phys. Rev. B **18**, 2840 (1978).

[289] S. Aubry, Physica D: Nonlin. Phen. **7**, 240 (1983).

[290] M. Peyrard and S. Aubry, J. Phys. C: Solid State Phys. **16**, 1593 (1983).

[291] B. B. Mandelbrot, *The Fractal Geometry of Nature* (W.H. Freeman, San Francisco, 1982).

[292] R. C. Black and I. I. Satija, Phys. Rev. B **44**, 4089 (1991).

[293] B. Sutherland, Phys. Rev. A **8**, 2514 (1973).

[294] S. E. Burkov, B. E. C. Koltenbah, and L. W. Bruch, Phys. Rev. B **53**, 14179 (1996).

[295] W. L. McMillan, Phys. Rev. B **16**, 4655 (1977).

[296] A. D. Novaco, Phys. Rev. B **22**, 1645 (1980).

[297] R. Peierls, Proc. of the Phys. Soc. **52**, 34 (1940).

[298] F. R. N. Nabarro, Proc. Phys. Soc. **59**, 256 (1947).

[299] R. Boesch, P. Stancioff, and C. R. Willis, Phys. Rev. B **38**, 6713 (1988).

[300] P. Stancioff, C. Willis, M. El-Batanouny, and S. Burdick, Phys. Rev. B **33**, 1912 (1986).

[301] C. Willis, M. El-Batanouny, and P. Stancioff, Phys. Rev. B **33**, 1904 (1986).

[302] R. Boesch and C. R. Willis, Phys. Rev. B **42**, 6371 (1990).

[303] A. Igarashi and T. Munakata, J. Phys. Soc. Jpn. **58**, 4025 (1989).

[304] J. B. Sokoloff, Phys. Rev. B **16**, 3367 (1977).

[305] J. E. Sacco and J. B. Sokoloff, Phys. Rev. B **18**, 6549 (1978).

[306] M. Peyrard and M. D. Kruskal, Physica D: Nonlinear Phenomena **14**, 88 (1984).

[307] C. R. Willis and R. Boesch, Phys. Rev. B **41**, 4570 (1990).

[308] T. Munakata and A. Igarashi, Phys. Rev. B **46**, 13786 (1992).

[309] O. M. Braun, T. Dauxois, M. V. Paliy, and M. Peyrard, Phys. Rev. B **54**, 321 (1996).

[310] L. M. Floría and J. J. Mazo, Adv. in Phys. **45**, 505 (1996).

[311] F. C. Frank and J. H. van der Merwe, Proc. R. Soc. Lond. A **198**, 205 (1949).

[312] F. C. Frank and J. H. van der Merwe, Proc. R. Soc. Lond. A **198**, 216 (1949).

[313] I. Markov and V. Karaivanov, Thin Solid Films **61**, 115 (1979).

[314] J. A. Snyman and J. H. V. D. Merwe, Surface Science **42**, 190 (1974).

[315] Y. Braiman, J. Baumgarten, and J. Klafter, Phys. Rev. B **47**, 11159 (1993).

[316] Y. Braiman, J. Baumgarten, J. Jortner, and J. Klafter, Phys. Rev. Lett. **65**, 2398 (1990).

[317] S. R. Sharma, B. Bergersen, and B. Joos, Phys. Rev. B **29**, 6335 (1984).

[318] A. Kovalev, Fiz. Tverd. Tela **21**, 1729 (1979).

[319] A. Kwaśniewski, P. Machnikowski, and P. Magnuszewski, Phys. Rev. E **59**, 2347 (1999).

[320] Y. Braiman, F. Family, and H. G. E. Hentschel, Phys. Rev. E **53**, R3005 (1996).

[321] O. Braun, Surface Science **230**, 262 (1990).

[322] F. Borgonovi, I. Guarneri, and D. L. Shepelyansky, Phys. Rev. Lett. **63**, 2010 (1989).

[323] F. Borgonovi, I. Guarneri, and D. Shepelyansky, Z. Physik B - Condensed Matter **79**, 133 (1990).

[324] B. Hu and B. Li, Europhys. Lett. **46**, 655 (1999).

[325] C.-L. Ho and C.-I. Chou, Phys. Rev. E **63**, 016203 (2000).

[326] G. P. Berman, E. N. Bulgakov, and D. K. Campbell, Physica D: Nonlinear Phenomena **107**, 161 (1997).

[327] G. P. Berman, E. N. Bulgakov, and D. K. Campbell, Phys. Rev. B **49**, 8212 (1994).

[328] O. V. Zhirov, G. Casati, and D. L. Shepelyansky, Phys. Rev. E **67**, 056209 (2003).

[329] Y. Ma, J. Wang, X. Xu, Q. Wei, W. Zhu, and S. Kais, J. Phys. Soc. Jpn. **83**, 094605 (2014).

[330] Y. Ma, J. Wang, X. Xu, Q. Wei, and S. Kais, J. Phys. Soc. Jpn. **83**, 124603 (2014).

[331] P. M. Bonetti, A. Rucci, M. L. Chiofalo, and V. Vuletić, Phys. Rev. Research **3**, 013031 (2021).

[332] B. Hu and B. Li, Physica A **288**, 81 (2000).

[333] B. Hu and J. X. Wang, Phys. Rev. B **73**, 184305 (2006).

[334] M. Peyrard, ed., *Nonlinear Excitations in Biomolecules: Les Houches School, May 30 to June 4, 1994* (Springer Berlin Heidelberg, Berlin, Heidelberg, 1995).

[335] M. Dienwiebel, G. S. Verhoeven, N. Pradeep, J. W. M. Frenken, J. A. Heimberg, and H. W. Zandbergen, Phys. Rev. Lett. **92**, 126101 (2004).

[336] T. Bohlein, J. Mikhael, and C. Bechinger, Nature Mater **11**, 126 (2012).

[337] O. M. Braun, Yu. S. Kivshar, and I. I. Zelenskaya, Phys. Rev. B **41**, 7118 (1990).

[338] D. A. Gangloff, A. Bylinskii, and V. Vuletić, Phys. Rev. Research **2**, 013380 (2020).

[339] I. Counts, D. Gangloff, A. Bylinskii, J. Hur, R. Islam, and V. Vuletić, Phys. Rev. Lett. **119**, 043601 (2017).

[340] H. L. Partner, R. Nigmatullin, T. Burgermeister, J. Keller, K. Pyka, M. B. Plenio, A. Retzker, W. H. Zurek, A. del Campo, and T. E. Mehlstäubler, Physica B: Condensed Matter **460**, 114 (2015).

[341] J. Kiethe, R. Nigmatullin, T. Schmirander, D. Kalincev, and T. E. Mehlstäubler, New J. of Phys. **20**, 123017 (2018).

[342] U. Tanaka, M. Nakamura, K. Hayasaka, A. Bautista-Salvador, C. Ospelkaus, and T. E. Mehlstäubler, Quantum Sci. Technol. **6**, 024010 (2021).

[343] N. W. Ashcroft and N. D. Mermin, *Solid State Physics* (Holt, Rinehart and Winston, New York, 1976).

[344] D. W. Hahn and M. N. Özişik, *Heat Conduction* (John Wiley & Sons, Inc., Hoboken, NJ, USA, 2012).

[345] X.-L. Deng, D. Porras, and J. I. Cirac, Phys. Rev. A **72**, 063407 (2005).

[346] T. Kinoshita, T. Wenger, and D. S. Weiss, Nature **440**, 900 (2006).

[347] X.-L. Deng, D. Porras, and J. I. Cirac, Phys. Rev. A **77**, 033403 (2008).

[348] L. Timm, H. Weimer, L. Santos, and T. E. Mehlstäubler, Phys. Rev. Research **2**, 033198 (2020).

[349] L. Timm, H. Weimer, L. Santos, and T. E. Mehlstäubler, "Heat transport in a Coulomb ion crystal with a topological defect," (2023).

[350] F. Bloch, Z. Physik **52**, 555 (1929).

[351] C. Kittel, *Introduction to Solid State Physics*, 8th ed. (Wiley, Hoboken, NJ, 2005).

[352] E. Fermi, J. Pasta, and S. Ulam, Los Alamos Report No. LA-1940 (1955).

[353] E. Altman and R. Vosk, Annual Review of Condensed Matter Physics **6**, 383 (2015).

[354] L. Barbiero, C. Menotti, A. Recati, and L. Santos, Phys. Rev. B **92**, 180406 (2015).

[355] G. Clos, D. Porras, U. Warring, and T. Schaetz, Phys. Rev. Lett. **117**, 170401 (2016).

[356] N. Y. Yao, C. R. Laumann, J. I. Cirac, M. D. Lukin, and J. E. Moore, Phys. Rev. Lett. **117**, 240601 (2016).

[357] E. van Nieuwenburg, Y. Baum, and G. Refael, Proc Natl Acad Sci USA **116**, 9269 (2019).

[358] D. A. Abanin, E. Altman, I. Bloch, and M. Serbyn, Rev. Mod. Phys. **91**, 021001 (2019).

[359] R. Yao and J. Zakrzewski, Phys. Rev. B **102**, 014310 (2020).

[360] R. Yao and J. Zakrzewski, Phys. Rev. B **102**, 104203 (2020).

[361] V. Bormuth, V. Varga, J. Howard, and E. Schaffer, Science **325**, 870 (2009).

[362] S. W. Englander, N. R. Kallenbach, A. J. Heeger, J. A. Krumhansl, and S. Litwin, Proceedings of the National Academy of Sciences **77**, 7222 (1980).

[363] F. Kühner, J. Morfill, R. A. Neher, K. Blank, and H. E. Gaub, Biophysical Journal **92**, 2491 (2007).

[364] W. P. Su, J. R. Schrieffer, and A. J. Heeger, Phys. Rev. Lett. **42**, 1698 (1979).

[365] S. Haze, Y. Tateishi, A. Noguchi, K. Toyoda, and S. Urabe, Phys. Rev. A **85**, 031401 (2012).

[366] R. Matjeschk, C. Schneider, M. Enderlein, T. Huber, H. Schmitz, J. Glueckert, and T. Schaetz, New J. Phys. **14**, 035012 (2012).

[367] H. Schmitz, R. Matjeschk, Ch. Schneider, J. Glueckert, M. Enderlein, T. Huber, and T. Schaetz, Phys. Rev. Lett. **103**, 090504 (2009).

[368] F. Zähringer, G. Kirchmair, R. Gerritsma, E. Solano, R. Blatt, and C. F. Roos, Phys. Rev. Lett. **104**, 100503 (2010).

[369] R. Ohira, S. Kume, H. Takahashi, and K. Toyoda, Quantum Sci. Technol. **6**, 024015 (2021).

[370] Y. S. Kivshar and B. A. Malomed, Rev. Mod. Phys. **61**, 763 (1989).

[371] E. Schrödinger, Ann. Phys. **349**, 916 (1914).

[372] I. Newton, Phil. Trans. R. Soc. **22**, 824 (1701).

[373] J. B. J. Fourier, *Théorie Analytique de La Chaleur*, 1st ed. (Cambridge University Press, Cambridge, 2009).

[374] T. L. Bergman, A. Lavine, and F. P. Incropera, *Fundamentals of Heat and Mass Transfer*, 8th ed. (John Wiley & Sons, Inc., Hoboken, NJ, 2019).

[375] A. Casher and J. L. Lebowitz, J. of Math. Phys. **12**, 1701 (1971).

[376] F. Bonetto, J. L. Lebowitz, and L. Rey-Bellet, "Fourier's law: A challenge to theorists," in *Mathematical Physics 2000* (Imperial College Press, 2000) pp. 128–150.

[377] Z. Rieder, J. L. Lebowitz, and E. Lieb, Journal of Mathematical Physics **8**, 1073 (1967).

[378] H. Nakazawa, Progress of Theor.l Phys. Supp. **45**, 231 (1970).

[379] M. Born, Z. Physik **7**, 217 (1921).

[380] M. Born, *Atomtheorie des Festen Zustandes (Dynamik der Kristallgitter)* (Vieweg+Teubner Verlag, Wiesbaden, 1923).

[381] R. Peierls, Ann. Phys. **395**, 1055 (1929).

[382] Th. v. Kármán, Naturwissenschaften **17**, 385 (1929).

[383] C. W. Chang, D. Okawa, H. Garcia, A. Majumdar, and A. Zettl, Phys. Rev. Lett. **101**, 075903 (2008).

[384] P. L. Garrido, P. I. Hurtado, and B. Nadrowski, Phys. Rev. Lett. **86**, 5486 (2001).

[385] B. Hu, B. Li, and H. Zhao, Phys. Rev. E **57**, 2992 (1998).

[386] L. W. Lee and A. Dhar, Phys. Rev. Lett. **95**, 094302 (2005).

[387] B. Li, L. Wang, and B. Hu, Phys. Rev. Lett. **88**, 223901 (2002).

[388] T. Mai, A. Dhar, and O. Narayan, Phys. Rev. Lett. **98**, 184301 (2007).

[389] O. Narayan and S. Ramaswamy, Phys. Rev. Lett. **89**, 200601 (2002).

[390] A. V. Savin and O. V. Gendelman, Phys. Rev. E **67**, 041205 (2003).

[391] G.-D. Lin and L.-M. Duan, New J. of Phys. **13**, 075015 (2011).

[392] A. Asadian, D. Manzano, M. Tiersch, and H. J. Briegel, Phys. Rev. E **87**, 012109 (2013).

[393] R. R. Ávila, E. Pereira, and D. L. Teixeira, Physica A: Statistical Mechanics and its Applications **423**, 51 (2015).

[394] A. Bermudez, M. Bruderer, and M. B. Plenio, Phys. Rev. Lett. **111**, 040601 (2013).

[395] J. Brox, P. Kiefer, M. Bujak, T. Schaetz, and H. Landa, Phys. Rev. Lett. **119**, 153602 (2017).

[396] T. Chen, V. Balachandran, C. Guo, and D. Poletti, Phys. Rev. E **102**, 012155 (2020).

[397] N. Freitas, E. A. Martinez, and J. P. Paz, Phys. Scr. **91**, 013007 (2016).

[398] S. Iubini, P. Di Cintio, S. Lepri, R. Livi, and L. Casetti, Phys. Rev. E **97**, 032102 (2018).

[399] D. Manzano, M. Tiersch, A. Asadian, and H. J. Briegel, Phys. Rev. E **86**, 061118 (2012).

[400] Z.-C. Mao, Y.-Z. Xu, Q.-X. Mei, W.-D. Zhao, Y. Jiang, Z.-J. Cheng, X.-Y. Chang, L. He, L. Yao, Z.-C. Zhou, Y.-K. Wu, and L.-M. Duan, Phys. Rev. A **105**, 033107 (2022).

[401] J. P. Pekola and B. Karimi, Rev. Mod. Phys. **93**, 041001 (2021).

[402] J. Rossnagel, S. T. Dawkins, K. N. Tolazzi, O. Abah, E. Lutz, F. Schmidt-Kaler, and K. Singer, Science **352**, 325 (2016).

[403] A. Ruiz-García, J. J. Fernández, and D. Alonso, Phys. Rev. E **99**, 062105 (2019).

[404] A. Ruiz, D. Alonso, M. B. Plenio, and A. del Campo, Phys. Rev. B **89**, 214305 (2014).

[405] D. Segal and B. K. Agarwalla, Annu. Rev. Phys. Chem. **67**, 185 (2016).

[406] J. Wang, S. V. Dmitriev, and D. Xiong, Phys. Rev. Research **2**, 013179 (2020).

[407] O. V. Zhirov, J. Lages, and D. L. Shepelyansky, Eur. Phys. J. D **73**, 149 (2019).

[408] P. E. Kloeden and E. Platen, *Numerical Solution of Stochastic Differential Equations* (Springer Berlin Heidelberg, Berlin, Heidelberg, 1992).

[409] E. A. Novikov, J. Exptl. Theoret. Phys. **20**, 1290 (1965).

[410] Z. Liu, L. Chen, J. Li, H. Zhang, C. Li, F. Zhou, S. Su, L. Yan, and M. Feng, Phys. Rev. A **102**, 033116 (2020).

[411] P. Weckesser, F. Thielemann, D. Hoenig, A. Lambrecht, L. Karpa, and T. Schaetz, Phys. Rev. A **103**, 013112 (2021).

[412] G.-D. Lin and L.-M. Duan, Quantum Inf Process **15**, 5299 (2016).

[413] H. E. Stanley, *Introduction to Phase Transitions and Critical Phenomena* (Oxford University Press, New York, 1987).

[414] R. J. Baxter, "Exactly Solved Models in Statistical Mechanics," in *Integrable Systems in Statistical Mechanics*, Vol. 1 (World Scientific, 1985) pp. 5–63.

[415] A. Dutta, G. Aeppli, B. K. Chakrabarti, U. Divakaran, T. F. Rosenbaum, and D. Sen, *Quantum Phase Transitions in Transverse Field Spin Models: From Statistical Physics to Quantum Information*, 1st ed. (Cambridge University Press, 2015).

[416] P. C. Haljan, K.-A. Brickman, L. Deslauriers, P. J. Lee, and C. Monroe, Phys. Rev. Lett. **94**, 153602 (2005).

[417] A. Bermudez, T. Schaetz, and D. Porras, New J. Phys. **14**, 053049 (2012).

[418] W. Chen, J. Gan, J.-N. Zhang, D. Matuskevich, and K. Kim, Chinese Phys. B **30**, 060311 (2021).

[419] K. Toyoda, Y. Matsuno, A. Noguchi, S. Haze, and S. Urabe, Phys. Rev. Lett. **111**, 160501 (2013).

[420] J. Zhang, B. T. Chow, S. Ejtemaee, and P. C. Haljan, npj Quantum Inf **9**, 68 (2023).

[421] T. Dessup, T. Maimbourg, C. Coste, and M. Saint Jean, Phys. Rev. E **91**, 022908 (2015).

[422] T. Dessup, C. Coste, and M. Saint Jean, Phys. Rev. E **91**, 032917 (2015).

[423] M. I. Dykman, R. Mannella, P. V. E. McClintock, F. Moss, and S. M. Soskin, Phys. Rev. A **37**, 1303 (1988).

[424] J. D. Baltrusch, C. Cormick, G. De Chiara, T. Calarco, and G. Morigi, Phys. Rev. A **84**, 063821 (2011).

[425] J. D. Baltrusch, C. Cormick, and G. Morigi, Phys. Rev. A **86**, 032104 (2012).

[426] T. Zanca, F. Pellegrini, G. E. Santoro, and E. Tosatti, Proc. Natl. Acad. Sci. U.S.A. **115**, 3547 (2018).

[427] D. Kalincev, L. S. Dreissen, A. P. Kulosa, C.-H. Yeh, H. A. Fürst, and T. E. Mehlstäubler, Quantum Sci. Technol. **6**, 034003 (2021).

[428] K. G. Johnson, J. D. Wong-Campos, A. Restelli, K. A. Landsman, B. Neyenhuis, J. Mizrahi, and C. Monroe, Review of Scientific Instruments **87**, 053110 (2016).

[429] J. Hubbard, Proc. R. Soc. Lond. A **276**, 238 (1963).

[430] A. Bermudez, T. Schaetz, and D. Porras, Phys. Rev. Lett. **107**, 150501 (2011).

[431] A. Bermudez and D. Porras, New J. Phys. **17**, 103021 (2015).

[432] J. Casanova, L. Lamata, I. L. Egusquiza, R. Gerritsma, C. F. Roos, J. J. García-Ripoll, and E. Solano, Phys. Rev. Lett. **107**, 260501 (2011).

[433] A. Bermudez, J. Almeida, F. Schmidt-Kaler, A. Retzker, and M. B. Plenio, Phys. Rev. Lett. **107**, 207209 (2011).

[434] A. Bermudez, J. Almeida, K. Ott, H. Kaufmann, S. Ulm, U. Poschinger, F. Schmidt-Kaler, A. Retzker, and M. B Plenio, New J. Phys. **14**, 093042 (2012).

[435] A. Bermudez and M. B. Plenio, Phys. Rev. Lett. **109**, 010501 (2012).

[436] J. W. Britton, B. C. Sawyer, A. C. Keith, C.-C. J. Wang, J. K. Freericks, H. Uys, M. J. Biercuk, and J. J. Bollinger, Nature **484**, 489 (2012).

[437] A. Friedenauer, H. Schmitz, J. T. Glueckert, D. Porras, and T. Schaetz, Nature Phys **4**, 757 (2008).

[438] R. Schmied, J. H. Wesenberg, and D. Leibfried, New J. Phys. **13**, 115011 (2011).

[439] A. Eckardt, Rev. Mod. Phys. **89**, 011004 (2017).

[440] S. Geier, N. Thaicharoen, C. Hainaut, T. Franz, A. Salzinger, A. Tebben, D. Grimshandl, G. Zürn, and M. Weidemüller, Science **374**, 1149 (2021).

[441] P. Hauke, O. Tieleman, A. Celi, C. Ölschläger, J. Simonet, J. Struck, M. Weinberg, P. Windpassinger, K. Sengstock, M. Lewenstein, and A. Eckardt, Phys. Rev. Lett. **109**, 145301 (2012).

[442] H. Labuhn, D. Barredo, S. Ravets, S. de Léséleuc, T. Macrì, T. Lahaye, and A. Browaeys, Nature **534**, 667 (2016).

[443] Y.-J. Lin, K. Jiménez-García, and I. B. Spielman, Nature **471**, 83 (2011).

[444] M. S. Rudner, N. H. Lindner, E. Berg, and M. Levin, Phys. Rev. X **3**, 031005 (2013).

[445] C. Sanner, N. Huntemann, R. Lange, C. Tamm, E. Peik, M. S. Safronova, and S. G. Porsev, Nature **567**, 204 (2019).

[446] A. D. Greentree, C. Tahan, J. H. Cole, and L. C. L. Hollenberg, Nature Phys **2**, 856 (2006).

[447] M. J. Hartmann, F. G. S. L. Brandão, and M. B. Plenio, Nature Phys **2**, 849 (2006).

[448] E. K. Irish, C. D. Ogden, and M. S. Kim, Phys. Rev. A **77**, 033801 (2008).

[449] J. Koch and K. Le Hur, Phys. Rev. A **80**, 023811 (2009).

[450] Q. Li, J.-L. Ma, T. Huang, L. Tan, H.-Q. Gu, and W.-M. Liu, EPL **134**, 20007 (2021).

[451] M. I. Makin, J. H. Cole, C. Tahan, L. C. L. Hollenberg, and A. D. Greentree, Phys. Rev. A **77**, 053819 (2008).

[452] M. I. Makin, J. H. Cole, C. D. Hill, A. D. Greentree, and L. C. L. Hollenberg, Phys. Rev. A **80**, 043842 (2009).

[453] A. Mering, M. Fleischhauer, P. A. Ivanov, and K. Singer, Phys. Rev. A **80**, 053821 (2009).

[454] C. D. Ogden, E. K. Irish, and M. S. Kim, Phys. Rev. A **78**, 063805 (2008).

[455] R. Peña, F. Torres, and G. Romero, New J. Phys. **22**, 033034 (2020).

[456] D. Rossini and R. Fazio, Phys. Rev. Lett. **99**, 186401 (2007).

[457] D. Rossini, R. Fazio, and G. Santoro, Europhys. Lett. **83**, 47011 (2008).

[458] S. Schmidt and G. Blatter, Phys. Rev. Lett. **103**, 086403 (2009).

[459] M. T. C. Wong and C. K. Law, Phys. Rev. A **83**, 055802 (2011).

[460] J. Dalibard, F. Gerbier, G. Juzeliūnas, and P. Öhberg, Rev. Mod. Phys. **83**, 1523 (2011).

[461] X.-L. Qi and S.-C. Zhang, Rev. Mod. Phys. **83**, 1057 (2011).

[462] M. Aidelsburger, M. Atala, M. Lohse, J. T. Barreiro, B. Paredes, and I. Bloch, Phys. Rev. Lett. **111**, 185301 (2013).

[463] H. Miyake, G. A. Siviloglou, C. J. Kennedy, W. C. Burton, and W. Ketterle, Phys. Rev. Lett. **111**, 185302 (2013).

[464] T. Shi and J. I. Cirac, Phys. Rev. A **87**, 013606 (2013).

[465] N. Goldman, G. Juzeliūnas, P. Öhberg, and I. B. Spielman, Rep. Prog. Phys. **77**, 126401 (2014).

[466] N. Goldman and J. Dalibard, Phys. Rev. X **4**, 031027 (2014).

[467] N. R. Cooper, J. Dalibard, and I. B. Spielman, Rev. Mod. Phys. **91**, 015005 (2019).

[468] M. Bukov, L. D'Alessio, and A. Polkovnikov, Advances in Physics **64**, 139 (2015).

[469] P. Kiefer, F. Hakelberg, M. Wittemer, A. Bermúdez, D. Porras, U. Warring, and T. Schaetz, Phys. Rev. Lett. **123**, 213605 (2019).

[470] K. Wintersperger, C. Braun, F. N. Ünal, A. Eckardt, M. D. Liberto, N. Goldman, I. Bloch, and M. Aidelsburger, Nat. Phys. **16**, 1058 (2020).

[471] C. Weitenberg and J. Simonet, Nat. Phys. **17**, 1342 (2021).

[472] A. Bermudez, N. Goldman, A. Kubasiak, M. Lewenstein, and M. A. Martin-Delgado, New J. Phys. **12**, 033041 (2010).

[473] F. Hakelberg, P. Kiefer, M. Wittemer, U. Warring, and T. Schaetz, Phys. Rev. Lett. **123**, 100504 (2019).

[474] M. Mielenz, H. Kalis, M. Wittemer, F. Hakelberg, U. Warring, R. Schmied, M. Blain, P. Maunz, D. L. Moehring, D. Leibfried, and T. Schaetz, Nat Commun **7**, 11839 (2016).

[475] M. Aidelsburger, S. Nascimbene, and N. Goldman, Comptes Rendus Physique **19**, 394 (2018).

[476] D. G. Angelakis, ed., *Quantum Simulations with Photons and Polaritons*, Quantum Science and Technology (Springer International Publishing, Cham, 2017).

[477] J. Larson and T. Mavrogordatos, *The Jaynes–Cummings Model and Its Descendants: Modern Research Directions* (IOP Publishing, 2021).

[478] M. P. A. Fisher, P. B. Weichman, G. Grinstein, and D. S. Fisher, Phys. Rev. B **40**, 546 (1989).

[479] T. D. Kühner and H. Monien, Phys. Rev. B **58**, R14741 (1998).

[480] M. Greiner, O. Mandel, T. Esslinger, T. W. Hänsch, and I. Bloch, Nature **415**, 39 (2002).

[481] L. Tonks, Phys. Rev. **50**, 955 (1936).

[482] M. Girardeau, Journal of Mathematical Physics **1**, 516 (1960).

[483] K. Winkler, G. Thalhammer, F. Lang, R. Grimm, J. Hecker Denschlag, A. J. Daley, A. Kantian, H. P. Büchler, and P. Zoller, Nature **441**, 853 (2006).

[484] P. M. Preiss, R. Ma, M. E. Tai, A. Lukin, M. Rispoli, P. Zupancic, Y. Lahini, R. Islam, and M. Greiner, Science **347**, 1229 (2015).

[485] J. H. Van Vleck, Phys. Rev. **33**, 467 (1929).

[486] I. Shavitt and L. T. Redmon, The Journal of Chemical Physics **73**, 5711 (1980).

[487] Y. Wang, S. Shevate, T. M. Wintermantel, M. Morgado, G. Lochead, and S. Whitlock, npj Quantum Inf **6**, 54 (2020).

[488] A. Bermudez, M. A. Martin-Delgado, and D. Porras, New J. Phys. **12**, 123016 (2010).

[489] N. Trautmann and P. Hauke, Phys. Rev. A **97**, 023606 (2018).

[490] S. Diehl, A. Micheli, A. Kantian, B. Kraus, H. P. Büchler, and P. Zoller, Nature Phys **4**, 878 (2008).

[491] A. Giraldo, B. Krauskopf, N. G. R. Broderick, J. A. Levenson, and A. M. Yacomotti, New J. Phys. **22**, 043009 (2020).

[492] A. Le Boité, G. Orso, and C. Ciuti, Phys. Rev. Lett. **110**, 233601 (2013).

[493] A. Le Boité, G. Orso, and C. Ciuti, Phys. Rev. A **90**, 063821 (2014).

[494] U. Naether, F. Quijandría, J. J. García-Ripoll, and D. Zueco, Phys. Rev. A **91**, 033823 (2015).

[495] T. Tomita, S. Nakajima, I. Danshita, Y. Takasu, and Y. Takahashi, Sci. Adv. **3**, e1701513 (2017).

[496] F. Vicentini, F. Minganti, R. Rota, G. Orso, and C. Ciuti, Phys. Rev. A **97**, 013853 (2018).

[497] H. Weimer, A. Kshetrimayum, and R. Orús, Rev. Mod. Phys. **93**, 015008 (2021).

[498] T. Dessup, T. Maimbourg, C. Coste, and M. Saint Jean, Phys. Rev. E **91**, 022908 (2015).

[499] Y. H. Teoh, M. Sajjan, Z. Sun, F. Rajabi, and R. Islam, Phys. Rev. A **104**, 022420 (2021).

[500] D. Kielpinski, B. E. King, C. J. Myatt, C. A. Sackett, Q. A. Turchette, W. M. Itano, C. Monroe, D. J. Wineland, and W. H. Zurek, Phys. Rev. A **61**, 032310 (2000).

[501] D. J. Larson, J. C. Bergquist, J. J. Bollinger, W. M. Itano, and D. J. Wineland, Phys. Rev. Lett. **57**, 70 (1986).

[502] I. Cohen and A. Retzker, Phys. Rev. Lett. **112**, 040503 (2014).

[503] I. Cohen, P. Richerme, Z.-X. Gong, C. Monroe, and A. Retzker, Phys. Rev. A **92**, 012334 (2015).

Glossary

This document is incomplete. The external file associated with the glossary 'main' (which should be called `PhDThesis_Timm_AcceptedClean.gls`) hasn't been created.

Check the contents of the file `PhDThesis_Timm_AcceptedClean.glo`. If it's empty, that means you haven't indexed any of your entries in this glossary (using commands like `\gls` or `\glsadd`) so this list can't be generated. If the file isn't empty, the document build process hasn't been completed.

If you don't want this glossary, add `nomain` to your package option list when you load `glossaries-extra.sty`. For example:

```
\usepackage[nomain]{glossaries-extra}
```

Try one of the following:

- Add `automake` to your package option list when you load `glossaries-extra.sty`. For example:

  ```
  \usepackage[automake]{glossaries-extra}
  ```

- Run the external (Lua) application:

  ```
  makeglossaries-lite.lua "PhDThesis_Timm_AcceptedClean"
  ```

- Run the external (Perl) application:

  ```
  makeglossaries "PhDThesis_Timm_AcceptedClean"
  ```

Then rerun LaTeX on this document.

This message will be removed once the problem has been fixed.

Curriculum vitae

Personal information

Name	Lars Timm
Gender	male
Date of Birth	8th of February 1995
Place of Birth	Berlin-Neukölln
Nationality	German

Education

2019 - 2023	**PhD Physics**, Gottfried Wilhelm Leibniz Universität Hannover, Hanover, Germany
2017 - 2018	**ERASMUS Semester**, Chalmers University of Technology, Gothenburg, Sweden
2016 - 2019	**M.Sc. Physics**, Gottfried Wilhelm Leibniz Universität Hannover, Hanover, Germany
2013 - 2016	**B.Sc. Physics**, Technische Universität Braunschweig, Braunschweig, Germany
2012 - 2013	**Voluntary year**, Kinderzentrum Pelzerhaken, Neustadt i. H., Germany
2004 - 2012	**Secondary School**, Klaus-Groth-Schule, Neumünster, Germany

List of Publications

- L. Timm, H. Weimer, L. Santos and T.E. Mehlstäubler
  Heat transport in a Coulomb ion crystal with a topological defect
  arXiv:2306:05845

- L. Timm, L.A. Rüffert, H. Weimer, L. Santos and T.E. Mehlstäubler
  Quantum nanofriction in trapped ion chains with a topological defect
  Phys. Rev. Research 3, 043141 (2021)

- J. Kiethe, L. Timm, H. Landa, D. Kalincev, G. Morigi, T.E. Mehlstäubler
  Finite-temperature spectrum at the symmetry-breaking linear to zigzag transition
  Phys. Rev. B 103, 104106 (2021)

- L. Timm, H. Weimer, L. Santos, T.E. Mehlstäubler
  Energy localization in an atomic chain with a topological soliton
  Phys. Rev. Research 2, 033198 (2020)